Narrowing down supernova progenitors with (spectro)polarimetry

Aleksandar Cikota

München 2018

Narrowing down supernova progenitors with (spectro)polarimetry

Aleksandar Cikota

Dissertation
an der Fakultät für Physik
der Ludwig–Maximilians–Universität
München

vorgelegt von
Aleksandar Cikota
aus Osijek, Kroatien

München, den 9.5.2018

Erstgutachter: Prof. Dr. A. W. A. Pauldrach
Zweitgutachter: Prof. Dr. A. Weiss
Tag der mündlichen Prüfung: 17.7.2018

In memory of my father.

Zusammenfassung

Unter vielen Anwendungsbeispielen in der Astrophysik erlaubt uns Breitbandpolarimetrie und Spektropolarimetrie die Staubeigenschaften und dreidimensionalen Formen von punktförmigen Lichtquellen zu erforschen, wie beispielsweise globale Asymmetrien und in Supernova-Explosionen ausgestoßenes Material.

Durch Staub stark gerötete Supernovae vom Typ Ia (SN Ia) mit niedrigen Proportionalitätsfaktor R_V zwischen dem Extinktionskoeffizienten und dem Farbexzess haben zudem außergewöhnliche lineare Polarisationskurven, die steil in Richtung blauer Wellenlängen ansteigen und Spitzenpolarisationswerte bei kurzen Wellenlängen erreichen ($\lambda_{\rm max} \lesssim 0.4\mu m$). Es ist nicht klar, warum Sichtlinien zu den SN Ia solch unterschiedliche Polarisationsprofile im Vergleich zu den interstellaren Sichtlinien in der Milchstraße haben, die normalerweise einen $\lambda_{\rm max}$ von $\sim 0.55\mu m$ haben.

Wir haben Polarisationsprofile von Sternen unserer Galaxie mit niedrigen R_V-Werten und abnormalen Extinktionskurven untersucht mit dem Ziel, Ähnlichkeiten zu der Polarisationsprofilen zu finden, die wir entlang den SN Ia Sichtlinien beobachten. Wir fanden, dass die Polarisationskurven konsistent sind mit einer größeren kohärenten Probe von Galaktischen Sternen aus der Literatur und keine Ähnlichkeit zu den Polarisationskurven zeigen, die in Richtung von SNe Ia mit niedrigen R_V-Werten beobachtet wurden. Es existiert eine Korrelation zwischen den Serkowski-Parametern K und $\lambda_{\rm max}$, allerdings haben wir keine signifikante Korrelation zwischen R_V und $\lambda_{\rm max}$ gefunden.

Unsere Simulationen zeigen, dass die K - $\lambda_{\rm max}$ Beziehung eine intrinsische Eigenschaft der Polarisation ist. Wir haben gezeigt, dass, um Polarisationskurven mit normalen λ_{max}-Werten und niedrigen R_V-Werten zu reproduzieren, eine Vielzahl von großen ($a \geq 0.1\mu m$) interstellaren Silikatkörnern im Staub enthalten sein muss.

Darüber hinaus untersuchten wir Kontinuumpolarisationsmessungen einer Ansammlung von Sternen auf dem asymptotischen Riesenast (AGB Sternen) und Post-AGB-Sternen (Proto-Planetarischen-Nebeln, PPN) aus der Literatur. Dabei fanden wir, dass einige PPNe ähnliche Polarisationskurven zu denen, entlang der SN Ia Sichtlinien, aufweisen. Diese Polarisationskurven der PPN werden durch Streuung am zirkumstellaren Staub erzeugt. Wir deuten an, dass anhand der Ähnlichkeit der Kontinuumpolarisationskurven, die Möglichkeit existiert, dass zumindest einige SN Ia während der Post-AGB-Phase des Begleitungsternes explodieren könnten, indem ein Weißer Zwerg mit dem Kern des Riesen verschmilzt. Wir spekulieren, dass die beobachtbare Ähnlichkeit der Polarisationskurven das "Core-Degenrate" Vorlöufermodell unterstützt.

Unter Verwendung von Archivdaten von 35 SNe Ia, beobachtet in insgesamt 128 Epochen mit FORS, untersuchten wir die Polarisation der Si II Linie, die eine zeitliche Entwicklung mit unterschiedlichen Polarisationsmaxima in unterschiedlichen Zeitepochen relativ zur maximalen Helligkeit zeigt. Wir haben die Δm_{15}-$P_{\rm SiII}$ Beziehung reproduziert und gezeigt, dass Objekte geringer Leuchkraft und übergangsobjekte niedrigere Polarisationswerte haben und sich unterhalb der Δm_{15}-$P_{\rm SiII}$ Beziehung befinden. Wir fanden eine statistisch signifikante Beziehung zwischen dem Grad der linearen Polarisation der Si II Linie und der Geschwindigkeit der Si II Line und weisen darauf hin, dass dies zusammen mit der Δm_{15}-$P_{\rm SiII}$ Beziehung mit dem Modell der verzögerten Detonation (Delayed-Detonation model, DDT) übereinstimmt. Eine Auswahl der SN Ia, die in mehreren Epochen beobachtet wurden, zeigt eine Entwicklung der Si II Linie in Form von Schleifen im Q–U Raum, die durch eine zeitliche Änderung der projizierten Geometrie des Silizium-Ausstoßes, während der nach innen gerichteten Bewegung der Photosphäre, erklärt werden kann. Zuletzt verglichen wir unsere statistische Stichprobe der Si II-Polarisation mit Vorhersagen für das DDT Modell, das Doppeldetonations Modell (DDET) und das Model der gewaltsamen Verschmelzung. Der Großteil der Beobachtungen ist mit den Vorhersagen für die DDT und DDET-Modelle konsistent aber zwischen diesen beiden kann nicht unterscheiden werden.

Ungewöhnlich helle Supernovae (Superluminous Supernovae, SLSN) sind die hellsten Supernova Explosionen im Universum. Ein mögliches Szenario, das solche Ereignisse erklären könnte, ist, dass wasserstoffarme SLSN-I von einem internen Motor, wie beispielsweise einem Magnetar oder einem akkretierenden Schwarzen Loch, angetrieben werden. Wir haben zum ersten Mal die zirkulare Polarisation von zwei SLSNe-I gemessen, um das Vorhandensein starker Magnetfelder oder kollimierter Jets zu testen, die das Licht zirkular polarisieren können. Beide SLSNe zeigen keinen Hinweis auf zirkular polarisiertes Licht. Trotz des fehlgeschlagenen Nachweises diskutieren wir, warum das Magnetarszenario nicht als treibender Motor ausgeschlossen werden kann. Darüber hinaus sind SLSNe in Galaxien mit extrem hoher Sternbildung zu finden und wahrscheinlich mit dem Tod sehr massiver Sterne verbunden. Ein Kennzeichen von sehr massiven Vorläufern wäre eine Tendenz zur Explosion in sehr dichten, im UV hellen, blauen Regionen. Wir untersuchten räumlich aufgelöste Eigenschaften der Muttergalaxien von zwei nahen wasserstoffarmen SLSN mit in mehreren Filtern aufgenommenen Beobachtungen mit dem *Hubble Space Telescope* und integraler Feldspektroskopie mit dem Multi Unit Spectroscopic Explorer (VLT/MUSE). Wir finden Anzeichen von Interaktion in beiden Galaxien und mutmaßen, dass die SLSN Explosionen von Sternen stammen könnten, die in durch Interaktion getriggerten Sternentstehungsgebieten erzeugt wurden. Wir haben gezeigt, dass hochauflösende Bildgebung und integrale Feldspektroskopie grundlegend sind für ein besseres Verständnis der SLSN Explosionsstellen und der Erforschung der Sternentstehung quer durch die Galaxien.

Abstract

Polarimetry (in its imaging and spectroscopic flavors) has very diverse applications in modern astrophysics and offers independent means for addressing a number of open problems. Among these, and particularly relevant in the field of Supernovae (hereafter SN), are the study of inter/circum-stellar dust properties and the analysis of the three-dimensional geometrical properties of unresolved sources. The latter provides insights on global and local asymmetries of SN explosions. These aspects are fundamental for our understanding of the phenomenon and are hardly approachable by any other observational technique. This thesis presents a number of applications of polarimetry to the SN field, with particular attention to the nature of their progenitors.

The first topic discussed in this thesis addresses a problem that has emerged more than a decade ago and concerns thermonuclear SN. The lines of sight to these objects typically show total-to-selective extinction ratio values, R_V, that are systematically lower than what is typical in the Galaxy. Recent polarimetric studies of highly reddened type Ia supernovae (SNe Ia) with low R_V values have revealed peculiar linear polarization curves raising toward blue wavelengths, with peak polarizations at short wavelengths ($\lambda_{\rm max} \lesssim 0.4\mu m$). These profiles clearly deviate for what is observed in the Milky Way (where sightlines to normal stars displays polarization curves with $\lambda_{\rm max} \sim 0.55\mu m$), for reasons that are not well understood and may be related to the environment in which these explosions occur (in terms of peculiar dust properties) and/or to local effects (e.g. scattering by circumstellar dust).

For this purpose, we investigate polarization profiles for a sample of Galactic stars with low R_V values, along anomalous extinction sightlines, with the aim of finding possible similarities with the polarization profiles that we observe in SN Ia sightlines. We find that the polarization curves are consistent with those of a larger coherent sample of Galactic stars from the literature, and do not show any similarity to the polarization curves observed toward SNe Ia with low R_V values. There is a correlation between the best-fit Serkowski parameters K and $\lambda_{\rm max}$, but we did not find any significant correlation between R_V and $\lambda_{\rm max}$. Our simulations show that the K-$\lambda_{\rm max}$ relationship is an intrinsic property of polarization. We have also shown that in order to reproduce polarization curves with normal $\lambda_{\rm max}$ and low R_V values, a population of large (a $\geq$ 0.1 μm) interstellar silicate grains must be contained in the dust. Furthermore, we examined continuum polarization measurements of a sample of asymptotic giant branch (AGB) and post-AGB stars (PPNe) from the literature, finding that some PPNe do have polarization curves similar to those observed along SNe Ia sight lines. The polarization detected in PPNe is known to be produced by scattering on circumstellar dust. In this context, we discuss the similarity and the possibility that at least some SNe Ia might explode during the post-AGB phase of their binary companion. We speculate that the peculiar SNe Ia polarization curves might provide observational support to the core-degenerate progenitor model for thermonuclear explosions.

The explosion geometry problem was tackled with a statistical approach, using archival data of 35 SNe Ia, observed with VLT-FORS at 128 epochs in total. In particular, we examined the polarization of the Si II line, which displays an evolution in time with a variety of peak polarization degrees, at different epochs relative to peak brightness. We reproduced the Δm_{15}–$P_{\rm SiII}$ relationship, and show that subluminous and transitional objects display lower polarization values, below the Δm_{15}–$P_{\rm SiII}$ relationship. We found a statistically significant relationship between the degree of linear polarization and the expansion velocity deduced for the Si II line, and suggest that this, along with the Δm_{15}–$P_{\rm SiII}$ relationship, is consistent with the delayed-detonation (DDT) model. A subsample of SNe, which have been observed at multiple epochs, displays an evolution the Si II line in form of Q–U loops, which may be explained by an evolution of the projected silicon ejecta geometry, as the time evolves and the photosphere recedes into the ejecta. Finally, we compared our statistical sample of the Si II polarization to predictions for the DDT, doubledetonation (DDET), and violent merger models. The observations are consistent, but not distinguishable, between predictions for the DDT and DDET models.

Superluminous supernovae (SLSNe) are the most luminous SNe in the universe. One possible scenario that might explain such luminosities is that SLSNe-I are powered by an internal engine different from core-collapse or thermonuclear runaway, such as a magnetar or an accreting black hole. In this framework, for the first time we measured circular polarization of two SLSNe-I, to test the presence of strong magnetic fields or collimated jets that can circularly polarize light. Both SLSNe show no evidence of circularly polarized light. Despite a non-detection, we discuss why the magnetar scneario can not be excluded as the powering engine. Moreover, SLSNe are found in extreme starforming galaxies and are probably connected with the death of massive stars. One hallmark of very massive progenitors would be a tendency to explode in very dense, UV-bright, blue regions. We investigate resolved host galaxy properties of two nearby hydrogen-poor SLSNe, using *Hubble Space Telescope* multi-filter images, and Multi Unit Spectroscopic Explorer (VLT/MUSE). We find interaction signatures for both galaxies, and speculate that SLSN explosions may originate from stars generated during star-formation episodes triggered by interaction. We demonstrate that high resolution imaging and integral field spectroscopy are fundamental for a better understanding of SLSNe explosion sites and how star formation varies across their host galaxies.

Contents

List of Figures

List of Tables

1. Introduction

1.1. Motivation and goals

Type Ia Supernovae (SNe Ia) are used as standard candles (after applying proper scaling relations, see e.g., Phillips 1993) to measure the accelerated expansion of the Universe. The ultimate future goal is to constrain the nature of dark energy, which requires accurate measurements of the equation-of-state parameter w.

Several upcoming sky surveys are expected to produce a massive amount of supernova discoveries which will lead to an improvement in the statistics and advances in SN Ia cosmology. The Large Synoptic Survey Telescope (LSST) alone is expected to detect 50 000 SNe Ia per year. Furthermore, future space missions will allow us to extend the SN Ia Hubble diagram to unprecedented limits. For instance, the Wide-Field Infrared Survey Telescope (WFIRST) will extend to $z \sim 2$, while the James Webb Space Telescope (JWST) will push this limit to $z \sim 4$ (Hook, 2013).

However, despite the availability of large samples, accurately determining the equation-of-state parameter w is difficult, due to systematic sources of error, such as dust extinction, and evolutionary effects on the progenitor system. It is known that SNe Ia are exploding carbon-oxygen (C/O) white dwarfs close to the Chandrasekhar mass limit. However, their evolutionary path and their exact progenitor systems are still not known. Identifying the SN Ia progenitors is important, to understand the evolution of their luminosity with cosmic time, depending on e.g., metallicity, age, dust, etc. (Riess & Livio, 2006).

The forthcoming surveys will also increase the sample of Superluminous Supernovae (SLSNe), which constitute a newly discovered class of Supernovae, that are extremely bright. They may include a few remaining examples of deaths of extremely massive, low metallicity stars, that in the early Universe may have played an important role for re-ionisation of the Universe. Having a large sample will make it possible to also use these objects as cosmological probes (Scovacricchi et al., 2016). Therefore, it is important to understand their progenitors.

This thesis is thus focused on narrowing down the progenitors of SNe Ia and SLSNe. To this aim, we investigated the circumstellar environments of SNe Ia and their ejecta asymetries (see Chapter 5) using linear (spectro)polarimetry observations obtained with ESO's FOcal Reducer/low dispersion Spectrograph (FORS, see Chapter 2 or Cikota et al. 2017b), but also Galactic objects that have polarization or extinction properties similar to SNe Ia (see Chapter 3 or Cikota et al. 2018a; and Chapter 4 or Cikota et al. 2017c), with the goal of better understanding the explosion mechanism and the environment in which they take place.

Furthermore, to learn more about the SLSNe, we tested the magnetar scenario using circular polarimetry (see Chapter 6 or Cikota et al. 2018b), and additionally investigated their host galaxies environment using integral-field spectroscopy data of a SLSN host galaxy for first time (see Chapter 7 or Cikota et al. 2017a).

1.2. Polarization

Polarimetry is a technique that provides additional information to those given by simple intensity measurements (photometry and spectroscopy) and has many examples of applications in astrophysics. For instance, using imaging (i.e., broad-band) polarimetry, and spectropolarimetry, one can derive dust properties (size, shape, orientation and composition, see e.g., Serkowski et al. 1975); scattering properties of reflecting screens (e.g., circumstellar dust shells, light echoes, extra-solar planets, etc.); stellar and galactic magnetic fields (see e.g., Scarrott 1996, Scarrott et al. 1996); and three-dimensional shapes of point sources (e.g., global and ejecta asymmetries of supernova explosions, see Wang & Wheeler 2008).

1.2.1. Mathematical description of the concept of polarization

The concept of polarization (see Clarke 2010 for a general introduction, and Patat 2017 for a more astronomically-oriented discussion) can be described considering a classical electromagnetic wave. Let us assume that the wave travels along the z axis of a Cartesian frame.

The electrical field, measured in a plane normal to the direction of propagation along the z axis, can be described as:

$$\begin{aligned} E_x &= E_{x0} cos(2\pi\nu t + \delta_x), \\ E_y &= E_{y0} cos(2\pi\nu t + \delta_y), \end{aligned} \tag{1.1}$$

where E_{x0} and E_{y0} are the amplitudes of the electrical wave components, ν is the frequency, and δ_x, δ_y are the phases of the components. The equations can be expanded and combined to:

$$\frac{E_x^2}{E_{x0}^2} + \frac{E_y^2}{E_{y0}^2} - \frac{2E_x E_y cos(\delta_y - \delta_x)}{E_{x0}^2 E_{y0}^2} = sin^2(\delta_y - \delta_x), \tag{1.2}$$

which represents the polarization ellipse.

Under the assumption that $E_{x0} = E_{y0}$, and in case of a phase difference $\delta_y - \delta_x = 0$, the ellipse degenerates to a line segment, which means that the electrical field oscillates along a constant direction (linear polarization); or in case of a phase difference $\delta_y - \delta_x = \pi/2$, the electrical field rotates in the xy plane, and the ellipse becomes a circle (circular polarization).

Thus, the polarization can be described in terms of E_{x0}, E_{y0}, δ_x, and δ_y, which are not directly measurable[1]. However those four parameters can be combined to provide a more meaningful set of parameters to describe the ellipse.

If we apply a rotation to the axial frame through χ, so that the axes lie along the same direction as the major and minor axes of the ellipse (Fig. 1.1), the polarization ellipse can be written in the canonical form:

$$\left(\frac{E'_x}{a}\right)^2 + \left(\frac{E'_y}{b}\right)^2 = 1, \tag{1.3}$$

where

[1]There are no devices that can measure polarization directly. Polarization is derived measuring intensities along a set of directions.

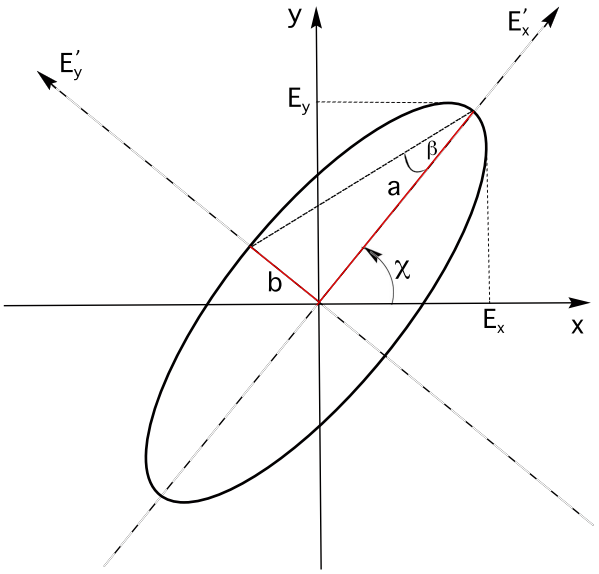

Figure 1.1.: Polarization ellipse.

$$a^2 = E_{x0}^2 sin^2\chi - E_{x0}E_{y0}sin(\delta_y - \delta_x)sin2\chi + E_{y0}^2 cos^2\chi$$
$$b^2 = E_{x0}^2 cos^2\chi + E_{x0}E_{y0}sin(\delta_y - \delta_x)sin2\chi + E_{y0}^2 sin^2\chi. \quad (1.4)$$

From Equations 1.4 , it can be shown that

$$a^2 + b^2 = E_{x0}^2 + E_{y0}^2. \quad (1.5)$$

From Figure 1.1, we can see that tan β = b/a.

Now we can describe the ellipse in terms of two angles: χ, defining the orientation, and is the ellipticity angle β. The angles are related to the amplitude of the electric wave, and phase shift as following:

$$tan2\chi = \frac{2E_{x0}E_{y0}cos(\delta_y - \delta_x)}{E_{x0}^2 - E_{y0}^2} \quad (1.6)$$

and

$$sin2\beta = \frac{2E_{x0}E_{y0}sin(\delta_y - \delta_x)}{E_{x0}^2 + E_{y0}^2}. \quad (1.7)$$

The size of the ellipse is proportional to the intensity of the beam and may be written as:

$$I = E_{x0}^2 + E_{y0}^2. \quad (1.8)$$

It is also convenient to define:

$$I_{diff} = E_{x0}^2 - E_{y0}^2 \equiv Icos2\beta cos2\chi, \quad (1.9)$$

$$I_{cos} = 2E_{x0}E_{y0}cos(\delta_y - \delta_x) \equiv Icos2\beta sin2\chi, \quad (1.10)$$

and

$$I_{sin} = 2E_{x0}E_{y0}sin(\delta_y - \delta_x) \equiv Isin2\beta. \quad (1.11)$$

Table 1.1.: Stokes vectors for some polarization states

Polarization state	Stokes vector
Natural	$(1,0,0,0)^T$
Linear at 0°	$(1,1,0,0)^T$
Linear at 90°	$(1,-1,0,0)^T$
Linear at 45°	$(1,0,1,0)^T$
Linear at 135°	$(1,0,-1,0)^T$
Right-handed circular	$(1,0,0,1)^T$
Left-handed circular	$(1,0,0,-1)^T$

^{T} is the transpose of a row vector.

We can rewrite the Eq. 1.6 and Eq. 1.7 to:

$$\begin{aligned} tan2\chi &= I_{cos}/I_{diff}, \\ sin2\beta &= I_{sin}/I. \end{aligned} \tag{1.12}$$

Note also that $I^2 = I^2_{diff} + I^2_{cos} + I^2_{sin}$.

1.2.1.1. Stokes parameters

When practically determining the quantities which describe the ellipse, the measurement corresponds to the average of the ellipse's behaviour integrated over time and over a given bandwidth.

For convenience, we can write:

$$\begin{aligned} I &= \langle E^2_{x0} + E^2_{y0} \rangle_{\lambda,t} \\ Q &= \langle E^2_{x0} - E^2_{y0} \rangle_{\lambda,t} \\ U &= \langle 2E_{x0}E_{y0}cos(\delta_y - \delta_x) \rangle_{\lambda,t} \\ V &= \langle 2E_{x0}E_{y0}sin(\delta_y - \delta_x) \rangle_{\lambda,t} \end{aligned} \tag{1.13}$$

The (I,Q,U,V) parameters are the *Stokes parameters*, first time introduced in Stokes (1852).

By combining Equations 1.8–1.11 with the definition of Stokes parameters given in Eq. 1.13, we can re-write the Stokes parameters, normalized to the intensity, I, as:

$$\begin{aligned} Q/I &= cos2\beta cos2\chi \\ U/I &= cos2\beta sin2\chi \\ V/I &= sin2\beta. \end{aligned} \tag{1.14}$$

It is common to write the Stokes parameters in form of of a quadri-dimensional vector, **S**{I,Q,U,V}, called the *Stokes vector*. Some examples of simple polarization states are given in Table 1.1.

The polarization degree is given by

$$P = \frac{\sqrt{Q^2 + U^2 + V^2}}{I}, \tag{1.15}$$

and can be separated into linear

$$P_L = \frac{\sqrt{Q^2 + U^2}}{I}, \tag{1.16}$$

with an polarization angle

$$\theta_0 = \frac{1}{2} arctan(U_0/Q_0); \tag{1.17}$$

and circular:

$$P_C = \frac{V}{I}. \tag{1.18}$$

If P=0, then Q=U=V=0. This case corresponds to natural (fully unpolarized) light, while in case of totally polarized light, P=1, then $I^2=Q^2+U^2+V^2$.

The Stokes parameters are additive, so that any quasi-monochromatic light beam can be considered as the sum of a completely polarized beam and a completely unpolarized beam, $I = I_{pol} + I_{nat}$:

$$\begin{pmatrix} I \\ Q \\ U \\ V \end{pmatrix} = \begin{pmatrix} \sqrt{Q^2 + U^2 + V^2} \\ Q \\ U \\ V \end{pmatrix} + \begin{pmatrix} I - \sqrt{Q^2 + U^2 + V^2} \\ 0 \\ 0 \\ 0 \end{pmatrix}$$

1.2.2. Instruments and observations

Stokes parameters are derived by measuring a set of intensities along certain directions.

To achieve this, we commonly use instruments that contain full linear polarizers and some means of either rotating the instrument or rotating the electric field with wave plates (half-wave plate, or quarter-wave plate).

A polarizer is an optical element that from which the emergent beam is linearly polarized regardless of the state of polarization of the incident beam. Many polarizers rely on birefringence, which is a property of a material that has a refractive index, which depends on the polarization and propagation direction of light.

A wave plate is an optical element with two orthogonal principal axes (the fast axis, and slow axis), which have two different refractive indices, such that a linearly polarized beam with polarization parallel to one of the principal axes is propagated without change in its polarization state. The wave-plate is used to introduce a phase change, and because of this it is also indicated as ”retarder”.

A half-wave plate (HWP, or $\lambda/2$ plate) produces a retardation of the electric field that is polarized parallel to one of the principal axes by half a wavelength (corresponding to a phase change equal to π), with respect to perpendicularly polarized light. It can rotate the polarization direction of linearly polarized light by a selectable angle. A quater-wave plate (corresponding to a phase change equal to $\lambda/4$ plate) produces a retardation of light polarized parallel to one of the principal axes by a quarter wavelength (or corresponding to a phase change equal to $\pi/2$), with respect to perpendicularly polarized light. When the angles are properly adjusted, it can make circularly or elliptically polarized light from linearly polarized light, and it can create linearly polarized from circularly polarized light (Bagnulo et al., 2009).

There are several kinds of polarimeters, but here we will consider one with a built in retarder wave plate followed by a Wollaston prism as a polarizer. The Wollaston prism (named after William Hyde Wollaston, 1820) is an optical device that polarizes light using a birefringent material, such as quartz or calcite. The incident light is separated into two outgoing beams (ordinary and extraordinary) with

orthogonal linearly polarized states. The beams diverge by an angle, indicated as throw, which is typically ~ 10-20 arcseconds. The design of a beam-splitting polarimeter was suggested by Appenzeller (1967), and is implemented in many astronomical instruments.

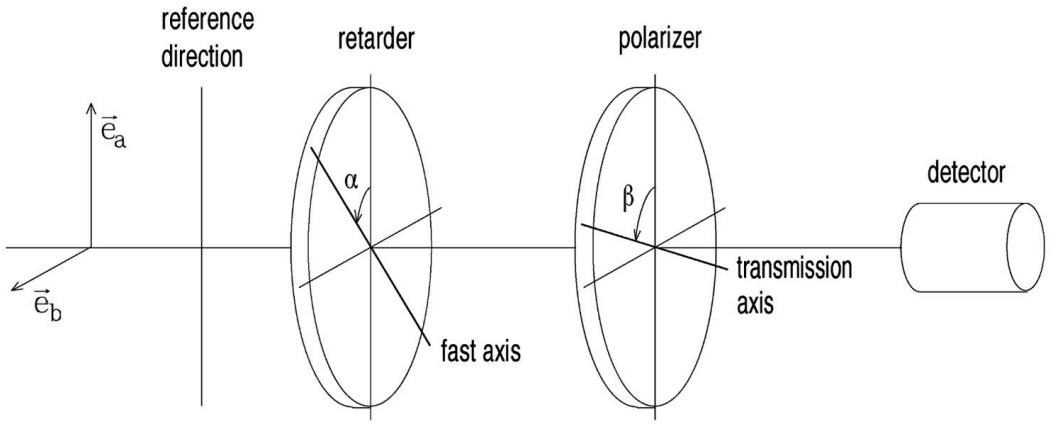

Figure 1.2.: Schematic illustration of an ideal polarimeter. (Source: Landi Degl'Innocenti & Landolfi 2004).

Figure 1.2 shows an example of an ideal polarimeter (Landi Degl'Innocenti & Landolfi, 2004). We define α as the angle between the reference direction and the fast axis of the retarder wave plate, counted counterclockwise from the reference direction; β is the position angle of the transmission axis of the linear polarizer counted counterclockwise from the reference direction; γ is the phase retardance introduced by the retarder wave plate.

The signal measured at the detector can be calculated with the following equation, from Landi Degl'Innocenti & Landolfi (2004):

$$\begin{aligned} S(\alpha,\beta,\gamma) \propto \frac{1}{2}\{I &+ [Qcos2\alpha + Usin2\alpha]\, cos(2\beta - 2\alpha) \\ &- [Qsin2\alpha - Ucos2\alpha]\, sin(2\beta - 2\alpha) cos\gamma \\ &+ Vsin(2\beta - 2\alpha) sin\gamma\} \end{aligned} \tag{1.19}$$

For a half wave plate we adopt $\gamma = \pi$, and for a quarter-wave plate $\gamma = \pi/2$ (Appenzeller, 1967).

Thus, we can measure the Stokes Q using a half-wave plate ($\gamma = \pi$), and setting α to 0° (or to any multiple of 45°); and the Stokes U by setting α to 22.5° (or to any angle differing from 22.5° by a multiple of 45°). The measurement of Stokes V can be undertaken with a quarter-wave plate ($\gamma = \pi/2$), and by setting the angle α to 45° (or to any angle differing from 45° by a multiple of 90°).

However, in practice, the sky transparency and seeing variations introduce artificial flux variations that turn into spurious polarization signal. The problem is solved by introducing the Wollaston prism, and measuring the normalized flux differences by obtaining at least two directions simultaneously (Patat, 2017).

When using a Wollaston prism, there will be two outgoing polarized beams, which define an principal plane, one in the direction parallel to that plane and one in the direction perpendicular to it

(ordinary and extraordinary beams). The parallel beam and the perpendicular beam will be associated to the β values 0° and 90°, respectively.

Fig. 1.3 shows an example of the two outgoing beams split by a Wollaston prism, taken with the FOcal Reducer/low dispersion Spectrograph 2 (FORS2), mounted at the Very Large Telescope, which we used to obtain the majority of data in this thesis (see Chapter 2 for discussion of stability and accuracy of FORS2).

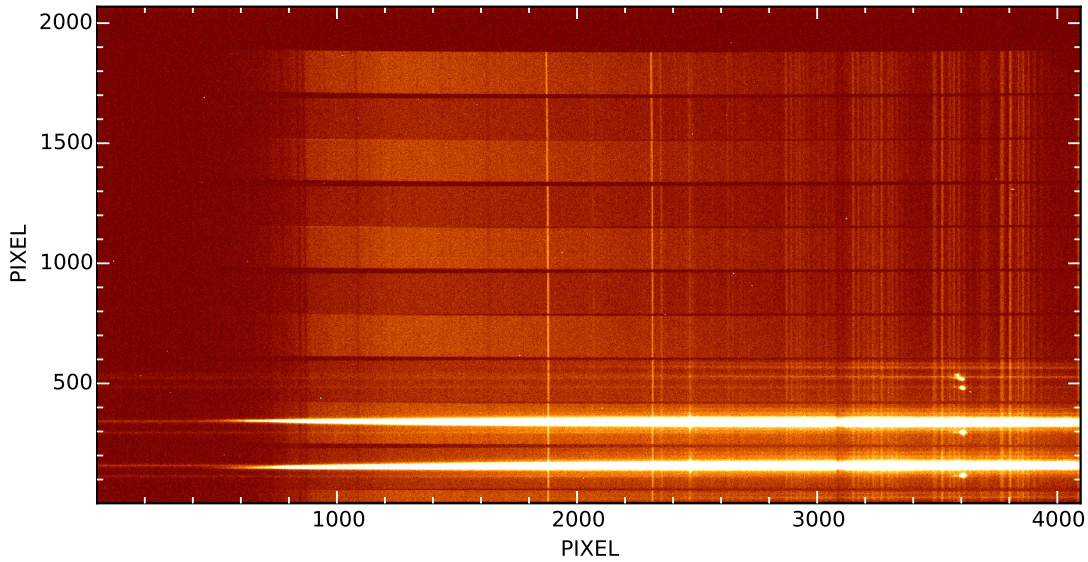

Figure 1.3.: An example image acquired with FORS2 in PMOS mode. Shown is the upper CCD chip (CHIP1). The spectrum is split by the Wollaston prism in an ordinary (upper) and extra-ordinary (bottom) beam, separated by 22".

1.2.3. Polarization mechanisms

The main mechanisms responsible of linear polarization in the majority of astrophysical sources are: scattering on electrons (Thompson scattering), molecules (Rayleigh scattering), small grains (Mie scattering), resonant scattering (e.g., in emission lines in Quasars, see e.g., Lee & Blandford 1997) and dichroic absorption of aligned non-spherical grains.
Furthermore, circular polarization is mainly produced in strong magnetic fields (e.g., in some White Dwarfs).

1.2.3.1. Linear continuum polarization

There are three relevant continuum polarization mechanisms that we need to consider towards supernova sight lines:

(i) Polarization produced due to linear dichroism in non-spherical grains. When light passes through the interstellar medium, or a cloud of non-spherical supramagnetic dust grains, which are oriented among the galactic magnetic field, the electric vector of the light wave parallel to the

major axis of the dust grains will experience higher extinction than light waves parallel to the minor axis of the dust grain (see Fig. 1.4), and therefore we will observe a net polarization (van de Hulst, 1957; Martin, 1974; Shapiro, 1975).

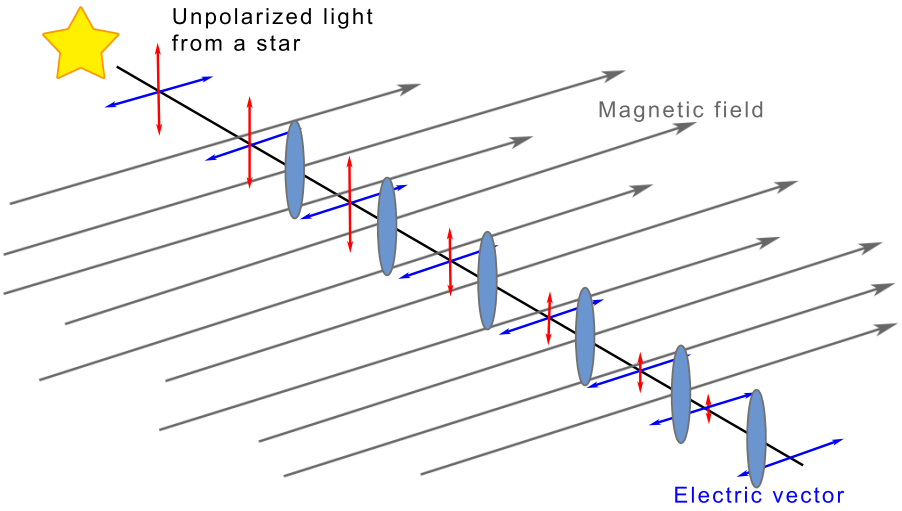

Figure 1.4.: Polarization produced due to linear dichroism in non spherical grains.

The Serkowski curve (Serkowski et al., 1975) is an empirical description of the wavelength dependence, which characterizes such interstellar linear polarization:

$$\frac{P(\lambda)}{P_{\max}} = \exp\left[-K\ln^2\left(\frac{\lambda_{\max}}{\lambda}\right)\right], \tag{1.20}$$

where the wavelength of peak polarization, $\lambda_{\max}$, depends on the dust grain size distribution. For an enhanced abundance of small dust grains, $\lambda_{\max}$ moves to shorter wavelengths, and for an enhanced abundance of large dust grains to longer wavelengths. Serkowski et al. (1975) also found that $R_V \approx 5.5\ \lambda_{\max}$, where $\lambda_{\max}$ is in μm (see Fig. 1.5).

(ii) Polarization by scattering from nearby material. Single scattering of nearby dust clouds or sheets produces polarized light perpendicular to the plane containing the light source, the scattering element and the observer (Fig. 1.6). The polarization curve produced by scattering is given by:

$$P(\lambda) = c_R \times \lambda^{-4}, \tag{1.21}$$

where c_R is the amplitude of the scattering (e.g., c_R=0.027 ± 0.002 %, derived by polarization curve fitting for target #46 in Andersson et al. (2013). The index of the power-law is not well constrained, and is usually chosen to be -4, appropriate to both Rayleigh scattering from polarizable molecules and Mie scattering in the small grain limit (Andersson et al., 2013).

(iii) Polarization induced by electron scattering in globally aspherical photospheres. In case of spherically symmetric photospheres, the intensity of scattered (linearly polarized) light from free electrons will be equal in orthogonal directions, and thus, we won't observe a net polarization, while in case of an aspherical photosphere, the net intensity of scattered light perpendicular to the major

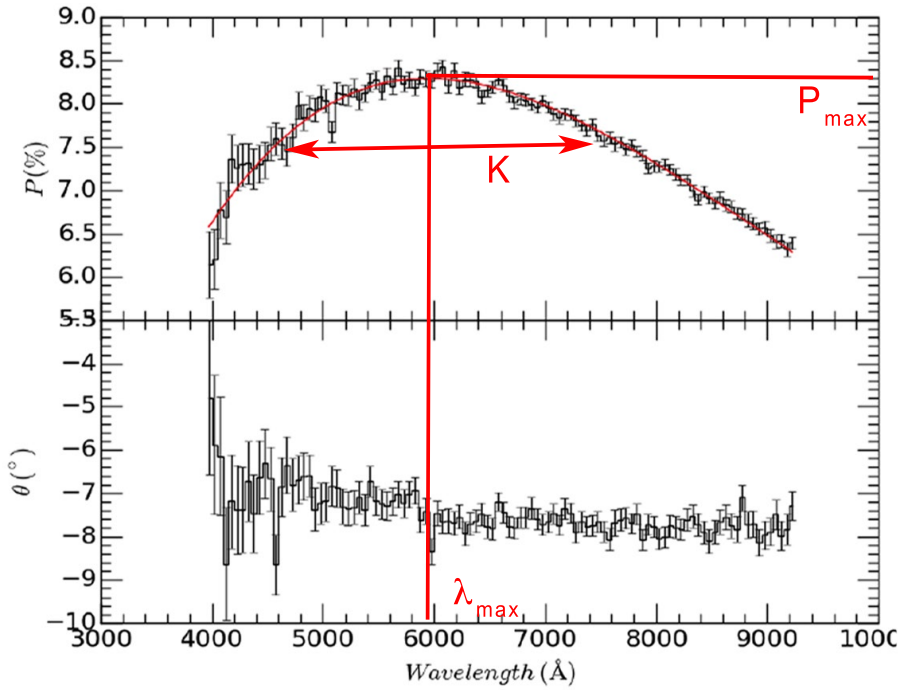

Figure 1.5.: Shown is a linear polarization curve of Vela1 95, a standard star for linear polarization. The red line displays the Serkowski curve fitted to the data, which can be parametrized with the wavelength at peak polarization, λ_{max}, degree of peak polarization P_{max}, and K, which depends on the shape of the curve. For low K values the curve is flat and broad, while for higher K values the curve is steeper and narrower.

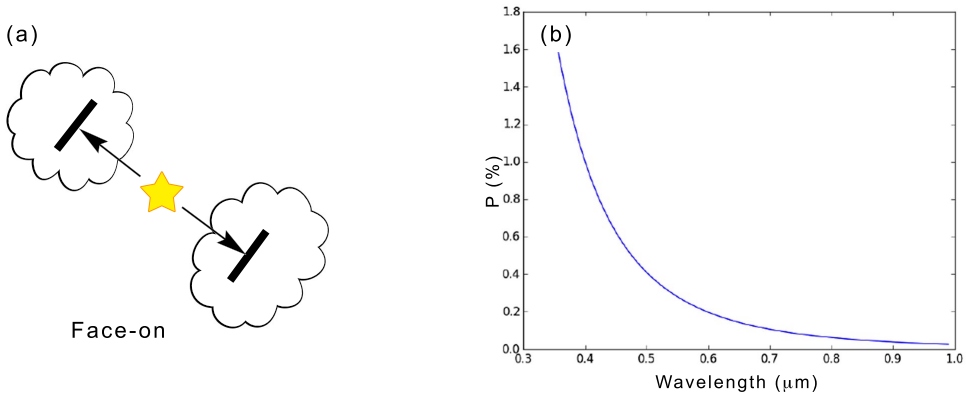

Figure 1.6.: Polarization by scattering from nearby material. (a) Single scattered light of nearby dust clouds produces polarized light perpendicular to the projected line between the light source and the scattering material. (b) The polarization curve produced by scattering follows a power-law.

axis of the projected photosphere will be larger that the intensity of the scattered light perpendicular to the minor axis, and therefore, we will observe a net polarization (see Fig. 1.7, and e.g., Hoflich 1991).

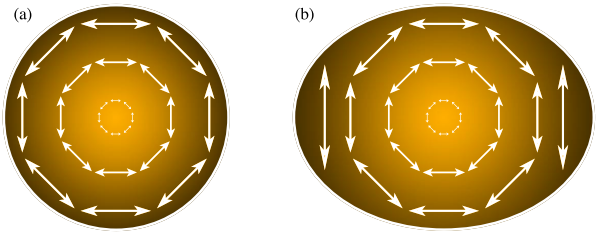

Figure 1.7.: Illustrative production of continuum polarization in aspherical photospheres. (a) In case of a spherical SN photosphere, we will observe a net polarization of P=0%. (b) In case of an aspherical photosphere, we will observe a net continuum polarization P > 0%.

1.2.3.2. Linear polarization of spectral lines

In general SN Ia explosions are globally very spherical (Hoflich, 1991)), however, measuring the polarization of spectral lines can give us insight into the chemical asymmetries of the ejecta, which depend on the explosion scenario, and thus on the progenitor system. Here we will provide a simplified explanation the mechanism of how the line polarization is produced, at the wavelengths corresponding to strong absorption lines.

Figure 1.8 illustrates the electron-scattering dominated photosphere of a SN. Light scattered by the electrons will be polarized. In case of a spherical photosphere, there will be an equal amount of polarized light coming from all directions (Figure 1.8a), and therefore, we will observe a null polarization. However, if there is aspherically distributed material in front of the photosphere, it will block only part of the photodisk, and we will observe a net polarization P > 0% at the wavelengths corresponding to strong absorption lines (Figure 1.8b).

Depending on the geometry of the blocking material, we will observe see loops in the Q–U plane. If the distribution of the absorbers (or clumps) is not spherically symmetric, and do not have a common symmetry axis, they will block parts of photoshpere with different Doppler velocities and we will observe a smooth change in the position angle as a function of Doppler velocities, i.e., we will observe loops in the Q–U plane (see Tanaka et al. 2017 for a more detailed explanation, and also Wang & Wheeler 2008). However, in case of an axisymmetric distribution (e.g., a torus, or bipolar ejecta), we will observe polarization, but no loops in the Q–U plane.

As a product of the explosive nucleosynthesis, different elements can have different geometrical and velocity distributions, which in turn produce different polarization signatures.

Because SN explosions are homologous, velocity can be remapped into radial positions, hence providing unique information on the chemical distribution and its geometry, which constitutes the great diagnostic power of spectropolarimetry.

1.2.3.3. Circular polarization

Circularly polarized light can be produced in strong magnetic fields. Kemp (1970) predicted that a "gray-body" model in a magnetic field will emit a fraction of circularly polarized light. The degree of polarization, q, is proportional to the emitting wavelength, λ, and the strength of the magnetic field, B

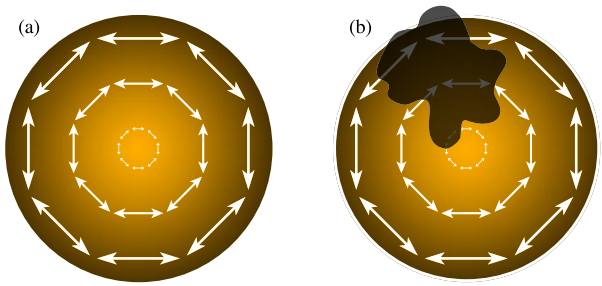

Figure 1.8.: Illustrative production of line polarization. (a) In case of a spherical SN photosphere, we will observe a net polarization of P=0%. (b) If there is an aspherical distribution of material in front of the photosphere, it will block predominantly unpolarized light, and we will observe a net polarization P > 0%.

(see Eq. 7 and 16 in Kemp, 1970), and is given by:

$$q(\lambda) \simeq -\frac{\lambda e B}{4\pi m c}, \tag{1.22}$$

where e and m are the electron's charge and mass respectively, and c is the speed of light.

Circular polarization has been observed in white dwarfs with strong magnetic fields. For instance, Kemp et al. (1970), and Angel et al. (1972) observed strong circular polarization, at the level of $1-3\%$, in visible light, and 8.5-15% in the infrared (Kemp & Swedlund, 1970) for Grw+70°8247. For this white dwarf they estimate a mean projected B field of 1×10^7 G.

1.3. Supernovae

In the following we will focus on Type Ia and Superluminous events, which will be discussed in detail in the rest of the thesis.

1.3.1. Supernova classification

Supernovae are classified spectroscopically according to the spectral lines of different chemical elements that appear in their spectra near the peak luminosity. The first classification of Supernovae was based on to presence or absence of hydrogen (H) lines by Minkowski (1941). He identified two groups in a spectroscopic sample of 14 supernovae: Type I, those that did not show H features in their spectra, and Type II, which did show H in their spectra (see Gal-Yam, 2016, for a review).

In the 80's the sample of observed supernovae increased, and Type I supernovae were further divided based on the presence of Silicon (Si) and Helium (He).

Elias et al. (1985) presented infrared data for 11 Type I supernovae, combined them with other published data for Type I supernovae, and noticed that their light curves fall into two well-defined groups: the more common Type Ia supernovae that show strong, variable, absorption at 1.2 μm, and possibly at 3.5 μm, while the second type, Type Ib supernovae, show no such absorption and have a slower decline after maximum. They also identify SNe Ia as potentially valuable for distance determination, because of a low dispersion in color and absolute magnitude.

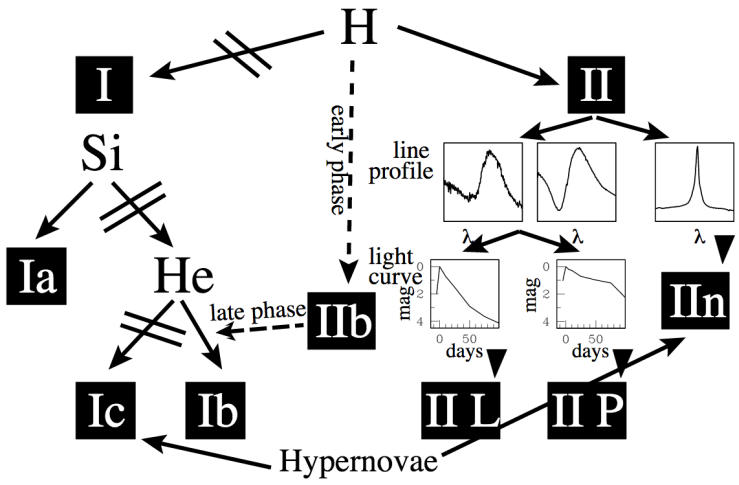

Figure 1.9.: A detailed supernova classification requires spectral and light curve analysis. Source: Cappellaro & Turatto (2001).

Harkness et al. (1987) definitely identified helium in spectra of Type Ib SNe near peak brightness, and summarize the arguments that SNe Ib result from core collapse in moderately massive stars. Wheeler & Harkness (1990) introduced, in a review paper, Type Ic SNe as a subclass which lacks the evidence of Si near maximum that characterizes SN Ia, but they have only weak indications of He, compared to Type Ib.

Among the hydrogen-rich Type II SNe, Barbon et al. (1979) analyzed photometric observations of 23 supernovae, and divided them according to the light curve shapes into two sub-classes: the ones characterized by a plateau at intermediate phase (Type II-P), and the ones which exhibits an almost linear decline (Type II-L).

From the spectroscopic point of view, there are two classes of Type II SNe. Filippenko (1988) introduced Type IIb SNe, which have the spectral properties of type II near maximum brightness (i.e., they are hydrogen rich), and display properties of type Ib supernovae at late epochs (i.e., they show no hydrogen, but helium). Schlegel (1990) presented a summary of Type II observations, and suggests to introduce a new class of SNe that show strong and relatively narrow emission lines of hydrogen (Type IIn). The classification of classical SNe described above is summarized in Fig. 1.9.

More recently, Woosley & Bloom (2006) introduced a sub-classification of Type Ic SNe, called "Type Ic-BL", which show evidence for broad lines, indicative of high-velocity ejecta, and accompany some of the GRBs (GRB-SNe). Furthermore, Superluminous supernovae (SLSNe) is a new class of SNe that are more luminous than classical SNe ($M \leq -21$ mag, see § 1.3.3, and Gal-Yam, 2012, for a review).

In addition to the morphological approach described so far, SNe are also classified on the basis of the physical origin of their explosion (Gal-Yam, 2016): in core-collapse supernovae of massive stars (Type II, Type Ib and Type Ic, SLSNe), and thermonuclear explosions of white dwarfs (Type Ia).

1.3.2. Type Ia Supernovae

Supernovae Ia (SNe Ia) are exploding C/O White dwarfs (WD), close to the Chandrasekhar mass limit ($\sim$ 1.38 $M_\odot$, Arnett 1969; Nomoto 1982). They are bright, and good standardizable candles. Therefore, they were used as cosmological probes to measure the expansion of the universe (Riess et al., 1998; Perlmutter et al., 1999).

They are not all equally luminous, but there is a correlation, between their peak luminosity, M_{max}, and the shape of the light curve, characterized by the luminosity decline rate after maximum, known as the Phillips relationship:

$$\mathrm{M_{max}(B)} = -21.726 + 2.698\Delta \mathrm{m_{15}(B)}, \tag{1.23}$$

where Δm_{15} is the difference between peak brightness, and the brightness at 15 days past peak (Phillips, 1993).

The width of the light curve vs. peak luminosity is likely related to the mass of ^{56}Ni synthesized during the explosion, and perhaps also to the total ejecta mass (Taubenberger, 2017; Stritzinger et al., 2006; Scalzo et al., 2014). The majority of SNe Ia are "Branch normal", characterized with a prominent 6355Å Si II absorption line, expanding at $\sim$ 11000-15000 km s^{-1} around maximum light, as well as O, S and iron-group lines. Their typical peak brightness is M_B=-19.1 mag (Ashall et al., 2016), and they follow the Phillips relationship (see Fig. 1.10).

This rather homogeneous class is accompanied by peculiar objects, which can be grouped in the following sub-classes:

- **SNe 91bg-like** is named after the subluminous, and fast-declining prototype SN 1991bg (Filippenko et al., 1992; Leibundgut et al., 1993). Their luminosity at peak (in optical bands) is $\sim$1.5-2.5 mag lower that of normal SNe Ia, with red maximum-light colors, (B-V)$_{max}$ $\sim$ 0.5-0.6 mag (Taubenberger, 2017), that are redder than the color of normal SNe Ia at maximum light, (B-V)$_{max}$ $\sim$ 0.12 mag (see Blondin et al. 2012). It is interesting to note that spectropolarimetric observations of sub-luminous SN 1999by (Howell et al., 2001) and SN 2005ke (Patat et al., 2012) show low line polarizations, but relatively high intrinsic continuum polarization ($\sim$ 0.5%), compared to normal SNe Ia which typically show low continuum polarization ($\lesssim$ 0.2 %) , and stronger line polarization, up to 1% (see next subsection for polarization properties of SNe Ia).

- **91T-like SNe** are slightly ($\sim$0.2-0.5 mag) more luminous compared to the Phillips relationship. They are spectroscopically peculiar, because of Fe III absorption features, which dominate the early spectra (Taubenberger, 2017). A significant amount of iron-group elements, particularly ^{56}Ni, is required in the outer layers to reproduce the observed features at early times (Ruiz-Lapuente et al., 1992; Mazzali et al., 2005).

- **SNe Iax** are spectroscopically similar to SNe Ia, but have lower velocities, lower peak luminosities, and typically show absorption lines from higher-ionization species, which is consistent with hot photospheres (Foley et al., 2013). A possible progenitor scenario is one in which a binary system comprising a C/O WD that accretes matter from a He star and undergoes a significant deflagration(Foley et al., 2013).

- **SNe Ia-CSM** is a rare subclass of objects that shows a peculiar spectrum with strong hydrogen Balmer lines, which is interpreted as evidence of strong interaction with their circumstellar medium (Silverman et al., 2013).

- **Super-Chandrasekhar SNe Ia** are luminous events, about ∼ 1 mag brighter than normal SNe Ia. They have low expansion velocities, which Howell et al. (2006) attribute to a large ejecta mass, exceeding the Chandrasekhar-mass (Gal-Yam, 2017).

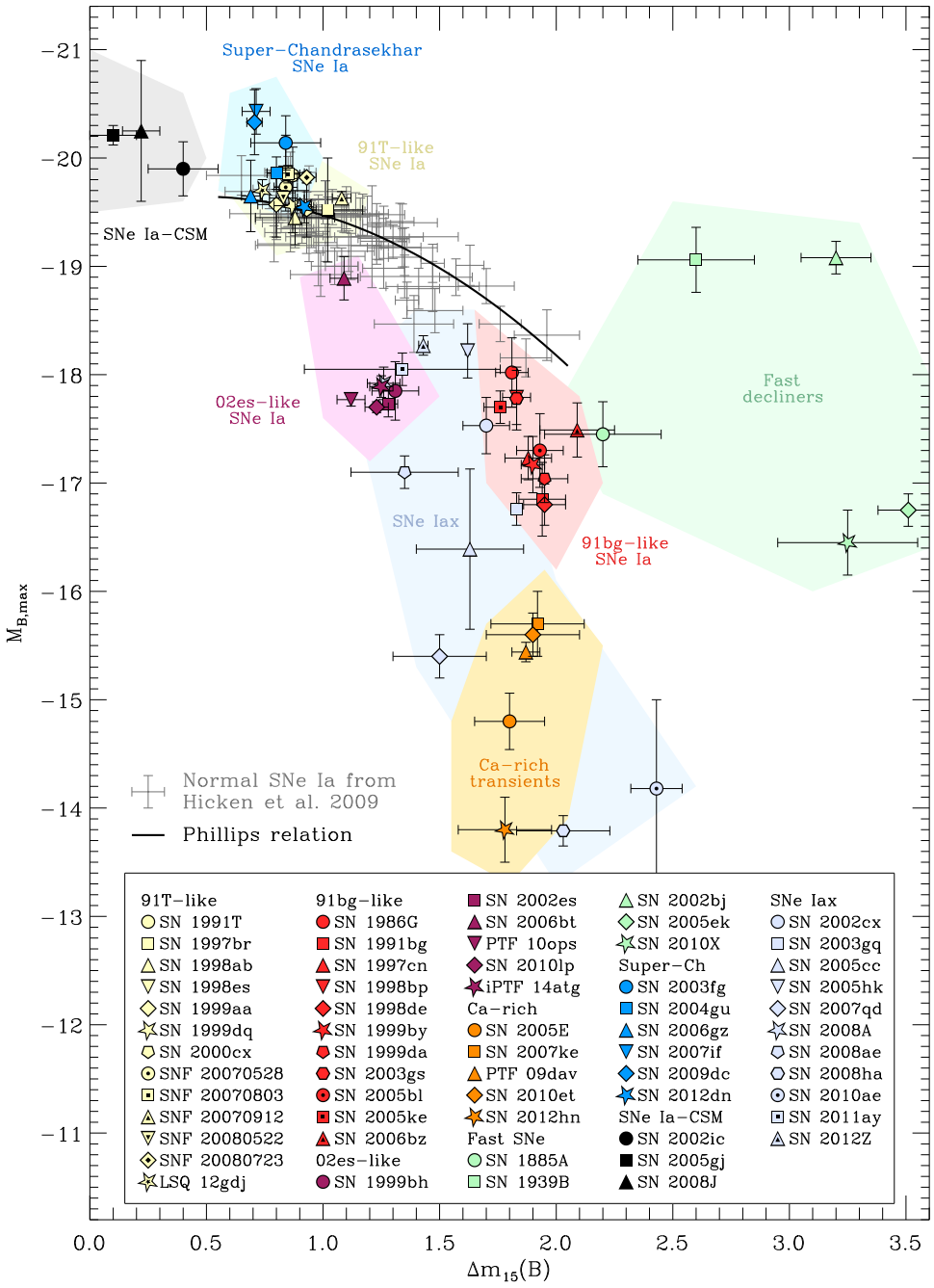

Figure 1.10.: Absolute magnitude of SN Ia plotted as a function of the decline rate, Δm_{15}. The black line indicates the Phillips relationship, and different colors indicate different classes of SNe Ia. Source: Taubenberger (2017).

1.3.2.1. Progenitor scenarios

A comprehensive review of all proposed progenitor models of Type Ia Supernovae with their strengths and weaknesses is given by Livio & Mazzali (2018).

There are four possibilities suggested as a potential progenitor for SNe Ia:

1. **Isolated White Dwarf scenario:** Chiosi et al. (2015) suggest that a thermonuclear explosion may occur in isolated carbon-oxygen white dwarfs, with a mass from 0.85-1.2 $M_{\odot}$. The explosion may be triggered by the energy produced by pycno-nuclear reactions (see Harrison 1964) between carbon and light elements (which occur in high density matter, in the core of a white dwarf, when nuclei are frozen in lattice structures), which remain inactive until the WD transits from liquid to the solid phase.

2. **Single-Degenerate scenario (SD):** In this scenario, a WD accretes material from a companion non-degenerate star (a main sequence star, sub-giant, red-giant, asymptoptic giant-branch star, or a helium star), until it reaches the Chandrasekhar mass limit, at which the thermonuclear explosion occurs (Whelan & Iben, 1973; Nomoto et al., 1984).

3. **Double-Degenerate scenario (DD):** In a binary system of two C/O white dwarfs of different masses, which are brought together sufficiently close by gravitational wave radiation (Webbink, 1984), the larger WD (less massive) will fill its Roche lobe and form a massive disk around the primary WD within a few orbital periods (e.g. Rasio & Shapiro, 1994). It has been shown that the accretion of the C/O rich material can lead to central carbon ignition and a SN Ia (e.g. Yoon et al., 2007; Sato et al., 2015).

   The carbon detonation can also occur due to compressional heating during a "violent merger" phase, in case both WDs have relatively high masses between 0.7-1.1 $M_{\odot}$ (see e.g. Sato et al., 2015).

   Another possibility of violent mergers is a third-body induced head-on collision, which can occur in dense stellar environments, for instance in globular clusters (see e.g. Rosswog et al., 2009).

4. **Core-Degenerate scenario:** In the Core-Degenerate scenario, a WD merges with the core of a companion AGB star, and explodes within less than $\sim 10^5$ years after a common envelope phase (Livio & Riess, 2003; Kashi & Soker, 2011). All evolutionary paths of binary systems that lead to a formation of a close white dwarf binary system evolve an asymptoptic giant-branch star. If the binary companions are sufficiently close, after the AGB star overflows its Roche lobe, the system will evolve to a common envelope phase (which is poorly understood), and the companions may spiral-in and will eventually merge (Jones & Boffin, 2017; Ivanova et al., 2013). The product after the merger will be a super-Chandrasekhar object, which will not explode immediately thereafter, because it is supported by rapid rotation. The explosion will occur after the star spins down through a magneto-dipole radiation torque (Yoon & Langer, 2005).

1.3.2.2. Polarization properties

Continuum polarization along the line of sight to SNe Ia

Patat et al. (2015) found that highly reddened SNe Ia with low R_V values display anomalous linear polarization curves, steeply rising towards blue wavelengths, with peak polarization at $\lambda_{max} \sim 0.43 \mu m$

for SN 1986G, and $\lambda_{max} \lesssim 0.4\mu$m for SN 2006X, SN 2008fp and SN 2014J, to be compared to normal Milky Way polarization curves with peak polarization at $\lambda_{max} \sim 0.55\mu m$ (see Fig. 1.11). Because SNe Ia have a negligible intrinsic continuum polarization (Wang & Wheeler, 2008), the anomalous polarization curves have to be associated with the properties of host galaxies dust, or be produced by circumstellar material. Zelaya et al. (2017a) expanded the sample of four SNe Ia investigated in Patat et al. (2015), and presented a study of 19 Type Ia SNe. They group the SNe in the "sodium-sample", consisting of 12 SNe which show higher continuum polarization values and interstellar Na I D lines at the redshift of their host galaxies, and the "non-sodium-sample" with no rest-frame Na I D lines and smaller peak polarization. Eight sodium-sample SNe have $\lambda_{\rm max} \lesssim 0.4\mu m$ and their polarization angles are aligned with their host galaxies spiral arms, which is evidence that the polarizing dust is likely located in their host galaxies, and aligned due to the host galaxies magnetic fields. The non-sodium-sample SNe are less polarized, with $P_{\rm max} \lesssim 0.5\%$, have $\lambda_{\rm max}$ values similar to the common Galactic dust (with $\lambda_{\rm max} \sim 0.55\mu m$), and their polarization angles do not align with host-galaxy features, which might be interpreted as the continuum polarization being produced by the Galactic foreground dust.

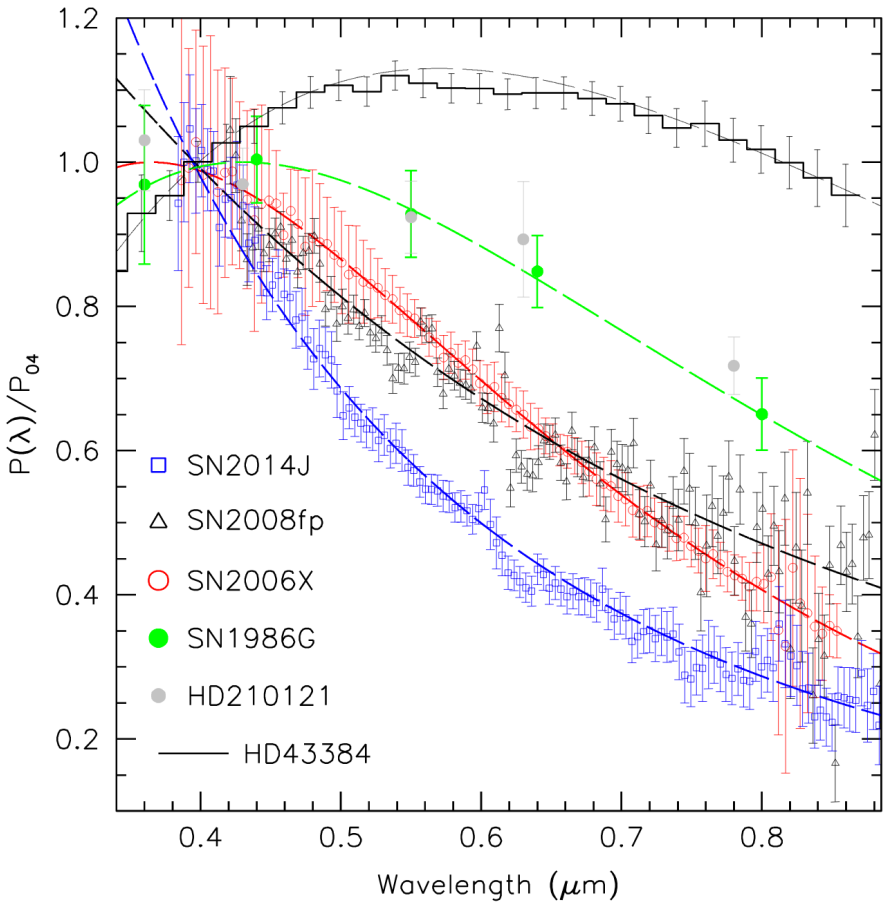

Figure 1.11.: Observed polarization curves for SN 1986G, SN 2006X, SN 2008fp, and SN 2014J, compared to HD 43384 (a polarized standard) and HD 210121 (a Galactic star with very low R_V). The dashed curves trace Serkowski law best fits. Source: Patat et al. (2015).

It is not understood why these reddened SN Ia sightlines show such a different polarization profile

compared to the typical Milky Way dust (see also Chapter 3, where we investigated polarization properties of stars with anomalous extinction curves). The most natural explanation is that the dust composition in the SN Ia host galaxies is different from that typical in the Galaxy.

However, there are alternative explanations. Scattering might explain the low R_V values, as well as the peculiar polarization profiles. As illustrated by Patat et al. (2015) (see their Fig. 6), the polarization profile of SN 2006X may, besides the Serkowski component, also have a component produced by Rayleigh scattering (see also Chapter 4 where we found common continuum polarization properties between SNe Ia and proto-planetary nebulae, whose polarization is produced by scattering). However, in case a light echo propagates through local dust, we expect to observe variability in R_V and polarization (Wang, 2005; Patat et al., 2006), which is was never observed (see Fig. 4 in Zelaya et al. 2017a). Yang et al. (2017) used HST observations to map the interstellar medium (ISM) around SN 2014J through light echoes. These authors observed two echo components: a diffuse ring and a luminous arc, produced through dust scattering of different grain sizes. From the wavelength dependence of the scattering optical depth, the arc dust favors a small R_V value of $\sim$ 1.4, which is consistent with the R_V measured along the direct line of sight, while the ring is consistent with a common Milky Way $R_V \sim 3$ value.

Another interesting explanation for the peculiar SNe Ia sightlines is given by Hoang (2017a) who simultaneously fits a two-component (interstellar and circumstellar) extinction and polarization model to photometric and (spectro)polarimetric observations of SNe 1986G, 2006X, 2008fp and 2014J, to investigate the grain size distribution and alignment functions of dust along those lines of sights. Hoang (2017a) could reproduce the observational data of SN 1986G and SN 2006X by assuming an enhanced abundance of small silicate grains in the interstellar dust only, while in case of SN 2014J, a contribution of circumstellar (CS) dust must be accounted for. In case of SN 2008fp, Hoang (2017a) found that the alignment of small dust grains must be as efficient as that of big grains, but the existence of CS dust is uncertain. Hoang (2017a) suggests that the enhanced abundance of small silicate grains might be produced by cloud collisions driven by the SN radiation pressure. Strong SN radiation might also induce efficient alignment of small grains via the radiative torque mechanism. However, in case of alignment via the radiative torque mechanism, the polarization angle alignment with host-galaxy features remains unexplained.

Intrinsic continuum polarization

The intrinsic continuum polarization in SNe Ia is typically $\lesssim$0.4%, which is consistent with global asphericities at the $\sim$ 10% level (Hoflich, 1991; Chornock & Filippenko, 2008).

The highest intrinsic continuum polarization was observed for the sub-luminous SN 1999by (Howell et al., 2001) and SN 2005ke (Patat et al., 2012), which showed an intrinsic polarization of $\sim$0.8% and $\sim$0.7%, respectively. Howell et al. (2001) spectropolarimetric data could be modeled by an oblate spheroid with an axial length ratio of 1.17, and Patat et al. (2012) suggest that the comparatively high level of continuum polarization of SN 2005ke is explained by a global asymmetry of $\sim$15%, which can be reproduced within the general context of a DD explosion.

The intrinsic continuum polarization in general decreases towards the blue end of the spectrum. Despite that the Thomson scattering is wavelength–independent, the decrease in the degree of polariza-

tion is due to depolarization by a large number of bound–bound transitions, primarily of iron–peak elements (Pinto & Eastman, 2000), in the UV and blue part of the spectrum (Chornock & Filippenko, 2008).

Line polarization

As previously explained, type Ia Supernovae show low continuum polarization, which implies that the explosions are globally spherical. This agrees with the shape of the known Type I SN remnants, which are essentially spherical. However, their polarization spectra display absorption line polarization (see Fig. 1.12), in particular before the peak brightness, which can be interpreted as chemical asymmetries in the ejecta (see Chapter 5).

Studying line polarization may lead to implications on the progenitor model and explosion scenario. There are numerous single object studies investigating line polarization of SNe Ia (for a review, see Table 1 in Wang & Wheeler 2008). For instance, Wang et al. (2006a) studied SN 2004dt, which displays a polarization across the Si II lines approaching ~2%, and thus, is the most highly polarized SN Ia ever observed. In contrast, the strong line of OI at 7774 Å shows little or no polarization.

Perhaps one of the most comprehensive single object studies was performed on SN 2006X, which occurred in the nearby M100, and Patat et al. (2009) obtained 8 epochs of high signal-to-noise data. They study the evolution of the polarization of Si II and Ca II lines, and suggest that the polarization of Ca II detected in their last epoch (+39 days past maximum light), coincides in velocity with the outer boundary of the Ca synthesized during the explosion in delayed-detonation models.

Porter et al. (2016) took spectropolarimetry of SN 2014J in M82 at six epochs. They suggest that that the explosion geometry of SN 2014J is generally spheroidal with a clumpy distribution of silicon.

In general, the most prominent line polarization was observed from the Si II 6355Å and the near-IR Ca II triplet. The maximum degree of polarization is typically ~ 1 %, and is reached few days before peak brightness. Wang et al. (2007) present polarization measurements of the Si II 6355Å line for a sample of 17 SNe Ia. They found a correlation between the degree of polarization and the light-curve decline rate, Δm_{15}. They suggest that this finding provides a strong support for the delayed-detonation models.

Furthermore, Bulla et al. (2016b) ran simulations to predict polarization signatures for the violent-merger model. They introduce polarization into the radiative transfer simulations of the Pakmor et al. (2012) model, and found that the polarization signal significantly varies with the viewing angle. In the equatorial plane polarization levels will be modest ($\lesssim$1%), while at orientations out of the equatorial plane, where the departures from a dominant axis are larger, the degrees of polarization will be higher, and may explain highly polarized events such as SN 2004dt (Wang et al., 2006a).

In a similar study, Bulla et al. (2016a) predict polarization signatures for the double-detonation (from Fink et al. 2010) and delayed-detonation (from Seitenzahl et al. 2013) models of Type Ia supernovae.

In the delayed-detonation model, a WD near the Chandrasekhar mass, which accretes material from a non-degenerate companion, explodes after an episode of slow carbon burning (carbon deflagration) near the center (Khokhlov, 1991; Bulla et al., 2016a), while in the double-detonation model, the explosion in the core of a sub-Chandrasekhar WD is triggered by a shock wave following a detonation

of the helium layer at the WD's surface, that has been accreted form a helium rich companion star (Fink et al., 2010).

For both explosion models, Bulla et al. (2016a) predict a modest degree of polarization ($\lesssim 1\%$), with peak continuum polarization of ~0.1–0.3 %, and prominent line polarization, in particular the Si II 6355Å line, and no polarization across the OI 7774 Å. The absence of polarization across the OI 7774 Å, reflects the fact that the oxygen is not a product of the thermonuclear burning, and oxygen originates from the original oxygen of the WD (which is supposed to be spherically distributed). This is consistent with the observed values in normal SNe Ia, and is an important result, placing a constraint on the explosion model.

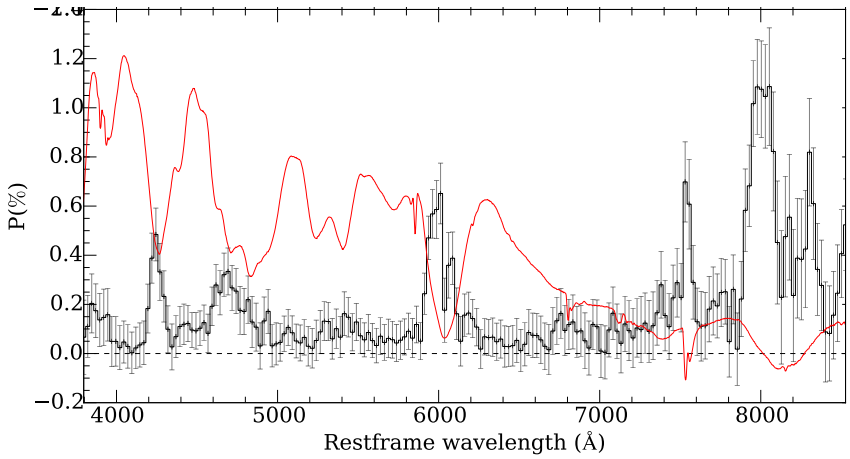

Figure 1.12.: Continuum subtracted polarization spectrum of SN 2002bo around peak brightness. The red line is the flux spectrum. The peak seen at ~7500Å is due to the strong telluric feature seen in the flux spectrum.

1.3.3. Superluminous Supernovae

Superluminous supernovae (SLSNe) constitute a new class of SNe that are more luminous than classical SNe ($M \leq -21$ mag, see Gal-Yam, 2012, for a review). Some SLSNe show hydrogen in their spectra (SLSN-II) and are mostly powered by the interaction between the SN ejecta and the circumstellar medium (CSM, Ofek et al., 2014; Inserra et al., 2016b). On the other hand, H-poor SLSNe (SLSN-I) do not show H in their spectra (Quimby et al., 2011) and are less understood. They might contain hydrogen, but it would be almost completely ionized near maximum, and therefore not be visible (Mazzali et al., 2016). Yan et al. (2015) have observed late-time hydrogen emission in one H-poor SLSNe. One possible powering source could be the spin-down of a magnetar (Kasen & Bildsten, 2010; Inserra et al., 2013; Nicholl et al., 2013, see also Chapter 6 where we test the magnetar scenario). Another possibility is the interaction between the ejecta and an H-poor CSM (Chatzopoulos et al., 2012; Vreeswijk et al., 2017; Sorokina et al., 2016). A third scenario could be a pulsational pair-instability SN (Woosley et al., 2007; Woosley, 2016), or pair-instability explosion of a very massive star (with a core of $\geq 50 M_{\odot}$, e.g., Gal-Yam et al., 2009; Dessart et al., 2013). The latter is perhaps limited only to slowly-declining H-poor SLSNe, SLSNe-R, with a declining rate consistent with the radioactive decay of ^{56}Ni and ^{56}Co.

Until recently, models predicted a long-rise in contradiction to observations (Chen et al., 2015b), but Kozyreva et al. (2017) showed that they can also be fast rising. The long rise time predicted by pair-instability supernova (PISN) models has been seen in at least one SLSN (Lunnan et al., 2016).

However, spectroscopic models predict spectra that are different from observations (Jerkstrand et al., 2016). SLSNe-R are a potential sub-class of SLSNe-I. The existence and characterization of this class is discussed in Gal-Yam (2012) and De Cia et al. (in prep.).

While the debate on the powering source of SLSN-I is ongoing, the general agreement is that these explosions are associated with the death of massive stars, given their total radiated energies ($E > 10^{51}$ ergs, Gal-Yam, 2012). The study of their host galaxies has revealed that SLSN-I require extreme hosts, e.g., with low-metallicity ($Z \leq 0.5 Z_{\odot}$) and a high rate of star formation (SFR) for their low mass (Neill et al., 2011; Lunnan et al., 2014; Perley et al., 2016; Chen et al., 2016b; Thöne et al., 2015; Schulze et al., 2016), and strong emission lines (Leloudas et al., 2015b). However, Perley et al. (2016) argue that a high rate of star formation is not required, since there are many counterexamples of SLSNe with low SFRs, based on slit spectroscopy. High-resolution observations with *Hubble Space Telescope (HST)* showed that the host galaxies of hydrogen-poor SLSNe are usually irregular dwarf galaxies with asymmetric morphology or multiple peaks (Lunnan et al., 2015; Angus et al., 2016).

Gamma-ray bursts (GRBs) are another energetic phenomenon likely associated with deaths of massive stars (Hjorth et al., 2003). Their host galaxies show similarities to the hosts of SLSNe (Lunnan et al., 2014), although the latter are more extreme (Vreeswijk et al., 2014; Leloudas et al., 2015b; Perley et al., 2016; Schulze et al., 2016). Fruchter et al. (2006) and Blanchard et al. (2016) showed that GRBs are more concentrated in the brightest regions of their host galaxies.

Similarly, if SLSNe are indeed associated with very massive stars, and their hosts are unusual for the young stellar content (Thöne et al., 2015; Leloudas et al., 2015b), one natural expectation is that they may explode in blue, UV bright, regions of their host galaxies, which are the most recent regions of massive star formation (see Chapter 7). This may be particularly relevant for pair-instability driven SLSNe-R, which are believed to have the most massive progenitors among SLSNe. Lunnan et al. (2015) found that the H-poor SLSNe sites are correlated with UV light, with a light fraction distribution between GRBs and an uniform distribution (see their Figure 6).

1.3.3.1. Linear polarimetry of Superluminous Supernovae

The majority of Superluminous Supernovae occurred at large distances, and were apparently faint, and thus it is hard to undertake polarimetry which requires high signal-to-noise ratio. Intrinsic linear polarization of SLSNe is, as in the case of SNe Ia, a measure of the supernova's photosphere spherical asymmetry projected on the sky. If the projection of the photosphere is not symmetric, more photons will be scattered by electrons along the photosphere's major axis than along the minor axis, which will produce net-polarization in the continuum (see e.g. Hoflich, 1991).

Only a few SLSNe have been studied using linear polarimetry:

- LSQ14mo, a fast-declining SLSN-I, did not show evidence for significant polarization or polarization evolution from −7 and up to +19 days with respect to maximum (Leloudas et al., 2015a).
- In the contrary, the slowly-evolving SN 2015bn did show an increase in polarization with time, that was attributed to the photosphere receding to inner layers of the explosion that are more asymmetric. Inserra et al. (2016a) obtained the first spectropolarimetric observations of SN 2015bn, a hydrogen poor SLSN-I, at −24 and +28 days, further showing that the geometry was consistent with an axisymmetric configuration (that could be consistent with a magnetar

scenario). The polarization increase was confirmed by Leloudas et al. (2017) who obtained multi-epoch imaging polarimetry between −20 and +46 days (at nine epochs in total), showing that the increase in polarization, from ∼ 0.54 % to ≳ 1.10%, was coincident with changes in the optical spectrum.

- PS15br is a SLSN-II, which was observed at 6 days past maximum, shows polarization of P = 0.93 ± 0.17% in V passband, although the source is not clear, whether intrinsic or interstellar (Inserra et al., 2018b).
- Bose et al. (2018) investigated Gaia17biu/SN 2017egm, which is a nearby SLSN-I that exploded in a "normal", massive, metal-rich spiral galaxy. They detected wavelength independent polarization at the ∼0.5% level, which suggests that there is a modest, global departure from spherical symmetry. SN 2017egm is a nearby SLSN-I is a "normal", massive, metal-rich spiral galaxy.

2. Performance of the spectropolarimetric mode of FORS2

The content of this chapter has been published in:
Cikota, A., Patat, F., Cikota, S., & Faran, T.
Monthly Notices of the Royal Astronomical Society, Volume 464, Volume 464, Issue 4, p.4146-4159

2.1. Introduction

Given the comparatively low levels of polarization that are typical supernova studies, it is important the polarimeter being used is properly calibrated. The main aim of this work is to provide a re-calibration of a sub-set of highly polarized standard stars, which are not too bright to be observed with large telescopes, and can be used to verify the performance of other similar instruments in the southern hemisphere. In addition, related to the fact that ESO's Quality Control Group monitors polarimetric standards since 2009, we test the performance of the FOcal Reducer and low dispersion Spectrograph (FORS2) instrument mounted at the Very Large Telescope (VLT), in terms of stability and accuracy, by means of a thorough analysis of archival calibration data of highly linearly polarized and unpolarized standard stars.

Fossati et al. (2007) presented an analysis of standard stars observations obtained between 1999 and 2005 in PMOS and imaging-polarimetry (IPOL) mode with FORS1. They investigated the FORS1 stability in both, PMOS and IPOL mode, and found a small instrumental offset in the Stokes Q parameter which appears in PMOS mode only. This study is meant to further investigate and characterize that offset using FORS2 data.

2.2. Instrumental setup and observations

FORS2 is currently mounted at the Cassegrain focus of the ESO's Antu VLT unit. This focal reducer is equipped with a polarimetric mode, which can be selected by introducing in the light path a Wollaston prism and a rotatable super-achromatic half-wave retarder plate coupled to a grism and/or a filter to perform linear imaging or spectro-polarimetry (Appenzeller, 1967; Appenzeller et al., 1998; ESO, 2015).

For our purposes, we selected eight standard stars with zero polarization, and six highly polarized standard stars extracted from the FORS Standard Fields and Stars list[1] (listed in Table 6.2). All stars from the FORS Standard Fields and Stars list (i.e., our sample), were also analyzed by Fossati et al. (2007). They additionally considered three polarized standard stars (HD 345310, HD 111579 and BD -13 5073), 8 unpolarized stars (WD 2359-434, WD 0310-688, WD 1616-154, WD 1620-391, HD 176425, WD 2007-303, WD 2039-202, WD 2149+021) and HD 64299, which was erroneously

[1] $https://www.eso.org/sci/facilities/paranal/instruments/fors/tools/FORS\_Std.html$

Table 2.1.: List of observed standard stars.

Name	RA (J2000)	DEC (J2000)	V (mag)	Spec. type	Type	No. of Epochs
HD 10038	01 37 18.59	-40 10 38.46	8.1	A2mA5-F0	unPol.	8
HD 13588	02 11 16.69	-46 35 06.17	7.9	A1m	unPol.	4
HD 42078	06 06 41.04	-42 17 55.69	6.2	Am	unPol.	5
HD 97689	11 13 50.75	-52 51 21.22	6.8	A0m	unPol.	12
WD 1615-154	16 17 55.26	-15 35 51.93	13.4	DA1.7	unPol.	1
WD 1620-391	16 23 33.84	-39 13 46.16	11.0	DA2	unPol.	7
WD 2039-202	20 42 34.75	-20 04 35.95	12.4	DA2.5	unPol.	2
WD 2149+021	21 52 25.38	+02 23 19.54	12.7	DA2.8	unPol.	1
NGC 2024 1	05 41 37.85	-01 54 36.5	12.2	B0.5V	Pol.	7
Vela1 95[a]	09 06 00.01	-47 18 58.2	12.1	OB+	Pol.	11
Hiltner 652[b]	17 43 19.59	-28 40 32.76	10.8	B1II-III	Pol.	8
HDE 316232	17 45 43.70	-29 13 18.15	10.4	O9IV	Pol.	1
BD -14 4922	18 11 58.10	-14 56 09.01	9.73	O9.5	Pol.	2
BD -12 5133	18 40 01.70	-12 24 06.92	10.4	B1V	Pol.	1

The coordinates, brightness and spectral type were taken from the SIMBAD Astronomical Database. Type indicates if the star is polarized (Pol.) or unpolarized (unPol.), and No. of Epochs is the number of epochs.

[a] in Fossati et al. (2007) designated as Ve 6-23.

[b] in Fossati et al. (2007) designated as CD-28 13479.

suggested as an unpolarized standard star, but is in fact polarized at the 0.1% level (see e.g., Masiero et al. (2007)).

From the archive we selected observations obtained in PMOS mode with grism 300V, without an order separating filter, and with the half-wave retarder plate positioned at angles of 0°, 22.5°, 45°, and 67.5°. The half-wave retarder plate angle is measured between the acceptance axis of the ordinary beam of the Wollaston prism (which is aligned to the north-south direction) and the fast axis of the retarder plate. In order to allow a time trend analysis, the stars were selected to have observations at multiple epochs (40 epochs in total of unpolarized, and 30 of polarized stars), spanning 5 years. The stars were placed on the central slit of the PMOS focal mask, very close to the optical axis of the instrument. The spectrum produced by the grism is split by the Wollaston prism into an ordinary (o) and extraordinary (e) beam, which are separated by a throw of about 22 arcseconds.

2.3. Data reduction

After excluding saturated frames, the data were reduced using standard procedures in IRAF. Wavelength calibration was achieved using He-Ne-Ar arc lamp exposure. The typical RMS accuracy is ~ 0.3 Å. Although it is very difficult to achieve a complete flat fielding correction in the presence of polarization optics, the effects of improper correction were minimized by taking advantage of the redundant number of half-wave positions (see Patat & Romaniello (2006)).

Ordinary and extra-ordinary beams were extracted in an unsupervised way using the PyRAF apextract.apall procedure, with a fixed aperture size of 10 pixels. To avoid spectrum tracing problems, the input frames were properly trimmed to exclude the low signal-to-noise at the edges of the spectral

range. The final effective wavelength range is 3950-9300 Å. We calculated the total flux in *BVRI* passbands by integrating the total flux weighted with Bessel's *BVRI* passband filters, and computed the synthetic broad-band polarization degree and polarization angle corresponding to each passband. We also binned the spectra in 50 Å bins, in order to obtain a larger signal-to-noise ratio, and calculated the Stokes parameters Q and U, polarization degree P, and polarization angle θ_P as a function of wavelength. The signal-to-noise ratio (SNR) is typically between 500 and 2000 per 50Å bin, tabulated for each individual epoch at a given wavelength in Table 2.4 and Table 2.5 for unpolarized and polarized standard stars respectively.

The Stokes parameters Q and U were derived via Fourier transformation, as described in the FORS2 User Manual:

$$\begin{aligned} Q &= \tfrac{2}{N} \textstyle\sum_{i=0}^{N-1} F(\theta_i) \cos(4\theta_i) \\ U &= \tfrac{2}{N} \textstyle\sum_{i=0}^{N-1} F(\theta_i) \sin(4\theta_i) \end{aligned} \tag{2.1}$$

where $F(\theta_i)$ are the normalized flux differences between the ordinary (f^o) and extra-ordinary (f^e) beams:

$$F(\theta_i) = \frac{f^o(\theta_i) - f^e(\theta_i)}{f^o(\theta_i) + f^e(\theta_i)} \tag{2.2}$$

at different half-wave retarder plate position angles $\theta_i = i * 22.5°$.

Although FORS2 is equipped with a super-achromatic half wave plate, residual retardance chromatism is present. The wavelength dependent retardance offset ($-\Delta\theta(\lambda)$) is tabulated in the FORS2 User Manual (ESO, 2015). The chromatism was corrected through the following rotation of the Stokes parameters (Bagnulo et al., 2009; Patat & Taubenberger, 2011):

$$\begin{aligned} Q_{\rm corrected} &= Q \cos 2\Delta\theta(\lambda) - U \sin 2\Delta\theta(\lambda) \\ U_{\rm corrected} &= Q \sin 2\Delta\theta(\lambda) + U \cos 2\Delta\theta(\lambda) \end{aligned} \tag{2.3}$$

Hereafter, $Q_{corrected}$ and $U_{corrected}$ are noted as Q and U.

Finally we calculate the polarization (eq. 5.4):

$$P = \sqrt{Q^2 + U^2} \tag{2.4}$$

and the polarization angle (eq. 5.5),

$$\theta = \frac{1}{2} \arctan(U/Q). \tag{2.5}$$

The statistical uncertainties were estimated using the prescriptions presented by Patat & Romaniello (2006).

The classical Serkowski parameters (Serkowski et al. (1975), eq. 4.1) were finally derived by linear least squares fits to the linear polarization $P(\lambda)$, yielding the peak polarization level ($P_{\rm max}$) and wavelength ($\lambda_{\rm max}$), and the width constant (K).

$$\frac{P(\lambda)}{P_{\rm max}} = \exp\left[-K \ln^2\left(\frac{\lambda_{\rm max}}{\lambda}\right)\right] \tag{2.6}$$

2.4. Results and Discussion

2.4.1. Unpolarized stars

The analysis of FORS2 linear polarization stability and accuracy is based on eight unpolarized standards stars, observed at 40 epochs in total, between 2010 and 2015 (see Table 2.1). For all stars

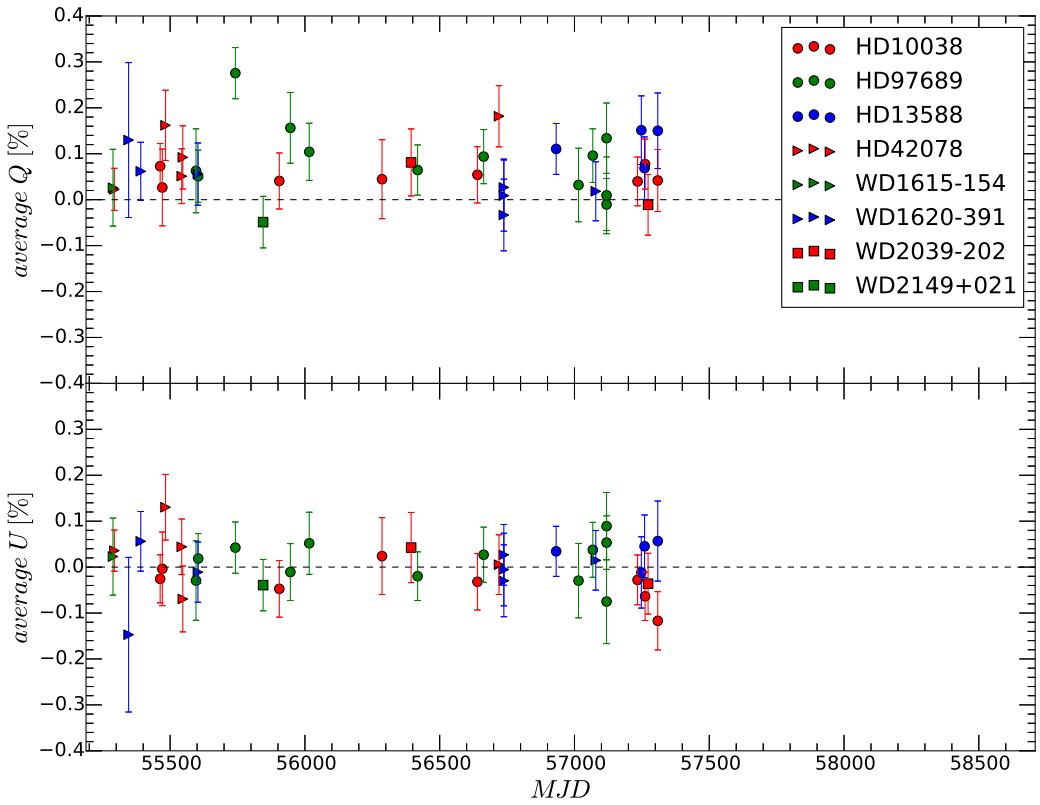

Figure 2.1.: Averaged Stokes parameters P_Q and P_U for the 8 unpolarized standard stars in the sample observed on 40 different epochs.

and each epoch, we calculated the mean value of the Stokes parameters P_Q and P_U in the 3950-9300 Å wavelength range (Passband "all" in Table 2.4), which is shown in Figure 2.1. The values do not show statistically significant variations over the full time range, with very similar standard deviations of P_Q and P_U. However, a small but statistically significant instrumental offset is detected in P_Q. The weighted mean of the Stokes parameter P_Q of all stars and epochs is 0.07±0.01%, while the corresponding value for P_U is 0.00±0.01%.

To investigate possible wavelength dependent effects, we calculated the weighted mean of P_Q and P_U as a function of wavelength using all observations of unpolarized standard stars. A clear, wavelength dependent offset is detected in Q (Figure 2.2). The first-order, best fit laws (red lines in Figure 2.2) are as follows:

$$\begin{aligned} Q(\lambda) &= [(9.66 \pm 1.04) \times 10^{-8}]\lambda + (3.29 \pm 6.34) \times 10^{-5} \\ U(\lambda) &= [(7.28 \pm 0.90) \times 10^{-8}]\lambda - (4.54 \pm 0.55) \times 10^{-4} \end{aligned} \tag{2.7}$$

where λ is expressed in Å. These relations provide a handy correction to be applied to the observed Q and U values. Rigorously speaking, this implicitly assumes that the correction is additive and does not depend on the incoming signal. This approximation probably holds only to first order. The exact prescription can only be obtained with a proper characterization of the Mueller matrices that describe the optical system, which is beyond the scope of this paper.

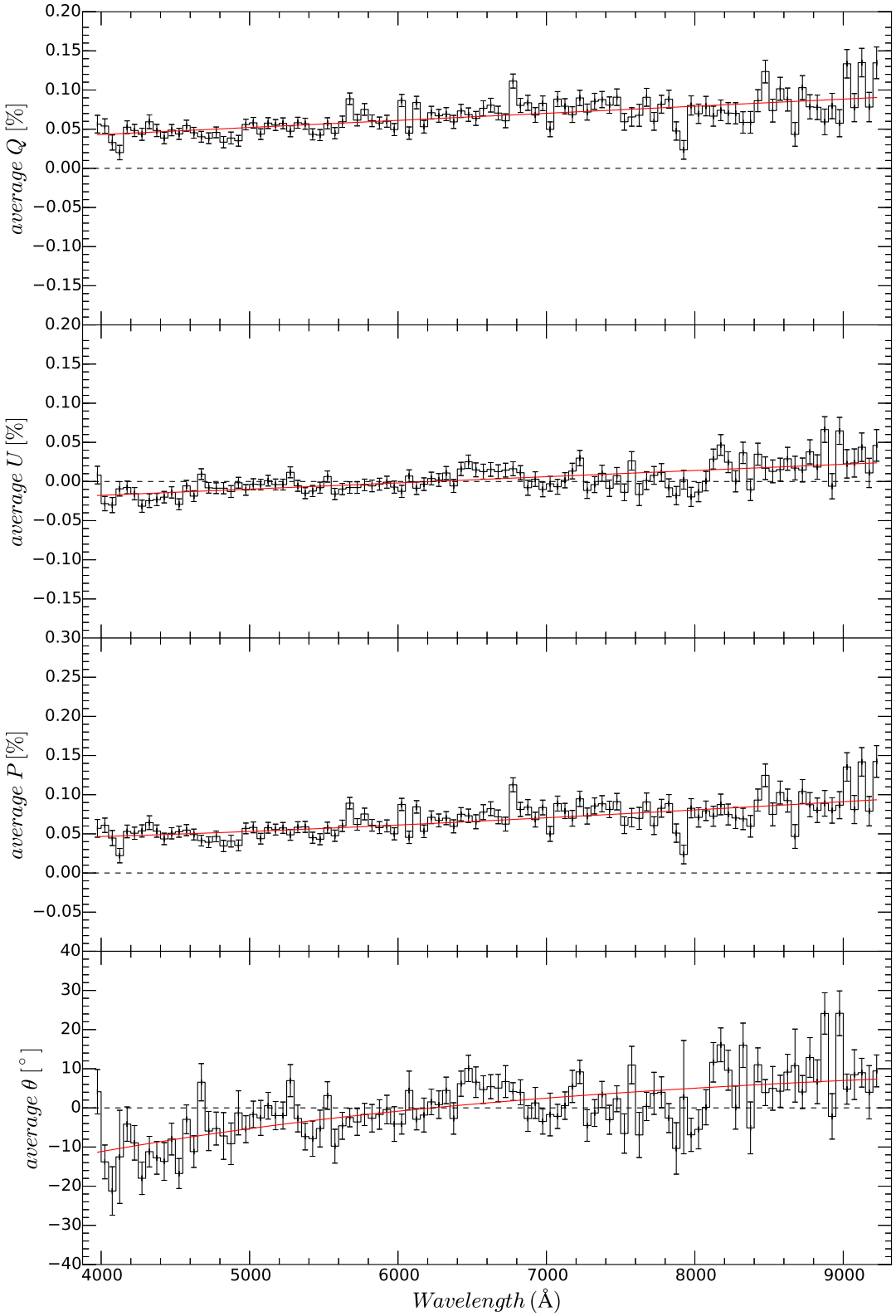

Figure 2.2.: Weighted means of Stokes parameters Q and U of all observations of unpolarized stars (8 objects, 40 epochs). The red lines are linear least-squares fits to the weighted averages Q and U. The polarization P and polarization angle θ were calculated from the weighted means of Q and U. The red curves over-plotted on P and θ were calculated from separate linear fits to $Q(\lambda)$ and $U(\lambda)$.

Table 2.2.: Weighted averages of polarized standard stars observed with FORS2.

						Serkowski law		
Name	Passband	P (%)	P_Q (%)	P_U (%)	θ(°)	$\lambda_{\max}$ (Å)	$P_{\max}$ (%)	K
Vela1 95						5864.5 ± 7.4	8.295 ± 0.004	1.34 ± 0.01
	B	7.645 ± 0.044	7.445 ± 0.044	-1.739 ± 0.046	172.76 ± 0.05			
	V	8.163 ± 0.011	7.834 ± 0.011	-2.295 ± 0.012	172.41 ± 0.02			
	R	7.927 ± 0.003	7.56 ± 0.003	-2.383 ± 0.003	172.06 ± 0.01			
	I	7.151 ± 0.002	6.9 ± 0.002	-1.881 ± 0.002	171.95 ± 0.01			
BD -14 4922						5452.5 ± 13.9	6.137 ± 0.007	1.3 ± 0.02
	B	5.801 ± 0.024	-0.992 ± 0.024	5.715 ± 0.024	49.7 ± 0.07			
	V	6.096 ± 0.012	-0.955 ± 0.012	6.021 ± 0.012	49.8 ± 0.05			
	R	5.818 ± 0.006	-0.864 ± 0.005	5.753 ± 0.006	49.7 ± 0.04			
	I	4.99 ± 0.006	-0.796 ± 0.006	4.926 ± 0.006	49.24 ± 0.05			
HDE 316232						5591.1 ± 18.3	5.017 ± 0.008	1.2 ± 0.03
	B	4.679 ± 0.023	4.637 ± 0.023	0.619 ± 0.021	3.61 ± 0.09			
	V	4.931 ± 0.014	4.901 ± 0.014	0.547 ± 0.012	3.51 ± 0.07			
	R	4.772 ± 0.007	4.745 ± 0.007	0.508 ± 0.006	3.37 ± 0.06			
	I	4.214 ± 0.008	4.176 ± 0.008	0.562 ± 0.007	3.53 ± 0.08			
Hiltner 652						5776.5 ± 9.0	6.467 ± 0.005	1.17 ± 0.01
	B	5.948 ± 0.017	5.948 ± 0.017	-0.054 ± 0.017	179.52 ± 0.05			
	V	6.371 ± 0.009	6.367 ± 0.009	-0.198 ± 0.009	179.44 ± 0.03			
	R	6.218 ± 0.004	6.214 ± 0.004	-0.218 ± 0.004	179.39 ± 0.03			
	I	5.613 ± 0.004	5.612 ± 0.004	-0.041 ± 0.004	179.46 ± 0.03			
NGC 2024 1						6340.4 ± 4.7	9.855 ± 0.004	1.29 ± 0.01
	B	8.602 ± 0.044	0.583 ± 0.045	-8.582 ± 0.044	136.43 ± 0.05			
	V	9.548 ± 0.013	0.122 ± 0.013	-9.546 ± 0.013	135.94 ± 0.02			
	R	9.671 ± 0.004	-0.0 ± 0.004	-9.67 ± 0.004	135.93 ± 0.01			
	I	9.009 ± 0.002	0.398 ± 0.002	-8.999 ± 0.002	135.9 ± 0.01			
BD -12 5133						5049.5 ± 35.5	4.369 ± 0.01	1.2 ± 0.04
	B	4.217 ± 0.027	1.688 ± 0.027	-3.865 ± 0.027	146.54 ± 0.12			
	V	4.266 ± 0.016	1.568 ± 0.016	-3.968 ± 0.016	145.88 ± 0.09			
	R	3.996 ± 0.008	1.406 ± 0.008	-3.74 ± 0.008	145.62 ± 0.08			
	I	3.348 ± 0.009	1.222 ± 0.009	-3.117 ± 0.009	145.28 ± 0.11			

Fossati et al. (2007) performed a similar analysis using observations of standard stars obtained with FORS1 from 1999 to 2005 in both spectropolarimetric (PMOS) and imaging polarimetry (IPOL) mode. For PMOS, they found that the weighted average of all P_U values in PMOS mode are consistent with a null value, but detected an offset of 0.07±0.01%, and 0.09±0.01 % in $P_Q(B)$ and $P_Q(V)$ respectively. They did not detect any offset in IPOL mode, and concluded that the P_Q offset may be associated with some, but not all, grism and filter combinations.

Our results, based on observations that were taken through the 300V grism (ID: +10) and no order-sorting filters, confirm the findings of Fossati et al. (2007) and lead us to conclude that the source of the instrumental polarization causing the offset in P_Q probably resides in the inclined surface of the prism that is coupled to the transmission grating in the FORS1 and FORS2 grisms.

2.4.2. Polarized stars

For our analysis we reduced a sample of six highly polarized standard stars (Table 6.2) observed with FORS2 between 2009 and 2015 on 30 different epochs. The data were corrected for instrumental polarization using the relations derived from the unpolarised stars (Eqs. 2.7). The results for the individual epochs are given in Table 2.5, while weighted means of all epochs are listed in Table 2.2. An example of polarization wavelength dependence is shown in Figure 2.3, and a Q/U diagram in Figure 2.4. As expected for polarization generated by interstellar dust sharing the same alignment angle, the polarization angle is constant, and the points on the Q/U diagram follow a straight line.

The wavelength dependence of the polarization angle was characterized by fitting a second order

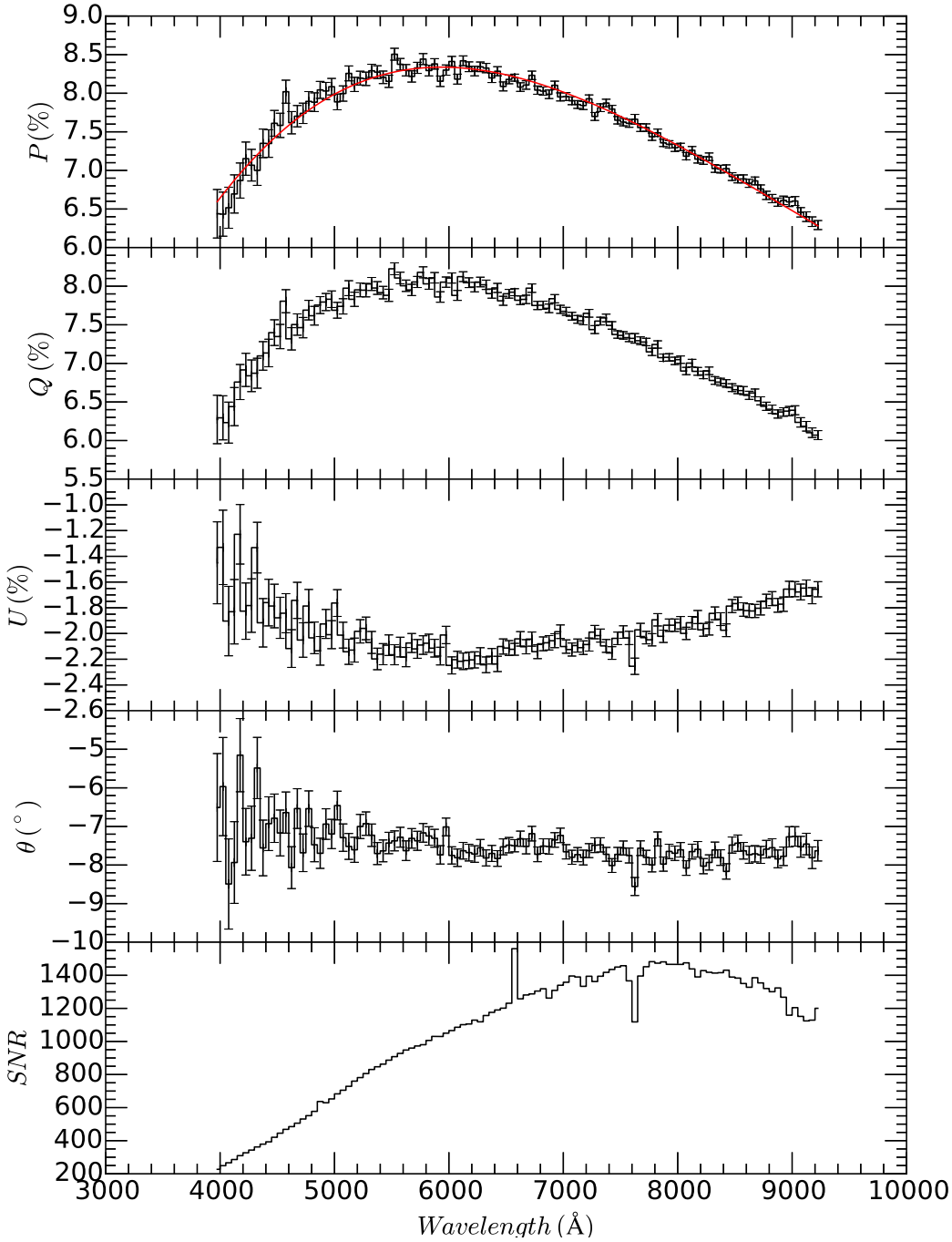

Figure 2.3.: Total polarization P, Stokes parameters Q and U, Polarization angle θ and SNR for Vela1 95 at epoch 2014-01-06. The bin width is 50 Å. The solid red line is the best fit Serkowski law.

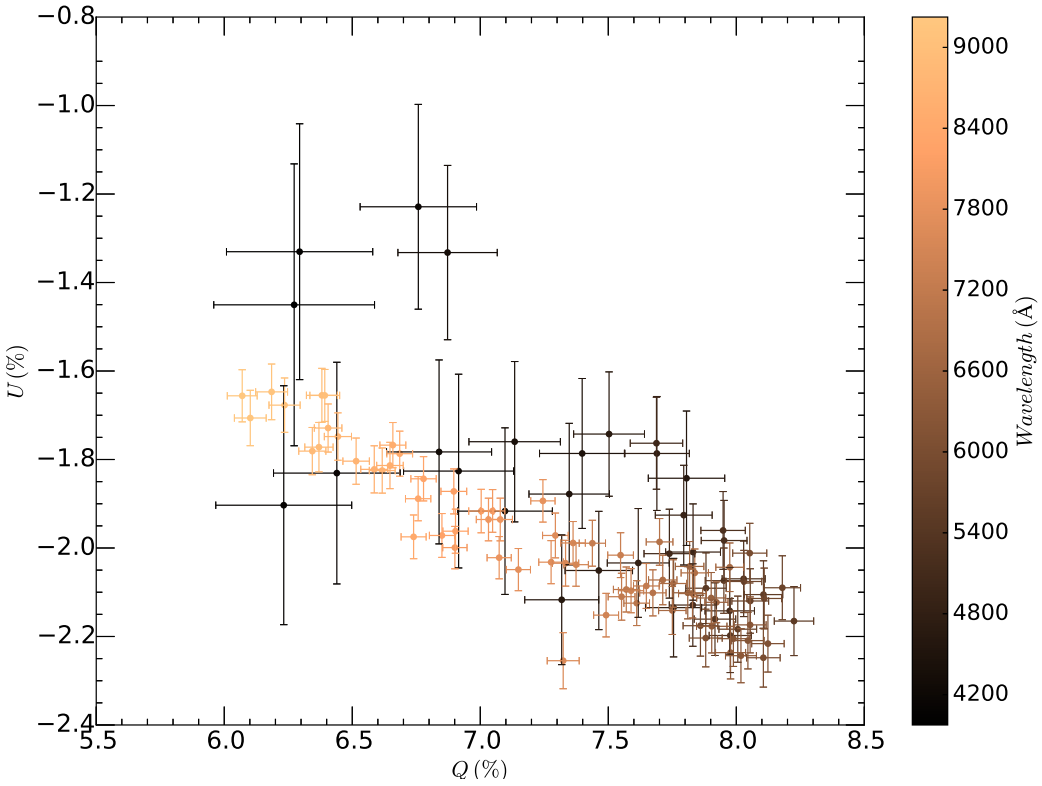

Figure 2.4.: Q/U diagram for for Vela1 95 at epoch 2014-01-06. The wavelength is color coded.

polynomial to the calculated weighted mean of the polarization angle (Figure 2.5). From the values of the best fit coefficients we conclude that there is no significant θ - λ dependence. The polarization angles are all constant to within the measurement errors, with slopes dθ/dλ between -2.5 and 0.53 degree/μm.

We tested the reproducibility of the observations using stars observed at least at two epochs: Vela1 95, Hiltner 652, NGC 2024 1 and BD-144922. An example for Vela1 95 is presented in Fig. 2.6. The root mean square deviation from the mean polarization values are 0.21% (Vela1 95, 11 epochs), 0.12% (Hiltner 652, 8 epochs), 0.12% (NGC 2024 1, 7 epochs), and 0.05% (BD-144922, 2 epochs).

We finally tested the HWP positioning stability, by calculating the residuals of the mean $\theta(\lambda)$ values for all epochs of the polarized stars. No systematic jumps are detected, while erratic fluctuations are present, with a peak-to-peak amplitude of about 1.2° and a standard deviation of 0.27° (Figure 2.7). Given the typical statistical errors of the single measurements, the observed fluctuations are statistically very significant and certainly not due to the photon noise. The most likely interpretation is a possible drift in the absolute positioning of the retarder plate and/or of the analyzer. The estimated rms deviation (~0.3 degrees) hence represents the typical maximum accuracy one can expect on the polarization angle for very high signal-to-noise ratios.

2.4.2.1. Comparison with the literature

We compared our synthetic broad-band results (Table 2.2) to those reported by Fossati et al. (2007) (their Table 2) and the values based on data taken with FORS1 during commissioning, given in the

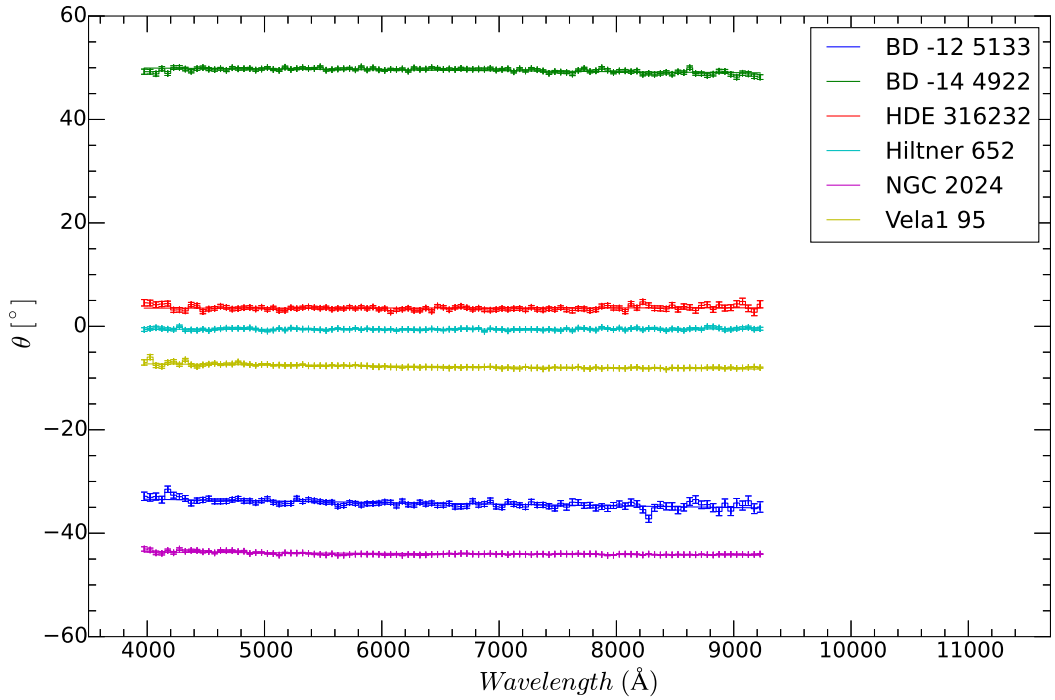

Figure 2.5.: Weighted mean of polarization angle θ as a function of wavelength.

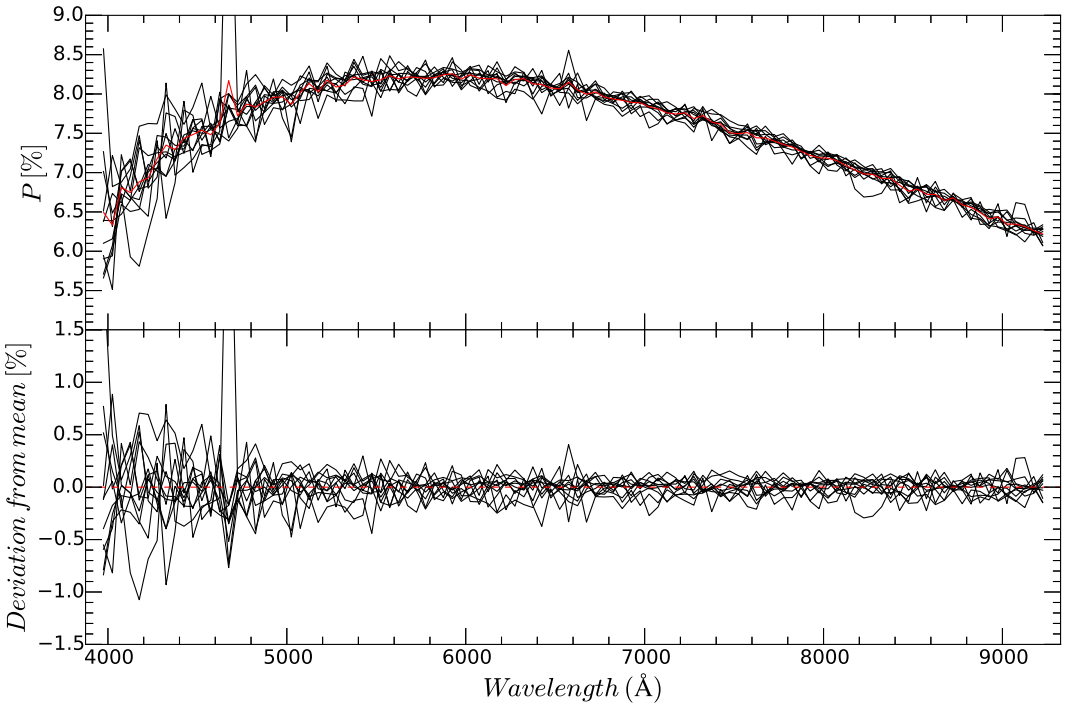

Figure 2.6.: Reproducibility of Vela1 95 polarization P. The bin width is 50 Å. The solid red line is the mean polarization of all 11 epochs. The deviations form the mean are shown in the bottom plot. The RMS of the deviation from the mean value is 0.21%.

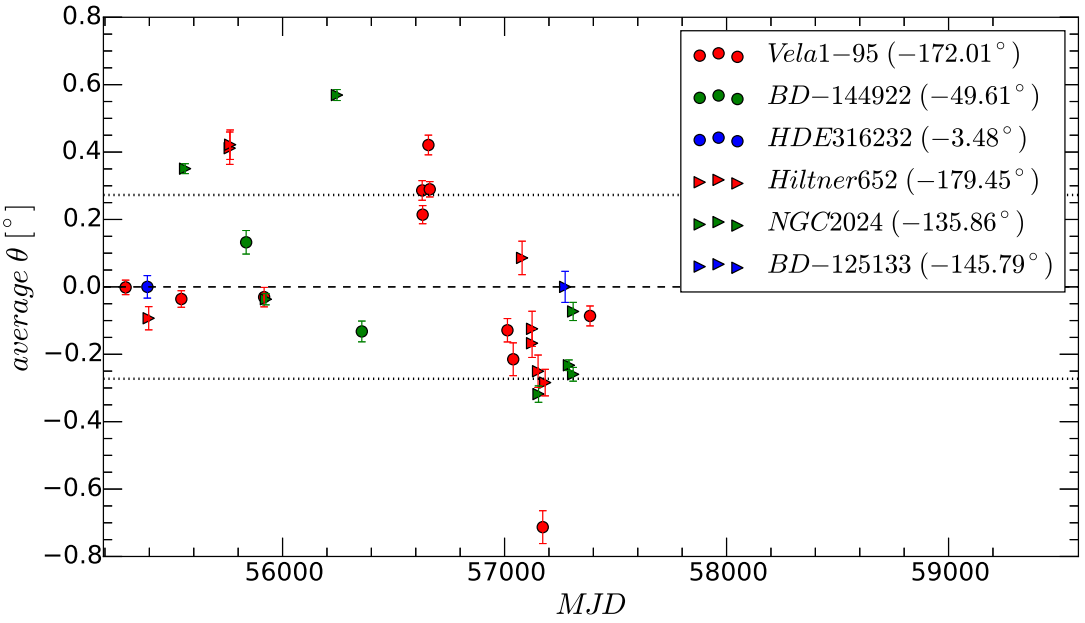

Figure 2.7.: Polarization angle stability. Shown are residuals of the averaged $\theta(\lambda)$ values for 30 epochs of 6 polarized standard stars.

FORS webpage[2]. Figure 2.8 shows the polarization and polarization angle differences, ΔP and $\Delta\theta$, between our measurements and those published in the literature: $\Delta P = P_{\text{Literature}} - P_{\text{This work}}$ and $\Delta\theta = \theta_{\text{Literature}} - \theta_{\text{This work}}$.

The average polarization deviation of all values, $\langle\Delta P\rangle$, obtained in PMOS mode by Fossati et al. (2007) from values obtained in this work is 0.01%, with a root mean square deviation of 0.17%. Also the values obtained by Fossati et al. (2007) in IPOL mode are consistent with our results, with an average $\langle\Delta P\rangle$ of -0.02% and an RMS of 0.15%. Our results are on average larger than the values given in the FORS webpage, with $\langle\Delta P\rangle$ = -0.15% and an RMS of 0.36%.

For the polarization angle, the average deviation from the PMOS values given in Fossati et al. (2007) is $\langle\Delta\theta\rangle$=0.17°, with an RMS of 0.91°; $\langle\Delta\theta\rangle$=-0.03°, with an RMS of 0.77° for IPOL mode values (Fossati et al., 2007); and $\langle\Delta\theta\rangle$=0.50°, with an RMS of 0.76° for the values given in the FORS webpage.

Thus, our results are, in general, in good agreement with previous estimates. The discrepancies with results given in Fossati et al. (2007) are consistent with the RMS variation found in the repeatability test (RMS $\lesssim$ 0.2%, see § 2.4.2), and might be due to star variability or instrumental effects (e.g., the HWP positioning uncertainty, see Figure 2.7), while the discrepancy from the values given in the FORS webpage is probably due to systematic differences between FORS2 and FORS1.

We also compared our Serkowski law fitting results for the 6 polarized standard stars to a data set of 105 objects studied by Whittet et al. (1992). They collected data obtained polarimetric observation in *UBVRIJHK* passbands using the Hartfield polarimeter (described by Brindle et al. (1986), and Bailey & Hough (1982)) on the 3.9-m AAT at Siding Spring Observatory, and the 3.8-m UKIRT at Mauna Kea Observatory. As shown in Figure 2.9, our results deviate by 2-3σ from the best fit $\lambda_{\text{max}} - K$

[2] *http://www.eso.org/sci/facilities/paranal/instruments/fors/inst/pola.html*

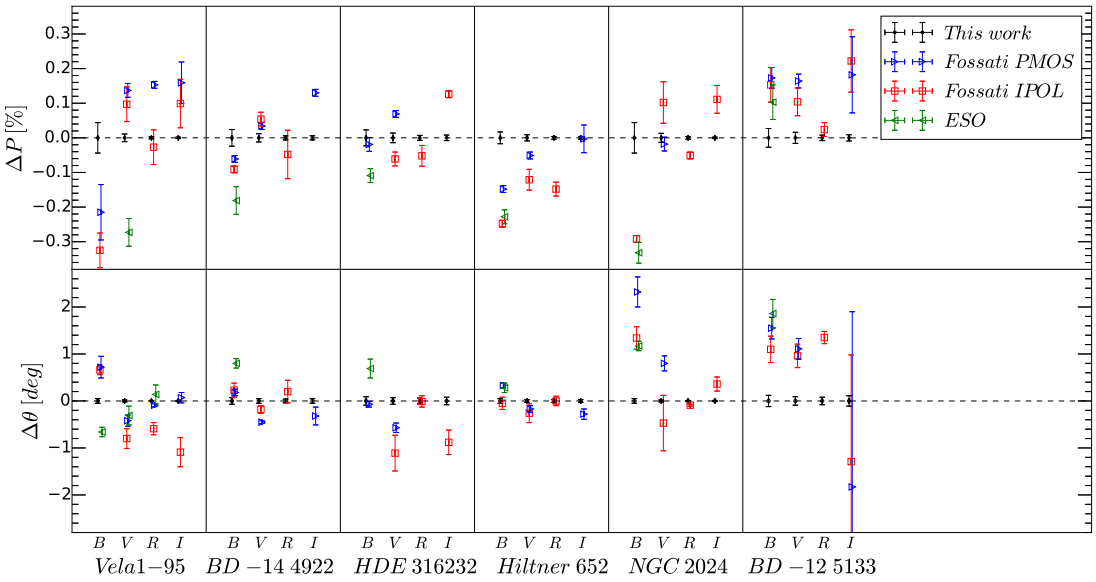

Figure 2.8.: Comparison between IPOL and PMOS values presented in Fossati et al. (2007) (their Table 2), the ESO values given in the FORS webpage, and the new values obtained in this work. ΔP and $\Delta\theta$ are offsets from values obtained in this work. Three data points are outside of axis limits: the offset, ΔP, from the ESO value for Vela1 95, is 0.60±0.03% and -0.76±0.04% in *B* and *R* band respectively, while ΔP in *B* band, from PMOS value (Fossati et al., 2007) for NGC 2024 1 is ΔP=-0.51±0.06%.

relation found by Whittet et al. (1992).

This deviation, which is statistically significant, cannot be explained by measurement errors, and calls for further investigation. For this reasons, we have looked in more detail the case of Vela1 95, which is included in the Whittet et al. sample. For this object, Whittet et al. (1992) determined a λ_{max}=5500±200 Å, P_{max}=8.08±0.07 % and K=1.10±0.06. From our data, we determined λ_{max}=5864±7 Å, P_{max}=8.295±0.004 % and K=1.34±0.01.

In Figure 2.10 we compare the Whittet et al. (1992) measurements of Vela1 95 to our FORS2 measurements. The figure also includes the Serkowski law best fit to Whittet et al.'s data (λ_{max}=5521±111 Å, P_{max}=8.08±0.07 % and K=1.10±0.05; which is consistent to the Serkowski fit parameters in Whittet et al. (1992)), compared to a fit to FORS2 data (λ_{max}=5864±7 Å, P_{max} = 8.295±0.004 % and K=1.34±0.01), and Whittet et al. *BVRI* data points only (λ_{max}=5606± 126 Å, P_{max}=8.11 ± 0.08 % and K=1.25±0.19). While the FORS2 data perfectly match the *B* and *V* measurements by Whittet et al., a significant difference is seen in *R* and *I* passbands. This strongly suggests that the problem does not reside in the different wavelength ranges used in the two studies. The explanation for the observed discrepancy is most likely related to the effective wavelengths adopted by Whittet et al. (1992) in their work. The authors list the bandpass properties in their Table 1. They also remark that their K measurements are at an effective wavelength of 2.04 μm rather than at the usual value of 2.2μm. This is justified by an absorption in the Foster prism, which narrows the passband and reduces the effective wavelength. However, the authors do not explain why they do not adopt the usual *R* and *I* values given in the instrument description (Brindle et al. (1986); Bailey & Hough (1982)). The central wavelengths reported by Whittet et al. (1992) are: 0.36 μm (U), 0.43 μm (B), 0.55 μm (V), 0.63 μm (R), 0.78 μm (I), 1.21 μm (J), 1.64 μm (H) and 2.04 μm (K). On the other hand, Brindle et al. (1986) list the following wavelengths: 0.36 μm (U), 0.43 μm (B), 0.55 μm (V), 0.72 μm (R), 0.80 μm (I), 1.2 μm (J), 1.64 μm

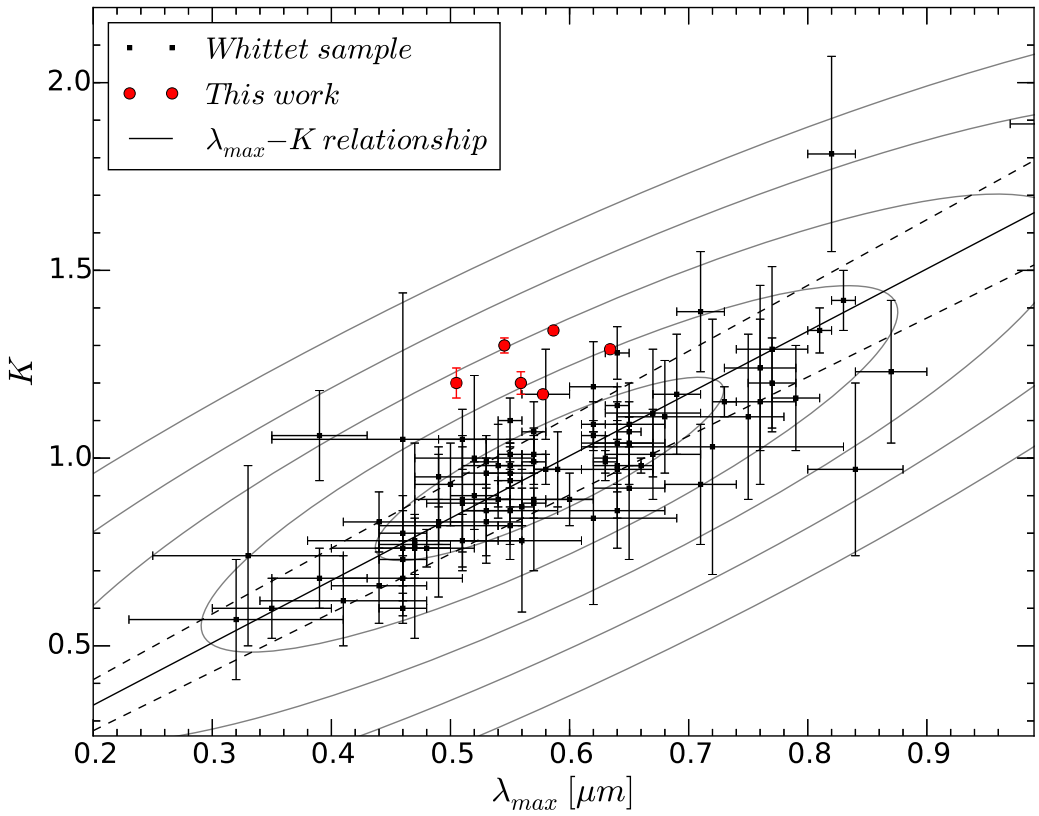

Figure 2.9.: $\lambda_{\rm max} - K$ plane containing our 6 standard stars (red dots) compared to the sample from Whittet et al. (1992) (black dots). The full line is the empirical $\lambda_{\rm max} - K$ relationship determined in Whittet et al. (1992), and the dashed lines trace the 1σ uncertainty. The gray curves are 1 to 5 sigma error ellipses.

(*H*) and 2.19 μm (*K*), which are also consistent with wavelengths in Bailey & Hough (1982), except that the latter specify 2.14 μm for the effective wavelength of the K passband. The difference in the *R* and *I* effective wavelengths is evident.

When using 0.72 μm and 0.80 μm for *R* and *I* respectively, a Serkowski law fit to all polarimetric points gives: $\lambda_{\rm max}$=5732±160 Å, $P_{\rm max}$=8.28±0.12 % and K=1.24±0.09. When fitting the *BVRI* data only, the best fit parameters are: $\lambda_{\rm max}$=5834±168 Å, $P_{\rm max}$=8.42±0.22 % and K=1.65±0.45. The results are summarized in Table 2.3. Since spectropolarimetric data do not suffer from the additional problem caused by the need of properly characterizing the photometric system, and given the superior quality of the data presented here and its higher signal to noise, we tend to believe our results are very robust and provide a solid reference. On these grounds, we suspect that the $\lambda_{\rm max}$, $P_{\rm max}$ and K values reported by Whittet et al. (1992) are systematically smaller than real. We will further investigate this problem and its consequences in a separate study, using observations along the lines of sight to a larger sample of Galactic reddened stars.

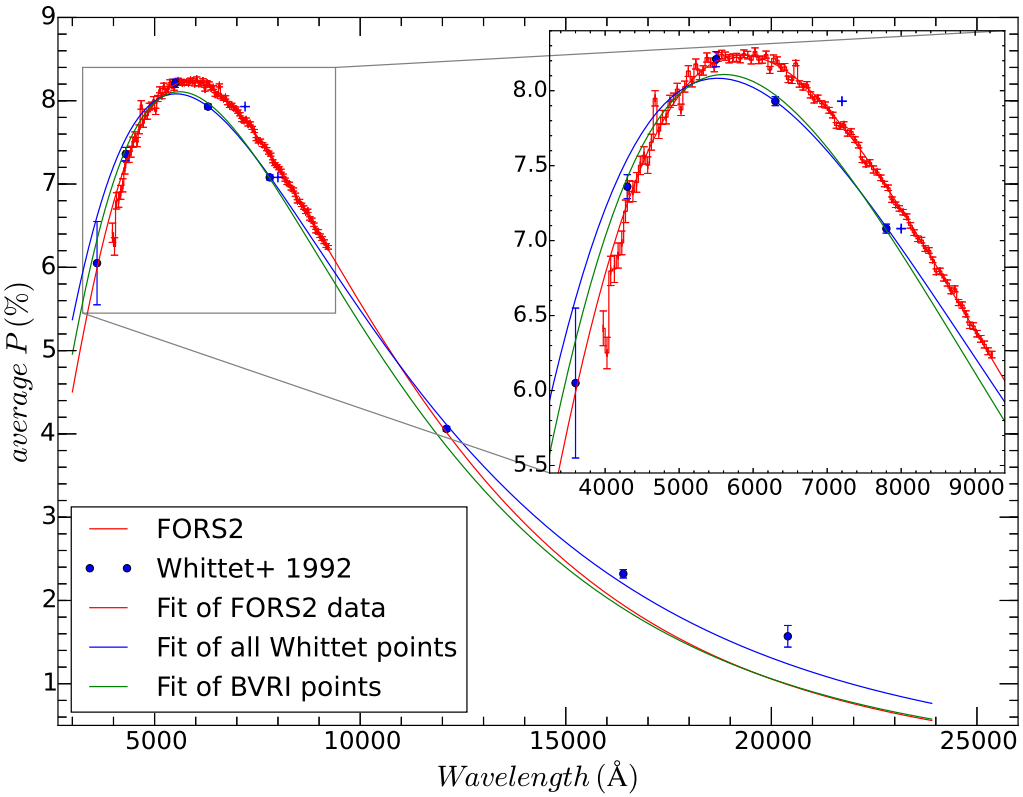

Figure 2.10.: Comparison between Whittet et al. (1992) polarimetric measurements (blue dots) and spectropolarimetric FORS2 data (red line) for Vela1 95. The colored curves trace a best fit Serkowski law to all data points (blue), *BVRI* data points only (green) and FORS2 data (red). Blue '+' signs mark the effective wavelengths of *R* (0.72 μm) and *I* (0.80 μm) passbands, as specified in Brindle et al. (1986) and Bailey & Hough (1982).

Table 2.3.: Serkowski parameters comparison table.

	λ_{max} (Å)	P_{max} (%)	K
Whittet et al. (1992)	5500 ± 200	8.08 ± 0.07	1.10 ± 0.06
Best fit to FORS2 data	5864 ± 7	8.295 ± 0.004	1.34 ± 0.01
Best fit to all Whittet et al. data points	5521 ± 111	8.08 ± 0.07	1.10 ± 0.05
Best fit to Whittet et al. *BVRI* data only	5606 ± 126	8.11 ± 0.08	1.25 ± 0.19
Best fit to Whittet et al. *UBVR'I'JHK* data	5732 ± 160	8.28 ± 0.12	1.24 ± 0.09
Best fit to Whittet et al. *BVR'I'* data only	5834 ± 168	8.42 ± 0.22	1.65 ± 0.45

R' and *I'* indicate the modified passband wavelengths, 0.72 μm and 0.80 μm for *R* and *I* respectively.

2.5. Summary and conclusions

In this study we used archival FORS2 observations of polarimetric standard stars to characterize the performance and stability of FORS2 mounted at the VLT. For this purpose we analyzed 8 unpolarized standard stars observed on 40 epochs, and 6 polarized standard stars (30 epochs). Our main results can be summarized as follows:

1. We confirm the instrumental wavelength dependent polarization detected by Fossati et al. (2007).

The spurious signal steadily grows from the blue to the red, ranging from 0.05% (4000Å) to 0.10% (9000Å). The vectorial correction for P_Q and P_U (see Equation 2.7) can be applied to the observed Stokes parameters. The physical cause of this instrumental polarization is still unclear, but it is most likely related to the tilted surfaces of the despersive element.

2. We tested the repeatability of total linear polarization using observations of polarized standard stars spanning 5 years. The RMS variation is $\lesssim 0.2\%$. For comparison, the typical error per 50Å bin for a single epoch is $\lesssim 0.1\%$.

3. Using the same sample of polarized stars, we tested the HWP positioning stability, and found a RMS of 0.27°. For comparison, the typical uncertainty in the weighted mean is $\sigma_\theta \lesssim 0.05°$, while the typical uncertainty per 50Å bin for a single epoch is $\lesssim 0.5°$.

4. Our analysis confirms that FORS2 can achieve a maximum accuracy of ~0.1% and ~0.3 degrees in polarization degree and angle, respectively. These values, which represent the instrumental limits of this focal reducer, are shown to be stable over timescales of years.

5. As a by-product of our analysis, we studied the wavelength dependence of linear polarization for our set of polarized standard stars. Our polarization results are in good agreement with those reported in the literature (see Figure 2.8). Peak polarization ($P_{\rm max}$), peak wavelength ($\lambda_{\rm max}$) and width parameter (K) were determined via least squares fit of the classical Serkowski law to the observed data.

6. Given the larger telescope size and the superb performance of FORS2, the data presented in this work provide a robust re-calibration of a selected set of linear polarization standard stars that can be reliably used for both checking the performance of other polarimeters and calibrating scientific data obtained with those instruments.

7. A comparison between the $\lambda_{\rm max}$-K values presented in this work and those reported by Whittet et al. (1992) reveals a systematic and statistically significant deviation, with our K values being larger. While this is partially caused by the shorter wavelength range covered by our FORS2 observations (4000-9000Å to be compared to the *UBVRIJHK* measurements by Whitthet et al.), it is clear that this cannot fully explain the observed differences. A closer investigation shows that the K values reported by Whittet et al. (1992) are most likely offset because of incorrect effective wavelengths for *R* and *I* passbands. This is clearly visible when comparing the data for the standard star Vela1 95, which is common to both data sets.

8. We expect that further studies, including larger sets of reddened Galactic stars, will show the same systematic discrepancy.

Acknowledgements

Based on observations made with ESO Telescopes at the Paranal Observatory under programme ID 60.A-9800, 60.A-9203, 084.B-0217, 084.D-0799, 085.D-0391, 089.D-0515, 091.D-0401, 290.D-5009.

Table 2.4.: Unpolarized stars.

Name	Epoch	Passband	P_Q (%)	P_U (%)	S/N
HD10038	2010-09-24	all	0.076 ± 0.05	-0.025 ± 0.052	
		B	0.065 ± 0.012	-0.02 ± 0.013	1553
		V	0.065 ± 0.009	-0.025 ± 0.01	1927
		R	0.079 ± 0.005	-0.034 ± 0.006	1726
		I	0.077 ± 0.007	-0.032 ± 0.008	1282
HD10038	2010-10-02	all	0.027 ± 0.084	-0.002 ± 0.08	
		B	0.023 ± 0.022	0.027 ± 0.021	908
		V	0.012 ± 0.016	0.011 ± 0.015	1174
		R	0.023 ± 0.009	0.008 ± 0.009	1062
		I	0.013 ± 0.012	-0.008 ± 0.011	799
HD10038	2011-12-10	all	0.041 ± 0.061	-0.048 ± 0.062	
		B	0.031 ± 0.014	-0.055 ± 0.014	1317
		V	0.035 ± 0.011	-0.053 ± 0.012	1608
		R	0.049 ± 0.007	-0.064 ± 0.007	1428
		I	0.045 ± 0.009	-0.042 ± 0.009	1050
HD10038	2012-12-25	all	0.043 ± 0.086	0.021 ± 0.084	
		B	0.045 ± 0.021	-0.0 ± 0.02	917
		V	0.046 ± 0.016	0.005 ± 0.016	1152
		R	0.051 ± 0.009	0.023 ± 0.009	1032
		I	0.044 ± 0.012	0.038 ± 0.012	768
HD10038	2013-12-14	all	0.052 ± 0.061	-0.031 ± 0.062	
		B	0.041 ± 0.014	-0.062 ± 0.014	1334
		V	0.046 ± 0.011	-0.033 ± 0.012	1608
		R	0.055 ± 0.007	-0.032 ± 0.007	1424
		I	0.059 ± 0.009	-0.007 ± 0.009	1045
HD10038	2015-07-31	all	0.04 ± 0.053	-0.029 ± 0.054	
		B	0.037 ± 0.014	-0.034 ± 0.014	1378
		V	0.032 ± 0.011	-0.023 ± 0.011	1760
		R	0.041 ± 0.006	-0.028 ± 0.006	1600
		I	0.032 ± 0.008	-0.025 ± 0.008	1230
HD10038	2015-08-28	all	0.078 ± 0.055	-0.063 ± 0.053	
		B	0.03 ± 0.013	-0.07 ± 0.013	1459
		V	0.065 ± 0.01	-0.056 ± 0.01	1806
		R	0.083 ± 0.006	-0.06 ± 0.006	1621
		I	0.094 ± 0.008	-0.046 ± 0.008	1214
HD10038	2015-10-14	all	0.041 ± 0.068	-0.117 ± 0.064	
		B	-0.003 ± 0.017	-0.117 ± 0.016	1185
		V	0.053 ± 0.013	-0.09 ± 0.012	1478
		R	0.063 ± 0.007	-0.108 ± 0.007	1331
		I	0.054 ± 0.01	-0.146 ± 0.009	1002
HD13588	2014-10-02	all	0.11 ± 0.056	0.034 ± 0.055	
		B	0.154 ± 0.014	0.001 ± 0.014	1360
		V	0.101 ± 0.011	0.021 ± 0.011	1751
		R	0.106 ± 0.006	0.05 ± 0.006	1586
		I	0.113 ± 0.008	0.048 ± 0.008	1196
HD13588	2015-08-14	all	0.151 ± 0.075	-0.011 ± 0.078	
		B	0.099 ± 0.017	-0.058 ± 0.017	1054
		V	0.147 ± 0.014	0.002 ± 0.015	1273
		R	0.15 ± 0.008	-0.02 ± 0.009	1127
		I	0.165 ± 0.011	-0.01 ± 0.011	831
HD13588	2015-08-26	all	0.067 ± 0.068	0.047 ± 0.068	
		B	0.049 ± 0.015	0.027 ± 0.015	1635
		V	0.057 ± 0.013	0.038 ± 0.013	1952
		R	0.067 ± 0.007	0.042 ± 0.007	1713
		I	0.074 ± 0.01	0.057 ± 0.01	1249
HD13588	2015-10-14	all	0.149 ± 0.082	0.055 ± 0.087	
		B	0.084 ± 0.018	0.029 ± 0.019	1303
		V	0.134 ± 0.016	0.04 ± 0.016	1573
		R	0.164 ± 0.009	0.048 ± 0.01	1389
		I	0.183 ± 0.012	0.081 ± 0.013	1023
HD97689	2011-02-04	all	0.063 ± 0.092	-0.028 ± 0.087	
		B	0.036 ± 0.021	-0.051 ± 0.02	912
		V	0.057 ± 0.017	-0.018 ± 0.016	1123
		R	0.07 ± 0.01	-0.006 ± 0.009	996

Table 2.4.: continued.

Name	Epoch	Passband	P_Q (%)	P_U (%)	S/N
		I	0.065 ± 0.013	-0.014 ± 0.013	733
HD97689	2011-02-12	all	0.051 ± 0.057	0.017 ± 0.055	
		B	0.047 ± 0.012	-0.014 ± 0.012	1533
		V	0.038 ± 0.01	0.003 ± 0.01	1843
		R	0.05 ± 0.006	0.007 ± 0.006	1613
		I	0.044 ± 0.008	0.048 ± 0.008	1154
HD97689	2011-06-30	all	0.275 ± 0.056	0.042 ± 0.056	
		B	0.183 ± 0.013	0.014 ± 0.012	1470
		V	0.235 ± 0.01	0.029 ± 0.01	1781
		R	0.266 ± 0.006	0.043 ± 0.006	1571
		I	0.333 ± 0.008	0.066 ± 0.008	1147
HD97689	2012-01-20	all	0.159 ± 0.077	-0.012 ± 0.062	
		B	0.113 ± 0.019	0.01 ± 0.015	1152
		V	0.144 ± 0.015	-0.006 ± 0.012	1442
		R	0.138 ± 0.008	-0.001 ± 0.007	1294
		I	0.173 ± 0.011	-0.039 ± 0.009	960
HD97689	2012-03-30	all	0.104 ± 0.062	0.051 ± 0.068	
		B	0.089 ± 0.014	0.019 ± 0.016	1232
		V	0.085 ± 0.012	0.025 ± 0.013	1522
		R	0.104 ± 0.007	0.047 ± 0.007	1356
		I	0.122 ± 0.009	0.084 ± 0.01	999
HD97689	2013-05-06	all	0.062 ± 0.055	-0.022 ± 0.053	
		B	0.071 ± 0.013	-0.008 ± 0.012	1482
		V	0.064 ± 0.01	-0.041 ± 0.01	1835
		R	0.065 ± 0.006	-0.02 ± 0.006	1631
		I	0.063 ± 0.008	-0.039 ± 0.008	1201
HD97689	2014-01-06	all	0.095 ± 0.059	0.026 ± 0.06	
		B	0.065 ± 0.014	-0.015 ± 0.014	1343
		V	0.075 ± 0.011	0.011 ± 0.011	1661
		R	0.096 ± 0.006	0.026 ± 0.006	1483
		I	0.109 ± 0.008	0.058 ± 0.009	1094
HD97689	2014-12-24	all	0.033 ± 0.08	-0.028 ± 0.081	
		B	0.008 ± 0.018	-0.015 ± 0.018	1022
		V	0.018 ± 0.015	-0.018 ± 0.015	1229
		R	0.033 ± 0.009	-0.045 ± 0.009	1082
		I	0.036 ± 0.012	-0.035 ± 0.012	794
HD97689	2015-02-15	all	0.099 ± 0.059	0.035 ± 0.06	
		B	0.055 ± 0.013	0.017 ± 0.013	1387
		V	0.043 ± 0.011	0.025 ± 0.011	1705
		R	0.066 ± 0.006	0.03 ± 0.006	1501
		I	0.143 ± 0.009	0.016 ± 0.009	1092
HD97689	2015-04-07	all	-0.01 ± 0.057	0.053 ± 0.058	
		B	-0.012 ± 0.014	0.042 ± 0.014	1334
		V	0.001 ± 0.011	0.054 ± 0.011	1691
		R	-0.004 ± 0.006	0.048 ± 0.006	1523
		I	-0.024 ± 0.008	0.048 ± 0.008	1141
HD97689	2015-04-07	all	0.009 ± 0.084	-0.078 ± 0.092	
		B	-0.041 ± 0.023	-0.066 ± 0.025	829
		V	-0.018 ± 0.017	-0.018 ± 0.019	1073
		R	-0.006 ± 0.009	-0.058 ± 0.01	985
		I	0.053 ± 0.012	-0.122 ± 0.013	776
HD97689	2015-04-07	all	0.137 ± 0.077	0.089 ± 0.074	
		B	0.142 ± 0.021	0.002 ± 0.02	976
		V	0.103 ± 0.016	0.045 ± 0.015	1246
		R	0.135 ± 0.009	0.082 ± 0.008	1140
		I	0.136 ± 0.011	0.151 ± 0.01	894
HD42078	2010-04-07	all	0.024 ± 0.046	0.035 ± 0.045	
		B	0.066 ± 0.01	0.035 ± 0.01	1854
		V	0.041 ± 0.008	0.056 ± 0.008	2217
		R	0.046 ± 0.005	0.053 ± 0.005	1949
		I	-0.009 ± 0.007	0.011 ± 0.007	1419
HD42078	2010-10-14	all	0.161 ± 0.077	0.13 ± 0.072	
		B	0.132 ± 0.019	0.077 ± 0.018	1096
		V	0.143 ± 0.015	0.056 ± 0.014	1367

Table 2.4.: continued.

Name	Epoch	Passband	P_Q (%)	P_U (%)	S/N
		R	0.162 ± 0.008	0.086 ± 0.008	1230
		I	0.191 ± 0.011	0.186 ± 0.01	924
HD42078	2010-12-13	all	0.053 ± 0.06	0.044 ± 0.061	
		B	0.051 ± 0.013	0.034 ± 0.014	1379
		V	0.046 ± 0.011	0.026 ± 0.011	1661
		R	0.055 ± 0.006	0.045 ± 0.007	1459
		I	0.061 ± 0.009	0.055 ± 0.009	1065
HD42078	2010-12-17	all	0.092 ± 0.069	-0.07 ± 0.072	
		B	0.089 ± 0.015	-0.077 ± 0.016	1183
		V	0.078 ± 0.013	-0.067 ± 0.013	1415
		R	0.101 ± 0.008	-0.08 ± 0.008	1246
		I	0.101 ± 0.01	-0.063 ± 0.011	911
HD42078	2014-03-04	all	0.173 ± 0.066	0.025 ± 0.065	
		B	0.158 ± 0.009	-0.059 ± 0.009	1604
		V	0.17 ± 0.01	-0.048 ± 0.009	1651
		R	0.204 ± 0.006	-0.013 ± 0.006	1348
		I	0.202 ± 0.011	0.087 ± 0.01	830
WD1615-154	2010-04-02	all	0.022 ± 0.083	0.023 ± 0.084	
		B	-0.007 ± 0.011	-0.006 ± 0.011	1440
		V	-0.028 ± 0.013	-0.003 ± 0.013	1388
		R	0.003 ± 0.009	0.029 ± 0.009	1088
		I	0.038 ± 0.013	0.014 ± 0.013	720
WD1620-391	2010-05-30	all	0.12 ± 0.168	-0.136 ± 0.168	
		B	0.014 ± 0.019	-0.059 ± 0.018	794
		V	0.124 ± 0.024	-0.01 ± 0.023	751
		R	0.115 ± 0.017	0.01 ± 0.017	547
		I	0.348 ± 0.028	-0.34 ± 0.028	339
WD1620-391	2010-07-14	all	0.062 ± 0.063	0.055 ± 0.065	
		B	0.042 ± 0.01	0.01 ± 0.01	1743
		V	0.038 ± 0.01	0.028 ± 0.011	1818
		R	0.06 ± 0.007	0.048 ± 0.007	1466
		I	0.078 ± 0.01	0.089 ± 0.01	992
WD1620-391	2011-02-11	all	0.056 ± 0.068	-0.011 ± 0.065	
		B	0.05 ± 0.01	-0.002 ± 0.01	1596
		V	0.053 ± 0.011	0.017 ± 0.01	1699
		R	0.068 ± 0.007	0.004 ± 0.007	1372
		I	0.057 ± 0.01	-0.049 ± 0.01	922
WD1620-391	2014-03-22	all	0.016 ± 0.062	0.026 ± 0.066	
		B	0.017 ± 0.009	0.004 ± 0.01	1746
		V	0.036 ± 0.01	-0.004 ± 0.011	1814
		R	0.047 ± 0.006	-0.01 ± 0.007	1447
		I	-0.023 ± 0.01	0.045 ± 0.01	968
WD1620-391	2014-03-22	all	0.009 ± 0.077	-0.004 ± 0.079	
		B	0.008 ± 0.011	-0.011 ± 0.012	1396
		V	-0.004 ± 0.012	0.015 ± 0.013	1452
		R	0.005 ± 0.008	0.016 ± 0.008	1160
		I	0.005 ± 0.012	-0.04 ± 0.012	778
WD1620-391	2014-03-22	all	-0.036 ± 0.078	-0.029 ± 0.078	
		B	-0.029 ± 0.011	-0.008 ± 0.011	1399
		V	-0.033 ± 0.013	-0.029 ± 0.013	1455
		R	-0.049 ± 0.008	-0.024 ± 0.008	1162
		I	-0.076 ± 0.012	-0.054 ± 0.012	778
WD1620-391	2015-02-26	all	0.018 ± 0.064	0.012 ± 0.065	
		B	-0.007 ± 0.009	-0.017 ± 0.009	1714
		V	0.001 ± 0.01	-0.005 ± 0.01	1775
		R	0.006 ± 0.007	-0.009 ± 0.007	1415
		I	0.038 ± 0.01	0.029 ± 0.01	942
WD2039-202	2013-04-12	all	0.079 ± 0.073	0.038 ± 0.076	
		B	0.046 ± 0.012	-0.068 ± 0.013	1308
		V	0.072 ± 0.012	-0.009 ± 0.013	1464
		R	0.073 ± 0.008	0.014 ± 0.008	1199
		I	0.08 ± 0.011	0.05 ± 0.012	815
WD2039-202	2015-09-08	all	-0.011 ± 0.066	-0.039 ± 0.066	
		B	-0.003 ± 0.01	-0.038 ± 0.01	2143

Table 2.4.: continued.

Name	Epoch	Passband	P_Q (%)	P_U (%)	S/N
		V	-0.008 ± 0.011	-0.056 ± 0.011	2275
		R	-0.006 ± 0.007	-0.041 ± 0.007	1831
		I	-0.02 ± 0.01	-0.039 ± 0.01	1234
WD2149+021	2011-10-11	all	-0.048 ± 0.056	-0.038 ± 0.056	
		B	-0.087 ± 0.009	-0.018 ± 0.009	1776
		V	-0.026 ± 0.009	-0.057 ± 0.009	2011
		R	-0.029 ± 0.006	-0.041 ± 0.006	1625
		I	-0.055 ± 0.009	-0.058 ± 0.009	1091

The signal-to-noise ratio, S/N, in individual bands is the average SNR between two 50Å bins, from 4250-4350Å (*B* band), 5450-5550Å (*V*), 6250-6350Å (*R*) and 7650-7850Å (*I*).

Table 2.5.: Polarized stars.

								Serkowski law		
Name	Epoch	Passband	P (%)	P_Q (%)	P_U (%)	θ(°)	S/N	λ_{max} (Å)	P_{max} (%)	K
Vela1-95	2010-04-07							5848.2 ± 21.9	8.36 ± 0.01	1.34 ± 0.03
		B	7.69 ± 0.1	7.48 ± 0.1	-1.79 ± 0.1	172.72 ± 0.13	405			
		V	8.23 ± 0.03	7.9 ± 0.03	-2.3 ± 0.03	172.43 ± 0.06	965			
		R	7.99 ± 0.01	7.61 ± 0.01	-2.42 ± 0.01	171.97 ± 0.04	1210			
		I	7.2 ± 0.01	6.95 ± 0.01	-1.91 ± 0.01	171.87 ± 0.03	1516			
Vela1-95	2010-12-14							5877.1 ± 22.8	8.27 ± 0.01	1.34 ± 0.03
		B	7.58 ± 0.12	7.39 ± 0.12	-1.68 ± 0.14	172.7 ± 0.15	328			
		V	8.14 ± 0.03	7.8 ± 0.03	-2.32 ± 0.04	172.27 ± 0.07	801			
		R	7.91 ± 0.01	7.54 ± 0.01	-2.41 ± 0.01	171.91 ± 0.04	1013			
		I	7.14 ± 0.01	6.88 ± 0.01	-1.89 ± 0.01	171.87 ± 0.04	1287			
Vela1-95	2011-12-22							5908.3 ± 25.1	8.25 ± 0.02	1.4 ± 0.04
		B	7.58 ± 0.14	7.37 ± 0.14	-1.78 ± 0.14	172.53 ± 0.18	304			
		V	8.08 ± 0.04	7.75 ± 0.04	-2.3 ± 0.04	172.3 ± 0.08	739			
		R	7.91 ± 0.01	7.55 ± 0.01	-2.38 ± 0.01	172.06 ± 0.05	930			
		I	7.11 ± 0.01	6.85 ± 0.01	-1.91 ± 0.01	171.76 ± 0.05	1175			
Vela1-95	2013-12-03							5913.5 ± 17.4	8.29 ± 0.01	1.38 ± 0.02
		B	7.59 ± 0.15	7.41 ± 0.15	-1.65 ± 0.17	173.13 ± 0.18	378			
		V	8.13 ± 0.04	7.83 ± 0.04	-2.2 ± 0.04	172.78 ± 0.08	911			
		R	7.94 ± 0.01	7.59 ± 0.01	-2.32 ± 0.01	172.32 ± 0.05	1157			
		I	7.17 ± 0.01	6.93 ± 0.01	-1.85 ± 0.01	172.1 ± 0.05	1486			
Vela1-95	2013-12-05							5869.6 ± 23.3	8.31 ± 0.01	1.36 ± 0.03
		B	7.63 ± 0.14	7.43 ± 0.14	-1.72 ± 0.17	172.83 ± 0.17	301			
		V	8.17 ± 0.04	7.85 ± 0.04	-2.27 ± 0.04	172.56 ± 0.08	740			
		R	7.93 ± 0.01	7.58 ± 0.01	-2.35 ± 0.01	172.19 ± 0.05	951			
		I	7.17 ± 0.01	6.92 ± 0.01	-1.85 ± 0.01	172.1 ± 0.04	1240			
Vela1-95	2013-12-31							5848.3 ± 21.6	8.28 ± 0.01	1.34 ± 0.03
		B	7.68 ± 0.15	7.51 ± 0.15	-1.61 ± 0.15	173.19 ± 0.18	290			
		V	8.15 ± 0.04	7.86 ± 0.04	-2.16 ± 0.04	172.89 ± 0.08	695			
		R	7.91 ± 0.01	7.58 ± 0.01	-2.28 ± 0.01	172.42 ± 0.05	880			
		I	7.14 ± 0.01	6.91 ± 0.01	-1.81 ± 0.01	172.22 ± 0.05	1127			
Vela1-95	2014-01-06							5881.1 ± 19.3	8.32 ± 0.01	1.35 ± 0.03
		B	7.63 ± 0.12	7.45 ± 0.12	-1.67 ± 0.13	172.86 ± 0.14	352			
		V	8.19 ± 0.03	7.88 ± 0.03	-2.25 ± 0.03	172.59 ± 0.06	874			
		R	7.95 ± 0.01	7.61 ± 0.01	-2.32 ± 0.01	172.35 ± 0.04	1123			
		I	7.19 ± 0.01	6.95 ± 0.01	-1.85 ± 0.01	172.11 ± 0.04	1467			
Vela1-95	2014-12-22							5831.1 ± 31.7	8.26 ± 0.02	1.34 ± 0.04
		B	7.57 ± 0.18	7.36 ± 0.18	-1.78 ± 0.18	172.5 ± 0.21	244			
		V	8.18 ± 0.05	7.82 ± 0.05	-2.39 ± 0.05	171.97 ± 0.1	585			
		R	7.87 ± 0.01	7.49 ± 0.01	-2.43 ± 0.01	171.77 ± 0.06	742			
		I	7.12 ± 0.01	6.86 ± 0.01	-1.89 ± 0.01	171.87 ± 0.05	960			
Vela1-95	2015-01-17							5695.0 ± 83.7	8.23 ± 0.04	1.21 ± 0.09
		B	7.72 ± 0.24	7.51 ± 0.24	-1.77 ± 0.26	172.63 ± 0.28	171			
		V	8.11 ± 0.06	7.76 ± 0.06	-2.37 ± 0.07	172.02 ± 0.13	415			
		R	7.81 ± 0.02	7.43 ± 0.02	-2.42 ± 0.02	171.8 ± 0.08	526			
		I	7.03 ± 0.01	6.76 ± 0.01	-1.91 ± 0.01	171.69 ± 0.08	678			
Vela1-95	2015-05-30							5866.9 ± 40.9	8.18 ± 0.02	1.3 ± 0.05
		B	7.52 ± 0.25	7.16 ± 0.25	-2.3 ± 0.25	170.57 ± 0.31	168			
		V	8.05 ± 0.06	7.64 ± 0.06	-2.53 ± 0.06	171.38 ± 0.14	422			
		R	7.84 ± 0.02	7.41 ± 0.02	-2.57 ± 0.02	171.21 ± 0.08	539			
		I	7.09 ± 0.01	6.8 ± 0.01	-2.02 ± 0.01	171.3 ± 0.08	695			
Vela1-95	2015-12-29							5692.1 ± 30.6	8.34 ± 0.02	1.22 ± 0.03
		B	7.9 ± 0.18	7.72 ± 0.18	-1.69 ± 0.18	173.17 ± 0.2	260			
		V	8.21 ± 0.04	7.86 ± 0.04	-2.37 ± 0.04	172.23 ± 0.09	673			
		R	7.91 ± 0.01	7.52 ± 0.01	-2.45 ± 0.01	171.82 ± 0.05	879			
		I	7.11 ± 0.01	6.86 ± 0.01	-1.89 ± 0.01	171.86 ± 0.05	1184			
BD-144922	2011-10-02							5429.6 ± 21.0	6.14 ± 0.01	1.33 ± 0.03
		B	5.82 ± 0.04	-1.06 ± 0.04	5.72 ± 0.04	50.01 ± 0.11	667			
		V	6.09 ± 0.02	-0.99 ± 0.02	6.01 ± 0.02	50.0 ± 0.07	1133			
		R	5.8 ± 0.01	-0.88 ± 0.01	5.73 ± 0.01	49.85 ± 0.06	1180			
		I	4.96 ± 0.01	-0.8 ± 0.01	4.89 ± 0.01	49.29 ± 0.07	1096			
BD-144922	2013-03-06							5470.4 ± 18.6	6.14 ± 0.01	1.32 ± 0.03
		B	5.79 ± 0.03	-0.95 ± 0.03	5.71 ± 0.03	49.5 ± 0.09	812			
		V	6.1 ± 0.02	-0.93 ± 0.02	6.03 ± 0.02	49.66 ± 0.06	1296			

Table 2.5.: continued.

Name	Epoch	Passband	P (%)	P_Q (%)	P_U (%)	θ(°)	S/N	Serkowski law		
								$\lambda_{\max}$ (Å)	$P_{\max}$ (%)	K
		R	5.83 ± 0.01	-0.85 ± 0.01	5.77 ± 0.01	49.58 ± 0.05	1302			
		I	5.02 ± 0.01	-0.79 ± 0.01	4.96 ± 0.01	49.18 ± 0.07	1126			
HDE316232	2010-07-14							5591.1 ± 18.3	5.02 ± 0.01	1.22 ± 0.03
		B	4.68 ± 0.02	4.64 ± 0.02	0.62 ± 0.02	3.61 ± 0.09	1063			
		V	4.93 ± 0.01	4.9 ± 0.01	0.55 ± 0.01	3.51 ± 0.07	1529			
		R	4.77 ± 0.01	4.75 ± 0.01	0.51 ± 0.01	3.37 ± 0.06	1499			
		I	4.21 ± 0.01	4.18 ± 0.01	0.56 ± 0.01	3.53 ± 0.08	1272			
Hiltner652	2010-07-20							5770.2 ± 18.3	6.46 ± 0.01	1.2 ± 0.03
		B	5.94 ± 0.04	5.94 ± 0.04	-0.08 ± 0.04	179.32 ± 0.11	691			
		V	6.37 ± 0.02	6.37 ± 0.02	-0.21 ± 0.02	179.39 ± 0.07	1083			
		R	6.21 ± 0.01	6.21 ± 0.01	-0.23 ± 0.01	179.3 ± 0.06	1106			
		I	5.6 ± 0.01	5.6 ± 0.01	-0.05 ± 0.01	179.43 ± 0.07	978			
Hiltner652	2011-07-20							5807.4 ± 31.3	6.48 ± 0.02	1.24 ± 0.05
		B	5.95 ± 0.06	5.95 ± 0.06	0.03 ± 0.05	179.85 ± 0.16	477			
		V	6.36 ± 0.03	6.36 ± 0.03	-0.09 ± 0.03	179.94 ± 0.1	772			
		R	6.24 ± 0.01	6.24 ± 0.01	-0.12 ± 0.01	179.81 ± 0.08	797			
		I	5.62 ± 0.01	5.62 ± 0.01	0.05 ± 0.01	179.93 ± 0.1	714			
Hiltner652	2011-07-22							5816.4 ± 26.7	6.51 ± 0.01	1.15 ± 0.04
		B	5.97 ± 0.05	5.97 ± 0.05	0.04 ± 0.05	0.09 ± 0.13	529			
		V	6.42 ± 0.02	6.42 ± 0.02	-0.13 ± 0.02	179.69 ± 0.09	831			
		R	6.29 ± 0.01	6.29 ± 0.01	-0.13 ± 0.01	179.84 ± 0.07	839			
		I	5.71 ± 0.01	5.71 ± 0.01	0.08 ± 0.01	0.07 ± 0.09	723			
Hiltner652	2015-02-26							5788.8 ± 30.8	6.49 ± 0.02	1.16 ± 0.05
		B	5.96 ± 0.06	5.96 ± 0.06	0.02 ± 0.06	179.94 ± 0.16	436			
		V	6.41 ± 0.03	6.41 ± 0.03	-0.17 ± 0.03	179.55 ± 0.1	715			
		R	6.24 ± 0.01	6.23 ± 0.01	-0.2 ± 0.01	179.49 ± 0.08	740			
		I	5.65 ± 0.01	5.65 ± 0.01	-0.05 ± 0.01	179.41 ± 0.1	675			
Hiltner652	2015-04-12							5795.0 ± 23.8	6.46 ± 0.01	1.15 ± 0.04
		B	5.95 ± 0.05	5.95 ± 0.05	-0.11 ± 0.05	179.18 ± 0.14	516			
		V	6.36 ± 0.02	6.36 ± 0.02	-0.23 ± 0.02	179.29 ± 0.09	865			
		R	6.22 ± 0.01	6.21 ± 0.01	-0.26 ± 0.01	179.21 ± 0.07	900			
		I	5.66 ± 0.01	5.66 ± 0.01	-0.06 ± 0.01	179.31 ± 0.09	794			
Hiltner652	2015-04-12							5759.0 ± 24.8	6.51 ± 0.01	1.16 ± 0.04
		B	6.01 ± 0.06	6.0 ± 0.06	-0.09 ± 0.06	179.39 ± 0.17	569			
		V	6.41 ± 0.03	6.41 ± 0.03	-0.24 ± 0.03	179.26 ± 0.11	939			
		R	6.26 ± 0.01	6.26 ± 0.01	-0.22 ± 0.01	179.38 ± 0.09	968			
		I	5.66 ± 0.01	5.66 ± 0.01	-0.06 ± 0.01	179.37 ± 0.11	843			
Hiltner652	2015-05-09							5763.9 ± 32.9	6.4 ± 0.02	1.2 ± 0.05
		B	5.88 ± 0.05	5.88 ± 0.05	-0.07 ± 0.05	179.46 ± 0.15	479			
		V	6.31 ± 0.03	6.31 ± 0.03	-0.24 ± 0.03	179.23 ± 0.1	756			
		R	6.15 ± 0.01	6.15 ± 0.01	-0.26 ± 0.01	179.21 ± 0.08	773			
		I	5.52 ± 0.01	5.52 ± 0.01	-0.11 ± 0.01	179.07 ± 0.1	709			
Hiltner652	2015-06-10							5726.7 ± 25.8	6.42 ± 0.01	1.16 ± 0.04
		B	5.94 ± 0.04	5.94 ± 0.04	-0.11 ± 0.04	179.26 ± 0.12	600			
		V	6.34 ± 0.02	6.33 ± 0.02	-0.25 ± 0.02	179.25 ± 0.08	933			
		R	6.17 ± 0.01	6.16 ± 0.01	-0.27 ± 0.01	179.05 ± 0.07	949			
		I	5.53 ± 0.01	5.53 ± 0.01	-0.1 ± 0.01	179.14 ± 0.08	831			
NGC2024	2010-12-31							6355.6 ± 10.1	9.87 ± 0.01	1.31 ± 0.02
		B	8.53 ± 0.1	0.74 ± 0.1	-8.5 ± 0.1	136.8 ± 0.1	449			
		V	9.55 ± 0.03	0.25 ± 0.03	-9.54 ± 0.03	136.33 ± 0.05	1008			
		R	9.67 ± 0.01	0.09 ± 0.01	-9.67 ± 0.01	136.19 ± 0.03	1314			
		I	9.02 ± 0.0	0.49 ± 0.0	-9.0 ± 0.0	136.18 ± 0.02	1832			
NGC2024	2011-12-30							6337.7 ± 11.7	9.78 ± 0.01	1.26 ± 0.02
		B	8.56 ± 0.12	0.63 ± 0.11	-8.54 ± 0.12	136.62 ± 0.12	408			
		V	9.46 ± 0.03	0.13 ± 0.03	-9.46 ± 0.03	136.0 ± 0.05	927			
		R	9.59 ± 0.01	-0.02 ± 0.01	-9.59 ± 0.01	135.91 ± 0.03	1214			
		I	8.95 ± 0.01	0.34 ± 0.0	-8.95 ± 0.01	135.73 ± 0.02	1692			
NGC2024	2012-11-14							6308.6 ± 12.4	9.95 ± 0.01	1.26 ± 0.02
		B	8.7 ± 0.12	0.74 ± 0.11	-8.67 ± 0.12	137.0 ± 0.11	408			
		V	9.64 ± 0.03	0.27 ± 0.03	-9.63 ± 0.03	136.39 ± 0.05	911			
		R	9.75 ± 0.01	0.18 ± 0.01	-9.75 ± 0.01	136.47 ± 0.03	1193			
		I	9.08 ± 0.01	0.56 ± 0.01	-9.06 ± 0.01	136.4 ± 0.02	1662			
NGC2024	2015-05-11							6366.5 ± 13.0	10.0 ± 0.01	1.27 ± 0.02
		B	8.69 ± 0.09	0.37 ± 0.11	-8.68 ± 0.09	135.74 ± 0.12	364			
		V	9.64 ± 0.03	-0.04 ± 0.04	-9.64 ± 0.03	135.31 ± 0.06	735			
		R	9.86 ± 0.01	-0.11 ± 0.01	-9.85 ± 0.01	135.48 ± 0.04	845			
		I	9.19 ± 0.01	0.3 ± 0.01	-9.18 ± 0.01	135.59 ± 0.04	1016			
NGC2024	2015-09-25							6310.4 ± 12.9	9.81 ± 0.01	1.27 ± 0.02
		B	8.57 ± 0.11	0.52 ± 0.11	-8.55 ± 0.11	136.22 ± 0.11	427			
		V	9.51 ± 0.03	0.04 ± 0.03	-9.51 ± 0.03	135.68 ± 0.05	944			
		R	9.62 ± 0.01	-0.1 ± 0.01	-9.62 ± 0.01	135.64 ± 0.03	1230			
		I	8.95 ± 0.0	0.3 ± 0.01	-8.94 ± 0.0	135.58 ± 0.02	1703			
NGC2024	2015-10-14							6363.9 ± 14.9	9.81 ± 0.01	1.3 ± 0.02
		B	8.47 ± 0.15	0.41 ± 0.16	-8.46 ± 0.15	135.91 ± 0.15	306			
		V	9.49 ± 0.04	-0.0 ± 0.04	-9.49 ± 0.04	135.61 ± 0.07	701			
		R	9.62 ± 0.01	-0.14 ± 0.01	-9.62 ± 0.01	135.53 ± 0.04	927			
		I	8.99 ± 0.01	0.31 ± 0.01	-8.98 ± 0.01	135.6 ± 0.03	1327			
NGC2024	2015-10-14							6339.6 ± 13.7	9.81 ± 0.01	1.25 ± 0.02
		B	8.58 ± 0.21	0.57 ± 0.21	-8.56 ± 0.21	136.29 ± 0.2	309			
		V	9.5 ± 0.06	0.05 ± 0.06	-9.5 ± 0.06	135.73 ± 0.09	710			
		R	9.62 ± 0.01	-0.09 ± 0.01	-9.62 ± 0.01	135.7 ± 0.05	943			
		I	8.98 ± 0.01	0.37 ± 0.01	-8.97 ± 0.01	135.82 ± 0.04	1358			
BD-125133	2015-09-08							5049.5 ± 35.5	4.37 ± 0.01	1.17 ± 0.04
		B	4.22 ± 0.03	1.69 ± 0.03	-3.86 ± 0.03	146.54 ± 0.12	845			
		V	4.27 ± 0.02	1.57 ± 0.02	-3.97 ± 0.02	145.88 ± 0.09	1252			
		R	4.0 ± 0.01	1.41 ± 0.01	-3.74 ± 0.01	145.62 ± 0.08	1213			
		I	3.35 ± 0.01	1.22 ± 0.01	-3.12 ± 0.01	145.28 ± 0.11	1049			

The polarization angle, θ, in individual bands is the average polarization angle from 3980-4920Å (*B* band), 5070-5950Å (*V*), 5890-5890Å (*R*) and 7310-8810Å (*I*). The signal-to-noise ratio, S/N, in individual bands is the average SNR between two 50Å bins, from 4250-4350Å (*B*), 5450-5550Å (*V*), 6250-6350Å (*R*) and 7650-7850Å (*I*).

3. Spectropolarimetry of Galactic stars with anomalous extinction sightlines

The content of this chapter corresponds to:
Cikota, A., Hoang, T., Taubenberger, S., et al.
accepted for publication in *Astronomy & Astrophysics*

3.1. Introduction

The motivation to study anomalous sightlines toward highly reddened Galactic stars derives from type Ia supernova (SN) observations that show peculiar extinction curves with very low R_V values, as well as peculiar polarization wavelength dependencies (polarization curves).

Past studies that included large samples of SNe Ia showed that the total-to-selective visual extinction ratio, R_V, of dust in type Ia SN host galaxies ranges from 1 to 3.5 and is in most cases lower than the average value of Milky Way dust, R_V ∼3.1 (Riess et al., 1996; Phillips et al., 1999; Altavilla et al., 2004; Reindl et al., 2005; Conley et al., 2007; Wang et al., 2006b; Goobar, 2008; Nobili & Goobar, 2008; Kessler et al., 2009; Hicken et al., 2009b; Folatelli et al., 2010; Lampeitl et al., 2010; Mandel et al., 2011; Cikota et al., 2016).

Observations of individual highly reddened SNe Ia also reveal host galaxy dust with low R_V values, for instance, R_V=2.57$^{+0.23}_{-0.21}$ for the line of sight of SN 1986G (Phillips et al., 2013), $R_V \sim 1.48$ for SN 2006X (Wang et al., 2008a), R_V=1.20 $^{+0.26}_{-0.14}$ for SN 2008fp (Phillips et al., 2013), and R_V^{obs}=1.64±0.16 for SN 2014J (Foley et al., 2014).

Linear (spectro)polarimetric observations of these four SNe also display anomalous interstellar polarization curves (Patat et al., 2015), steeply rising toward blue wavelengths. Patat et al. (2015) fitted their observations with a Serkowski curve (Serkowski et al., 1975) to characterize the polarization curves.

The Serkowski curve is an empirical wavelength dependence of interstellar linear polarization:

$$\frac{P(\lambda)}{P_{\max}} = \exp\left[-K \ln^2\left(\frac{\lambda_{\max}}{\lambda}\right)\right] \tag{3.1}$$

The wavelength of peak polarization, $\lambda_{\max}$, depends on the dust grain size distribution. For an enhanced abundance of small dust grains, $\lambda_{\max}$ moves to shorter wavelengths, and for an enhanced abundance of large dust grains, it moves to longer wavelengths. Thus, linear spectropolarimetry probes the alignment of dust grains and the size distribution of the aligned dust grains.

Patat et al. (2015) found that the polarization curve of all 4 SNe display an anomalous behavior, with $\lambda_{\max} \sim 0.43\mu m$ for SN 1986G, and $\lambda_{\max} \lesssim 0.4\mu m$ for SN 2006X, SN 2008fp, and SN 2014J. Because SNe Ia have a negligible intrinsic continuum polarization (Wang & Wheeler, 2008), the anomalous polarization curves likely have to be associated with the properties of host galaxies dust. Zelaya et al. (2017a) expanded the sample of 4 SNe Ia investigated in Patat et al. (2015), and presented a study of 19 type Ia SNe. They grouped the SNe into the ”sodium-sample”, consisting of 12 SNe that

show higher continuum polarization values and interstellar Na I D lines at the redshift of their host galaxies, and the "non-sodium-sample" with no rest-frame Na I D lines and smaller peak polarization. Eight sodium-sample SNe have $\lambda_{\rm max} \lesssim 0.4\mu m$, and their polarization angles are aligned with the spiral arms of their host galaxies, which is evidence that the polarizing dust is likely located in their host galaxies and aligned due to the magnetic fields of the host galaxies. The non-sodium-sample SNe are less strongly polarized, with $P_{\rm max} \lesssim 0.5\%$, have $\lambda_{\rm max}$ values similar to the common Galactic dust (with $\lambda_{\rm max} \sim 0.55\mu m$), and their polarization angles do not align with host-galaxy features, which might be interpreted as the continuum polarization being produced by the Galactic foreground dust.

It is not understood why these reddened SN Ia sightlines show such a different polarization profile compared to the typical Milky Way dust. A natural explanation is that the composition of dust in the SN Ia host galaxies is different from that in the Galaxy.

However, there are alternative explanations. Scattering might explain the low R_V values as well as the peculiar polarization profiles. As illustrated by Patat et al. (2015) (see their Fig. 6), the polarization profile of SN 2006X may, in addition to the Serkowski component, also have a component induced by Rayleigh scattering. However, if a light echo propagates through local dust, we expect to observe variability in R_V and polarization (Wang, 2005), which is usually not the case (see Fig. 4 in Zelaya et al. 2017a). Yang et al. (2017) used observations made with the Hubble Space Telescope (HST) to map the interstellar medium (ISM) around SN 2014J through light echoes. These authors observed two echo components: a diffuse ring and a luminous arc, produced through dust scattering of different grain sizes. From the wavelength dependence of the scattering optical depth, the arc dust favors a low R_V value of ~ 1.4, which is consistent with the R_V measured along the direct line of sight, while the ring is consistent with a common Milky Way $R_V \sim 3$ value.

Another interesting explanation for the peculiar SNe Ia sightlines is given by Hoang (2017a), who simultaneously fit a two-component (interstellar and circumstellar) extinction and polarization model to photometric and (spectro-) polarimetric observations of SNe 1986G, 2006X, 2008fp, and 2014J to investigate the grain size distribution and alignment functions of dust along these lines of sights. Hoang (2017a) were able to reproduce the observational data of SN 1986G and SN 2006X by assuming an enhanced abundance of small silicate grains in the interstellar dust only, while in the case of SN 2014J, a contribution of circumstellar (CS) dust must be accounted for. In the case of SN 2008fp, Hoang (2017a) found that the alignment of small dust grains must be as efficient as that of large grains, but the existence of CS dust is uncertain. Hoang (2017a) suggested that the enhanced abundance of small silicate grains might be produced by cloud collisions driven by the SN radiation pressure. Strong SN radiation might also induce efficient alignment of small grains via the radiative torque mechanism. However, in the case of alignment via the radiative torque mechanism, the polarization angle alignment with host-galaxy features remains unexplained.

The aim of this work is to investigate Galactic stars with low R_V values with spectropolarimetry, in order to possibly find similarities to the polarization curves observed toward SNe Ia. Numerical simulations are used to infer general properties of interstellar dust toward these stars by simultaneously fitting to extinction curves with low R_V values and normal polarization curves.

The chapter is structured as follows: in Sect. 3.2 we describe our sample of stars, in Sect. 3.3 the instruments and observing strategies, in Sect. 3.4 we present the data processing and results, in Sect. 3.5 the analysis of the observations, in Sect. 3.6 we run simulations in order to interpret the observed data, in Sect. 3.7 we discuss the results, and finally we summarize and conclude in Sect. 7.6.

Table 3.1.: List of observed stars.

Name	RA (J2000)	DEC (J2000)	V (mag)	B-V (mag)	Spec. type	Type	Telescope	No. of Epochs	Comment
BD +23 3762	19 45 42.31	+23 59 04.0	9.34	0.62	B0.5III	SCI	CAHA	1	HD 344880, Star in Association
BD +45 3341	20 57 02.68	+46 32 44.7	8.73	0.38	B1II	SCI	CAHA	2	
HD 1337	00 17 43.06	+51 25 59.1	6.14	-0.13	O9.2II+O8V	SCI	CAHA	3	W UMa type
							Asiago	2	
HD 137569	15 26 20.82	+14 41 36.3	7.91	-0.05	B9Iab:p	SCI	CAHA	2	Post-AGB Star (proto-PN)
							Asiago	2	
							VLT	2 free + 4 GG435	
HD 144579	16 04 56.79	+39 09 23.4	6.67	0.73	G8V	unPolStd	CAHA	2	High proper motion
							Asiago	1	
HD 154445	17 05 32.26	-00 53 31.5	5.61	0.12	B1V	PolStd	CAHA	2	HR 6353
HD 194092	20 22 05.44	+40 59 08.2	8.28	0.09	B0.5III	SCI	CAHA	1	Star in Cluster
							Asiago	1	
HD 28446	04 32 01.84	+53 54 39.1	5.77	0.10	B0III+B0IV/V	SCI	CAHA	2	Triple star (DL Cam)
							Asiago	1	
HD 43384	06 16 58.71	+23 44 27.3	6.25	0.45	B3Iab	PolStd	CAHA	2	Pulsating variable Star
							Asiago	3	
HD 90508	10 28 03.88	+48 47 05.7	6.43	0.60	G0V	unPolStd	CAHA	1	Double star
							Asiago	2	
HD 39587	05 54 22.98	+20 16 34.2	4.40	0.60	G0VCH+M	unPolStd	Asiago	2	Variable of RS CVn type
HD 54439	07 08 23.20	-11 51 08.6	7.68	0.05	B2/3II	SCI	Asiago	1	
							VLT	1 free + 1 GG435	
HD 14357	02 21 10.44	+56 51 56.4	8.52	0.31	B2III	SCI	Asiago	1	Star in cluster
HD 21291	03 29 04.13	+59 56 25.2	4.22	0.41	B9Ia	PolStd	Asiago	1	Pulsating variable Star
HD 73420	08 36 37.12	-44 04 48.2	8.85	0.07	B2III/III	SCI	VLT	1 free + 1 GG435	
HD 78785	09 08 24.09	-46 15 13.3	8.60	0.51	B2III	SCI	VLT	1 free + 2 GG435	
HD 96042	11 03 40.56	-59 25 59.1	8.23	0.18	B1(V)ne	SCI	VLT	2 free + 2 GG435	Emission-line Star
HD 141318	15 51 06.80	-55 03 19.9	5.77	-0.01	B2III	SCI	VLT	2 free + 2 GG435	Pulsating variable Star
HD 152245	16 54 00.48	-40 31 58.2	8.37	0.13	B0Ib	SCI	VLT	1 free + 2 GG435	Star in Cluster
HD 152853	16 58 07.93	-45 58 56.5	7.94	0.11	B2III	SCI	VLT	1 free + 1 GG435	Star in Cluster

The coordinates, brightness and spectral type were taken from the SIMBAD Astronomical Database. Type indicates if the star is a polarized standard star (PolStd), unpolarized standard star (unPolStd) or one of our science targets (SCI). No. of Epochs is the number of epochs observed with a particular instrument: FORS2 (VLT), CAFOS (CAHA) or AFOSC (Asiago).

3.2. Target sample

We selected our targets from the samples presented by Mazzei & Barbaro (2008, 2011). Mazzei & Barbaro (2011) obtained 785 extinction curves for sightlines with $E(B-V) \geqslant 0.2$ mag (Savage et al., 1985), observed with the Astronomical Netherlands Satellite (ANS) in five UV bands ($1/\lambda$ = 6.46, 5.56, 4.55, 4.01 and 3.04 μm^{-1}) (Wesselius et al., 1982). They combined the UV observations with Two-Micron All-Sky Survey (2MASS) observations in the near-infrared J, H, and K bands, applied a least-squares fit of the standard Cardelli, Clayton, & Mathis (1989) extinction curve (CCM) with different R_V values, and determined the residual differences between the observed values and best-fit CCM curve at five UV wavelengths. The curves were classified as anomalous if at least one UV wavelength deviated by more than 2σ from the best-fit standard CCM curve. Twenty curves with weaker UV bumps and steeper far-UV slopes (type A), or with stronger bumps and smoother far-UV rises (type B) compared to their best-fit CCM curve, were analyzed in Mazzei & Barbaro (2008). Mazzei & Barbaro (2011) focus on 64 lines of sight for which the corresponding best-fit CCM curve is always well below ($\geqslant 2\sigma$) or well above the observed data (type C curves), with some exception at $1/\lambda$ = 3.01 for five curves (see bottom panel of Fig. 1 in Mazzei & Barbaro 2011). They conclude that the sightlines characterized by anomalous type C extinction curves require lower dust abundances than environments characterized by normal CCM extinction curves.

From these 64 anomalous lines of sight, we selected 14 lines of sight with the lowest R_V values and observed them with the FOcal Reducer and low dispersion Spectrograph (FORS2), the Asiago Faint Object Spectrograph and Camera (AFOSC), and the Calar Alto Faint Object Spectrograph (CAFOS). The observed targets are listed in Table 6.2. Additionally, we used archival HPOL data for 3 stars.

3.3. Instruments and methods

We observed our targets using three different instruments and telescopes: the FOcal Reducer and low dispersion Spectrograph (FORS2) in spectropolarimetric mode (PMOS) mounted on the UT1 Cassegrain focus of the Very Large Telescope (VLT) in Chile; the Asiago Faint Object Spectrograph and Camera (AFOSC) mounted at the 1.82 m Copernico telescope at the Asiago Observatory in northern Italy; and the Calar Alto Faint Object Spectrograph (CAFOS) mounted at the Calar Alto 2.2 m telescope in Andalusia, Spain.

The characteristics of the instruments and corresponding differences in the data reduction are described in the following subsections.

3.3.1. FORS2 at the VLT

FORS2 in PMOS mode is a dual-beam polarimeter. The spectrum produced by the grism is split by the Wollaston prism into two beams with orthogonal directions of polarization: ordinary (o) and extraordinary (e) beam. The data used in this work were obtained with the 300V grism, with and without the GG435 filter, and with the half-wave retarder plate positioned at angles of 0°, 22.5°, 45°, and 67.5° (Program ID: 094.C-0686). The half-wave retarder plate angle is measured between the acceptance axis of the ordinary beam of the Wollaston prism (which is aligned to the north-south direction) and the fast axis of the retarder plate.

The data were reduced using standard procedures in IRAF. Wavelength calibration was achieved using He-Ne-Ar arc lamp exposures. The typical RMS accuracy is ~ 0.3 Å. The data were bias subtracted, but not flat-field corrected. However, the effects of improper correction were minimized by taking advantage of the redundant number of half-wave positions (see Patat & Romaniello, 2006).

Ordinary and extra-ordinary beams were extracted in an unsupervised way using the PyRAF apextract.apall procedure, with a fixed aperture size of 10 pixels. The synthetic broadband polarization degree was computed by integrating the total flux weighted with Bessel's BVRI passband filters. We binned the spectra in 50 Å bins, in order to obtain a higher signal-to-noise ratio, and calculated the Stokes parameters Q and U, polarization degree P, and polarization angle θ_P as a function of wavelength.

The Stokes parameters Q and U were derived via Fourier transformation, as described in the FORS2 User Manual (ESO, 2015):

$$\begin{array}{l} Q = \frac{2}{N} \sum_{i=0}^{N-1} F(\theta_i) \cos(4\theta_i) \\ U = \frac{2}{N} \sum_{i=0}^{N-1} F(\theta_i) \sin(4\theta_i) \end{array} , \tag{3.2}$$

where $F(\theta_i)$ are the normalized flux differences between the ordinary (f^o) and extra-ordinary (f^e) beams:

$$F(\theta_i) = \frac{f^o(\theta_i) - f^e(\theta_i)}{f^o(\theta_i) + f^e(\theta_i)} \tag{3.3}$$

at different half-wave retarder plate position angles $\theta_i = i * 22.5°$.

Although FORS2 is equipped with a super-achromatic half-wave plate, residual retardance chromatism is present. The wavelength dependent retardance offset ($\Delta\theta(\lambda)$) is tabulated in the FORS2 User Manual. The chromatism was corrected through the following rotation of the Stokes parameters:

$$\begin{array}{l} Q_0 = Q \cos 2\Delta\theta(\lambda) - U \sin 2\Delta\theta(\lambda) \\ U_0 = Q \sin 2\Delta\theta(\lambda) + U \cos 2\Delta\theta(\lambda) \end{array} . \tag{3.4}$$

Finally we calculated the polarization:

$$P = \sqrt{Q^2 + U^2} \tag{3.5}$$

and the polarization angle:

$$\theta_0 = \frac{1}{2} \arctan(U_0/Q_0). \tag{3.6}$$

The reliability of data obtained with FORS2 is demonstrated in Cikota et al. (2017b). They used archival data of polarized and unpolarized stars to test the stability and capabilities of the spectropolarimetric mode (PMOS) of the FORS2 instrument, and found a good temporal stability since FORS2 was commissioned, and a good observational repeatability of total linear polarization measurements with an RMS $\lesssim 0.21\%$. Cikota et al. (2017b) also found a small ($\lesssim 0.1\%$) instrumental polarization and fit linear functions to correct Stokes Q and U, which we applied to the FORS2 data in this work.

3.3.2. AFOSC at the 1.82 m Copernico telescope

Spectropolarimetry with AFOSC was obtained using a simple combination of two Wollaston prisms and two wedges, a grism, and a slit mask of 2.5 arcsec wide and 20 arcsec long slitlets. This configuration permits measurements of the polarized flux at four polarimetric channels simultaneously, that is, at angles 0, 45, 90 and 135 degrees, without the need of a half-wave retarder plate (Oliva, 1997). For any given rotator adapter angle θ_i , four fluxes can be measured. We group them into two groups, which we call ordinary (O) and extraordinary (E). We indicate them as $f_{O1,i}$, $f_{E1,i}$ and $f_{O2,i}$, $f_{E2,i}$. We used them to indicate the generic four beams f_0, f_{90} and f_{45}, f_{135}, respectively.

However, in order to remove possible instrumental problems (i.e., imperfect beam splitting, flat fielding, etc.) it is convenient to obtain at least two sets of data. This can be achieved by rotating the instrument by 90 degrees with respect to the sky, so that a pair-wise swap between the corresponding polarimeter channels, 0 to 90 and 45 to 135 degrees, is performed.

The final Q and U were obtained via the Fourier approach:

$$\begin{array}{l} Q = \frac{1}{N} \sum_{i=0}^{N-1} (F_{1,i} \cos(2\theta_i) - F_{2,i} \sin(2\theta_i)) \\ U = \frac{1}{N} \sum_{i=0}^{N-1} (F_{1,i} \sin(2\theta_i) + F_{2,i} \cos(2\theta_i)) \end{array} , \tag{3.7}$$

where N is the number of rotator adapter angles, $\theta_i = \frac{\pi}{4} i$, and $F_{1,i}$ and $F_{2,i}$ are normalized flux ratios:

$$\begin{array}{l} F_{1,i} = \frac{f_{O1,i} - f_{E1,i}}{f_{O1,i} + f_{E1,i}} \\ F_{2,i} = \frac{f_{O2,i} - f_{E2,i}}{f_{O2,i} + f_{E2,i}} \end{array} . \tag{3.8}$$

Finally, we calculated the polarization degree and angle as given in Eq. (5.4) and (5.5) respectively.

3.3.3. CAFOS at the Calar Alto 2.2 m telescope

CAFOS is a dual-beam polarimeter, similar to FORS2 in PMOS mode, composed of a half-wave retarder followed by a Wollaston prism that splits the incoming beam into an ordinary and an extra-ordinary beam. The data processing is as described for FORS2 in Sect. 3.3.1.

The CAFOS instrument was characterized in Patat & Taubenberger (2011). They used polarized standard stars to quantify the HWP chromatism, which causes a peak-to-peak oscillation of ~ 11 degrees. From observations of unpolarized standard stars, they found an instrumental polarization

likely produced by the telescope optics, which appears to be additive. The instrumental polarization is ~ 0.3 % between 4000 Å and 8600 Å, and grows to ~ 0.7 % below 4000 Å. It can be removed by subtracting the instrumental components in the Q–U Stokes plane. After correcting for the HWP chromatism and instrumental polarization, Patat & Taubenberger (2011) concluded that an accuracy of ~ 0.1 % can be reached with four HWP angles and a sufficient signal-to-noise ratio.

3.4. Data processing and results

The data were obtained with FORS2 in eight different nights between 2014-10-10 and 2015-02-06 (Program ID: 094.C-0686), with CAFOS in the night of 2015-04-29, and with AFOSC in five nights at three observing runs starting on 2015-02-09, 2015-03-09, and 2016-08-02.

3.4.1. Standard stars

We investigate the accuracy and reliability of the instruments using unpolarized and polarized standard stars. Cikota et al. (2017b) used archival data of eight unpolarized standard stars observed at 40 epochs between 2009 and 2016 to test the stability and capabilities of the spectropolarimetric mode (PMOS) of the FORS2 instrument. They showed that the polarization degree and angle are stable at the level of $\lesssim 0.1\%$ and $\lesssim 0.2$ degrees, respectively. They found a small ($\lesssim 0.1\%$) wavelength-dependent instrumental polarization and derived linear functions for the Stokes Q and U, which we applied to the observed Stokes parameters. In this paper, we therefore focus on unpolarized and polarized standard stars observed with CAFOS and AFOSC.

Two unpolarized standard stars (HD 144579, and HD 90508), and two polarized standard stars (HD 154445 and HD 43384) were observed with CAFOS. We did not find any significant instrumental polarization in the CAFOS observations, and the polarization values are consistent with the literature. The results are given in Sect. A.1.1.

We used observations of three unpolarized standard stars to investigate possible instrumental polarization of AFOSC: HD 90508, HD 39587 and HD 144579; and three polarized standard stars to test the reliability: HD 43384, HD 21291, and HD 198478. We did not detect any significant instrumental polarization, but the polarization degrees of polarized stars observed at different epochs vary by ~0.3%. The inconsistencies might be caused by diffraction of light from the edge of the slit (see Keller C.U. in Trujillo-Bueno et al., 2002, p. 303) or by an inaccuracy of the instruments rotation angle (see Bagnulo et al. (2017)). The results are given in Sect. A.1.2.

3.4.2. FORS2 science data

FORS2 is the most stable instrument used in this work, and we are confident that the data gained with FORS2 are accurate and can be used as reference for comparison to other instruments (see Cikota et al. 2017b). Eight stars with anomalous extinction sightlines were observed with FORS2 (see Table 6.2). HD 54439 was also observed with AFOSC, and HD 137569 was observed with all three instruments, FORS2, CAFOS, and AFOSC, which we briefly discuss in this section. HD 78785, HD 141318, HD 152853, HD 152245, HD 73420, and HD 96042 were observed only with FORS2.

We extracted the spectra and calculated the polarization dependencies as described in Sect. 3.3.1. The correction for the instrumental polarization determined in Cikota et al. (2017b) was also applied to Stokes Q and U. The targets have been observed with and without the GG435 filter. The GG435 filter blocks the blue light and thus prevents the second order spectrum. However, the effect in polarization is very small, and significant only for very blue spectral energy distributions and when

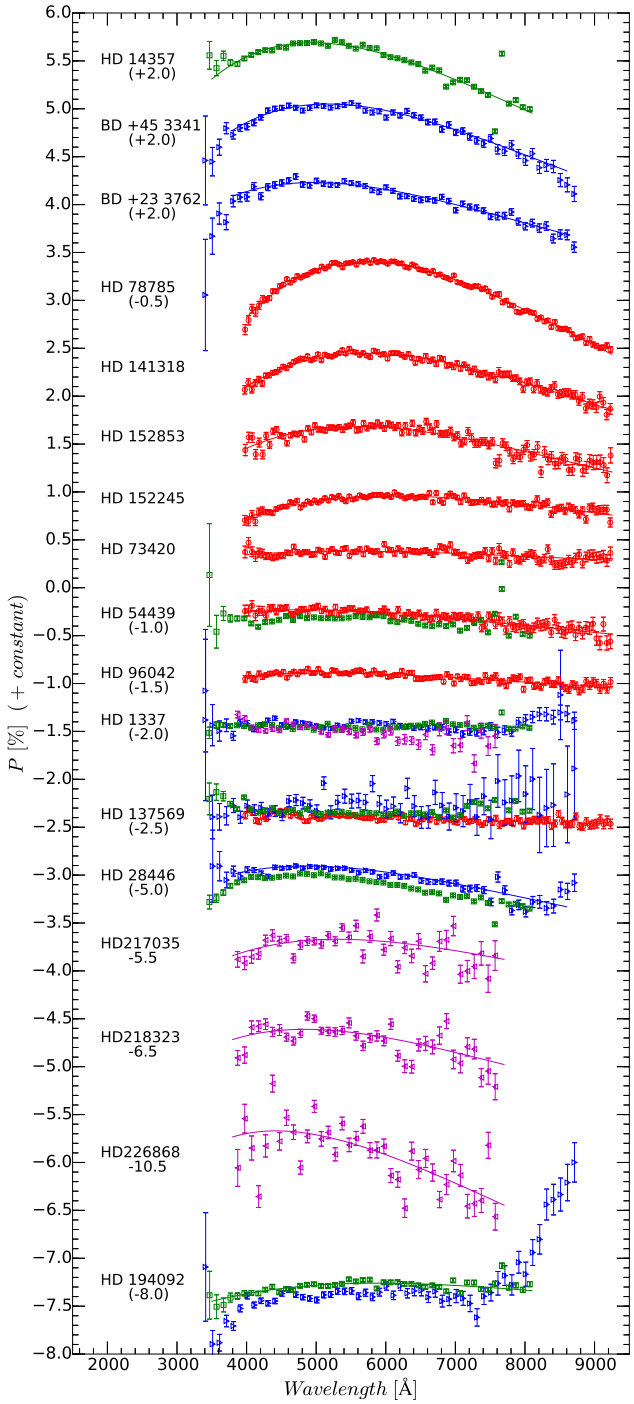

Figure 3.1.: Weighted averages of observed polarization curves for all science targets, derived with different instruments. The red circles show observations performed with FORS2, blue triangles with CAFOS, green squares with AFOSC, and left-pointing purple triangles with HPOL. The full lines denote the Serkowski fits, as parametrized in Table 3.3.

measuring line polarization (Patat et al., 2010). For our reddened targets, the second-order polarization is negligible. Therefore, for wavelengths λ¿4250Å, we calculated the weighted mean of all epochs, and for wavelengths λ¡4250Å, we calculated the weighted mean of all epochs taken without the GG435 filter. We then merged both ranges to one polarization spectrum and parameterized it by fitting a Serkowski curve (Eq. 4.1) to the data. The individual results can be found in Table A.2. The polarization dependencies are shown in Fig. 3.1, and the Serkowski parameters are given in Table 3.3.

HD 137569 is an interesting case because it has relatively high reddening $E(B-V) \sim 0.40$ mag (Mazzei & Barbaro, 2011), but its polarization degree is consistent with zero (Fig. 3.1). Its mean Stokes Q and U are -0.07 ± 0.05 % and 0.01 ± 0.03 %. HD 137569 was also observed with CAFOS and AFOSC, and the results are consistent with the FORS2 observations. Furthermore, HD 137569 is a spectroscopic binary with a period of 529.8 days, and shows observational signatures normally seen in post-AGB stars (Giridhar & Arellano Ferro, 2005). This is interesting, because sightlines to post-AGB stars usually show continuum polarization (Johnson & Jones, 1991).

3.4.3. CAFOS science data

Six stars with anomalous extinction sightlines were observed with CAFOS. HD 1337 and HD 28446 were also observed with AFOSC, and HD 137569 was additionally observed with both FORS2 and AFOSC (see also Sect. 3.4.2). BD +45 3341, BD +23 3762, and HD 194092 were observed only with CAFOS.

After the beam extraction using the apextract.apall procedure of PyRAF, we binned the spectra into 100Å wide bins and calculated the polarization as described in Sect. 3.3.3. Finally, we fit the Serkowski curve in the range between 3800-8600Å. The individual results are listed in Table A.3. The polarization dependencies are shown in Fig. 3.1, and the Serkowski parameters are listed in Table 3.3. Below we discuss the interesting cases.

3.4.3.1. HD 1337

HD 1337 is a close spectroscopic binary star, with a period of 3.52 days (Pourbaix et al., 2004), and may be surrounded by a common-envelope, where significant dust amounts may be produced (Lü et al. (2013). HD 1337 has a constant polarization degree of ~ 0.55 %. The CAFOS observations are also consistent with the AFOSC observations, which confirms the polarization wavelength independence (see Fig. 3.1). In this case, the Serkowski fit is not meaningful.

3.4.3.2. HD 194092

For HD 194092, the polarization observed by CAFOS follows a Serkowski curve until 7250Å, when it starts to steeply increase from p~ 0.5 % to p~ 2 % at 8650 Å. The steep increase is not present in the AFOSC observations and is an artifact that we cannot explain. Thus, we fit the Serkowski curve in the range from 3800-7250Å, and find $\lambda_{\rm max}$ = 5728 ± 235 Å, $p_{\rm max}$ = 0.64 ± 0.01 % and K = 1.46 ± 0.47.

3.4.4. AFOSC science data

Six stars with anomalous extinction sightlines have been observed with AFOSC. HD 28446, HD 1337, and HD 194092 were also observed with CAFOS and HD 54439 with FORS2, while HD 137569 was additionally observed with CAFOS and FORS2 (see also Sect. 3.4.2). HD 14357 was observed only with AFOSC.

We extracted the beams from 3400-8150 Å using the same standard procedures in IRAF as for the extraction of FORS2 and CAFOS spectra, binned the data to 100Å wide bins, and calculated the polarization as described in Sect. 3.3.2. The polarization spectra from 3500-8150Å were fitted with a Serkowski curve, excluding the range from 7500-7700 Å, which is contaminated by the telluric O_2 line.

The unpolarized standard stars are consistent with zero, which implies that there is no significant instrumental polarization (Sect. A.1.2). However, based on the measurements of the polarized standard stars HD 43384 and HD 21291 (see Sect. A.1.2), which show a negative offset compared to the literature values, we conclude that the accuracy of the polarization measurements is within ~ 0.4 %. HD 28446 and HD 54439 show an offset of $\sim$ -0.1 % compared to the results achieved with CAFOS and FORS2, respectively, while the measurements of HD 1337 are consistent with the CAFOS measurements, and the measurements of HD 137569 are consistent with the FORS2 and CAFOS measurements (Fig. 3.1). The individual results are listed in Table A.4.

HD 14357 is the only AFOSC target that has no common observations with another instrument. From the Serkowski fit, we determined $\lambda_{\rm max} = 4942 \pm 31$ Å, $p_{\rm max} = 3.69 \pm 0.01$ % and $K = 0.91 \pm 0.04$. Based on HD 43384 and other polarized stars, the $\lambda_{\rm max}$ and K values are probably accurate, while there might be a negative offset, $\lesssim 0.4$ %, to the true value of $p_{\rm max}$.

3.4.5. HPOL science data

We found archival data for HD 1337 (which was also observed with CAFOS and AFOSC), and three additional stars of the Mazzei & Barbaro (2011) sample in the University of Wisconsin's Pine Bluff Observatory (PBO) HPOL spectropolarimeter (mounted at the 0.9 m f/13.5 cassegrain) data set. All targets were observed prior to the instrument update in 1995, when HPOL was providing spectropolarimetry over the range of 3200Å to 7750Å, with a spectral resolution of 25Å. A half-wave plate was rotated to eight distinct angles to provide the spectropolarimetric modulation (Wolff et al., 1996).

The HPOL data are available in the Mikulski Archive for Space Telescopes (MAST) at the Space Telescope Science Institute. They include the Stokes parameters Q and U, and the error as a function of wavelength.

We calculated the polarization and polarization angle using equations 5.4 and 5.5, and fit a Serkowski curve to the data (equation 4.1). The results are given in Table 3.3.

3.4.6. Literature science data

We found polarization measurements in the literature (Coyne et al., 1974; Serkowski et al., 1975) of eight stars of the Mazzei & Barbaro (2011) sample. Three of the stars have been observed in this work with FORS2, AFOSC, or CAFOS, and for two stars, we found archival HPOL data. The stars were observed with broadband polarimeters and were characterized by fitting the Serkowski curve (Table 3.2). However, because the authors assumed a fixed K=1.15, we could only partially use the measurements from Coyne et al. (1974) and Serkowski et al. (1975) in our further analysis.

3.5. Data analysis

Figure 3.2 shows the sample of 15 anomalous sightlines (listed in Table 3.3, excluding HD 137569 and HD 1337), compared to a sample of Galactic stars observed by Whittet et al. (1992) and a sample SNe Ia from Patat et al. (2015) and Zelaya et al. (2017a) (see Appendix A.2).

Table 3.2.: λ_{max} and P_{max} from literature

Name	λ_{max} (Å)	P_{max} (%)	Reference
HD 2619	4900 ± 100	4.82 ± 0.32	Coyne et al. (1974)
HD 37061	6300 ± 400	1.63 ± 0.19	Coyne et al. (1974)
HD 168021	5900 ± 100	2.13 ± 0.03	Serkowski et al. (1975)
HD 28446[b,c]	5500 ± 100	2.01 ± 0.10	Coyne et al. (1974)
HD 226868[d]	5000 ± 100	5.04 ± 0.25	Coyne et al. (1974)
HD 218323[d]	5200 ± 200	1.95 ± 0.14	Coyne et al. (1974)
HD 78785[a]	5800 ± 224	4.05 ± 0.04	Serkowski et al. (1975)
HD 141318[a]	5700 ± 100	2.42 ± 0.08	Serkowski et al. (1975)

[a] Also observed with FORS2.
[b] Also observed with AFOSC.
[c] Also observed with CAFOS.
[d] Also observed with HPOL.

Table 3.3.: Final Serkowski parameters

Name	Telescope	Serkowski parameters		
		λ_{max} (Å)	p_{max} (%)	K
HD 137569[a]	VLT	...	~ 0.1	...
HD 54439	VLT	4859 ± 129	0.77 ± 0.01	0.97 ± 0.10
HD 73420	VLT	5465 ± 175	0.38 ± 0.01	1.04 ± 0.21
HD 78785	VLT	5732 ± 8	3.90 ± 0.01	1.25 ± 0.01
HD 96042	VLT	5109 ± 124	0.61 ± 0.01	0.84 ± 0.09
HD 141318	VLT	5719 ± 17	2.45 ± 0.01	1.19 ± 0.03
HD 152245	VLT	6169 ± 33	0.96 ± 0.01	1.41 ± 0.07
HD 152853	VLT	5584 ± 46	1.69 ± 0.01	1.30 ± 0.07
BD +23 3762	CAHA	4965 ± 61	2.23 ± 0.01	0.92 ± 0.06
BD +45 3341	CAHA	5166 ± 31	3.05 ± 0.01	1.00 ± 0.05
HD 1337[a]	CAHA	...	0.55 ± 0.01	...
HD 28446	CAHA	4865 ± 76	2.10 ± 0.01	0.70 ± 0.07
HD 194092	Asiago	5884 ± 107	0.74 ± 0.01	1.09 ± 0.18
HD 14357	Asiago	4942 ± 31	3.69 ± 0.01	0.91 ± 0.04
HD 226868	HPOL	4425 ± 262	4.83 ± 0.04	0.57 ± 0.14
HD 218323	HPOL	4837 ± 128	1.89 ± 0.01	1.00 ± 0.20
HD 217035	HPOL	5309 ± 126	1.83 ± 0.02	0.88 ± 0.23

[a] HD 137569 and HD 1337 have constant polarization curves which could not be fit with a Serkowski curve.

Mazzei & Barbaro (2011) used models of Weingartner & Draine (2001, hereafter WD01) and the updates by Draine & Li (2007) to compute grain-size distributions for spherical grains of amorphous silicate and carbonaceous grains consisting of graphite grains and polycyclic aromatic hydrogenated (PAH) molecules. As described in Mazzei & Barbaro (2011), they best-fit the extinction curves with models as described above (Sect. 3.2) to derive the properties of the dust in terms of dust-to-gas ratios, abundance ratios, and small-to-large grain size ratios of carbon and of silicon. They excluded HD 1337 (a W UMa type variable) and HD 137569 (a post-AGB star) from their analysis before performing the modeling because of the extremely low CCM R_V values of these sightlines, $R_V \approx 0.6$ and $R_V \approx 1.1$, respectively, which are well outside the range explored by CCM extinction curves.

We combined the λ_{max} values from this work with the results of WD01 best-fit models of Mazzei & Barbaro (2011, their Table 4), and computed the Pearson correlation coefficient, ρ, and the p-value for testing the non-correlation between λ_{max} and their derived dust-to-gas ratio ($\frac{\rho_d}{\rho_H}$), carbon and silicon abundances compared to solar values ($\frac{C}{C_\odot}$, $\frac{Si}{Si_\odot}$), R_V value, the ratio between reddening and total hydrogen column density ($\frac{E(B-V)}{N_H}$), and small-to-large grain size ratios of carbon (R_C) and silicon (R_{Si}). They considered grains as small if their size is $\leqslant 0.01$ μm, and otherwise as large. We note

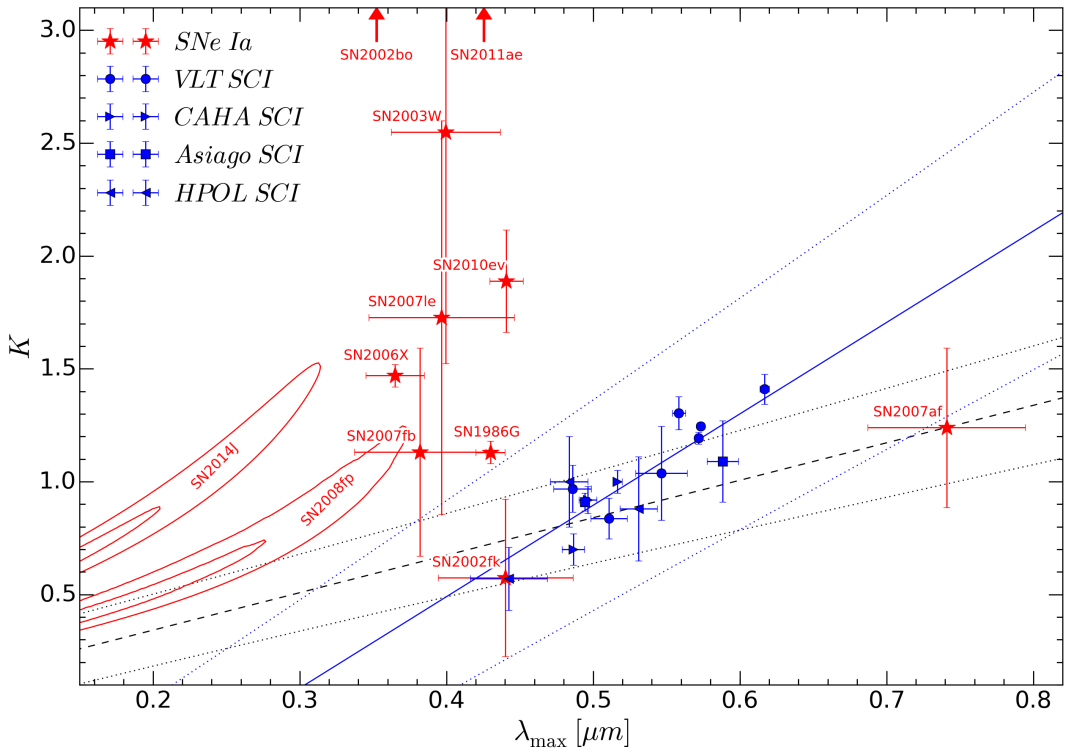

Figure 3.2.: Stars with anomalous extinction sightlines in the λ_{max}-K plane. Blue color shows stars with anomalous sightlines observed with FORS2 (circles), CAHA (right pointing triangles), AFOSC (squared), and HPOL (left pointing triangles). The solid blue line represents the linear best fit to the sample, and it's 1σ deviation (dotted). The dashed black line traces the Whittet et al. (1992) relation and its 3σ uncertainty (dotted). For comparison, a sample of SNe Ia from Patat et al. (2015) and Zelaya et al. 2017a (see Appendix A.2) are marked with star symbols, and red contours, which indicate the 10 and 20 σ confidence levels for SN 2008fp and SN 2014J.

that a detailed analysis and discussion of the WD01 best-fit model results for the whole sample of 64 anomalous sightlines is given in Mazzei & Barbaro (2011).

The strongest correlation we found between λ_{max} and R_{Si}, with a correlation factor of ρ = 0.50, and the p-value for testing non-correlation of p=0.10, while there is no correlation between λ_{max} and other parameters ($\rho \lesssim 0.25$). We also added three stars observed by HPOL and three stars from the literature (Coyne et al., 1974; Serkowski et al., 1975) to the sample and repeated the same correlation tests. These additional stars have anomalous extinction sightlines (Mazzei & Barbaro, 2011), but higher R_V values than our observed sample (see Table 3.4). After including the three HPOL observations and three stars from literature, the $R_{Si} - \lambda_{max}$ correlation factor drops to ρ = -0.06. The $R_{Si} - \lambda_{max}$ correlation is shown in Fig. 3.4. However, these results should be taken with care because when we fit the data, we assumed no uncertainty in R_{Si}. This may be problematic because the realistic uncertainty in the model quantities should be considerable, probably larger than in λ_{max}, which is a simple measurement. In this way, the fit is strongly driven by the few stars with very low λ_{max} errors. The relationship is further discussed in Sect. 3.7.7.

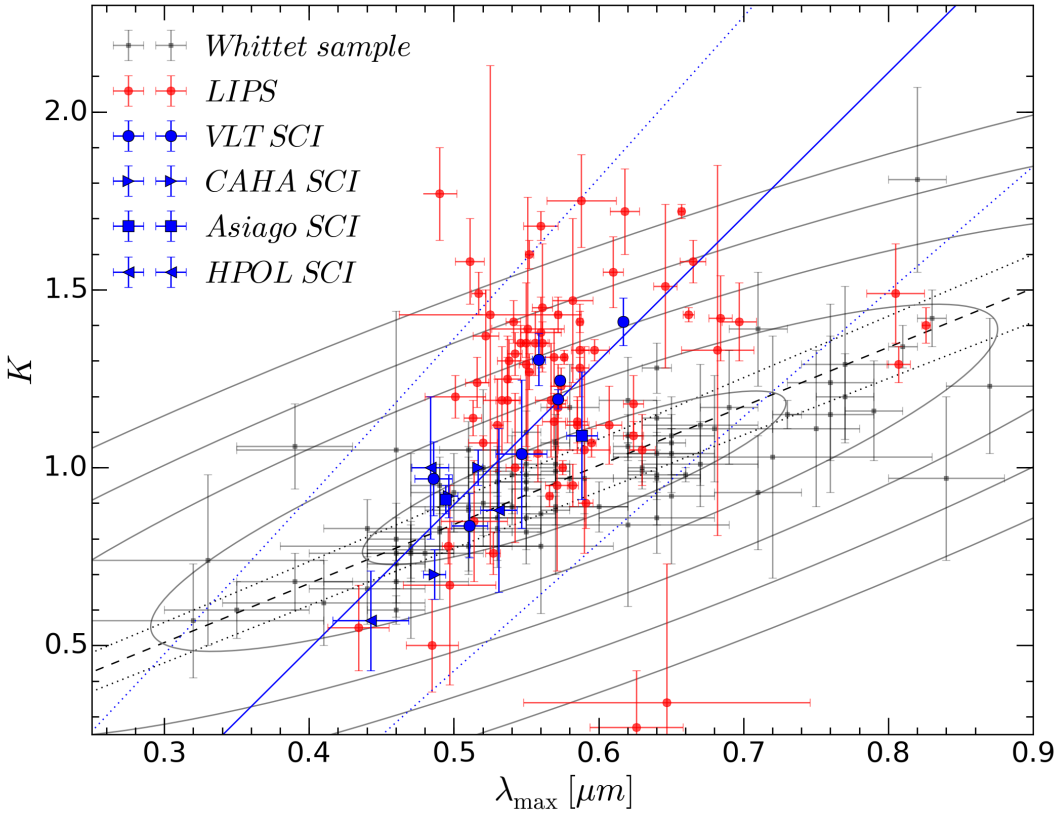

Figure 3.3.: Comparison of our sample of stars with anomalous extinction sightlines (blue symbols) to the Whittet et al. (1992) sample (gray squares) and the LIPS sample (Bagnulo et al. (2017), red circles). The gray ellipses represent 1-5σ confidence levels for the Whittet et al. (1992) sample. The dashed black line traces the Whittet et al. (1992) relation and its 1σ uncertainty (dotted).

3.6. Dust properties inferred from simulations

The properties of dust grains toward the considered stars were obtained in Mazzei & Barbaro (2008), where the authors performed theoretical model fitting to the anomalous extinction curves. The authors found that to reproduce the anomalous extinction, silicate grains must be concentrated in small sizes of $a < 0.1\,\mu$m (see also Mazzei & Barbaro 2011). Such small silicate grains cannot reproduce the normal $\lambda_{\max}$ that is measured. In this section, we therefore infer the essential dust properties (i.e., size distribution and alignment) by fitting both extinction curves with low R_V values and normal polarization curves. The results are used to interpret the $\lambda_{\max}$–K relationship, the deviation of K from the average value from a sample of "normal" Galactic stars, and to test the relationship between $R_{\rm Si}$ and $\lambda_{\max}$.

Table 3.4.: Observational data and results of modeling

Name	Mazzei & Barbaro (2011)					Wegner (2002)			λ_{max} (Å)	λ_{max} Reference
	Sp.	$E(B-V)$ (mag)	CCM R_V	R_V	$\frac{R_{Si}}{10^2}$	Sp.	E(B-V) (mag)	R_V		
HD 54439	B2III	0.28	2.13 ± 0.41	1.98	0.82	B1V	0.28	2.88	4859 ± 129	This work (VLT)
HD 73420	B2II/III	0.37	2.47 ± 0.32	2.24	2.3	...	...	...	5465 ± 175	This work (VLT)
HD 78785	B2II	0.76	2.55 ± 0.17	2.29	3.4	B2II	0.67	3.08	5732 ± 8.2	This work (VLT)
HD 96042	O9.5V	0.48	1.97 ± 0.24	1.87	5.2	B1V	0.41	3.05	5109 ± 124	This work (VLT)
HD 141318	B2II	0.30	1.95 ± 0.18	1.77	3.6	...	...	...	5719 ± 17	This work (VLT)
HD 152245	B0III	0.42	2.25 ± 0.29	2.02	3.7	B0Ib	0.31	2.95	6169 ± 33	This work (VLT)
HD 152853	B2II/III	0.37	2.50 ± 0.33	2.19	0.91	...	...	...	5584 ± 46	This work (VLT)
BD+23 3762	B0.5III	1.05	2.47 ± 0.12	2.15	1.3	...	...	...	4965 ± 61	This work (CAHA)
BD+45 3341	B1II	0.74	2.46 ± 0.17	2.22	2.84	...	...	...	5166 ± 31	This work (CAHA)
HD 28446	B0III	0.46	2.46 ± 0.26	2.20	1.6	...	...	...	4865 ± 76	This work (CAHA)
HD 194092	B0.5III	0.41	2.50 ± 0.30	2.18	3.6	...	...	...	5884 ± 107	This work (Asiago)
HD 14357	B2II	0.56	2.31 ± 0.21	2.12	1.4	B1.5II	0.49	2.88	4942 ± 31	This work (Asiago)
HD 226868	B0Ib	1.08	3.20 ± 0.14	2.78	3.3	B0Ib	1.03	3.32	4424.6 ± 262.4	(This work, HPOL)
HD 218323	B0III	0.90	2.55 ± 0.15	2.30	2.6	...	...	...	4836.7 ± 128.2	(This work, HPOL)
HD 217035	B0V	0.76	2.77 ± 0.18	2.44	0.5	...	...	...	5309.3 ± 125.9	(This work, HPOL)
HD 2619	B0.5III	0.85	2.55 ± 0.15	2.34	3.5	...	...	...	4900 ± 100	Coyne et al. (1974)
HD 37061	B1V	0.52	4.50 ± 0.38	3.82	0.8	B0.5V	0.47	4.14	6300 ± 400	Coyne et al. (1974)
HD 168021	B0Ib	0.55	3.15 ± 0.27	2.74	0.02	...	...	...	5900 ± 100	Serkowski et al. (1975)

Spectral Type (Sp.), $E(B-V)$ and CCM R_V, R_V and R_{Si} are taken from Table 1 and 4 of Mazzei & Barbaro (2011). The Sp. and $E(B-V)$ values in Mazzei & Barbaro (2011) are taken from Savage et al. (1985). "CCM R_V" is determined by fitting the IR observations with the CCM extinction curve, while "R_V" is determined from the best-fit of WD01 model to all observed data (see Mazzei & Barbaro 2011). For comparison, cols. 7-9 report Sp., E(B-V) and R_V values for seven common stars from Wegner (2002).

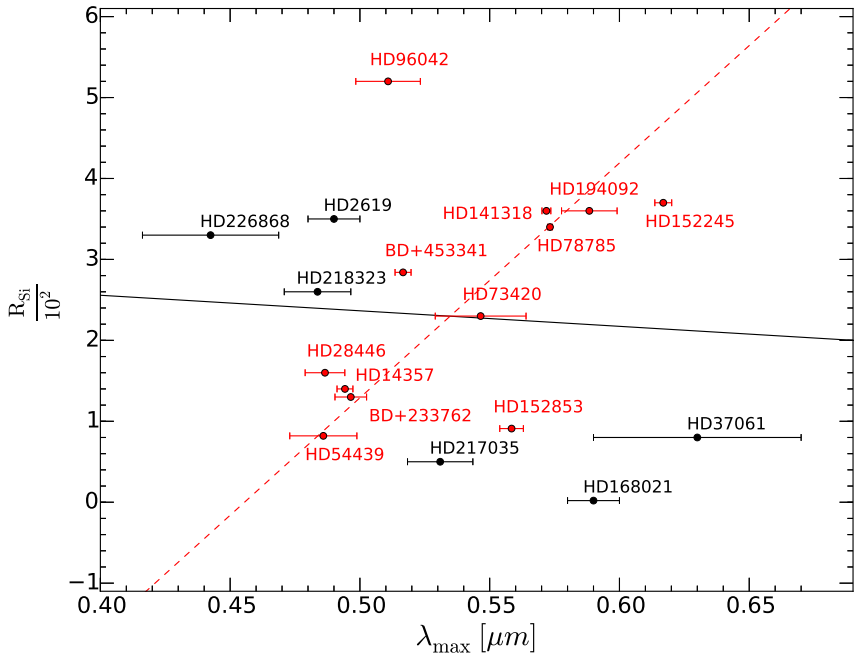

Figure 3.4.: R_{Si}–λ_{max} relationship. The red dots are stars observed with FORS2, AFOSC and CAFOS, and the black dots are 7 additional measurements from HPOL or from the literature. The red dashed line is the linear least-square fit to the red dots, and the black solid line is the linear least-square fit to all data.

3.6.1. Dust model and observational constrains

3.6.1.1. Dust model: size distribution

We adopted a mixed-dust model consisting of astronomical silicate and carbonaceous grains (see Weingartner & Draine, 2001, hereafter WD01). The same size distribution model was also used in Mazzei & Barbaro (2011). We assumed that grains have oblate spheroidal shapes, and let a be the effective grain size defined as the radius of the equivalent sphere with the same volume as the grain.

Following WD01, the grain size distribution of dust component j is described by an analytical function:

$$\frac{dn_j}{n_{\rm H}\,da} = D_j(a) + \frac{C_j}{a}\left(\frac{a}{a_{t,j}}\right)^{\alpha_j} F(a;\beta_j, a_{t,g})G(a; a_{t,j}, a_{c,j}), \tag{3.9}$$

where a is the grain size, $j = sil, carb$ for silicate and carbonaceous compositions, $D_j(a)$ is the size distribution for very small grains, $a_{t,j}$, $a_{c,j}$ are model parameters, and C_j is a constant determined by the total gas-to-dust mass ratio.

The coefficients F and G read

$$F(a;\beta_j, a_{t,j}) = 1 + \beta_j\, a/a_{t,j} \text{ for } \beta_j > 0, \tag{3.10}$$
$$F(a;\beta_j, a_{t,j}) = (1 - \beta_j\, a/a_{t,j})^{-1} \text{ for } \beta_j < 0, \tag{3.11}$$

and

$$G(a; a_{t,j}, a_{c,j}) = 1 \text{ for } a < a_{t,j}, \tag{3.12}$$
$$G(a; a_{t,j}, a_{c,j}) = \exp\left(-[(a - a_{t,j})/a_{c,j}]^3\right) \text{ for } a > a_{t,j}. \tag{3.13}$$

The term $D_j = 0$ for $j = sil$. For very small carbonaceous grains (i.e., PAHs), $D_j(a)$ is described by a log-normal size distribution containing a parameter b_C that denotes the fraction of C abundance present in very small sizes (see WD01 for more detail). Thus, the grain size distribution is completely described by a set of 11 parameters: α_j,β_j, $a_{t,j}$, $a_{c,j}$, and C_j , where $j = sil, carb$ for silicate and carbonaceous compositions, and b_C.

3.6.1.2. Dust model: alignment function

Let $f_{\rm ali}$ be the fraction of grains that are perfectly aligned with the symmetry axis $\hat{a}_1$ along the magnetic field B. The fraction of grains that are randomly oriented is thus $1 - f_{\rm ali}$. To parameterize the dependence of $f_{\rm ali}$ on the grain size, we introduce the following function:

$$f_{\rm ali}(a; a_{\rm ali}, f_{\rm min}, f_{\rm max}) = f_{\rm min} + \left[1 - \exp\left(-\frac{a}{a_{\rm ali}}\right)^3\right](f_{\rm max} - f_{\rm min}), \tag{3.14}$$

where $a_{\rm ali}$ describes the minimum size of aligned grains, $f_{\rm max}$ describes the maximum degree of grain alignment, and $f_{\rm min}$ accounts for some residual small degree of alignment of very small grains. This alignment function reflects the modern understanding of grain alignment, where large grains are efficiently aligned by radiative torques (see, e.g., Hoang & Lazarian 2016) and small grains are weakly aligned by paramagnetic relaxation (Hoang et al., 2014).

3.6.2. Extinction and polarization model

3.6.2.1. Extinction

The extinction of starlight due to scattering and absorption by interstellar grains in units of magnitude is given by

$$\frac{A(\lambda)}{N_{\rm H}} = 1.086 \sum_{j=sil,carb} \int_{a_{\rm min}}^{a_{\rm max}} C_{\rm ext}^{j}(a,\lambda) \left(\frac{dn_j}{da}\right) da, \tag{3.15}$$

where $C_{\rm ext}$ is the extinction cross-section, $a_{\rm min}$ and $a_{\rm max}$ are the lower and upper cutoffs of the grain size distribution, and $N_{\rm H}$ is the total gas column density along the sightline.

3.6.2.2. Polarization

Modeling the starlight polarization by aligned grains is rather complicated because it requires a detailed knowledge of the orientation of grains with the magnetic field and the magnetic field geometry along the line of sight. Specifically, a realistic modeling needs to take into account the nutation of the grain symmetry axis $\hat{\mathbf{a}}_1$ around the angular momentum J, the precession of J around B, and the distribution function of the cone angle between J and B (Hong & Greenberg 1980; see Voshchinnikov 2012 for a review). However, an analytical distribution function for the cone angle is not known for the popular alignment mechanism by radiative torques (see Lazarian et al. 2015 and Andersson et al. 2015 for latest reviews). Therefore we adopted a picket-fence (PF) alignment model to compute the polarization, as used in previous works (Kim & Martin 1995; Draine & Allaf-Akbari 2006; Draine & Fraisse 2009; Hoang et al. 2013; Hoang et al. 2014). The essence of the PF model is as follows.

First, the oblate grain is assumed to be spinning around the symmetry axis $\hat{\mathbf{a}}_1$ (i.e., having perfect internal alignment). The magnetic field B is assumed to lie in the plane of the sky $\hat{\mathbf{x}}\hat{\mathbf{y}}$ with $B\|\hat{\mathbf{x}}$, and the line of sight is directed along $\hat{\mathbf{z}}$. Therefore, the polarization cross-section contributed by the perfectly aligned grains is $C_x - C_y = (C_\| - C_\perp) f_{\rm ali}$, where $C_\|$ and $C_\perp$ are the cross-section for the incident electric field parallel and perpendicular to the symmetry axis, respectively (see Hoang et al. 2013). Of $(1 - f_{\rm ali})$ randomly oriented grains, the fraction of grains that are aligned with $\hat{\mathbf{x}}, \hat{\mathbf{y}}, \hat{\mathbf{z}}$ are equal, of $(1 - f_{\rm ali})/3$. The total polarization produced by grains with $\hat{\mathbf{a}}_1 \| B$ is then $C_x - C_y = (C_\| - C_\perp)(f_{\rm ali} + (1 - f_{\rm ali})/3)$. The polarization by grains aligned with $\hat{\mathbf{a}}_1 \| \hat{\mathbf{y}}$ is $(1 - f_{\rm ali})/3(C_\| - C_\perp)/3$. Thus, the total polarization cross-section is $C_x - C_y = (C_\| - C_\perp)[(1 + 2f_{\rm ali}) - (1 - f_{\rm ali})]/3 = C_{\rm pol} f_{\rm ali}$.

Because graphite grains are not aligned with the magnetic field (Chiar et al. 2006; Hoang & Lazarian 2016), we assumed that only silicate grains are aligned, while carbonaceous grains are randomly oriented. Therefore, the degree of polarization of starlight due to differential extinction by aligned grains along the line of sight is computed by

$$\frac{p(\lambda)}{N_{\rm H}} = \int_{a_{\rm min}}^{a_{\rm max}} \frac{1}{2} C_{\rm pol}^{\rm sil}(a,\lambda) f_{\rm ali}(a) \frac{dn_{\rm sil}}{da} da, \tag{3.16}$$

where $C_{\rm pol}^{\rm sil}$ is the polarization cross-section of silicate oblate grains, and $f_{\rm ali}$ is given by Equation (3.14). Here we take $C_{\rm ext}$ and $C_{\rm pol}$ computed for different grain sizes and wavelengths from Hoang et al. (2013).

We note that magnetic fields may be varying for the different stars. However, we here do not attempt to infer a dust model for each specific sightline. Instead, we only attempt to infer the general features of dust size distribution and alignment functions for this group of stars with anomalous R_V and normal λ_{max}. Detailed modeling for each specific star is beyond the scope of this paper.

3.6.3. Numerical modeling and results

3.6.3.1. Numerical method

Inverse modeling has frequently been used to infer the grain size distribution of dust grains in the ISM of the Milky Way (Kim & Martin 1995), and in nearby galaxies (e.g., Small Magellanic Cloud (Clayton et al., 2003). Draine & Fraisse (2009) used the Levenberg-Marquart (LM) method to infer both the grain size distribution and alignment function of interstellar grains in the Galaxy characterized by the typical values of $R_V = 3.1$ and $\lambda_{\rm max} = 0.55\,\mu$m. A simulation-based inversion technique was developed in Hoang et al. (2013, 2014) to find the best-fit grain size distribution and alignment function for interstellar grains in the SNe Ia hosted galaxies with anomalous extinction and polarization data. Although the Monte Carlo simulations demonstrate some advantage (e.g., problem with local minima), its convergence is much slower than the LM method. Thus we adopted the LM method for our modeling.

The goodness of fit of the model $F_{\rm mod}$ to observed data $F_{\rm obs}$ is governed by χ^2_F , which is defined as follows:

$$\chi^2_F = \sum_i \frac{(F_{\rm mod}(\lambda_i) - F_{\rm obs}(\lambda_i))^2}{F_{\rm err}(\lambda_i)^2}, \tag{3.17}$$

where $F_{\rm err}(\lambda)$ is the error in the measurement at wavelength λ.

When we assume the same errors at all wavelengths, the total χ^2 can be written as

$$\chi^2 = \chi^2_{\rm ext} + \eta_{\rm pol}\chi^2_{\rm pol} + \chi^2_{\rm vol}, \tag{3.18}$$

where $\chi^2_{\rm ext}$ and $\chi^2_{\rm pol}$ are evaluated using Eq. (3.17) for $F = A$ and $F = P$, respectively, $\chi^2_{\rm vol}$ describes the volume constraint determined by the depletion of elements into dust, and $\eta_{\rm pol}$ is a coefficient introduced to adjust the fit to the polarization. The initial value of $\eta_{\rm pol} = 1$ is chosen. When the fit to the polarization is poor, we can increase $\eta_{\rm pol}$. Here, we evaluate $\chi^2_{\rm vol} = \chi^2_{\rm vol,sil} + \chi^2_{\rm vol,carb} = (V_{\rm sil}/V_{\rm sil,0} - 1)^2 + (V_{\rm carb}/V_{\rm carb,0} - 1)^2$, where $V_{\rm sil,0} = 2.98 \times 10^{-27}{\rm cm}^3$ per H nucleon and $V_{\rm carb,0} = 2.07 \times 10^{-27}{\rm cm}^3$ per H nucleon (see WD01).

We search the best-fit values of α_j, β_j, $a_{t,j}$, $a_{c,j}$, and c_j , where $j = sil, carb$ and two parameters for grain alignment ($a_{\rm ali}, f_{\rm min}$) by minimizing χ^2 (Eq. 3.18) using the LM method from the publicly available package lmfit-py[1]. The errors from observed data are assumed to be 10%.

We note that in WD01, the parameter $a_{c,\rm sil}$ was fixed to $0.1\,\mu$m. However, Mazzei & Barbaro (2008) found that the best fit to the extinction for these anomalous stars requires $a_{c,\rm sil}$ to be reduced to $0.01\,\mu$m, which corresponds to most Si being present in small grains of $a \le 0.01\,\mu$m. We treated $a_{c,\rm sil}$ as a model parameter. Furthermore, because we have $R_V < 4$, grain growth is not expected, thus we constrained the size cutoff parameters $a_{c,\rm carb} \le 0.5\,\mu$m and $a_{c,\rm sil} \le 0.5\,\mu$m.

3.6.3.2. Model setup

The sightlines of the considered stars have anomalous extinction curves, with lower R_V than the standard value of $R_V = 3.1$ for the Milky Way. However, the polarization data appear to be normal, with a peak wavelength $\lambda_{\rm max} > 0.4\,\mu$m. For our inverse modeling, we accordingly considered a fixed extinction curve described by a low value of $R_V = 2.5$. For the polarization data, we considered six different values of $\lambda_{\rm max} = 0.45, 0.51, 0.53, 0.55, 0.60,$ and $0.65\,\mu$m, which fully covers the range of

[1] http://cars9.uchicago.edu/software/python/lmfit/index.html

$\lambda_{\rm max}$ inferred from observations shown in Table 3.4. For a given R_V, we generated (i.e., constructed) the extinction data (hereafter, generated extinction curves) using the Cardelli et al. (1989) extinction law. For a given $\lambda_{\rm max}$, we generated the polarization data (hereafter, generated polarization curves) using the Serkowski curve with $K = k_1\lambda_{\rm max} + k_2$ (see Hoang 2017a for details). Here, we adopted a standard relationship with $k_1 = 1.66$ and $k_2 = 0.01$ from Whittet et al. (1992).

Because the extinction and polarization data in the far-UV ($\lambda < 0.25\,\mu$m) toward the considered stars are unavailable, we did not attempt to invert the data in the far-UV, which is mainly contributed by ultrasmall grains (including PAHs). Thus, we considered $\lambda = 0.25 - 2.5\,\mu$m and computed the extinction and polarization model given by Equations (3.15) and (3.16), respectively. We used 32 bins of grain size in the range from $a_{\rm min} = 3.5$ Å to $a_{\rm max} = 1\,\mu$m and 32 wavelength bins.

Furthermore, we note that while we used the standard Serkowski curve to generate the polarization data, observational studies show differences in the amount of UV polarization relative to that in the visual Serkowski curve. Clayton et al. (1995) found that UV polarimetry measurements of 7 out of 14 sightlines with $\lambda_{max} \geq 0.54\,\mu m$ agree well with an extrapolation of the Serkowski curve into the UV, while the other 7 sightlines with $\lambda_{max} \leq 0.53\,\mu m$ show polarization excess compared to the Serkowski extrapolation. They found a relationship between λ_{max}^{-1} and the relative UV polarization $p(6\,\mu m^{-1})/p_{max}$ (see also Martin et al. 1999). Anderson et al. (1996) found that at least half of their sample of 35 sightlines for which they have reliable UV observations did not agree well compared to the Serkowski extrapolation from visual and near-IR parameters. An increase/decrease in the UV polarization would lead to an increase/decrease in the degree of alignment of small grains inferred from simulations, whereas the alignment of large grains (a ¿ 0.1 μm) that dominates the visible-IR polarization would be unchanged. The grain size distributions would be slightly changed (see Hoang et al. 2014).

The important constraint for the polarization model (see Sect. 3.6.2.2) and the alignment function $f_{\rm ali}(a)$ is that for the maximum polarization efficiency $p_{\rm max}/A(\lambda_{\rm max}) = 3\%\,{\rm mag}^{-1}$ (see Draine 2003 for a review), we expect that the conditions for grain alignment are optimal, which corresponds to the case in which the alignment of large grains can be perfect, and the magnetic field is regular and perpendicular to the line of sight. Thus, we set $f_{\rm ali}(a = a_{\rm max}) = 1$.

3.6.3.3. Results

Figure 3.5 shows the best-fit polarization and extinction curves for the different $\lambda_{\rm max}$. The fit to the extinction curve is good, but the model overestimates the extinction for $\lambda \geq 1\,\mu$m for $\lambda_{\rm max} = 0.53 - 0.65\,\mu$m. For the polarization, the fit is excellent for $\lambda_{\rm max} < 0.6\,\mu$m, but the model (see Sect. 3.6.2.2) overestimates the polarization at $\lambda < 0.25\,\mu$m for $\lambda_{\rm max} = 0.6\,\mu$m and $0.65\,\mu$m.

Figure 3.6 shows the best-fit size distributions for silicate and carbonaceous grains. The size distribution appears to change slightly with $\lambda_{\rm max}$, which is expected due to the fixed R_V. To reproduce the typical $\lambda_{\rm max}$, there must be a population of large silicate grains of $a \geq 0.1\,\mu$m. This is different from the results obtained by Mazzei & Barbaro (2008), where the authors only performed the fitting to the extinction curves and found a lack of large silicate grains, but large grains in the carbonacous grain size distribution.

Figure 3.7 shows the best-fit alignment function for the different $\lambda_{\rm max}$. When $\lambda_{\rm max}$ decreases, the alignment function tends to shift to smaller sizes. Moreover, the alignment of small grains ($a < 0.05\,\mu$m) is increased with decreasing $\lambda_{\rm max}$. This trend is consistent with the results from Hoang et al. (2014), where the modeling was done for the cases with normal extinction curves (i.e., $R_V \sim 3.1$) and excess UV polarization.

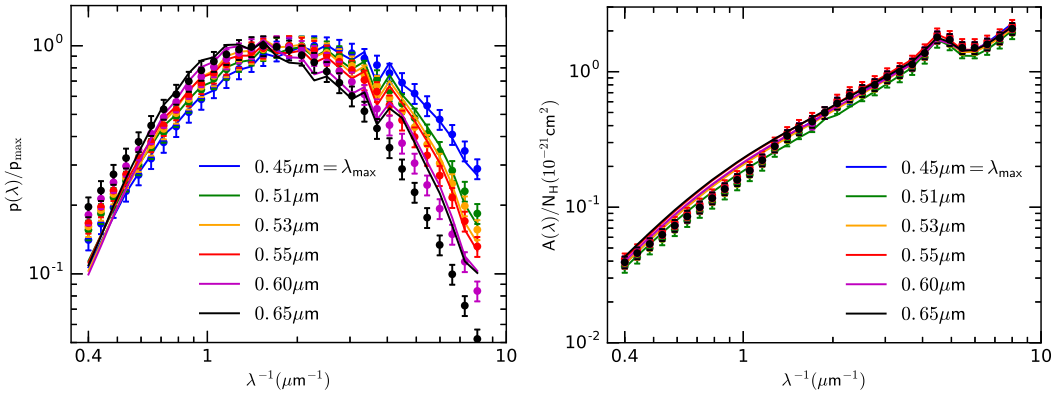

Figure 3.5.: Left panel: Best-fit models vs. generated (i.e., constructed) polarization curves for six different models described by $\lambda_{\rm max}$. Right panel: Best-fit models vs. generated extinction curves with a low R_V = 2.5. Filled circles show the generated data, and solid lines show our best-fit models.

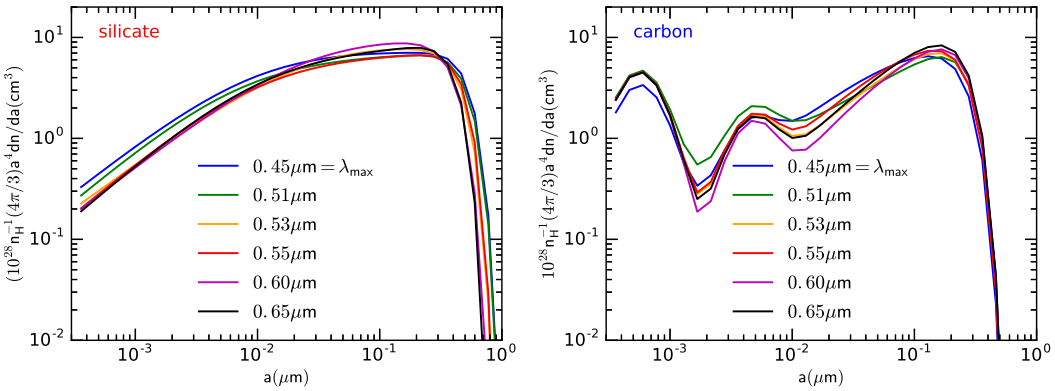

Figure 3.6.: Best-fit grain size distribution for silicate (left panel) and carbonaceous grains (right panel). Six different models described by $\lambda_{\rm max}$ are considered. Large silicate grains of size $a \geq 0.1\,\mu$m are present to reproduce normal $\lambda_{\rm max}$.

3.7. Discussion

3.7.1. Comparison to supernovae Ia and normal Galactic stars

The main aim of this work is to investigate the polarization profiles of Galactic stars with low R_V values, with the aim to try to find similar polarization behavior, as we observe in highly reddened SNe Ia with low R_V values, with the polarization degree rising toward blue wavelengths (see, e.g., Fig. 2 in Patat et al. 2015). However, none of the stars with anomalous extinction sightlines in our sample display such polarization curves that steeply rise toward the blue (Fig. 3.1).

Figure 3.2 shows our sample of stars with anomalous extinction sightlines in the $\lambda_{\rm max}$–K plane compared to a sample of SNe Ia from Patat et al. (2015) and Zelaya et al. (2017a) (see Appendix A.2). Despite the low R_V values, our sample has normal polarization curves with a mean $\lambda_{\rm max} \sim 0.53\,\mu$m. The Serkowski parameters K and $\lambda_{\rm max}$ are related (ρ=0.87, p=3×10^{-5}), and can be described as a linear function of $\lambda_{\rm max}$: K= -1.13 ± 0.34 + (4.05 ± 0.64)$\lambda_{\rm max}$. This is steeper than the empirical relationship found by Whittet et al. (1992): K=0.01 ± 0.05 + (1.66 ± 0.09)$\lambda_{\rm max}$ (see also Wilking et al. 1980, 1982). However, the K–$\lambda_{\rm max}$ relationship in Whittet et al. (1992) was determined from a chosen

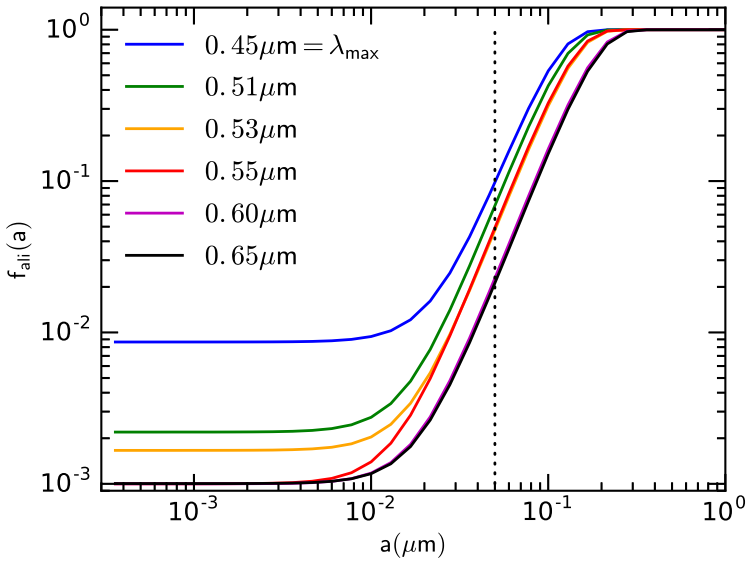

Figure 3.7.: Best-fit alignment function of silicates for the different models given by λ_{max}. The dotted line marks the typical grain size a=0.05 μm. The alignment function tends to shift to smaller sizes as λ_{max} decreases.

sample of sightlines toward stars with a variety of interstellar environments, including dense clouds, diffuse clouds, and low-density interstellar material.

Fig. 3.3 shows a direct comparison of our sample with the Whittet et al. (1992) sample and the Large Interstellar Polarization Survey (LIPS) sample (Bagnulo et al., 2017). Despite the difference in the slope, our sample is consistent within 3σ with the Whittet et al. (1992) sample and also coincides well with the LIPS sample, which has many outliers from the K–λ_{max} relationship.

For comparison, SNe Ia with low R_V values have $\lambda_{max} \lesssim 0.45\,\mu$m, and higher K values, above the the Whittet et al. (1992) λ_{max}–K relationship, due to the steep rise of the polarization curve toward the blue. There are two exceptions: SN 2002fk and SN 2007af, which are consistent (within the errors) with the Galactic stars sample and have λ_{max} of ~ 0.44 μm and ~ 0.74 μm, respectively (Table A.1).

Cikota et al. (2017c) noted that some post-AGB stars (proto-planetary nebula, PPN) have polarization curves rising toward the blue, which are produced by CSM scattering (Oppenheimer et al., 2005). These polarization curves are remarkably similar to those observed toward highly reddened SNe Ia. They suggested that these polarization curves observed toward highly reddened SNe Ia might also be produced by CSM dust scattering. Furthermore, these SNe Ia might explode within a PPN. The main caveat is that if the polarization is produced by scattering, the polarization angles, which carry the geometrical imprint of the dust distribution in the PPN, are expected to be randomly orientated, while the observed polarization angles in sightlines of highly reddened SNe Ia show an alignment with the structure of their host galaxies, probably as a consequence of dust-grain alignment along the local magnetic field (Patat et al. 2015, see also Hoang 2017a).

3.7.2. $R_V - \lambda_{max}$ relationship

Serkowski et al. (1975) found that λ_{max} is correlated with the ratios of color excess, for example, $E(V-K)/E(B-V)$, and thus to the total-to-selective extinction ratio R_V. They found that $R_V = 5.5\,\lambda_{max}$, where λ_{max} is in μm. Whittet & van Breda (1978) deduced $R_V = (5.6 \pm 0.3)\lambda_{max}$ using a sample of carefully selected normal stars and therewith confirmed the result by Serkowski et al. (1975).

Clayton & Mathis (1988) confirmed that the λ_{max}–R_V relationship is real, and derived R_V = (-0.29 ± 0.74) + (6.67 ± 1.17)λ_{max} using a modified extinction law in which they forced the extinction to zero at infinite wavelengths. They also concluded that the variations in λ_{max} are produced by the dust grains' size distribution and not by a variation in the alignment of the dust grains.

However, our sample of anomalous extinction sightlines does not show any significant correlation between λ_{max} and R_V. The correlation coefficient is $\rho \leq 0.26$. The λ_{max} values are higher than expected from the λ_{max}–R_V relationship given in Whittet & van Breda (1978), for instance.

The most likely explanation is that while not all dust types contribute to polarization, all dust types do contribute to extinction, and thus to the R_V value. The polarization curve mainly depends on the dust grain size distribution of silicates because magnetic alignment is more efficient for silicates than, for instance, for carbonaceous dust grains (Somerville et al., 1994).

It has been shown in previous works that there is not necessarily a correlation between R_V and λ_{max}. Whittet et al. (1994) measured linear polarization toward the Chamaeleon I dark cloud and found only a weak correlation between R_V and λ_{max}. Whittet et al. (2001) presented observations of interstellar polarization for stars in the Taurus dark cloud and found no clear trend of increasing R_V with λ_{max} (see their Fig. 9). Their sample shows normal optical properties, with $R_V \sim 3$, while the λ_{max} values are higher than expected from observations toward normal stars (e.g., Whittet & van Breda, 1978). They suggested that the poor R_V–λ_{max} correlation can be explained by dust grain size dependent variations in alignment capabilities of the dust grains. The LIPS data (Bagnulo et al., 2017) do not follow any R_V–λ_{max} relationship either.

Another possibility is that the R_V values presented in Mazzei & Barbaro (2011) are lower than the true values. The CCM R_V values (listed in Table 3.4) were determined by best-fitting the IR observations with the CCM law (Table 1 in Mazzei & Barbaro 2011), and are consistent with estimates of R_V values following the methods in Fitzpatrick (1999a). The R_V values in Table 3.4 (taken from Table 4 in Mazzei & Barbaro 2011) were determined by best-fitting the whole extinction curve with the WD01 model (see Mazzei & Barbaro, 2011). It is important to note that Fitzpatrick & Massa (2007) showed that the relations between R_V and UV extinction can arise from sample selection and method, and that there is generally no correlation between the UV and IR portions of the Galactic extinction curves.

Wegner (2002) presented 436 extinction curves covering a wavelength range from UV to near-IR, including seven stars from our subsample: HD 14357, HD 37061, HD 54439, HD 78785, HD 96042, HD 152245, and HD 226868. They determined the R_V values by extrapolating the ratio E(λ-V)/E(B-V) to 1/λ=0, where the extinction should be zero, and found slightly higher values. The $E(B-V)$ and R_V values determined in Wegner (2002) of seven common stars are listed in Table 3.4. The R_V values determined by Wegner (2002) are 1.4 ± 0.2 times higher than the R_V values determined in Mazzei & Barbaro (2011) by best-fitting the WD01 model to observations, and 1.2 ± 0.2 times higher than the CCM R_V values determined by best-fitting the IR observations with the CCM law. A caveat of the extrapolation method is that IR emission from possible CS shells around Be stars might suggest increased R_V values (Wegner, 2002).

We also note that the $E(B-V)$ values used in Mazzei & Barbaro (2011) (and originally taken from Savage et al. 1985) of the common stars are ~1.1 ± 0.1 times higher than those in Wegner (2002), which also contributes to lower R_V values in Mazzei & Barbaro (2011) compared to values in Wegner (2002), and that the spectral types used in Savage et al. (1985) (used in Mazzei & Barbaro 2011) are different than those in Wegner 2002 (Table 3.4). Wegner (2002) took the spectral classification from the SIMBAD database and compared the most recent estimate with the most frequent estimate. The author found that for about 60% of his sample, the most frequent and most recent spectral and luminosity classes are the same, while there is a difference of 0.05 in the spectral class for about 18%

of stars, of 0.1 for 16%, and of 0.2 spectral class for 6%. This shows that the extinction curves of the same targets, computed by different authors, are slightly different.

Figure 3.8 shows the R_V values determined by best-fitting the IR extinction curves with the CCM law as a function of $\lambda_{\max}$ compared to the values determined from the best fit of the observed extinction curves by the WD01 models (both taken from Mazzei & Barbaro 2011) and the R_V values for seven common stars from Wegner (2002), determined by the extrapolation method (see Table 3.2). Four of seven stars with R_V values determined by Wegner (2002) lie within the Whittet & van Breda (1978) R_V relationship, while most of the stars with R_V values determined by best-fitting the CCM law and the WD01 model (Mazzei & Barbaro, 2011) are below the Whittet & van Breda (1978) relationship.

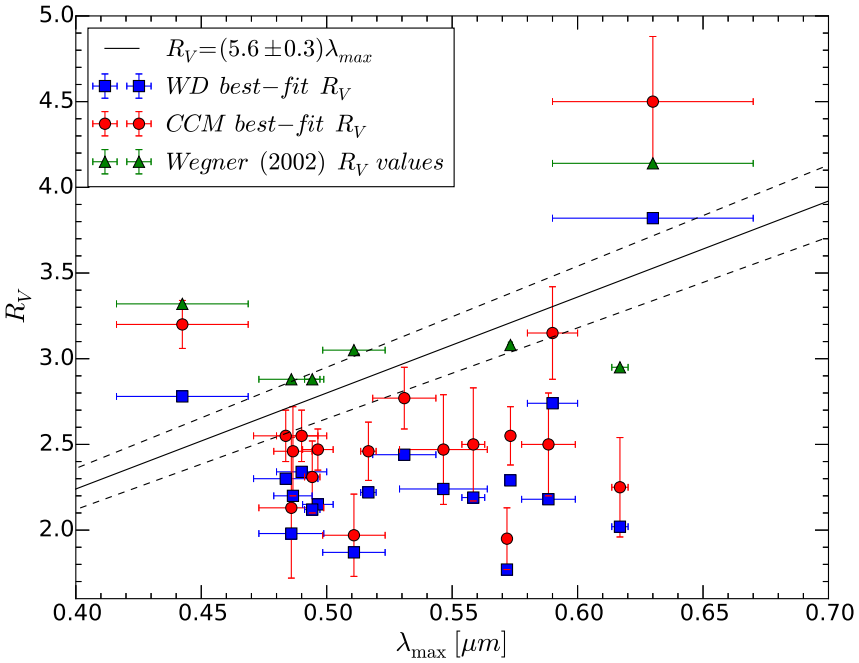

Figure 3.8.: R_V–$\lambda_{\max}$ plane. The red dots mark the CCM R_V values as a function of $\lambda_{\max}$ determined by best-fitting the IR extinction curves with the CCM extinction law, the blue dots mark the R_V values determined by fitting the WD01 model to all observations, and the green triangles mark the R_V values from Wegner (2002) determined by the extrapolation method (see Table 3.2). The black line shows the R_V relationship from Whittet & van Breda (1978) and its 1σ uncertainty.

3.7.3. $p_{\max}$ – $E(B-V)$ relationship

There is no clear correlation between the maximum polarization and color excess. Figure 3.9 shows the Serkowski et al. (1975) and Whittet et al. (1992) sample in the $p_{\max}$ – $E(B-V)$ plane compared to our sample of stars with anomalous sightlines. The scattered data in the plot shows no dependence of maximum polarization on reddening, but there is an upper limit depending on reddening (Serkowski et al., 1975) that is rarely exceeded: $p_{\max}(\%) = 9.0\ E(B-V)$ mag. We calculated the mean of the ratio $\langle p_{max}/E(B-V)\rangle$ for the different samples: $\langle p_{max}/E(B-V)\rangle$=6.2 ± 3.8 % mag^{-1} for the Serkowski et al. (1975) sample, $\langle p_{max}/E(B-V)\rangle$=4.6 ± 3.4 % mag^{-1} for the Whittet et al. (1992) sample, and $\langle p_{max}/E(B-V)\rangle$= 3.3 ± 2.1 % mag^{-1} for our sample. The low $\langle p_{max}/E(B-V)\rangle$ ratio of our

sample might also indicate that the silicate dust grains do not align as efficiently as the Serkowski et al. (1975) and Whittet et al. (1992) samples, but because of the small number of stars in our sample, we cannot draw such conclusions with high certainty. Another possible reason for the low ratios of $p_{max}/E(B-V)$ is a small angle between the direction of the magnetic field and the line of sight, that is expected to reduce $p_{max}/E(B-V)$, as discussed in previous works, for example, Hoang et al. (2014).

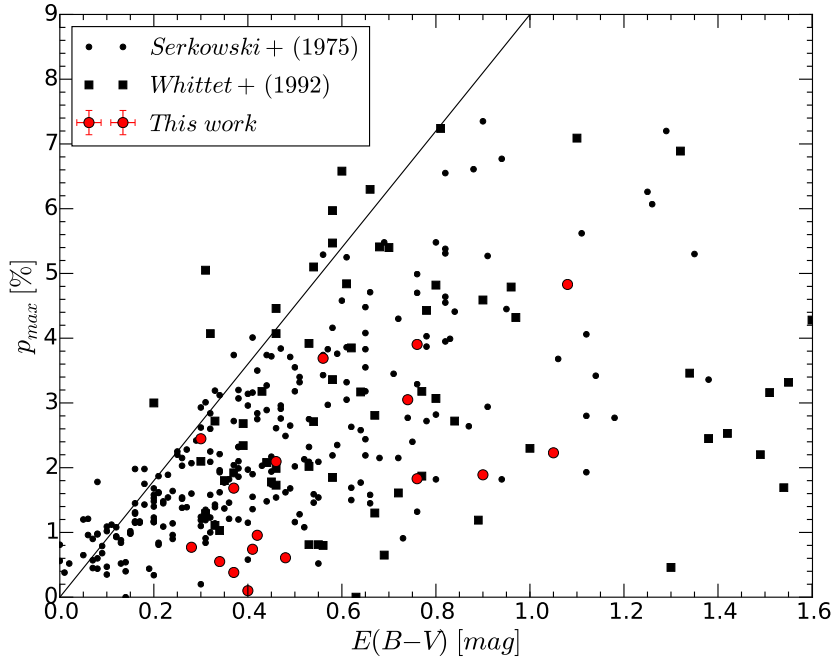

Figure 3.9.: Maximum interstellar polarization p_{max} vs. color excess $E(B-V)$ of stars from Whittet et al. 1992 (black squares), Serkowski et al. 1975 (black circles from), compared to our observed sample (red circles). The straight line denotes the upper limit $p_{max}(\%) = 9.0\ E(B-V)$ mag defined by Serkowski et al. (1975).

3.7.4. Which dust properties determine $\lambda_{\rm max}$?

For a given grain shape and dust optical constant, Equation (3.16) reveals that the polarization spectrum is determined by $dn/da \times f_{\rm ali}$, which is considered the size distribution of aligned grains, while the extinction (i.e., R_V) in Eq. (3.15) is only determined by dn/da. Thus, both a change in dn/da and $f_{\rm ali}$ affect the polarization spectrum.

Our simultaneous fitting to the extinction and polarization demonstrate that both grain alignment and size distribution are required to change in order to reproduce the variation of $\lambda_{\rm max}$ (see Figs. 3.6 and 3.7). However, the change in grain alignment is more prominent. Fig. 3.7 shows that the alignment of small grains required to reproduce $\lambda_{\rm max} = 0.45\,\mu$m is an order of magnitude higher than that required for $\lambda_{\rm max} = 0.55\,\mu$m. We note that the modeling here is carried out for a constant R_V. In the lines of sight where grain growth can take place, resulting in the increase of R_V, we expect both grain evolution and alignment to contribute to the variation of $\lambda_{\rm max}$ and K.

To test whether grain evolution can reproduce the observed data, we reran our simulations for the same six models by fixing the alignment function that reproduces the "standard" polarization curve with typical value $\lambda_{\rm max} = 0.55\,\mu$m. The size distributions dn_j/da was varied. We found that

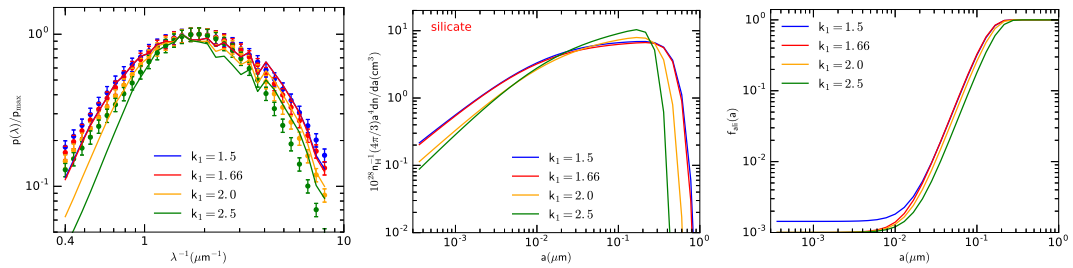

Figure 3.10.: Polarization curves (left panel), best-fit size distribution (middle panel), and best-fit alignment function (right panel) for the different values of k_1 , where $K = k_1\lambda_{\rm max} + 0.01$. The value of $\lambda_{\rm max} = 0.55\,\mu$m is fixed.

the variation of dn/da can reproduce the observed data to a satisfactory level only for the cases of $\lambda_{\rm max} = 0.51 - 0.55\,\mu$m, that is, $\lambda_{\rm max}$ is not much different from the standard value. Meanwhile, the fit to the models is poor when $\lambda_{\rm max}$ differs much from the typical value of $0.55\,\mu$m. This indicates that grain evolution alone cannot explain the wide range of $\lambda_{\rm max}$ that is observed.

3.7.5. Why is K correlated to $\lambda_{\rm max}$?

The dependence of K on $\lambda_{\rm max}$ appears to be an intrinsic property of the polarization. The Serkowski curve shows that a smaller K corresponds to a broader polarization profile. From the inverse modeling for a constant R_V, we find that the grain alignment function becomes broader (narrower) for lower (higher) values of $\lambda_{\rm max}$ as well as of K. This feature can be explained as follows. Each aligned grain of size a produces an individual polarization profile $C_{\rm pol}$ with the peak at $\lambda \sim 2\pi a$ (see Fig. 1 in Hoang et al. 2013). The polarization spectrum is the superimposition/integration over all grain sizes that are aligned. When the alignment function is broader, the superposition produces a broader polarization profile, or smaller K.

3.7.6. Deviation of K from the standard value

To explore the dust properties underlying the deviation of K from the typical value, we performed the fit for a fixed $\lambda_{\rm max}$ and varying k_1 (in $K = k_1\lambda_{\rm max} + 0.01$).

Figure 3.10 shows the best-fit models (left panel), alignment function (right panel), and size distribution (middle panel) for a fixed $\lambda_{\rm max} = 0.55\,\mu$m and varying K. We find that the increase of K is produced by the decrease of large Si grains ($a > 0.2\,\mu$m). At the same time, the alignment is shifted to the larger size when K increases, which is shown in Fig. 3.7 when $\lambda_{\rm max}$ (and K) is increased.

3.7.7. Relationship between $R_{\rm Si}$ and $\lambda_{\rm max}$

Figure 3.11 shows the dependence of $R_{\rm Si}$ on $\lambda_{\rm max}$. There is a slight decrease of $R_{\rm Si}$ with increasing $\lambda_{\rm max}$. This is straightforward because small grains are required to reproduce higher polarization in the UV when $\lambda_{\rm max}$ decreases.

The values $R_{\rm Si}$ from Fig. 3.4 were inferred from fitting only the extinction data (Mazzei & Barbaro, 2011). Thus, there is no direct relation between such inferred $R_{\rm Si}$ and $\lambda_{\rm max}$ that describes the polarization curve. It is known that a dust model that fits the extinction well may not reproduce the polarization data (e.g., dn/da $\sim$ a$^{-3.5}$ law by Mathis et al. 1977; see, e.g., Kim & Martin 1995; Draine & Fraisse 2009).

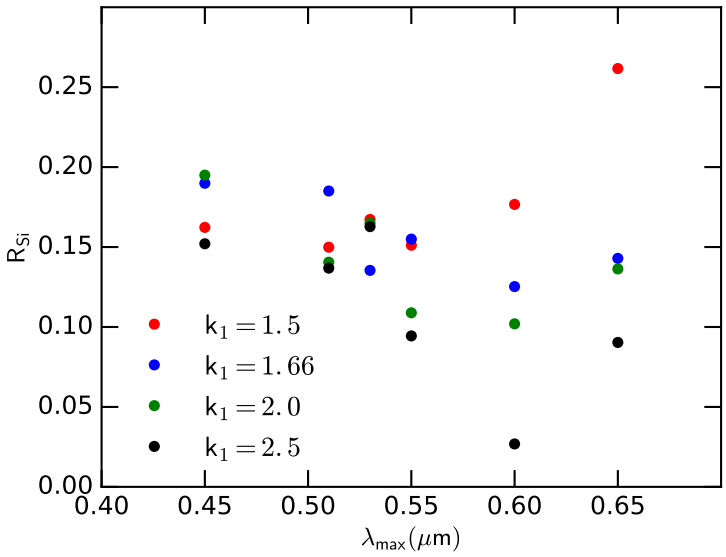

Figure 3.11.: Relative ratio of Si abundance in very small and large grain sizes vs. λ_{max}.

The scale difference between R_{Si} shown in Fig. 3.4 and Fig. 3.11 arises from the different ways of modeling. In Mazzei & Barbaro (2011), to reproduce the extinction curve with low R_V values, dust grains were found to be rather small ($\lesssim 0.05\ \mu m$), leading to a high value of R_{Si}. Such a dust model cannot reproduce the polarization data with standard λ_{max} that requires aligned large grains (i.e., larger $0.1\ \mu m$). Our best-fit models that simultaneously fit extinction and polarization data provide different size distributions that have large grains, leading to smaller R_{Si}.

3.8. Summary and conclusions

We investigated the linear polarization of 17 sightlines to Galactic stars with anomalous extinction laws and low total-to-selective visual extinction ratio, R_V, selected from the Mazzei & Barbaro (2011) sample, and adopted a simple dust model that can reproduce the observed sightlines with low R_V values and normal polarization curves. To do this, we adopted the Weingartner & Draine (2001) dust model and a picket-fence alignment model to compute extinction and polarization curves (see Sect. 3.6.2.2). Our results are summarized below.

1. Galactic stars with anomalous extinction sightlines, with low R_V values, show "normal" polarization curves with a mean $\lambda_{max} \sim 0.53 \mu m$. This can be explained by considering that not all dust that contributes to extinction also contributes to polarization. The polarization mainly depends on the dust grain size distribution of silicates, because grain alignment is more efficient for silicates than, for instance, for carbonaceous dust grains (Somerville et al., 1994), whereas R_V is strongly dependent on carbonaceous grains too.

2. There is no significant R_V–λ_{max} relation in our sample (Fig. 3.8). The λ_{max} values in our sample are higher than compared to normal stars that follow the empirical R_V–λ_{max} relationship described by Whittet & van Breda (1978), for instance.

3. Despite the low R_V value, there is no similarity between the polarization curves in the investigated sample and the polarization curves observed in reddened SNe Ia with low R_V values.

The polarization curves are consistent with a sample of Galactic stars observed by Whittet et al. (1992) within 3σ (Fig. 3.2).

4. The Serkowski parameters K and $\lambda_{\rm max}$ are correlated. However, we find a steeper slope (K = -1.13 ± 0.34 + (4.05 ± 0.64)$\lambda_{\rm max}$) in our sample than in the empirical relationship found by Whittet et al. (1992), for example.

5. Simulations show that to reproduce a polarization curve with the normal $\lambda_{\rm max}$ and low R_V, there must be a population of large interstellar silicate grains of size $a \geq 0.1\,\mu$m. This is different compared to results by Mazzei & Barbaro (2008, 2011), who only best-fit the extinction curves and found a lack of such large Si grains, but did find large carbonaceous grains. Moreover, variations in grain alignment and size distribution together are required to reproduce the variation in $\lambda_{\rm max}$ for a fixed, low, R_V value. However, a change in grain alignment has a greater effect.

6. By comparing the R_V values of the sample here considered with those in Wegner (2002) for a subset of our stars, we find some differences that are probably due to a different spectral classification and/or luminosity class adopted to derive their extinction curves (see Sect. 3.7.2). The $\lambda_{\rm max}$ value that we measure and the deviation from the empirical R_V–$\lambda_{\rm max}$ relationship may also suggest a spectral misclassification of some stars by Savage et al. (1985).

7. The K–$\lambda_{\rm max}$ relation appears to be an intrinsic property of the polarization. Simulations show that for a fixed R_V, the grain alignment function becomes narrower (broader) for a lower (higher) value of $\lambda_{\rm max}$ and K (see Sect. 3.7.5).

8. An increase in Serkowski parameter K and deviation from the standard value in the K–$\lambda_{\rm max}$ plane can be reproduced by a decreasing contribution of large Si grains (Fig. 3.10).

Acknowledgements

We thank an anonymous reviewer for useful comments that significantly improved the paper. This work is partially based on observations collected at the German-Spanish Astronomical Center, Calar Alto, jointly operated by the Max-Planck-Institut für Astronomie Heidelberg and the Instituto de Astrofisica de Andalucia (CSIC). T.H. acknowledges the support from the Basic Science Research Program through the National Research Foundation of Korea (NRF), funded by the Ministry of Education (2017R1D1A1B03035359). This work is based on observations made with ESO Telescopes at the Paranal Observatory under Program ID 094.C-0686, and partially based on observations collected with the Copernico telescope (Asiago, Italy) of the INAF - Osservatorio Astronomico di Padova. We also thank P. Ochner for taking some observations with AFOSC in service time. Some of the data presented in this work were obtained from the Mikulski Archive for Space Telescopes (MAST). STScI is operated by the Association of Universities for Research in Astronomy, Inc., under NASA contract NAS5-26555. Support for MAST for non-HST data is provided by the NASA Office of Space Science via grant NNX09AF08G and by other grants and contracts. ST acknowledges support from TRR33 "The Dark Universe" of the German Research Foundation.

4. Common continuum polarization properties: a possible link between proto-planetary nebulae and Type Ia Supernova progenitors

The content of this chapter has been published in:
Cikota, A., Patat, F., Cikota, S., Spyromilio, J., & Rau, G.
Monthly Notices of the Royal Astronomical Society, Volume 471, Issue 2, p.2111-2116

4.1. Introduction

Supernovae Ia (SNe Ia) are used as cosmological probes to measure the expansion of the universe. We are confident that a SN Ia is an exploding C/O White dwarf (WD), close to the Chandrasekhar mass limit ($\sim$ 1.38 $M_{\odot}$, Arnett 1969; Nomoto 1982). However, the evolutionary paths and specific progenitor systems are not known. The two main progenitor scenarios are the single degenerate (SD) model, in which a WD gains mass from a nondegenerate star through accretion (Whelan & Iben, 1973), and the double-degenerate (DD) model where two WDs merge (Iben & Tutukov, 1984).

Since the SD and DD models imply different circumstellar environments, studies of dust properties along the lines of sight of SNe Ia may provide insights on the nature of the progenitor system. SNe Ia observations have shown that dust along lines of sight to highly reddened SNe are characterized by low total-to-selective extinction values, $R_V \lesssim 2$ (see Cikota et al. 2016 for a review), compared to the average R_V of $\sim$ 3.1 in the Milky Way (Schlafly et al., 2017). Low R_V values can be produced by an enhanced abundance of small dust grains (Draine, 2003), or arise as a consequence of scattering (Wang, 2005; Patat, 2005).

Patat et al. (2015) found that highly reddened SN 1986G, SN 2006X, SN 2008fp and SN 2014J, all characterized by low R_V values (deduced from spectrophotometry), also showed peculiar non-time-variable continuum polarization wavelength properties (hereafter, we will use the term polarization curve to describe these) with peak polarization values in the blue ($\lambda_{max} \lesssim 0.4\mu m$). We expect that the wavelength of peak polarization, λ_{max}, depends on the dust grain size distribution of aligned grains (Kim & Martin, 1994). For an enhanced abundance of aligned small dust grains, λ_{max} shifts to shorter wavelengths, while for an enhanced abundance of aligned large dust grains to longer wavelengths (Serkowski et al., 1975).

It remains unclear whether the peculiar polarization curves that host galaxy dust exhibit along the lines of sight to SNe Ia is associated to the SN itself or the more general environment. Possible explanations are that the composition of interstellar dust in SNe Ia host galaxies (or at least in some of them) is different from the dust in our Galaxy, or that there is circumstellar dust with an enhanced abundance of small grains, possibly ejected from the progenitor system before the explosion.

There is evidence that circumstellar material (CSM) might contribute to the extinction of some SNe Ia. Patat et al. (2007) undertook high-resolution spectroscopy of the highly reddened SN 2006X. From observed time evolution of the Na I D doublet lines, which they attribute to changes in the CSM

ionization conditions induced by the variable supernova radiation field. Similarly, Simon et al. (2009) observed variable sodium absorption in SN 2007le, a low-extinction SNe Ia with E(B-V) ∼ 0.27 mag. Furthermore, Blondin et al. (2009) measured changes in the equivalent width of the Na I lines in SN 1999cl and SN 2006X. This detection of variable Na I D features in two of the most reddened SNe suggests that the change in equivalent width (EW) with time might be associated with circumstellar or interstellar absorption (Blondin et al., 2009). However, no such variation is detected in the highly reddened SN 2003cg (Elias-Rosa et al., 2006).

Another possibility is that light scattering on nearby dust contributes to both, low R_V values, and a different polarization curve. Patat et al. (2015) illustrate, assuming that the scattering and the dichroic components are parallel, that the polarization curve of SN 2006X may have a component induced by Rayleigh scattering in addition to the standard Serkowski component (see their Fig. 6).

We note that no time variability in R_V, nor in polarization (see discussion in §4.4 by Patat et al. 2015) is observed in these objects. Yang et al. (2017) used *HST* observations to map the ISM around SN 2014J through light echoes. They observed two echo components: a diffuse ring distributed over distances of ∼ 100-500 pc, and a luminous arc, produced through dust scattering of different grain sizes, at a distance of 228 ± 7 pc from the supernova. From the wavelength dependence of the scattering optical depth, they found that the arc favors small $R_V \sim 1.4$ values, which is consistent with the R_V measured along the direct line of sight, while the ring is consistent with a common Milky Way $R_V \sim 3$ value.

Hoang (2017b) fit a two-component (interstellar absorption and circumstellar scattering) dust model to photometric and (spectro)polarimetric observations of SN 1986G, SN 2006X, SN 2008fp and SN 2014J, to investigate the grain size distribution and alignment functions of dust along those lines of sight. The SN 1986G and SN 2006X observations could be reproduced assuming an enhanced abundance of small silicate grains in the interstellar dust only, while in the case of SN 2014J, a contribution by circumstellar (CS) dust scattering was required. In the case of SN 2008fp, Hoang (2017b) found that the alignment of small dust grains must be as efficient as that of large grains, but the existence of CS dust could not be ascertained and suggested that the enhanced abundance of small silicate grains might be produced by cloud collisions driven by the SN radiation pressure. We note that strong SN radiation may also induce efficient alignment of small grains via the radiative torque mechanism.

In this work we report a striking similarity between the polarization curves observed in proto-planetary nebulae (PPN) and those of highly-reddened SNe Ia (Fig. 4.1), and we discuss the possible implications of this finding on SNe Ia progenitors.

In section § 2 we describe the data, explain the methods and show the results, in section § 3 we discuss the results, while section § 4 summarizes our conclusions.

4.2. Data, methods and results

Bieging et al. (2006) presented linear spectropolarimetry of 21 asymptotic giant branch (AGB) and 13 post-AGB stars (i.e., proto-planetary nebulae, PPNe), and two R CrB stars. The polarization degree of AGB stars is smaller than that of PPNe (see their Table 1 and Figure 1), consistent with the findings of Johnson & Jones (1991) that polarization increases as the evolutionary state progresses from early AGBs to PPNe, while the subsequent planetary nebula (PN) stages show lower polarization degrees than PPNe. Bieging et al. (2006) investigated the time variability in polarization degree of AGB stars and PPNe, finding no systematic correlation between variations in polarization and the visible luminosity in AGB stars. Four of five PPNe, which were observed at multiple epochs, showed no

Table 4.1.: Serkowski parameters and polarization angles

	Serkowski parameters					
Name	λ_{max}(Å)	P_{max}(%)	K	$P_{4000Å}$(%)	θ (°)	dθ/dλ (deg μm^{-1})
IRAS 05341+0852	1952 ± 202	25.03 ± 2.58	0.94 ± 0.09	15.43 ± 2.77	146.3 ± 0.4	3.3 ± 0.5
IRAS 18095+2704	2862 ± 53	10.19 ± 0.12	1.07 ± 0.03	9.04 ± 0.16	15.1 ± 1.8	-19.0 ± 1.5
IRAS 07134+1005	3570 ± 38	5.53 ± 0.06	2.48 ± 0.06	5.36 ± 0.07	148.1 ± 4.8	32.0 ± 5.0
IRAS 22272+5435	3267 ± 341	4.14 ± 0.25	1.04 ± 0.17	3.97 ± 0.3	10.4 ± 1.9	-17.5 ± 2.3

variation in polarization, indicating that they have stable dust distribution evolving on timescales longer than a few years. Bieging et al. (2006) group their sample of 13 PPNe in two groups:

(i) objects with a nearly constant polarization (with fractional variation within ∼10%) across the observed wavelength range (∼4200–8400Å), and a nearly constant polarization angle (± 10°);

(ii) IRAS 05341+0852, IRAS 07134+1005, IRAS 18095+2704, and IRAS 22272+5435 – objects with significantly rising polarization from the red (∼ 8000Å) to the blue (∼ 4000Å), while the polarization angle remains nearly constant (± 10°). Those objects have similar polarization curves to SNe Ia. The polarization curves are shown in Figure 4.1. Bieging et al. (2006) argue that those objects are similar to IRAS 04296+3429 and IRAS 08005-2356. Models by Oppenheimer et al. (2005) suggest that the objects present a point-symmetric morphology and evacuated lobes, respectively, and that the increasing polarization towards the blue indicates a sharply peaked grain distribution of scattering particles. However, IRAS 04296+3429 and IRAS 08005-2356 have strongly wavelength dependent polarization angles (see Fig. 1 in Oppenheimer et al. 2005).

To parameterize the polarization curves in Bieging et al. (2006), and compare them to those derived for SNe Ia and a sample of Galactic stars (Whittet et al., 1992), we fit to the digitized data the empirical Serkowski curve (Serkowski et al., 1975):

$$\frac{P(\lambda)}{P_{max}} = \exp\left[-Kln^2\left(\frac{\lambda_{max}}{\lambda}\right)\right] \tag{4.1}$$

where λ_{max} is the wavelength at the peak polarization P_{max}, and K depends on the width of the polarization curve (lower Ks widen the curve). We also calculate the polarization angle, θ, and its wavelength dependency through the average slope $d\theta/d\lambda$. The results are given in Table 4.1, and shown in Fig. 4.2.

4.3. Discussion

Fig. 4.1 compares the continuum polarization curves of Type Ia SN 2006X and SN 2014J (Patat et al., 2015) with those of a Galactic star with (HD 141318; R_V = 1.95 ± 0.18, $P_{max} \sim 0.57\mu m$, Cikota et al. in prep.), and four PPNe Bieging et al. (2006).

The similarity between the polarization curves observed in SNe Ia and PPNe is intriguing (see Fig. 4.1): both SNe Ia and PPNe have steep polarization curves rising towards blue wavelengths. We know of no other stellar object showing such polarization curves in our Galaxy. For PPNe we know that the bulk of polarization is produced by CS dust scattering (Oppenheimer et al., 2005). This leads to the interesting possibility that also in SNe Ia sight lines, polarization produced by scattering of CS dust contributes to the observed continuum polarization rising towards blue wavelengths.

As discussed earlier, there may be different explanations for the polarization curves observed in highly reddened SNe Ia. They may be caused by interstellar host galaxy dust characterized by an increased abundance of small particles. Perhaps the strongest argument against our interpretation is the remarkably constant (wavelength independent) polarization angles with slopes of dθ/dλ = -0.8 ±

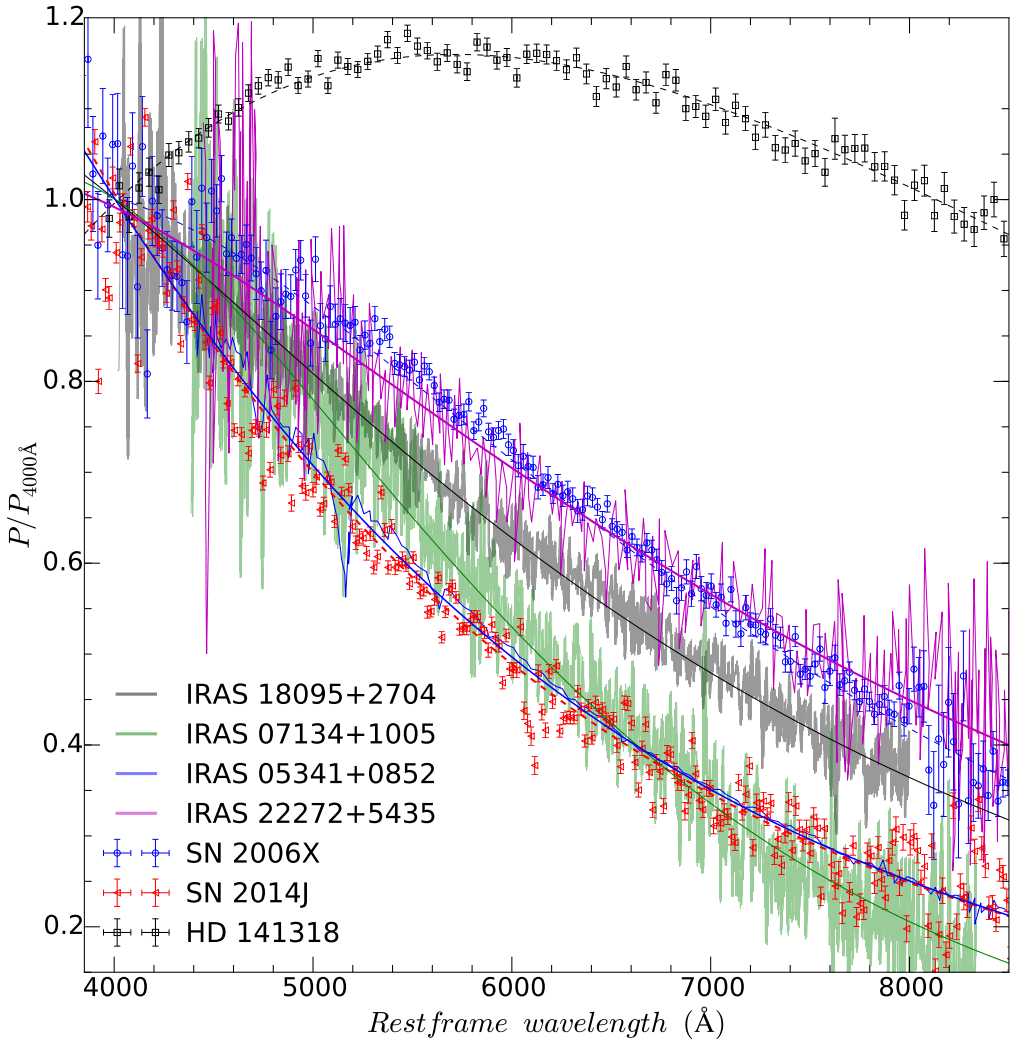

Figure 4.1.: Comparison between polarization curves of SN 2006X and SN 2014J (Patat et al., 2015), HD 141318 (Cikota et al., in prep.), and four PPNe (Bieging et al., 2006). HD 141318 is a star with $R_V = 1.95 \pm 0.18$, but has a normal polarization curve with $P_{max} \sim 0.57 \mu m$, while the SNe Ia and PPNe have polarization curves steeply increasing towards blue wavelengths.

0.5, 1.7 ± 1.4, and -0.9 ± 1.6 deg μm^{-1} for SN 2006X, SN 2008fp and SN 2014J respectively (Patat et al., 2015), which would indicate that all the dust grains are aligned in the same direction due to the host galaxy magnetic field. SN 1986G exhibited a slight wavelength dependence in the polarization angle with a slope of dθ/dλ = 4.5 ± 1.9 deg μm^{-1} (Hough et al., 1987), that might be explained by different polarization angles of various interstellar clouds along the line of sight. Zelaya et al. (2017b) has presented a study of continuum spectropolarimetry of 19 SNe Ia. 8 of 12 SNe (SN 2006X, SN 2014J, SN 2008fp, SN 2010ev, SN 2007le, SN 2002bo, SN 2007fb and SN 2003W, sorted according to polarization degree, from highest) which show Na I D (a known tracer of gas, metals and dust, see e.g., Fig. 6 in Richmond et al. 1994) at their host galaxy velocities, have higher polarization values with polarization curves rising towards the blue ($\lambda_{max} \lesssim 0.4 \mu m$). Moreover, their polarization angles appear to be wavelength independent (within the noise) and aligned with their host galaxy spiral arms, i.e., along the local magnetic field (Scarrott, 1996).

On the other hand, the PPNe exhibit mild wavelength dependencies in their polarization angles

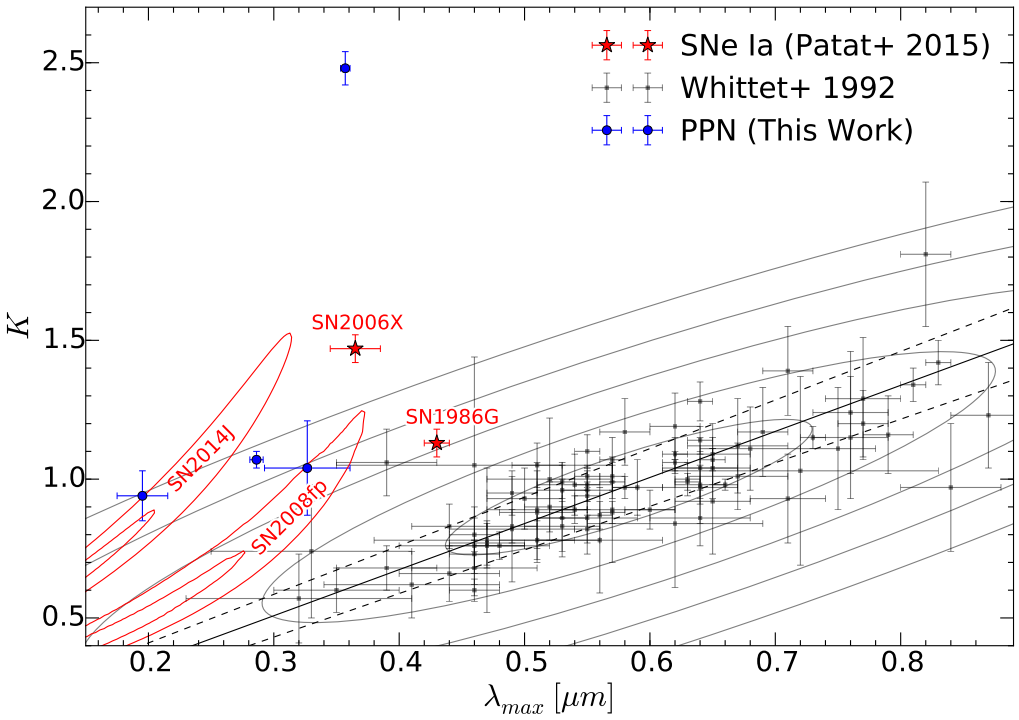

Figure 4.2.: SNe Ia (Patat et al., 2015) and PPNe compared to a sample of Milky Way stars (Whittet et al., 1992) in the $\lambda_{\max}$–K plane. The solid line is the empirical $\lambda_{\max}$–K relation derived by Whittet et al. (1992). Both, SNe Ia and PPNe have steeper curves (with higher K values) rising towards blue ($\lambda_{\max} \lesssim 0.4 \mu m$) compared to normal stars in the Milky Way.

(see Table 4.1). IRAS 05341+0852 has a slope dθ/dλ = 3.3 ± 0.5 deg μm^{-1}, which is comparable to SN 1986G, while IRAS 18095+2704, IRAS 07134+1005, and IRAS 22272+5435 have slopes between -19 and +32 deg μm^{-1}. IRAS Z02229+6208 and IRAS 22223+4327 from the first (i) group have as well constant polarization angles of 1.5 ± 1.3 and 3.9 ± 3.0 deg μm^{-1} respectively (see Fig. 1 in Bieging et al. 2006), however, their polarization curves are as well nearly constant, and thus not similar to the polarization curves of SNe Ia sight lines.

The level of continuum polarization is comparably high for both PPNe and SNe Ia. The polarization degree at 4000Å is 7.8 ± 0.2 %, 6.6 ± 0.1 %, 5.1 ± 0.1 %, and 2.6 ± 0.1 % for SN 2006X, SN 1986G, SN 2014J and SN 2008fp, respectively (Table 1 in Patat et al., 2015), and 15.4 ± 2.8 %, 9.0 ± 0.2 %, 5.4 ± 0.1 %, and 4.0 ± 0.3 % for IRAS 05341+0852, IRAS 18095+2704, IRAS 07134+1005, and IRAS 22272+5435, respectively (Table 4.1). Johnson & Jones (1991) found that the observed *UBVri* polarization degree depends of the evolutionary stage of the objects: the maximum polarization reaches 3% for red giants, 7% for late-AGB stars and 40% for PPNe, while young PNe show maximum polarizations up to 6%, and true PNe only up to $\lesssim$ 3%. Johnson & Jones (1991) explain the differences seen in various evolutionary stages as a consequence of the circumstellar dust shell becoming more dense and aspherical as the star evolves towards a PPN, and dust dissipates after the stage of a PPN towards a PN.

All four PPNe from second group, IRAS 05341+0852, IRAS 18095+2704, IRAS 07134+1005, and IRAS 22272+5435 have been observed as part of a *Hubble Space Telescope (HST)* survey of PPN candidates (Ueta et al., 2000). They show a bright central star embedded in a faint, optically thin, elliptically elongated shell (SOLE nebulae), in contrast to the bipolar form (DUPLEX nebula) which

is optically thick . The global polarization angle (measured on unresolved, ground-based images) is perpendicular to the major axes of IRAS 05341+0852 and IRAS 18095+2704 (see their Fig. 1). This is fully consistent with the polarization being generated by scattering and carrying the geometrical imprint of the dust distribution in the PPN. IRAS 07134+1005, and IRAS 22272+5435 are not that well resolved and have low ellipticities, so that such a comparison was not possible. This has an immediate consequence: in a sample of PPNe, the polarization angle is expected to be randomly distributed. On the other hand, the polarization observed in highly-reddened SNe Ia shows a clear alignment along the local magnetic field. This discrepancy remains an open issue with the association proposed here (see also Patat et al. 2015 and Hoang 2017b for more detailed discussions).

The sodium lines, Na I D, detected in the reddened SNe Ia spectra (Zelaya et al., 2017b), do not all necessarily originate in the ISM of the SN host galaxies. e.g., in the case of SN 2014J there is a number of components at different velocities (Patat et al., 2015). As Phillips et al. (2013) (see their § 4.6) suggest, high Na abundances might be produced in nova outbursts in the SD scenario. They suggest that the "blueshifted" Na I profiles (see Sternberg et al., 2011; Foley et al., 2012b), and large column densities might imply a progenitor system with an AGB star phase (Phillips et al., 2013, § 4.6). In fact, SN 1986G, SN 2006X and SN 2008fp (Patat et al., 2015), as well as SN 2002bo, SN 2007fb, and SN 2007le (Zelaya et al., 2017b) have Na I blueshifted lines (Sternberg et al., 2011; Foley et al., 2012b). For the remaining SN 2014J, SN 2010ev and SN 2003W, there are no measurements in Sternberg et al. (2011) nor Foley et al. (2012b).

In the case of SN 2008fp and SN 2006X there is clear evidence that most of the gas along the line of sight is in a molecular cloud with strong CN features (Cox & Patat, 2008; Patat et al., 2015). It is also interesting to note that the time-varying features in SN 2006X did show velocities between 50 and 100 km s^{-1} (Patat et al., 2007). The time-varying features were small in terms of EW, definitely smaller than the main saturated feature arising within the molecular cloud (see Fig. 1 in Patat et al., 2007). Thus, in this case, the closest time-varying material certainly does not explain the bulk of extinction. Whether the main saturated component, with a velocity difference of 50-100 km s^{-1} relative to the variable features, can be attributed to a hypothetical PPN or a more distant cloud can not be distinguished from the observations. On the other hand, SN 1986G and SN 2014J have a number of Na I and Ca II components at different velocities of comparable EW (see e.g., Fig. 5 in Patat et al., 2015), and do not show traces of CN.

Furthermore, Na I lines have also been observed in PPNe with bright and asymmetric circumstellar nebulae. For instance, Klochkova & Panchuk (2016) observed splitting and asymmetry of strong absorption lines, particularly of Ba II (while iron absorption lines are not split nor asymmetric), in post-AGB stars with C-rich circumstellar envelopes. V5112 Sgr, which was observed during multiple nights, also shows time-variability of the shape and positions of components of the split lines, in particular Ba II 4934 Å line, which shows most variability. V448 Lac shows variability in Ba II 6141 Å line. The blue component of Ba II coincides with the blue shift of the circumstellar Na I D lines, which indicates that Ba II also contains, besides a stellar component, a component that forms in the circumstellar envelope. Bakker et al. (1996) detected C_2, CN and Na I D absorption lines in HD 56126. They determined the velocities of individual components in Na I D1 and Na I D2, and distinguished their origin between photospheric, circumstellar and interstellar. The velocity difference between circumstellar and photospheric components is $\sim$ 14 km s^{-1} (see Table 6 in Bakker et al. 1996). Kipper (2007) analysed spectra of HD 161796 (a post-AGB star) and measured circumstellar and interstellar Na I D lines. The CS lines are shifted by -15.9 km s^{-1} relative to photospheric lines, and likely correspond to an expanding shell.

4.3.1. Possible implications on the SNe Ia progenitor systems

It is tempting to speculate that some SNe Ia with peculiar polarization curves exploded during a PPN phase of their companion star, and that the bulk of continuum polarization is produced by scattering from dust in a PPN, particularly because red giants, and late-AGB stars might play an important role in SNe Ia progenitor systems.

The PPN is a short phase ($\lesssim 10^4$ years) of an intermediate-mass star life, between the late AGB star and a planetary nebula (PN). The star leaves the AGB phase (i.e., the Thermal-Pulse-AGB, TP-AGB phase) once the envelope mass drops to ~ 0.01 $M_\odot$ (Blöcker, 2001; van Winckel, 2003). During the TP-phase the star may loose more than half of its initial mass (~43 % for an initial mass of 1 $M_\odot$; ~ 79% for an initial mass of 4 $M_\odot$; Marigo et al. 2013, 2017). The velocity of the circumstellar material (CSM) ejected during the AGB phase is slow ($\gtrsim 10$ km s^{-1}, see e.g., Maercker et al. 2012). Given an AGB lifetime of 1 Myr, and a ejecta velocity of 10 km s^{-1}, the material can spread to distances of up to 10 pc (see also Rau et al., 2015, 2017).

It is thought that during the PPN phase, collimated fast winds (¿150 km s^{-1}) form evacuated lobes (Oppenheimer et al., 2005; Ueta et al., 2000) in the previously ejected material. The PPN phase ends after the cool ($T_{eff} \lesssim 10^4 K$) post-AGB stellar core heats up to $\sim 3 \times 10^4 K$ and starts ionizing the surrounding material, becoming a PN.

However, the majority of PNe display morphologies that can not be explained in the context of a single-star scenario. Detailed *HST* observations of PNe revealed aspherical morphologies that can not be accounted for in a simple interacting stellar wind model. However, close binary stars might play a key role in the formation of aspherical PPNe and PNe and in shaping axisymmetric structures (Jones & Boffin, 2017). If the binary companion is sufficiently close, the AGB star will overflow its Roche lobe which leads to a poorly understood common envelope phase, and spiral-in of the companions orbit. Eventually the binary companions will merge (Jones & Boffin, 2017; Ivanova et al., 2013). Nordhaus & Blackman (2006) found that a common envelope evolution can lead to the ejection of envelope material predominantly in the orbital plane of the system, which can later be shaped by winds into bipolar structures.

We do not observe any polarization time-variability in SNe Ia. Thus, the scattering material is at least at a distance of ~ 350 AU (assuming an ejecta velocity of 10^4 km s^{-1}, and time of two months). Photoionization modeling suggests that CSM must be at a distance larger than $\sim 10^{16}$ cm from the SN explosion not to ionize Ca II, and cause Ca II time variability (Simon et al., 2009). Assuming a wind velocity of 100 km s^{-1}, it takes only ~32 years to form a cavity of that size. Also, since the SNe Ia light curve can be well approximated by a discrete duration flash time variability is expected, because at different times the light echo moves through different regions of the CSM (see Wang, 2005; Patat, 2005; Patat et al., 2006). In case of close (e.g., 0.01 ly) CSM, time variability is expected at all phases, and in case of distant (e.g., 1 ly) CSM, at late phases.

Kashi & Soker (2011) proposed a "core-degenerate" scenario that might explode as a Type Ia SN. They suggest that due to interaction of a WD – post-AGB-core system with a circumbinary disc (which gets formed during the final stages of the common envelope), the orbital separation might be much more reduced than expected due to the ejection of the common envelope alone. The small separation might lead to a merger at the end of the CE phase or short time after, while the core is still hot. After the merger, the rapidly rotating WD can collapse and explode after it looses sufficient angular momentum, which can last as long as $\sim 10^6$ years (Yoon & Langer, 2005). This might explain why we don't observe high continuum polarization in all SNe Ia. On the other hand, Kashi & Soker (2011) argue that in case of nearly equal masses of two WDs, the explosion can occur during the common envelope phase (van Kerkwijk et al., 2010). One should also consider the violent-merger

scenario between two White Dwarfs (i.e., an AGB-core and the companion WD). It is interesting to note that one fifth of all known close-binary central stars of planetary nebulae are double degenerate (Jones & Boffin, 2017). However, the explosion mechanism should be further investigated, and is beyond the scope of this paper.

4.4. Summary and conclusions

We examined spectropolarimetric data for a sample of 21 AGB and 13 post-AGB (i.e., PPNe) stars presented in Bieging et al. (2006). Our main results can be summarized as follows:

1. We found a remarkable similarity in polarization between a group of four PPNe and the continuum polarization curves observed in highly reddened Type Ia SN 1986G, SN 2006X, SN 2008fp and SN 2014J (Patat et al., 2015) (see Fig. 4.1, and Fig. 4.2). They both have steep continuum polarization curves rising towards the blue, with $\lambda_{max} \lesssim 0.4\mu m$, while the polarization angle is to a good approximation wavelength independent.

2. The polarization curves rising towards the blue wavelengths in those PPNe are explained in terms of scattering on CS dust grains (Oppenheimer et al., 2005). No other sight lines to any normal Galactic stars have similar polarization curves. This opens the intriguing possibility that also in the case of SNe Ia scattering may be playing an important role.

3. Furthermore, the similarity between the polarization curves of PPNe and SNe Ia suggests that at least some SNe Ia may be enshrouded by a PPN. However, the observed alignment along the local magnetic field which characterizes the polarization angle of SNe Ia still needs to be reconciled with the random alignment expected for PPN.

4. Close binary stars might play a key role in formation and shaping of PPNe (Jones & Boffin, 2017). We speculate that some SNe Ia might explode during the post-AGB phase, as a result of a merger between a WD and a post-AGB core companion (core-degenerate progenitor model, Kashi & Soker, 2011). Thus, the steeply rising polarization curves towards blue wavelengths, along some SNe Ia sight lines, may provide observational support for the core-degenerate progenitor model.

Acknowledgements

We would like to thank to Thiem Hoang for helpful discussions. AC thanks Dominic Bordelon and the ESO Library for preparing the BibTex file. HD 141318 was observed with ESO Telescopes at the Paranal Observatory under Programme ID 094.C-0686.

5. Linear spectropolarimetry of Type Ia Supernovae with VLT/FORS: A statistical analysis of linear polarization of the Si II line

The content of this chapter corresponds to:
Cikota, A., Patat, F., Wang, L., et al.
to be submitted.

5.1. Introduction

Type Ia supernovae are used as standard candles to measure the expansion of the Universe. Understanding their progenitor system and explosion mechanism is important in order to account for possible the systematic effects on the luminosity and hence on their reliability as cosmological probes.

Spectropolarimetry enables the investigation of the circumstellar environment by observing the continuum polarization, and to the study of the ejecta asymmetries and chemical structure, by observing the linear polarization of absorption lines, which may provide insights to conclusions on the explosion mechanism and the progenitor's nature. The mechanisms that produce the polarization observed in SN Ia are explained in Section 1.2.3.

In the previous chapter, we studied the continuum polarization and discuss possible implications on the progenitor system of SNe Ia. For more information on continuum polarization along the lines of sight to SNe Ia, see also Patat et al. (2015), Zelaya et al. (2017b) and Cikota et al. (2017c).

In this chapter we will exclusively focus on the linear polarization in the absorption lines, particularly the silicon line, because it is the most prominent polarized line, along with the Ca II triplet, which however, often is often characterized by a low signal-to-noise ratio. The statistical study is based on a sample of 35 SNe Ia observed with FORS1 (before 2005) and FORS2, mounted at the Cassegrain focus of one of the units of the ESO's Very Large Telescope.

In Sect. 5.2 we describe the instruments, the observations, and our sample of SNe Ia. In Sect. 5.3 we present the methods used to reduce the data, in Sect. 5.4 we show and discuss the results, and finally summarize the main results and conclusions in Sect. 5.5.

5.1.1. Line polarization predictions for different SN Ia explosion models

Bulla et al. (2016b) ran simulations to predict polarization signatures for the violent-merger model, which is supposed to be highly asymmetric, hence describing what can be considered as a limit case. They introduce polarization treatment into the radiative transfer simulations based on the Pakmor et al. (2012) explosion model and found that the polarization signal significantly varies with the viewing angle. In the equatorial plane of the explosion, the polarization levels will be modest, $\lesssim$1%, while at orientations out of the equatorial plane, where the departures from a dominant axis are higher, the

degrees of polarization will be higher (up to ∼1-2%), and may explain highly polarized events such as SN 2004dt.

In a similar study, Bulla et al. (2016a) predict polarization signatures for the double-detonation (from Fink et al. 2010) and delayed-detonation (from Seitenzahl et al. 2013) models of Type Ia supernovae.

In the delayed-detonation model, a White Dwarf near the Chandrasekhar mass, which accretes material from a non-degenerate companion, explodes after an episode of slow carbon burning (carbon deflagration) near the center (Khokhlov, 1991; Bulla et al., 2016a), while in the double-detonation model, the explosion in the core of a sub-Chandrasekhar WD is triggered by a shock wave following a detonation of the helium layer at the WD's surface, that has been accreted form a helium rich companion star (Fink et al., 2010).

Bulla et al. (2016a) predict modest degrees of polarization ($\lesssim 1\%$) for both explosion models, with peak continuum polarization of ∼0.1–0.3 %, and prominent line polarization, in particular the Si II 6355Å line, and no polarization across the OI 7774 Å, which is consistent with the observed values in normal SNe Ia.

5.2. Observations and data

5.2.1. Instruments and observations

Our targets were observed with the FOcal Reducer and low dispersion Spectrograph (FORS) in spectropolarimetric mode (PMOS), mounted on the Cassegrain focus of the Very Large Telescope (VLT) at Cerro Paranal in Chile (Appenzeller et al., 1998).

Two versions of FORS were built, and moved to the different telescopes since the start of VLT operations. FORS1 was installed on Antu (UT1) and commissioned in 1998, while FORS2 was installed on Kueyen (UT1) one year later. They are largely identical with a number of differences, particularly, the polarimetric capabilities were offered only on FORS1. In June 2004, FORS1 was moved to Kueyen (UT2) and FORS2 to Antu (UT1), and in August 2008 the polarimetric capabilities were transferred from FORS1 to FORS2. In April 2009, FORS1 was dismounted to make room for a new instrument, X-shooter, so that currently only FORS2 is in operation.

FORS in PMOS mode is a dual-beam polarimeter, with a wavelength coverage from ∼330 – 1100 nm. It contains a Wollaston prism, which splits a spectrum produced by the grism into two beams with orthogonal directions of polarization, the ordinary (o) and extraordinary (e) beam.

The observations of the supernovae Ia in this work were obtained with FORS1 or FORS2, a 300V grism, with and/or without the order separating GG435 filter. The half-wave retarder plate (see 1.2.2) was positioned at four angles of 0°, 22.5°, 45°, and 67.5° per sequence. The ordinary and extraordinary beams were were extracted using standard procedures in IRAF (as described in Cikota et al. 2017b). Wavelength calibration was achieved using He-Ne-Ar arc lamp exposures. The typical RMS accuracy is ∼ 0.3 Å. The data have been bias subtracted, but not flat field corrected. However, the detector artifacts get reduced by taking a redundant number of half-wave positions (see Patat & Romaniello, 2006).

Fossati et al. (2007) analysed observations of standard stars for linear polarization obtained from 1999 to 2005 with FORS1, in imaging (IPOL) and spectropolarimetric (PMOS) mode. They found a good temporal stability and a small instrumental polarization in PMOS mode. In a similar study, Cikota et al. (2017b) tested the temporal stability of the PMOS mode of FORS2 since it was commissioned, using a sample of archival polarized and unpolarized standard stars, and found a good observational

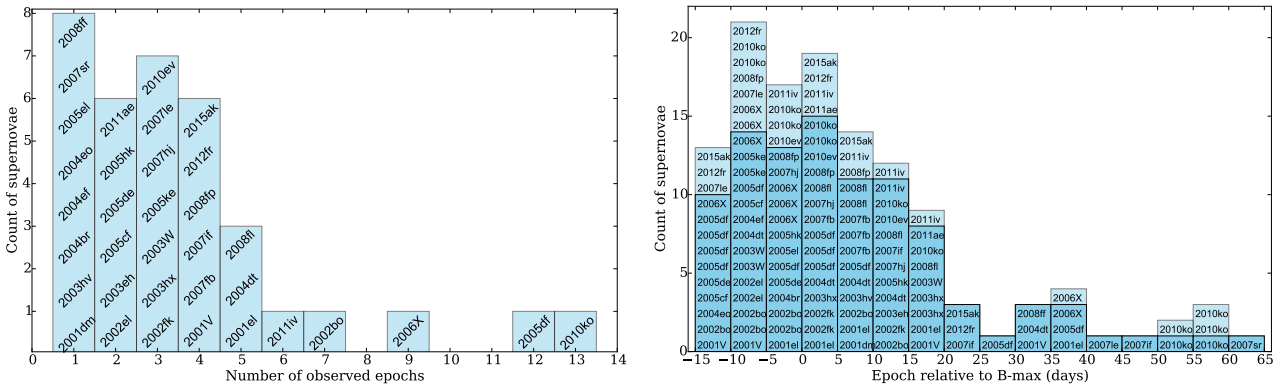

Figure 5.1.: *Left panel:* Distribution of number of epochs per SN. For example, SN 2001el, SN 2004dt and SN 2008fl have been observed at 5 epochs. *Right panel:* Distribution of observed epochs. For example, SN 2007if, SN 2012fr and SN 2015ak have been observed between 20 and 25 days past peak brightness. The dark blue color is the count of unique supernovae observed in a given epoch-bin. For example, there are 4 SNe observed observed between 35 and 40 days past peak brightness, however, only 3 unique, because SN 2006X has been observed twice during this period.

repeatability of total linear polarization measurements with an RMS $\lesssim 0.21\%$. They also confirmed and parameterized the small ($\lesssim 0.1\%$) instrumental polarization found by Fossati et al. (2007), that we correct by applying their linear functions to Stokes Q and U.

5.2.2. Supernova sample

In this work, we collected archival data of 35 SNe Ia, observed with FORS1 and FORS2 in spectropolarimetry mode, between 2001 and 2015, at 128 epochs in total. A list of the targets with some basic properties is provided in Table 5.1, while a full observing log is given in Table C.1. The observations in Table C.1 are grouped into individual epochs, separated by a space.

Figure 5.1 shows the number of observed epochs per supernova, and the distribution of observed epochs. Eight supernovae have been observed at a single epoch, while the most frequently observed supernovae are SN 2010ko (observed at 13 epochs), SN 2005df (12 epochs), SN 2006X (9 epochs) SN 2002bo (7 epochs) and SN 2011iv (6 epochs).

Our sample also contains a few spectroscopically peculiar objects. SN 2005ke is a 91bg-like object (Patat et al., 2012); SN 2005hk is a 2002cx-like object (Maund et al., 2010), while SN 2011iv and SN 2004eo are transitional objects (see Gall et al., 2017; Pastorello et al., 2007, respectively). Also a spectrum of SN 2007hj near maximum light shows similarities to several sub-luminous type Ia supernovae (Blondin et al., 2007).

5.3. Methods

5.3.1. Stokes parameters, polarization degree and polarization angle

The normalized Stokes parameters Q and U were derived following the recipe in the FORS2 User Manual (ESO, 2015):

$$\begin{aligned} Q &= \frac{2}{N} \sum_{i=0}^{N-1} F(\theta_i) \cos(4\theta_i) \\ U &= \frac{2}{N} \sum_{i=0}^{N-1} F(\theta_i) \sin(4\theta_i) \end{aligned} \tag{5.1}$$

Table 5.1.: SN Ia sample

Name	z	T_{Bmax} (MJD)	Δm_{15} (mag)	Epochs (days relative to T_{max})	References (z, T_{max}, Δm_{15})
SN 2001dm	0.01455	52128.0 ± 10.0	...	6.3	1, estimate , –
SN 2001V	0.01502	51972.58 ± 0.09	0.73 ± 0.03	-10.4, -6.4, 17.5, 30.6	2, SNooPy, 3
SN 2001el	0.00364	52182.5 ± 0.5	1.13 ± 0.04	-4.2, 0.7, 8.7, 17.7, 39.6	4, 5, 6
SN 2002bo	0.00424	52356.5 ± 0.2	1.12 ± 0.02	-11.4, -7.4, -6.4, -4.5, -1.4, 9.6, 12.6	7, 5, 6
SN 2002el	0.02469	52508.76 ± 0.05	1.38 ± 0.05	-8.6, -7.6	4, SNooPy, 3
SN 2002fk	0.007125	52547.9 ± 0.3	1.02 ± 0.04	0.4, 4.4, 13.4	8, 5, 6
SN 2003eh	0.02539	52782.0 ± 10.0	...	0.0, 12.0	9, estimate, –
SN 2003hv	0.005624	52891.2 ± 0.3	1.09 ± 0.02	6.1	4, 5, 6
SN 2003hx	0.007152	52892.5 ± 1.0	1.17 ± 0.12	4.8, 16.8, 18.8	1, 10, 11
SN 2003W	0.018107	52679.98 ± 0.11	1.3 ± 0.05	-8.7, -6.7, 16.1	4, SNooPy, 3
SN 2004br	0.019408	53147.9 ± 0.27	0.68 ± 0.15	-3.9	4, SNooPy, 12
SN 2004dt	0.01883	53239.98 ± 0.07	1.21 ± 0.05	-9.7, 4.4, 5.2, 10.3, 33.2	13, SNooPy, 3
SN 2004ef	0.028904	53264.4 ± 0.1	1.45 ± 0.01	-5.3	4, 5, 6
SN 2004eo	0.015701	53278.51 ± 0.03	1.32 ± 0.01	-10.4	2, 14, 6
SN 2005cf	0.006461	53533.94 ± 0.05	1.18 ± 0.0	-11.9, -5.8	7, SNooPy, Wang (priv. comm.)
SN 2005de	0.015184	53598.89 ± 0.05	1.41 ± 0.06	-10.9, -4.9	2, SNooPy, 3
SN 2005df	0.004316	53599.18 ± 0.1	1.05 ± 0.02	-10.8, -8.8, -7.8, -6.8, -2.8, 0.2, 4.2, 5.2, 8.2, 9.1, 29.2, 42.1	15, SNooPy, SNooPy
SN 2005el	0.01491	53647.0 ± 0.1	1.4 ± 0.01	-2.7	13, 5, 6
SN 2005hk	0.01306	53685.42 ± 0.14	1.47 ± 0.14	-2.3, 11.7	16, SNooPy, 17
SN 2005ke	0.00488	53699.16 ± 0.08	1.66 ± 0.14	-9.1, -8.1, 75.9	13, SNooPy, 17
SN 2006X	0.00524	53786.3 ± 0.1	1.09 ± 0.03	-10.9, -9.0, -8.1, -7.1, -4.0, -3.0, -1.9, 37.9, 38.9	13, 5, 6
SN 2007fb	0.018026	54288.41 ± 0.17	1.37 ± 0.01	3.0, 6.0, 6.9, 9.9	18, SNooPy, SNooPy
SN 2007hj	0.01289	54350.23 ± 0.1	1.95 ± 0.06	-1.1, 4.9, 10.9	13, SNooPy, 12
SN 2007if	0.073092	54343.1 ± 0.6	1.07 ± 0.03	13.1, 20.1, 45.0, 46.0	4, 5, 6
SN 2007le	0.005522	54399.3 ± 0.1	1.03 ± 0.02	-10.3, -5.1, 40.7	4, 5, 6
SN 2007sr	0.005417	54447.82 ± 0.24	1.05 ± 0.07	63.4	18, SNooPy, 12
SN 2008ff	0.0192	54704.21 ± 0.63	0.90 ± 0.06	31.0	19, 20, 21
SN 2008fl	0.0199	54720.79 ± 0.86	1.35 ± 0.07	2.2, 8.3, 9.2, 11.3, 15.3	22, 20, 21
SN 2008fp	0.005664	54730.9 ± 0.1	1.05 ± 0.01	-5.6, -0.5, 1.4, 5.4	4, 5, 6
SN 2010ev	0.009211	55385.09 ± 0.14	1.12 ± 0.02	-1.1, 2.9, 11.9	16, SNooPy, 23
SN 2010ko	0.0104	55545.23 ± 0.23	1.56 ± 0.05	-7.1, -6.0, -2.0, -1.2, 1.9, 3.9, 10.9, 15.9, 50.9, 51.8, 57.8, 58.8, 59.8	24, SNooPy, SNooPy
SN 2011ae	0.006046	55620.22 ± 0.39	...	4.0, 16.0	18, SNooPy, –
SN 2011iv	0.006494	55905.6 ± 0.05	1.77 ± 0.01	-0.4, 2.6, 5.6, 11.5, 12.5, 19.5	16, 25, 26
SN 2012fr	0.0054	56244.19 ± 0.0	0.8 ± 0.01	-12.1, -6.9, 1.0, 23.1	27, SNooPy, SNooPy
SN 2015ak	0.01	57268.13 ± 0.1	0.95 ± 0.01	-13.1, 4.9, 6.9, 23.9	spec. fit, SNooPy, SNooPy

References. SNooPy: see Sect. 5.3.3; 1: Silverman et al. (2012); 2: Ganeshalingam et al. (2013); 3: Wang et al. (2007); 4: Planck Collaboration et al. (2016); 5: Dhawan et al. (2015); 6: Dhawan et al. (2015); 7: Mandel et al. (2011); 8: Amanullah et al. (2010); 9: Prieto et al. (2008); 10: Misra et al. (2008); 11: Misra et al. (2008); 12: Ganeshalingam et al. (2010); 13: Folatelli et al. (2013); 14: Dhawan et al. (2015); 15: Yaron & Gal-Yam (2012); 16: Chomiuk et al. (2016); 17: Hicken et al. (2009a); 18: Friedman et al. (2015); 19: Tan (2008); 20: Krisciunas et al. (2017a); 21: Krisciunas et al. (2017a); 22: Pignata et al. (2008); 23: Gutiérrez et al. (2016); 24: Leonini & Brimacombe (2010); 25: Gall et al. (2017); 26: Gall et al. (2017); 27: Buil (2012).

where $F(\theta_i)$ are the normalized flux differences between the ordinary (f^o) and extra-ordinary (f^e) beams:

$$F(\theta_i) = \frac{f^o(\theta_i) - f^e(\theta_i)}{f^o(\theta_i) + f^e(\theta_i)} \tag{5.2}$$

at different half-wave retarder plate position angles $\theta_i = i * 22.5^\circ$ ($0 \leq i \leq 15$).

We correct the retardance chromatism of the super-achromatic half wave plate (HWP) through a rotation of the Stokes parameters:

$$\begin{aligned} Q_0 &= Q \cos 2\Delta\theta(\lambda) - U \sin 2\Delta\theta(\lambda) \\ U_0 &= Q \sin 2\Delta\theta(\lambda) + U \cos 2\Delta\theta(\lambda), \end{aligned} \tag{5.3}$$

using the wavelength dependent retardance offset ($\Delta\theta(\lambda)$), tabulated in the FORS2 User Manual.

Finally we calculated the polarization:

$$P = \sqrt{Q^2 + U^2} \tag{5.4}$$

and the polarization angle:

$$\theta_0 = \frac{1}{2} \arctan(U_0/Q_0). \tag{5.5}$$

5.3.2. Wavelet decomposition and continuum removal

In this work we focus on line polarization only, and do not investigate interstellar, circumstellar or intrinsic continuum polarization. Therefore, we are removing the whole continuum polarization without distinguishing between its three components.

There are different approaches to remove the interstellar continuum polarization (ISP). For instance, Patat et al. (2009) fit a third order polynomial to the degree of linear polarization for the last epoch of SN 2006X, and estimate the interstellar polarization Stokes as follows:

$$\begin{aligned} Q_{ISP}(\lambda) &= P_{ISP}(\lambda) cos(2\theta_{ISP}) \\ U_{ISP}(\lambda) &= P_{ISP}(\lambda) sin(2\theta_{ISP}), \end{aligned} \tag{5.6}$$

where they compute θ_{ISP} as the average within some line-free regions (note that θ_{ISP} is wavelength independent). Then they calculate the intrinsic SN polarization at all epochs by subtracting Q_{ISP} and U_{ISP} from the initial Stokes Q and U. SN 2006X has a strong ISP contribution, so that any intrinsic polarization was negligible. Also, Patat et al. (2009) use this method with the purpose to remove the ISP, but not all the continuum polarization.

The disadvantage of this method is that the SN intrinsic continuum polarization does not get subtracted, and that we need to assume a wavelength independent angle (which is only true in case of ISP, and polarization produced by scattering from nearby clouds) to remove the continuum. Furthermore, it is challenging to do this kind of subtraction in a systematic way for a large sample of data, in particular when the ISP is small, possibly comparable to the intrinsic.

Therefore, to subtract the continuum, we perform an à trous wavelet decomposition (Holschneider et al., 1989) of the ordinary and extraordinary beams, which allows us to distinguish between the continuum spectra and the line spectra in a systematic way.

The wavelet decomposition is a method to decompose a function into a set of J scales, by convolving the function with a convolution mask with an increasing size. Assuming a convolution mask (e.g., the commonly used Mexican hat, or simply a triangle), the first convolution is performed on the initial function $c_0(k)$, to generate $c_1(k)$. The difference $c_0(k) - c_1(k)$ is the first wavelet scale $w_1(k)$. The algorithm is then reapplied j times, using a double sized convolution mask, until scale J is reached (see also Wagers et al. (2010)).

The sum of all wavelet scales reproduces the original function (i.e., spectrum):

$$c_0(k) = c_J(k) + \sum_{j=1}^{J-1} w_j(k). \tag{5.7}$$

As a convolution mask, we follow Wagers et al. (2010), and use a five-bin symmetric triangle function with weights: 3/8,1/4, and 1/16.

Figure 5.2 shows an example of a wavelet decomposition of a spectrum into a "continuum" (sum of scales 9+10+11), "noise" (scales 1+2+3) and the remaining spectrum (scales 4+5+6+7+8).

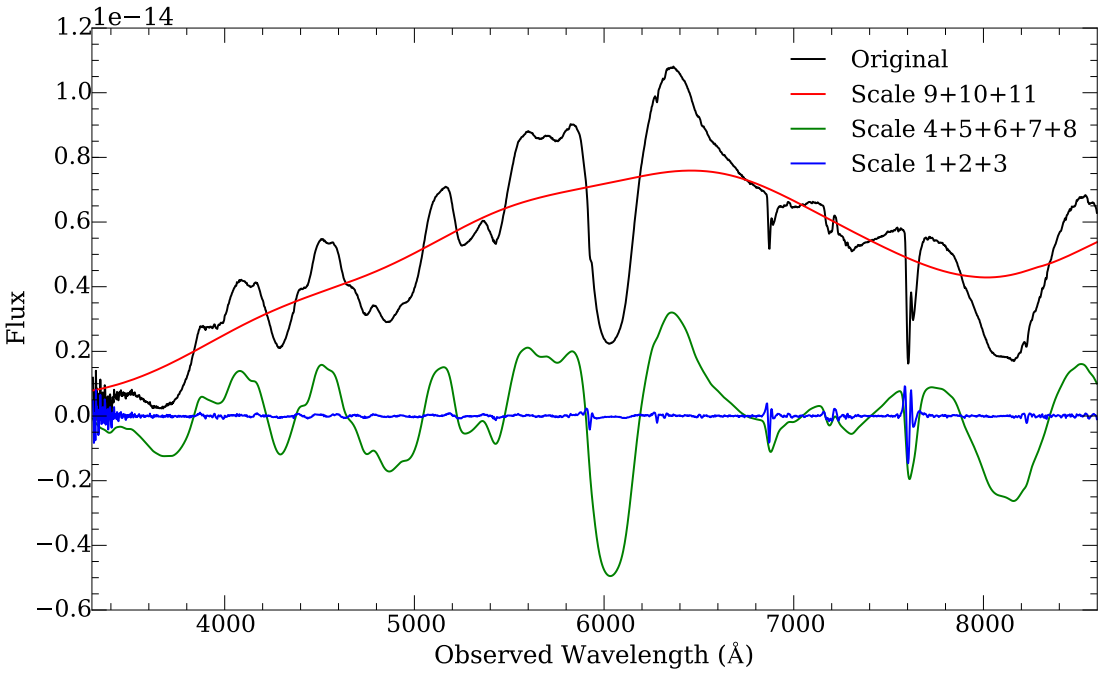

Figure 5.2.: Example of an à trous wavelet decomposition. The black line is an original spectrum, red, blue and green curves are the sum of the last three (9+10+11), first three (1+2+3) and middle 5 wavelet scales (4+5+6+7+8), respectively.

To determine the continuum polarization, we first calculate the total Stokes Q and U by summing all scales except the first three in order to reduce the noise, and following the equations in Sect 5.3.1. Then we calculate the continuum polarization (continuum Stokes Q and U), using the sum of first three scales only, which we then subtract from the total Stokes Q and U.

5.3.3. Light curve fitting

For a number of SNe Ia, for which we did not find the time of peak brightness, T_{max}, or Δm_{15} in the literature, we downloaded light curves from the Open Supernova Catalog[1], which is an online collection of observations and metadata for supernovae (Guillochon et al., 2017) and determined the missing parameters.

For this purpose, we fit the light curves using the SNooPy package (Burns et al., 2011, 2015), in order to determine the time of peak brightness, T_{max}, and Δm_{15}. SNnooPy contains tools for the analysis of SNe Ia photometry, and includes four models to fit the light curves. For our purpose, we used the "EBV_model", which is based on the empirical method for fitting multicolor light curves developed by Prieto et al. (2006). Figure 5.4 shows an example fit of SN 2005df observations.

A list of SNe Ia for which we fit their light curves, including the number of photometric observations used per passband filter, and the corresponding references for the observations, is given in Table C.2.

The results, i.e., the time of peak brightness, T_{max}, and Δm_{15}, are given in Table 5.1.

[1] https://sne.space

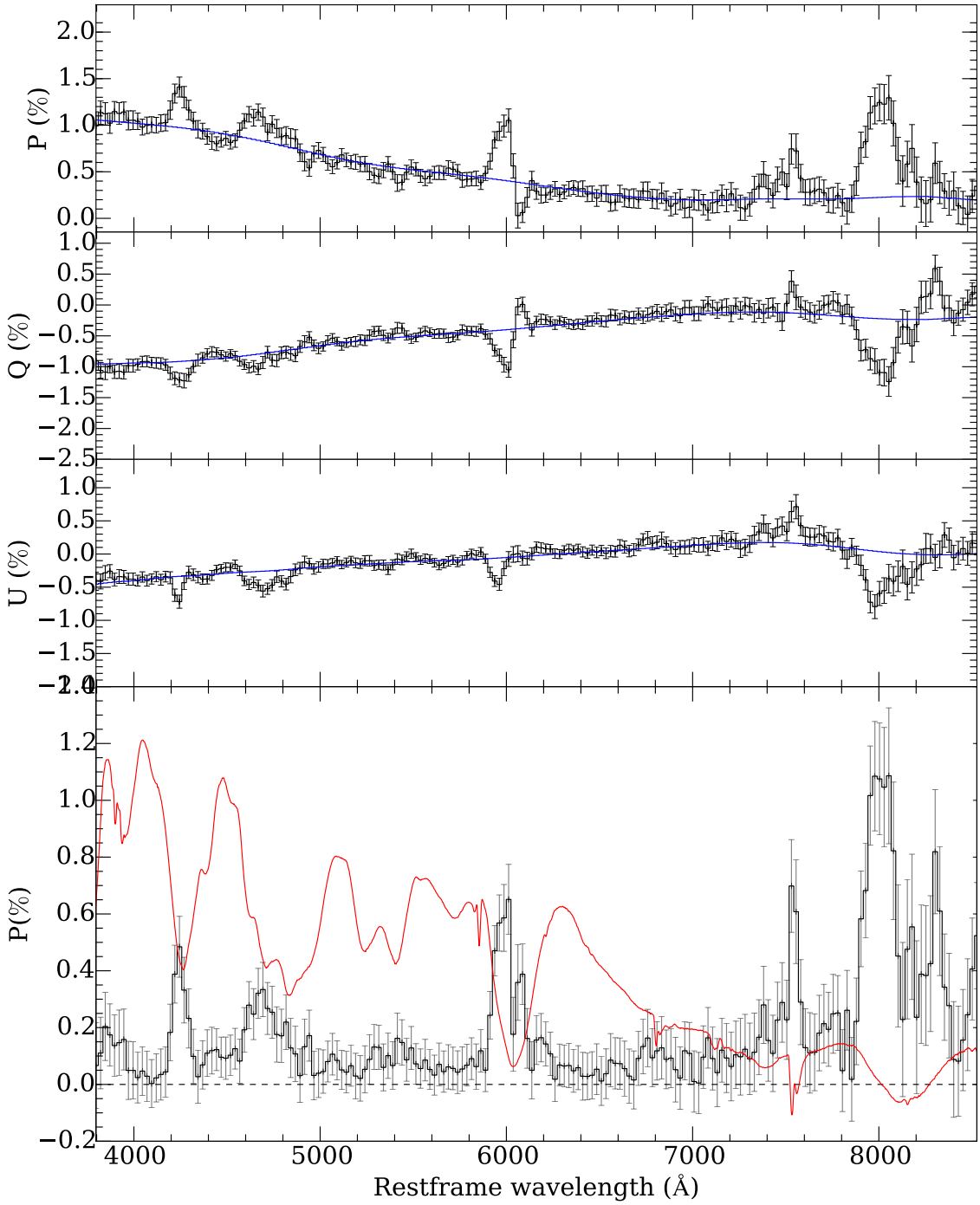

Figure 5.3.: Example of continuum subtraction from a polarization curve of SN 2002bo at -1 day relative to peak brightness. The top panel shows the total degree of polarization (black curve) and the continuum determined with wavelet decomposition (blue curve). The middle panels are Stokes Q and U. The bottom panel shows the polarization spectrum after continuum subtraction, compared to the flux spectrum (red curve). The λ 6355 Å Si II line, at $\sim$ 6000Å, displays two peaks, related to the high velocity and photospheric silicon components.

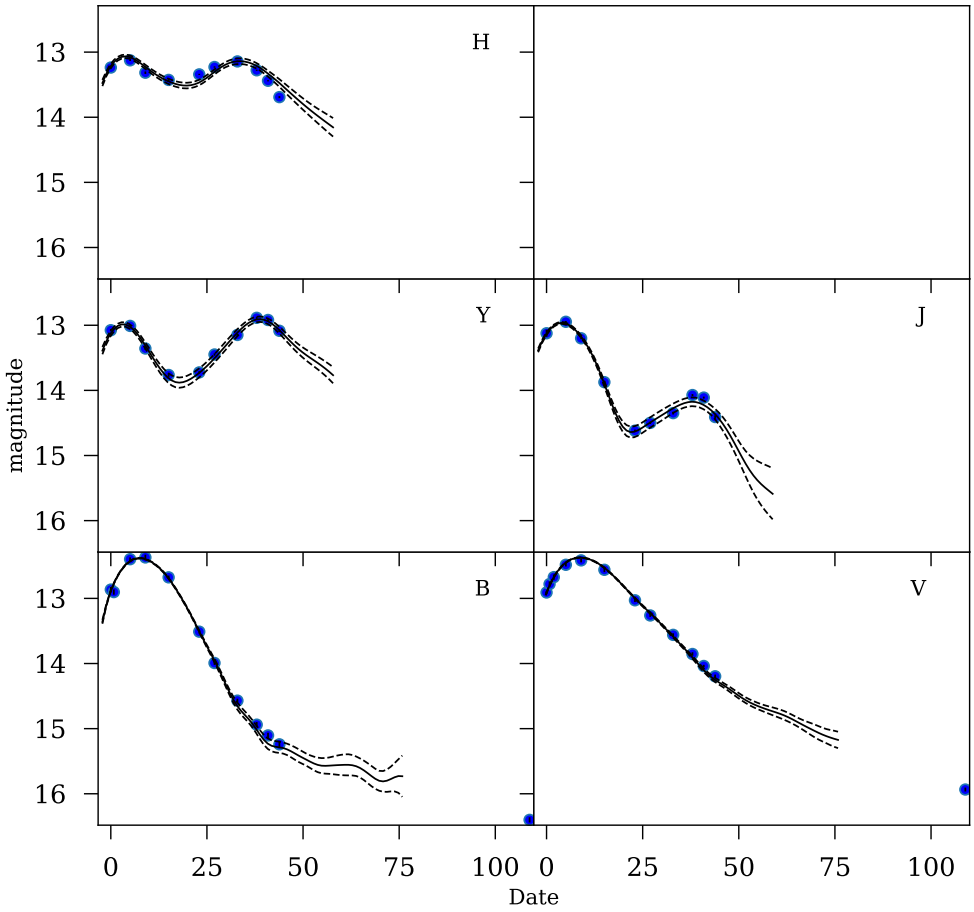

Figure 5.4.: An example of light curve fitting with SNooPy. Shown is a multi-color light curve fit to SN 2005df observations in 5 passband filters. The date on the x-axis is in units of days relative to an arbitrary zero-point.

5.3.4. Expansion velocities deduced from absorption lines

One of our main aims is the study of possible correlations between polarization (used as a proxy to asymmetries in the explosion) and other spectrophotometric properties that characterize the events. In particular, we focus here on the relationship between the line polarization and the expansion velocities. To measure the ejecta photospheric velocities, we use spectra from the Open Supernova Catalog, supplementary to our flux spectra (calculated by summing the ordinary and extraordinary beams) taken with VLT/FORS. A complete list of spectra taken from the Open Supernova Catalog is given in Table C.3.

After measuring the rest-frame wavelengths of the absorption minima for different lines, for different epochs, we calculate the line velocity and fit a polynomial function to the velocities, to determine the velocity at -5 days relative to peak brightness. Figure 5.5 shows an example fit to Si II 6355Å line velocities at different epochs, for SN 2005hk (the SN with lowest Si II expansion velocity in our sample), SN 2002bo, SN 2001el, and SN 2006X (the SN with the highest Si II expansion velocity in our sample). The results of the measurements are given in Table C.4.

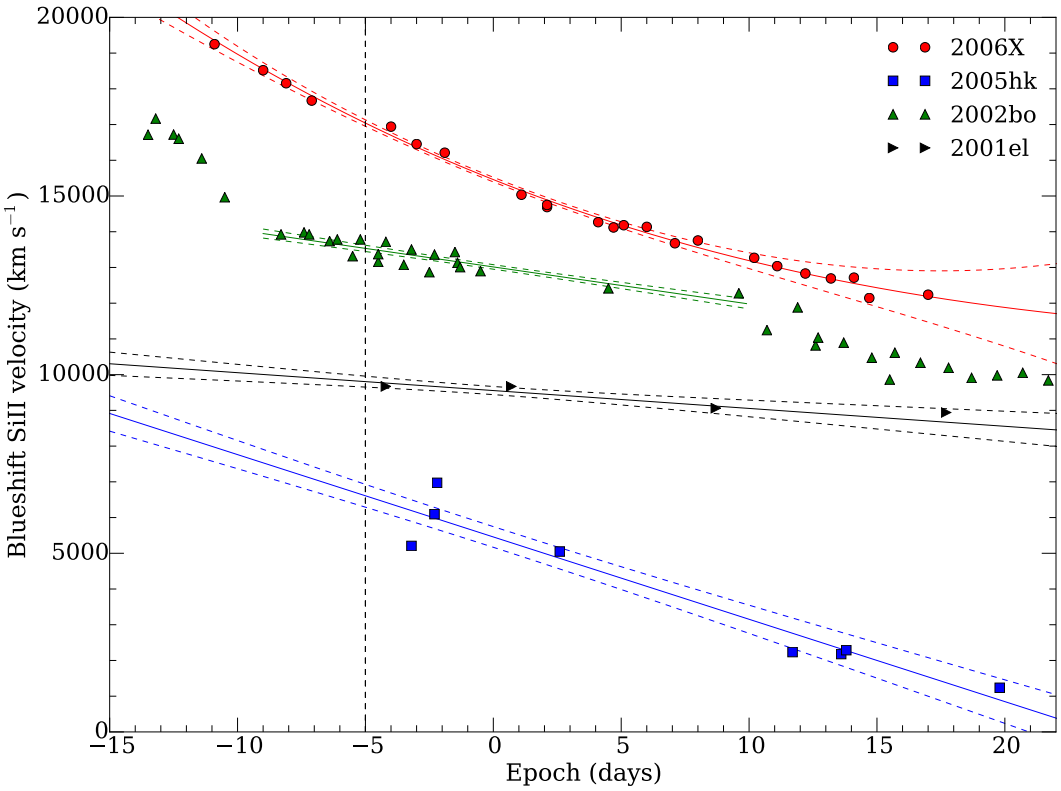

Figure 5.5.: A third order polynomial fit to the Si II 6355Å velocities for SN 2005hk, SN 2002bo, SN 2001el, and SN 2006X. The vertical black line indicates -5 days relative to peak brightness.

5.3.5. Line polarization measurements and P(epoch) fitting

Measuring the linear polarization of lines is challenging, because the peak polarization depends on the binning, and there are sometimes multiple peaks related to one absorption feature (e.g., the high velocity and photospheric Si II λ6355Å components).

To measure the peak polarization of a specific line, we first manually determine the lower and upper wavelength edges, containing the line of interest, from a plot with all VLT flux and polarization spectra.

For each polarization spectrum, we use three sets with different bin sizes of 25Å, 50Å and 100Å, and apply the polarization bias correction. Since the polarization is by definition a positive quantity (see Eq. 5.4), presence of noise introduces a biased, overestimated, value. We correct the polarization bias following the equation given in Wang et al. (1997):

$$P = (P_{\rm obs} - \sigma_P^2/P_{\rm obs}) \times h(P_{\rm obs} - \sigma_P), \tag{5.8}$$

where h is the Heaviside function.

Finally we measure the peak polarization value within the borders of the line. Fig. 5.6 shows the Si II 6355Å line of SN 2002bo at -1 day relative to peak brightness, at three different bin sizes. At this epoch, there are two peaks visible in the 25Å and 50Å binned data, the photospheric with the lower velocity, and the high velocity Si II line, while in the 100Å binned data the two peaks are blended.

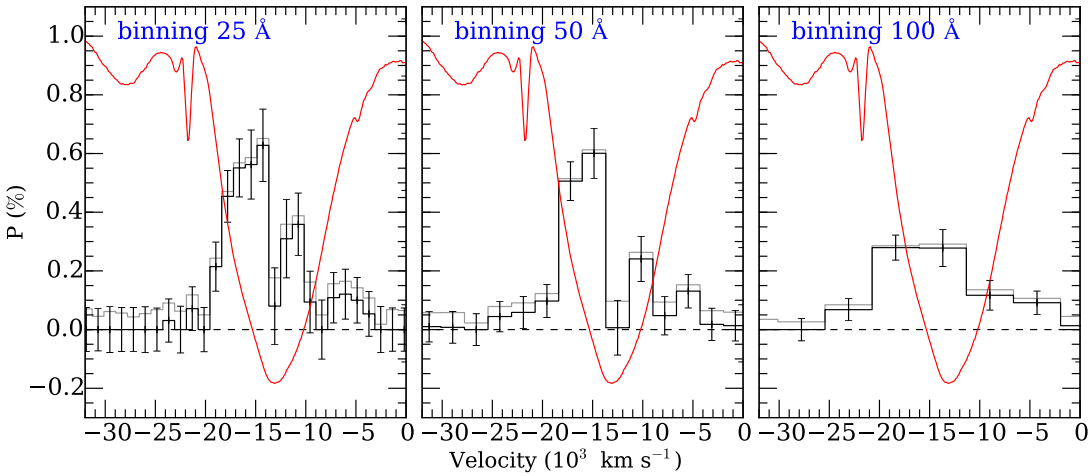

Figure 5.6.: Shown is the linear polarization of the Si II 6355Å line in SN 2002bo at -1 day relative to peak brightness. The three panels show the polarization degree derived with different bin sizes of 25 Å (left), 50 Å (middle) and 100 Å (right). The gray line is the bias uncorrected spectrum, while the red line is the flux spectrum of the Si II line.

After the data reduction, we can now investigate the evolution of the line polarization as a function of time. Fig. 5.7 shows Si II 6355Å polarization in SN 2006X, as a function of time, for three different binning sizes of 25Å, 50Å, and 100Å, compared to the measurements in Patat et al. (2009). This clearly shows that the measurements in highly binned data (100Å) exhibit less variability, and have lower values, while when the polarization is measured in data with smaller bin sizes (25Å and 50Å), the measured peak polarization is higher, but the scatter is also. The binning was chosen as a compromise between retaining spectral resolution and increasing the signal-to-noise.

A list of all Si II polarization measurements, for different bin sizes, is given in Table C.5, and plots of the line polarization and flux spectra of all SNe are presented in Appendix C.2.

To fit the lines in Fig. 5.7, $P_{SiII} = a\times(t-t_{max})^2+p_{max}$, we use a nested sampling algorithm (Skilling, 2004), and assume that the prior on the epoch of peak polarization, t_{max} is a uniform distribution between -10 and 0 days, the prior on the peak polarization p_{max} variable is a uniform distribution between 0 and 5%, and the prior on a is a uniform distribution between -1 and 0.

5.3.6. Analysis of the Q–U loops

The polarized lines sometimes display loops in the Stokes Q–U plane (Wang & Wheeler, 2008). To analyze the loops, we use polarization values calculated from spectra (ordinary and extraordinary) with bins of 50Å.

We parametrize those loops by determining the dominant axis (Wang & Wheeler, 2008, see), and its slope, and calculating the enclosed area within the loops. To calculate the area, we first construct a convex hull from the (Q,U) tuples. A convex hull of a set of points is the smallest convex set that contains the points (Barber et al., 1996). Then we calculate the area of the convex hull using the Shoelace algorithm (Braden, 1986). To estimate the error of the area, we run a Monte Carlo simulation by introducing a Gaussian error to the (Q,U) tuples, 10000 times for each epoch, and get a non-Gaussian distribution of the area values. We finally calculate the 25^{th} and 75^{th} percentile of the distribution to estimate the semi-interquartile range. Examples of loops are shown in Fig. 5.8.

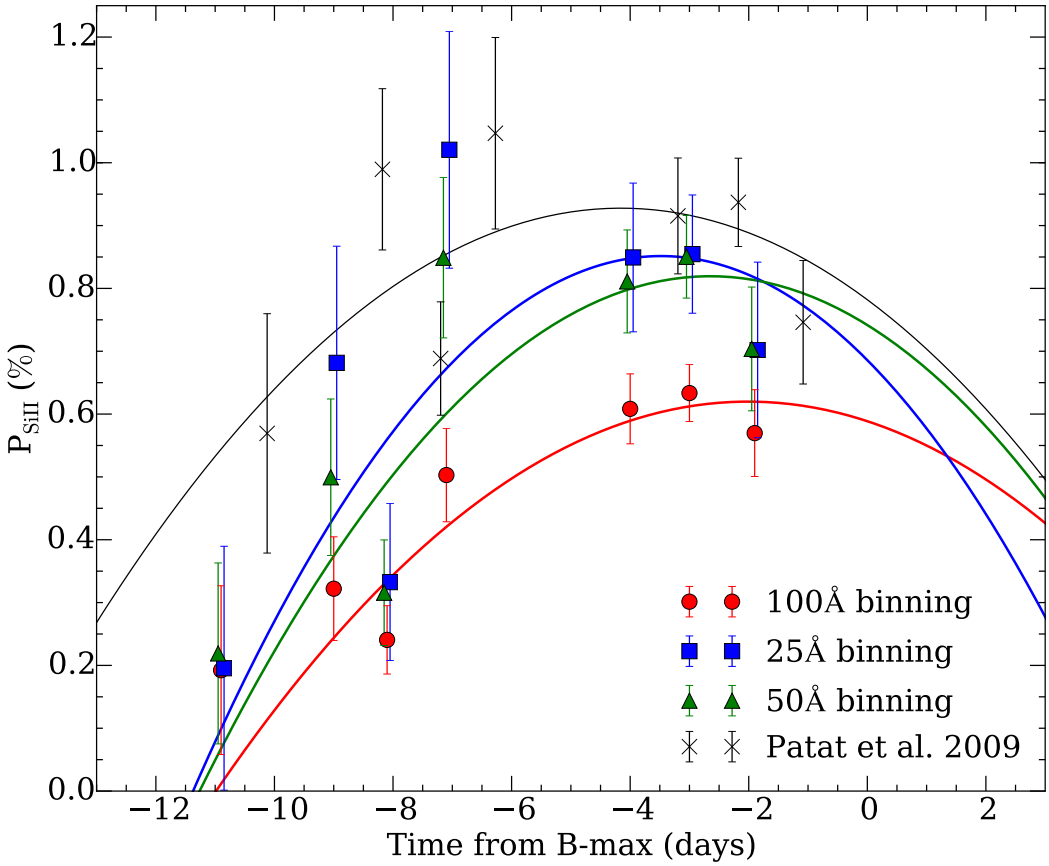

Figure 5.7.: Linear polarization of Si II 6355Å in SN 2006X, as a function of time, for three different binning sizes, compared to the measurements in Patat et al. (2009). Note that the time of peak brightness adopted in Patat et al. (2009) is ∼1 day earlier, than what is used in this work.

5.4. Results & discussion

Line polarization has implications on the progenitor model and the explosion mechanism (Wang & Wheeler, 2008; Bulla et al., 2015). The most prominent line polarization is observed in the Si II λ6355Å line and the near-IR Ca II triplet (see Wang & Wheeler, 2008, , and this work). The maximum degree of polarization is typically ∼1%, reached few days before peak brightness. In this section we show and discuss the evolution of the Si II polarization, and the evolution of the loops in the Q–U plane, the Δm_{15}–Si II polarization relationship, investigate and interpret the Si II velocity–polarization relationship, and finally compare our sample to simulations.

5.4.1. Epoch – polarization relationship

Figure 5.9 shows the time evolution of the Si II λ6355Å line for a selected subset of SNe Ia, that are well sampled in terms of time coverage, measured with a binning of 100Å. The evolution was discussed in Wang et al. (2007), who fit a time dependence of the degree of polarization with a second order polynomial: P_{SiII} = 0.65-0.041(t-5)-0.013(t+5)^2, where t is the time in days relative to the peak brightness in the B-band. However, as Porter et al. (2016) already noticed in the case of SN 2014J, there are a variety of peak polarization values, at different epochs.

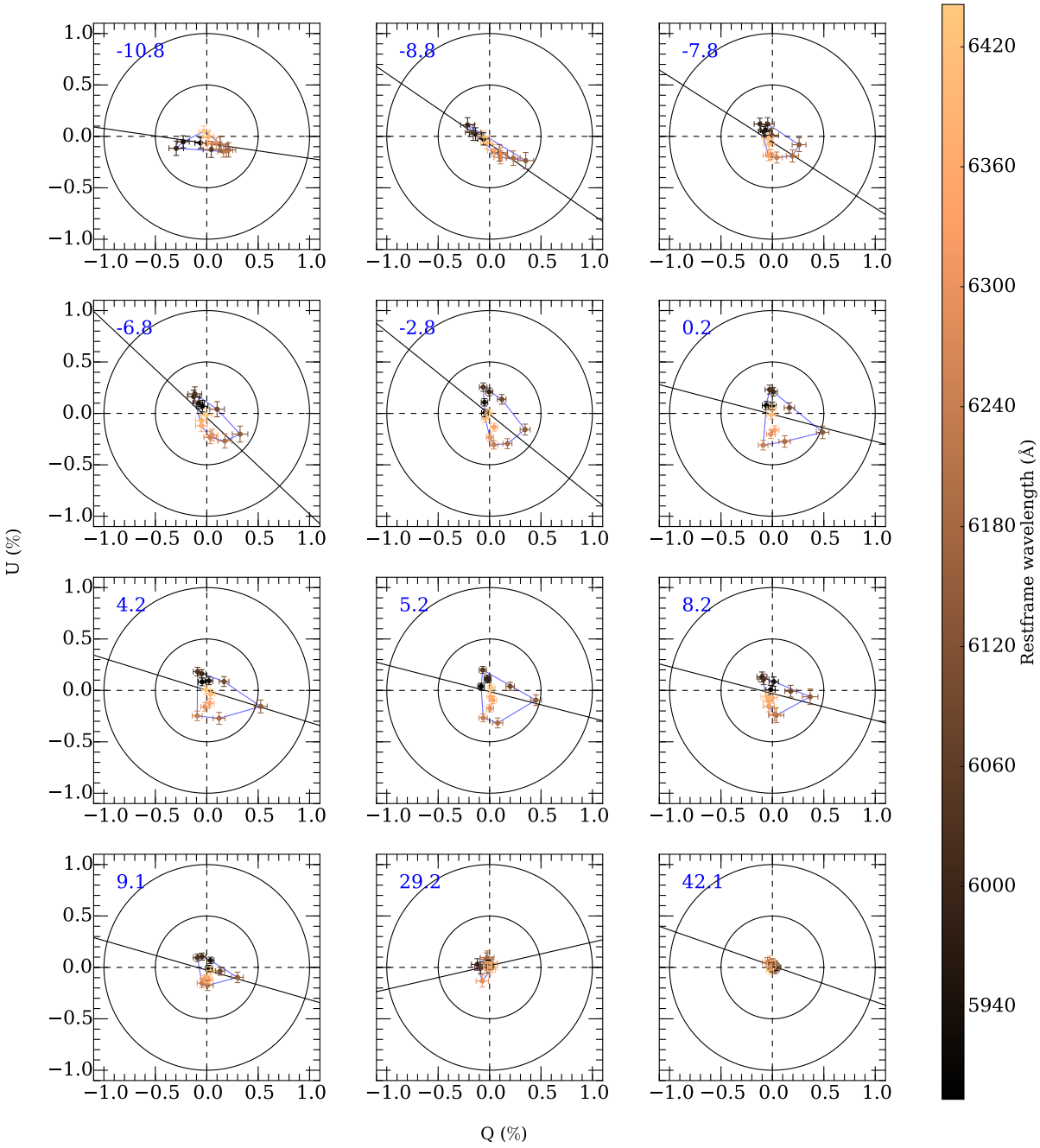

Figure 5.8.: Evolution of the Si II 6355Å line in the Q–U plane for SN 2005df. The panels show different epochs relative to peak brightness (indicated in the upper left corner of each insert). The blue lines indicate the convex hull used to calculate the area, and the black line traces the dominant axis computed using the displayed Q, U data.

Inspecting the polarization spectra, binned in bins of 25Å, we noticed that in some cases two Si II peaks are visible: SN 2002bo at epochs -4.5, -1.4 and 9.6; SN 2002el at -7.6 days; SN 2003W at all three observed epochs from -8.7 to 16.1 days, SN 2005df particularly at epochs -8.8 and -6.8; SN 2005el at -2.7 (the only observed epoch); SN 2007fb at 6 days past maximum; SN 2007hj at 4.9

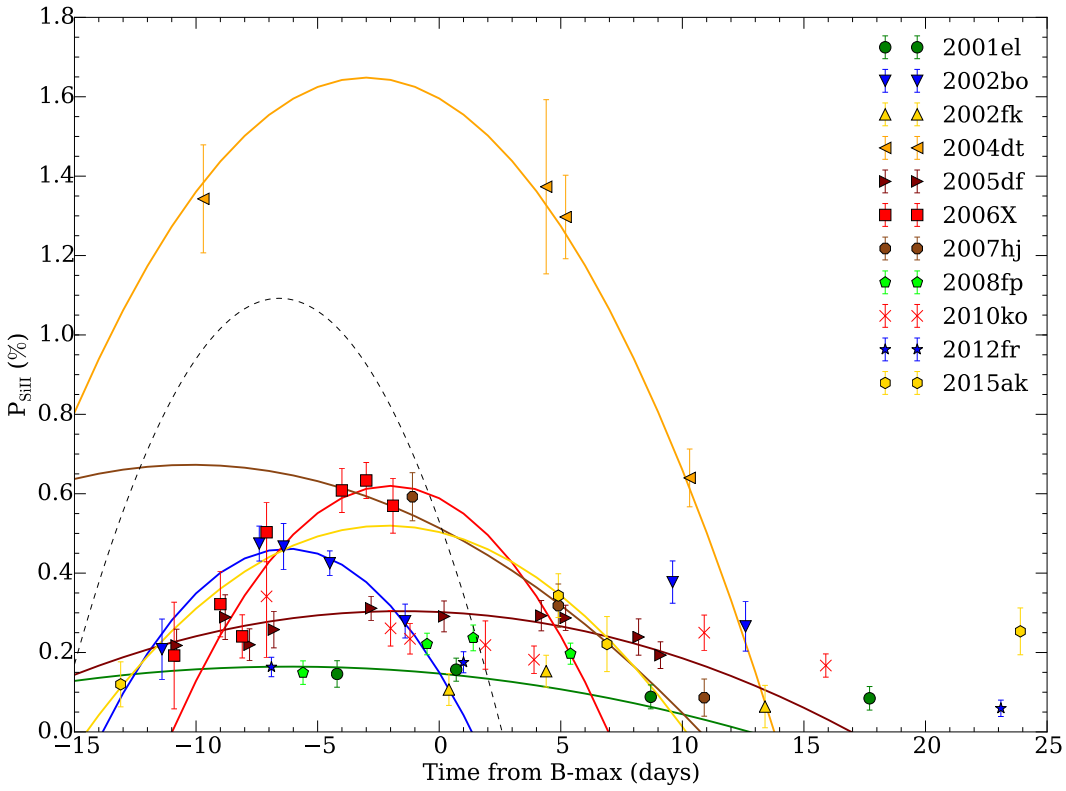

Figure 5.9.: Time evolution of the linear polarization of Si II λ6355Å line, for a sample of SNe Ia. For comparison, the dotted line shows the P_{SiII}–epoch fit from Wang et al. (2007). Note that our polarization measurements are lower because we use 100Å bins.

days; SN 2008 fp at -0.5 and 1.4; and SN 2010ev at -1.1 and 2.9 days.

The two peaks correspond to a high velocity and a lower velocity photospheric component of the Si II line (Mazzali et al., 2005). In SN 2002bo, between epochs -1.4 and 9.6, the polarization of the photoshperic component becomes (and stays) more prominent than the high velocity component. The same behaviour is observed in SN 2007fb between epochs 3.0 and 6.0; and in the case of SN 2010ev between 2.9 and 11.9 days.

5.4.2. Δm_{15} – P_{SiII} relationship

Wang et al. (2007) present polarization measurements of the Si II 6355Å line for a sample of 17 SNe Ia. They found a correlation between the degree of polarization of Si II and the light-curve decline rate, Δm_{15}: P_{SiII} = 0.48(03) + 1.33(15)(Δm_{15} - 1.1), where Δm_{15} is in magnitudes and P_{SiII} in percent. They argue that this trend provides strong support for delayed-detonation models, because, in a delayed detonation scenario, the dimmer SNe, which burn less material to thermonuclear equilibrium, are expected to have larger chemical irregularities (thus larger polarization). This is due to the fact that more complete burning tends to erase chemically clumpy structures, and produces less chemically-asymmetric explosions (see also Wang & Wheeler, 2008).

As part of our analysis, we studied the Δm_{15}-P_{SiII} relationship using our larger sample and compared our Si II polarization measurements to the literature. Figure 5.10 shows peak linear polarization measurements of the Si II 6355Å line, measured at 50Å binned data, compared to the Δm_{15}–P_{SiII}

relationship determined by Wang et al. (2007), and measurements by other works.

Our linear polarization measurements of the Si II line in SN 2002fk, SN 2001el and SN 2005cf, and SN 2004eo, are systematically lower compared to the literature, independent of the binning size, whereas our measured Si II polarization in SN 2004ef is lower in the case of the 100Å binned data, while consistent in the 25Å and 50Å binned data. The SNe in the yellow region of Figure 5.10 are subluminous and transitional objects. The 91bg-like SN 1999by (Wang et al., 2007), 2002cx-like SN 2005hk (Maund et al., 2010) and 91bg-like SN 2005ke (Patat et al., 2012) are well known subluminous events. SN 2011iv is a transitional object (Gall et al., 2017) which has photometric and spectroscopic properties between normal SNe Ia and subluminous, 91bg-like (see also Mazzali et al., 2018; Ashall et al., 2018). A near-maximum spectrum of SN 2007hj showed that it is similar to several sub-luminous type Ia supernovae, characterized by a strong Si II absorption feature at 580 nm (Blondin et al., 2007). Blondin et al. (2012) classified SN 2007hj as CL ("Cool"), which is characterized by deeper Si II λ 5972 absorption, often associated with low-luminosity objects.

Furthermore, Pastorello et al. (2007) suggest that SN 2004eo should be considered as a transitional supernova, and Blondin et al. (2012) classified it as CL.

SN 2004dt has an exceptionally high Si II line polarization (Wang et al., 2006a). Predictions of polarization in the violent merger scenario are in good agreement with such a high polarization degree (Bulla et al., 2016b), however, the explosion scenario is still debated (see also Altavilla et al., 2007). Along SN 2004dt, also SN 2003eh shows high polarization of Si II line ($\sim$ 0.8 %), however, it is not shown in Figure 5.10, because it lacks of photometric data, and therefore it was not possible to derive the decline decay rate Δm_{15}.

After removing the peculiar objects, the remaining data follow the Δm$_{15}$–P$_{\rm SiII}$ relationship, although the scatter is larger than for the measurements presented in Wang et al. (2007). Note that in Fig. 5.10, we plot the maximum polarization within a range of -10 to 0 day relative to peak brightness, but we do not correct the polarization to a specific epoch, because, as discussed in the previous section, the polarization evolves in a variety of different ways, and despite the similarity of some polarization-epoch curves, we did not identify a common pattern that could be used to normalize all of them.

5.4.3. Si II Velocity – polarization relationship

Among the various possible correlations that we explored, we found a strong linear correlation between the Si II polarization and the expansion velocity deduced from the same line.

Figure 5.11 shows a subset of our sample of SNe Ia that have at least one observation between -11.0 and 1.0 days relative to peak brightness. This selection produces a set of 23 SNe, observed within a relatively short range of time. The plot shows the maximum Si II polarization in that period, as a function of the Si II λ 6355 Å velocity at 5 days before peak brightness.

There are two clear outliers: SN 2004dt, which has been already studied by Wang et al. (2006a), and may be the result of a violent merger (Bulla et al., 2016b); and SN 2003eh, for which there is no photometry available in the literature, however, spectra observed at six epochs (see Table C.3), and our two spectropolarimetry observations at peak and 12 days past peak brightness are available (the epoch of peak brightness has been estimated from spectra and has a large uncertainty of $\pm$10 days). This object has been identified as a reddened SN Ia by Matheson et al. (2003). We confirm the classification using our VLT observations and the Supernova Identification (SNID) code (Blondin & Tonry, 2007). The spectrum of SN 2003eh at peak brightness best matches the spectrum of SN 2008ar at 7 days past peak brightness. The polarization spectra show a continuum, which is rising from red to blue wavelengths, and highly polarized lines, similar to SN 2004dt. The continuum polarization remains

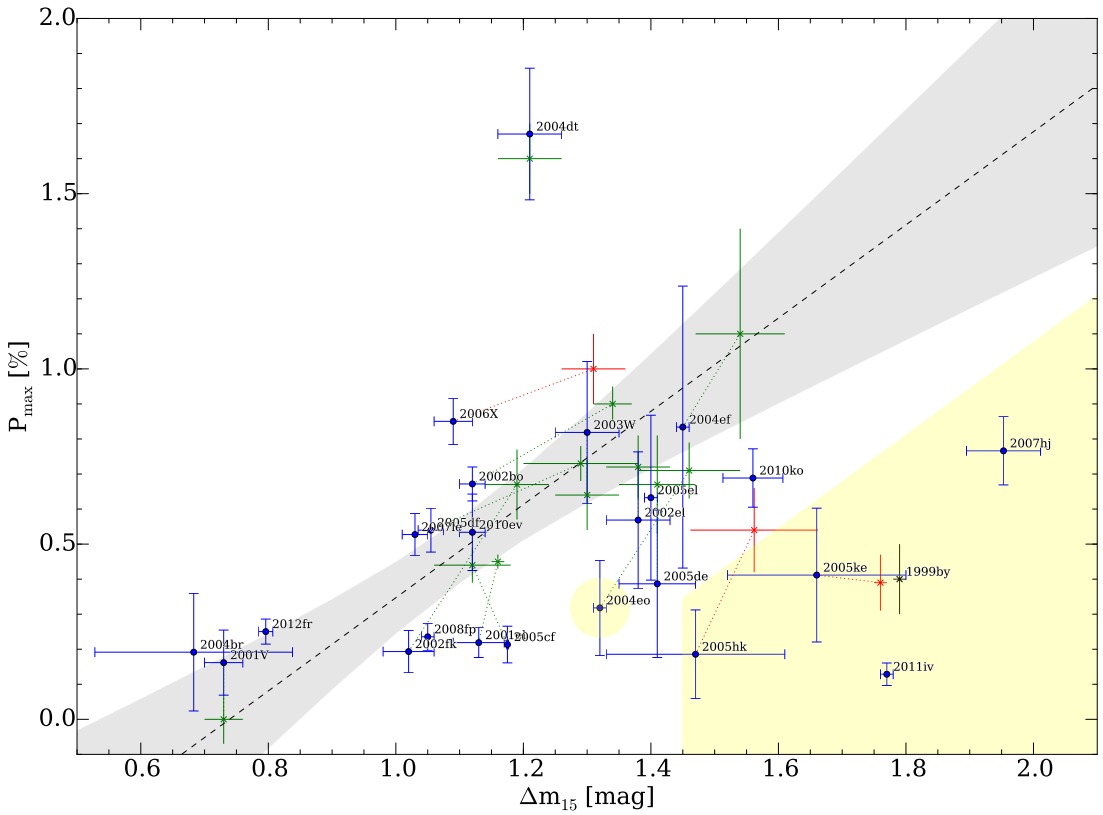

Figure 5.10.: Peak polarization of Si II line between epochs -10 and 0, as a function of Δm_{15} (blue dots). The black dashed line represents the Δm_{15}–P_{SiII} relationship determined by Wang et al. (2007), and the 3σ uncertainty (gray shaded area). Green 'x' symbols represent measurements of the SNe by Wang et al. (2007). For comparison we also show SN 2006X measured by Patat et al. (2009) (red 'x'), SN 2005hk (red 'x', Maund et al., 2010), SN 2005ke (red 'x', Patat et al., 2012) and SN 1999by (black 'x', Wang et al., 2007). The yellow area includes subluminous and transitional objects. Note that also SN 2004eo is classified as an transitional supernova.

constant at both epochs, and is most likely produced by interstellar or circumstellar dust, and reaches ~1.5 % at 4000 Å.

We test the correlation for different epoch ranges. In the tests, the outliers (SN 2004dt, subluminous and transitional objects) are excluded. The results are summarized in Table 5.2.

The black line in Fig. 5.11 is the linear least squares fit to the data. The best-fit P_{SiII}–$v_{SiII@-5d}$ relation can be written as follows:

$$P_{SiII} = (6.40 \times 10^{-5} \pm 1.28 \times 10^{-5}) \times v_{SiII@-5d} - 0.484 \pm 0.147, \quad (5.9)$$

where P_{SiII} is the polarization of the Si II λ5355Å line in percent, and $v_{SiII@-5d}$ is the blueshift velocity of the Si II λ5355Å line at -5 days relative to peak brightness in km s^{-1}. The Pearson correlation coefficient is $\rho = 0.8$. Note that relationship (5.9) is valid only for velocities higher than ~7500 km s^{-1}, because negative degrees of linear polarization are non-physical.

Very importantly, the velocity-polarization relationship may be explained in the context of a combination of an off-center delayed-detonation model and brightness decline. This can be understood with the following considerations. Within Chandrasekhar mass supernovae, and for the range of

Table 5.2.: Linear regression test results for the P_{SiII} vs. Si II velocity relationship

Epoch range	No.	ρ	p	α	β
-15.0 – 0.0	23	0.738	5.77×10^{-5}	$(5.93 \pm 1.38)\times10^{-5}$	-0.436 ± 0.161
-11.0 – 1.0	23	0.804	3.71×10^{-6}	$(6.40 \pm 1.28)\times10^{-5}$	-0.484 ± 0.147
-10.0 – 0.0	21	0.803	1.17×10^{-5}	$(6.39 \pm 1.37)\times10^{-5}$	-0.483 ± 0.159
-10.0 – -5.0	13	0.756	2.77×10^{-3}	$(6.53 \pm 2.16)\times10^{-5}$	-0.536 ± 0.259
-5.0 – 0.0	13	0.812	7.41×10^{-4}	$(6.34 \pm 1.40)\times10^{-5}$	-0.453 ± 0.163
0.0 – 5.0	13	0.391	0.187	$(2.45 \pm 2.00)\times10^{-5}$	-0.091 ± 0.223
0.0 – 10.0	15	0.375	0.169	$(3.98 \pm 2.09)\times10^{-5}$	-0.275 ± 0.233
5.0 – 10.0	9	0.404	0.281	$(4.21 \pm 3.80)\times10^{-5}$	-0.313 ± 0.411
10.0 – 20.0	13	0.806	0.87×10^{-3}	$(5.38 \pm 1.35)\times10^{-5}$	-0.440 ± 0.149
20.0 – 30.0	4	0.560	0.44	$(1.19 \pm 3.90)\times10^{-5}$	-0.054 ± 0.460

No. is the number of SNe included in the Epoch range. ρ and p are the Pearson's correlation coefficients, and the p-value, respectively. α and β are the slope and the y-intercept of a linear least squares fit, respectively.

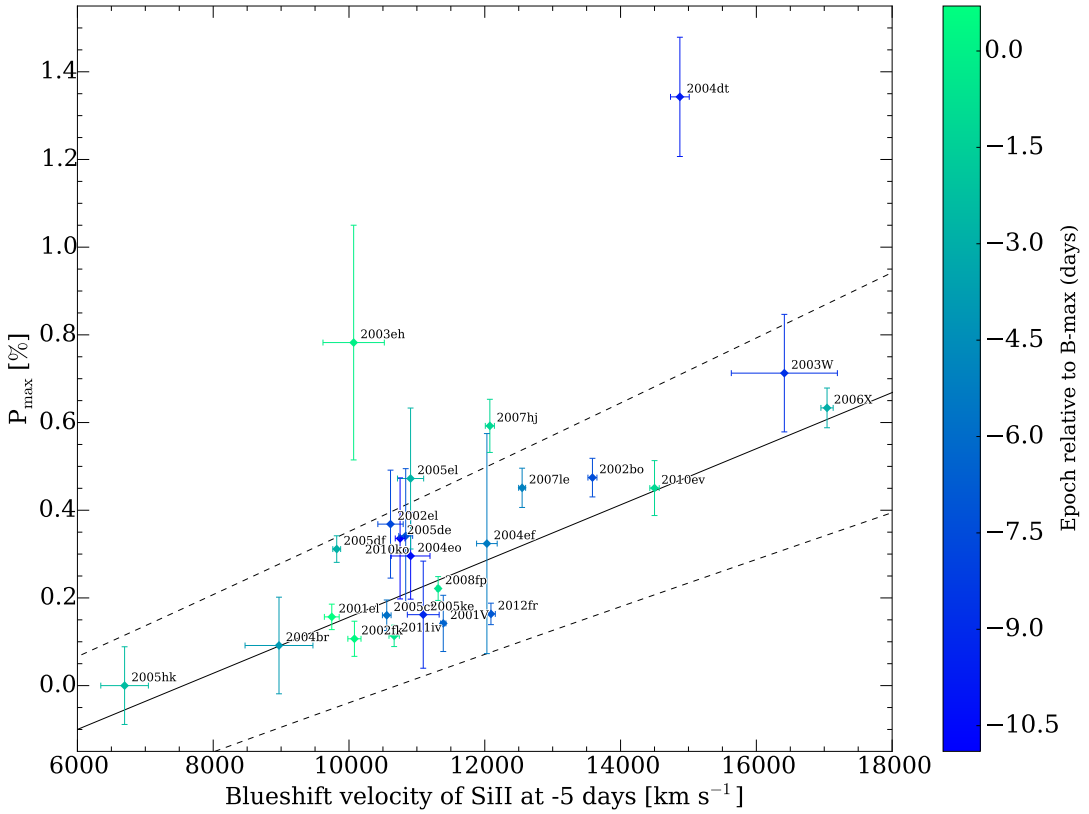

Figure 5.11.: Maximum linear polarization of the Si II λ 6355 Å line between -11 and 1 days relative to peak brightness, as a function of the Si II λ 6355 Å velocity at -5 days relative to peak brightness. The colors indicate the epoch relative to peak brightness. The bar to the right shows the color coding.

normally bright to subluminous supernovae, the brightness depends on the amount of ^{56}Ni produced in the explosion. Intermediate mass elements (including silicon) are produced in larger amounts with decreasing brightness. The models show that more silicon is produced, the silicon velocity range is larger (Höflich, priv. comm.; see also Höflich et al. 2006). Furthermore, as discussed in Wang et al. (2007), higher silicon polarization values suggest that there are compositional irregularities left in the central region by the pure deflagration phase, and thus less material is burned to thermonuclear

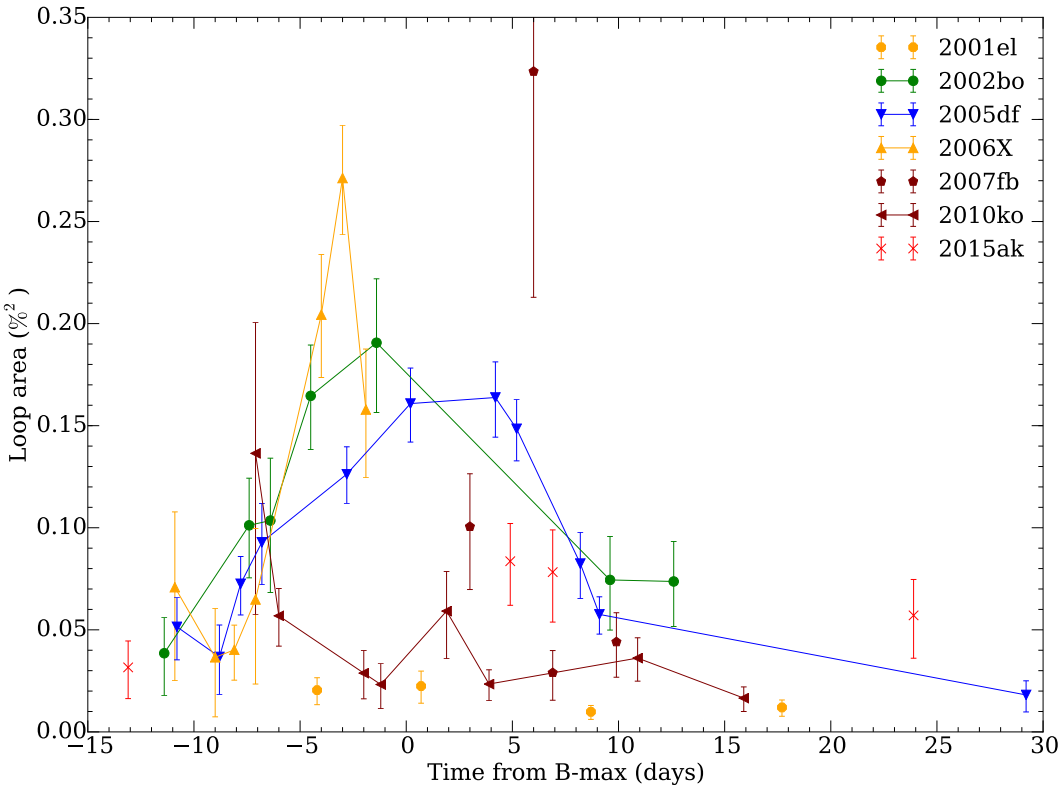

Figure 5.12.: The area contained in Q–U loops as a function of epoch. Shown are all supernovae that have been observed on at least four epochs (SN 2004dt is off scale in area). The lines connect measurements of SNe that have been observed on five epochs or more.

equilibrium.

5.4.4. Si II Q–U Loops

Some supernovae included in our sample display Q–U loops of the Si II line. The following objects show clear loops at multiple epochs: SN 2005df (at 8 different epoch from -7.8 to 9.1 days relative to peak brightness), SN 2006X (at five epochs from -8.1 to -1.9 days), SN 2002bo (at 5 epochs from -7.4 to 9.6 days), SN 2004dt (at 4 epochs from 4.4 to 33.2 days), SN 2007fb (at 3 and 6 days), and 2010ko (at 1.9 and 10.9 days). SN 2015ak shows a clear loop at 4.9 days, SN 2010ev at 11.9 days, SN 2011ae at 4 days, 2007hj at -1.1 days, 2005ke at -9.1 days, 2005cf at -5.8 days. SN 2001el (shows clear but small loops at epoch -4.2 and 0.7 days). Other SNe may show a loop on at least one epoch, but they are below the noise level and cannot be characterized in a statistically significant way.

To characterize in a quantitative way the evolution of the loops we calculated the area inside of the loops as described in Sect. 5.3.6. Figure 5.12 shows the area, A, as a function of epoch, for a subsample of SNe observed on at least 4 epochs before 30 days past peak brightness. The peculiar SN 2004dt is not shown, because the area is outside of the axis limits (A>0.32 $\%^2$, up to A~1.75 $\%^2$ at 4.4 days past peak).

To explore the effect of clumps on the polarization spectra and Q–U plane we run simple simulations (Bulla, priv. comm., see also Bulla 2017 for more details). In the simulations we make the following assumptions:

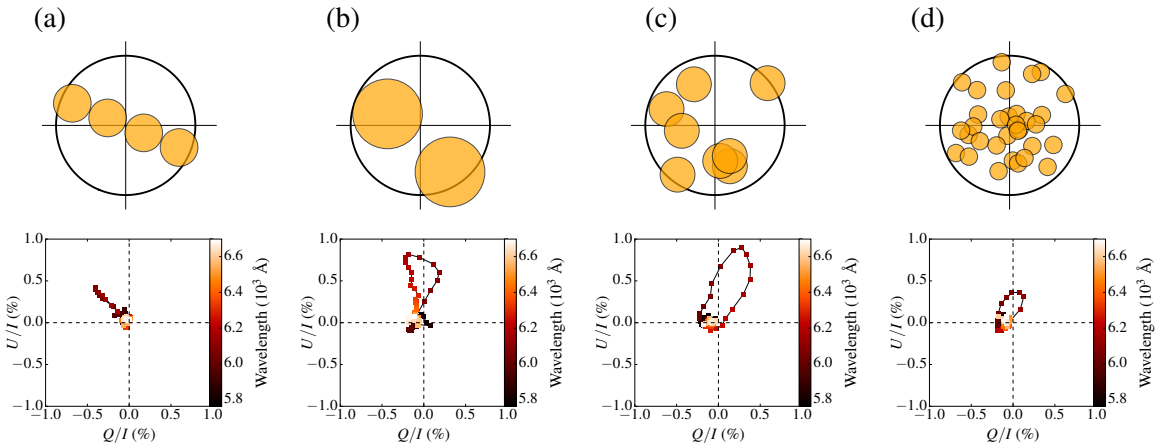

Figure 5.13.: Simulations of polarization induced by clumps, for four different scenarios. The upper panels illustrate the size and distribution of clumps, while the bottom panels show the resulting polarization in the Q–U plane. Panel (a) shows four clumps axisymmetrically distributed. It produces polarization, but no loops in the Q-U plane. The other three panels (b,c,d) show randomly distributed clumps, of different sizes. The smallest clumps produce small a loop, compared to the clumps of intermediate and large size.

- spherical ejecta
- photosphere at 10000 km s^{-1}
- roughly 0.5 $M_\odot$ above the photosphere
- outer boundary: $v_{outer} \sim 20\,000$ km s^{-1}
- density power law index = 7
- density at the photosphere = $7{\times}10^{-14}$ g cm^{-3}
- electron scattering optical depth: $\tau_{es} \sim 0.6$
- line opacity outside clumps: $\tau_{line} = 1$
- line opacity inside clumps: $\tau_{lineclumps} = 10$

The clump positions are generated randomly in regions of the ejecta moving toward the observer (blueshifted velocities). The Q and U signs are defined as in Bulla et al. (2015).

Also, the clump centers are randomly generated between the inner (photosphere) and outer boundary. Depending on the sizes, some regions of the clumps could actually fall either inside the photosphere or outside the ejecta (see upper panels in Figure 5.13).

Figure 5.13 shows simulations for four different scenarios. The left panel presents the case of four clumps with an axis-symmetric distribution, to simulate the effect of a torus. The clump sizes (in velocity space) are $v_{outer}/4.0 = 5000$ km s^{-1}. The other three panels show randomly distributed clumps, from left to right: 2 clumps with radius $v_{outer}/2 = 10\,000$ km s^{-1}, 8 clumps with radius $v_{outer}/4 = 5000$ km s^{-1}, and 32 clumps with radius $v_{outer}/8 = 2500$ km s^{-1}. The total covering factor of the clumps would be equal in the three simulations if there was no overlapping.

Non-zero polarization levels are found for all three simulations across the spectral line. In the case of an axis-symmetric distribution of the clumps, there are no loops in the Q–U plane, while for a non-axis-symmetric distributions, loops are produced. The loop areas look similar for the first two distributions, but are smaller in the third one with small clumps.

In SN 2005df, SN 2006X, and SN 2002bo, which have been observed on many epochs, we can observe the evolution of polarization of Si II line, from high polarization and no loops, over large loops, to small loops (see all plots in Appendix C.2). By comparing to the simple simulations, the evolution of loops can be explained by the change of the silicon ejecta size, from large axisymmetric structures, to large clumps, and finally to small clumps, as time evolves and the photosphere moves inwards.

5.4.5. Comparison to simulations

We compared our sample to simulations by Bulla et al. (2016b,a), who computed polarization spectra for different SN Ia explosion models. In particular, we examined the silicon line velocities and the Si II polarization in the polarization spectra of the delayed-detonation (DDT, Seitenzahl et al., 2013), double-detonation (Fink et al., 2010) and violent merger (Pakmor et al., 2012) models, at -5, -2.5, 0, 2.5, 5, 7.5 days relative to B-band maximum. We determined the maximum Si II polarization, and the wavelength of the absorption minimum to determine the photospheric expansion velocity.

These values are calculated for different viewing angles in each model. Specifically, we use only viewing angles for which we ran high signal-to-noise calculations: 5 orientations for DDT and violent merger models, and 3 orientations for double-detonation model. Choices of these angles are explained in Bulla et al. (2016b,a).

Figure 5.14 compares our observations to the delayed-detonation (DDT), violent merger, and double-detonation (DDET) models. The simulations show that the polarization degree of the Si II line in the violent merger observations are higher compared to the delayed-detonation and double-detonation models. Furthermore, the delayed-detonation and double-detonation models have a comparable degree of polarization. Our Si II line polarization observations are consistent with the predictions for the delayed-detonation and double-detonation models, while only SN 2004dt has a comparable polarization degree to the predictions for the violent-merger model.

Figure 5.15 shows the comparison between simulations and observations of the observed maximum polarization of the Si II line between -11 and 1 days relative to peak brightness, versus the Si II velocity at 5 days before the peak brightness. The DDT and DDET simulations results coincide with the observations, and the degree of Si II polarization in the violent merger simulation is offset from the DDT and DDET simulations. However, although the observations display a velocity-polarization trend, the velocity range of the simulations is not sufficient to reliably confirm a relationship.

5.5. Summary and conclusions

We reduced and examined archival spectropolarimetric data of a sample of 35 SNe Ia in a systematic way, observed with the FOcal Reducer and low dispersion Spectrograph between 2001 and 2015 at 128 epochs in total. To the best of our knowledge this is the largest polarimetric data-set ever examined. Our main results can be summarized as follows:

1. The linear polarization of the Si II λ6355Å line displays an evolution in time with a variety of peak polarization degrees from $\sim 0.1\%$–1.7% at epochs from -10 – 0 days relative to peak brightness (Fig. 5.9). This differs from previous studies based on smaller samples (Wang et al., 2007).

2. We populated the Δm_{15}–P_{SiII} plane, and re-analyzed the Δm_{15}–P_{SiII} relationship proposed by Wang et al. (2007). Although the overall behaviour is reproduced, our larger sample reveals a significantly larger scatter. We show that subluminous and transitional objects display lower

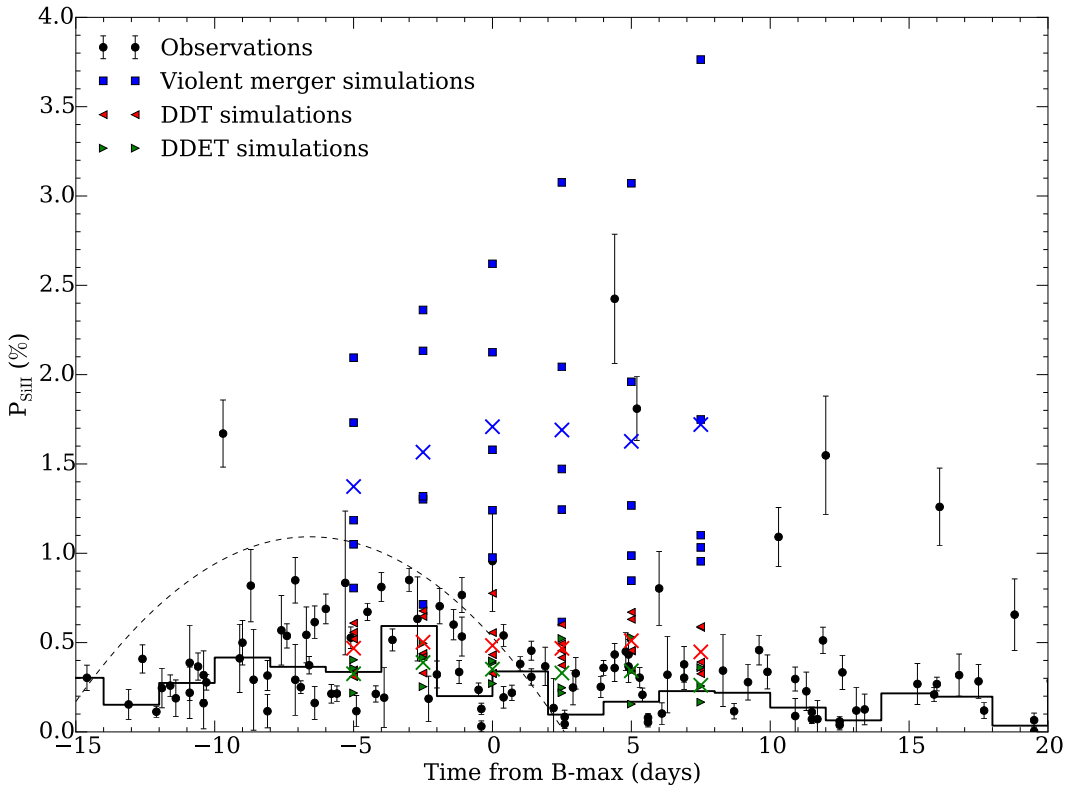

Figure 5.14.: Observed Si II λ6355Å for all epochs (black dots, measured on polarization spectra of 50Å bin size), compared to predictions by Bulla et al. (2016b,a) for the delayed-detonation (DDT, red triangles pointing left), violent merger (blue squares), and double-detonation (DDET, green triangles pointing right) models. Simulated values for multiple orientations at -5, -2.5, 0, 2.5, 5, 7.5 days relative to B-max are shown. The crosses mark the values averaged over all orientations, and the full black line is the weighted mean of our observations. For comparison, the dashed curve shows the $P_{SiII}(t)$ fit from Wang et al. (2007).

polarization values and are located below the main Δm_{15}–P_{SiII} relationship (Fig. 5.10). This confirms previous results based on smaller samples (Howell et al., 2001; Patat et al., 2012).

3. We found a statistically significant linear relationship ($\rho \gtrsim 0.8$) between the degree of linear polarization of Si II λ6355Å line before maximum with the Si II λ6355Å line velocity (Fig. 5.11). We suggest that this relationship, along with the Δm_{15}–P_{SiII} relationship (Wang et al., 2007) is consistent with the delayed-detonation model.

4. We investigate the evolution of the Si II line in the Q–U plane for a subsample of SNe, observed at multiple epochs, and run simple simulations to explore the effect of clumps on the polarization spectra. In the cases of SN 2005df, SN 2006X, and SN 2002bo, we observe the evolution of the formation of loops, growth, and shrinking of the loops (see all plots in Appendix C.2), which may be explained by the evolution of the projected silicon ejecta size, from large axisymmetric structures to large clumps, and finally to small clumps, as time evolves and the photosphere moves inwards.

5. We compared our sample of the Si II polarization to predictions calculated for the double-detonation, delayed detonation and violent merger models by Bulla et al. (2016b,a). Our Si

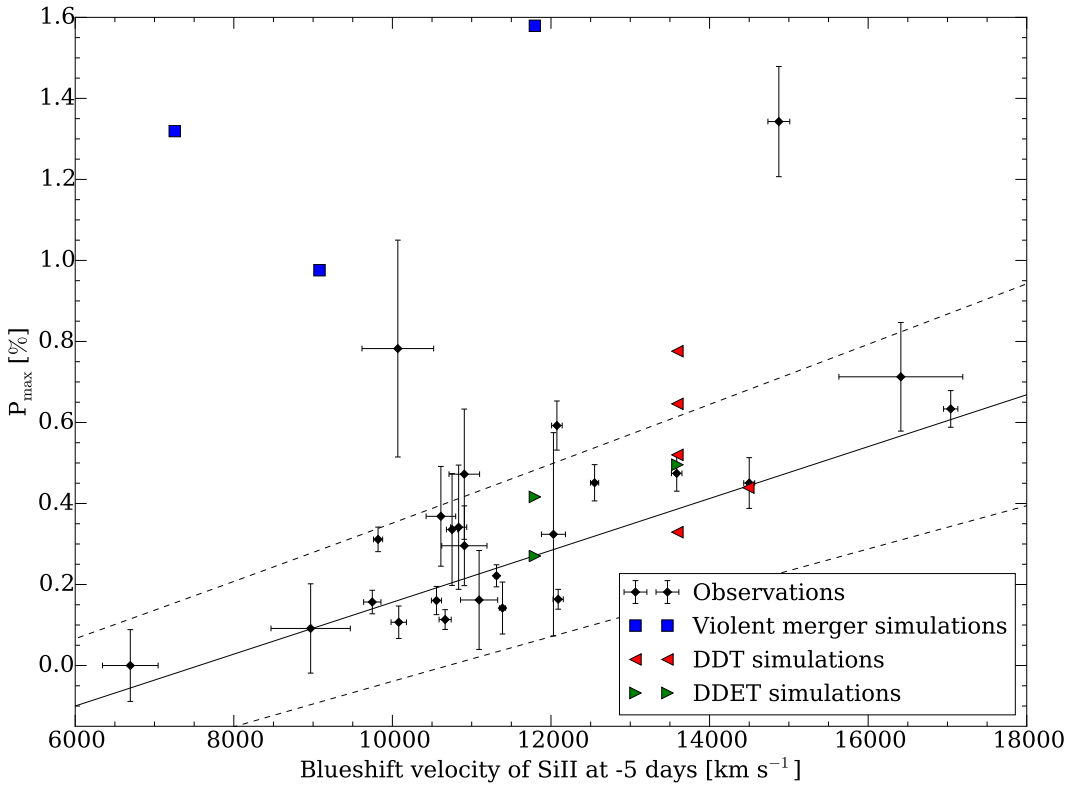

Figure 5.15.: The observed maximum polarization of the Si II λ6355Å line between -11 and 1 days relative to peak brightness, versus the Si II velocity at 5 days before the peak brightness (black dots), compared to simulations. Red triangles pointing left mark the delayed-detonation (DDT), blue squares the violent merger, and green triangles pointing right the double-detonation (DDET) model. The lines show the velocity-polarization relationship (solid line) and the uncertainty (dashed line).

II line polarization observations are consistent with the predictions for the delayed-detonation and double-detonation models, which have a comparable degree of polarization, while only SN 2004dt has a degree of polarization that is comparable to predictions for the violent-merger model.

6. We attempted to reproduce the Si II – velocity relationship using simulations by Bulla et al. (2016a,b). However, although the simulations show a global velocity-polarization trend, the velocity range of the simulations is not sufficient to reliably confirm the observed relationship.

Acknowledgements

Based on observations collected at the European Organisation for Astronomical Research in the Southern Hemisphere under ESO programmes 67.D-0517(A), 66.D-0328(A), 68.D-0571(A), 69.D-0438(A), 70.D-0111(A), 71.D-0141(A), 073.D-0771(A), 073.D-0565(A), 075.D-0628(A), 075.D-0213(A), 076.D-0178(A), 076.D-0177(A), 079.D-0090(A), 080.D-0108(A), 081.D-0557(A), 081.D-0558(A), 085.D-0731(A), 086.D-0262(A), 086.D-0262(B), 088.D-0502(A), 095.D-0848(A), 095.D-0848(B), 290.D-5009(A), 290.D-5009(B), 290.D-5009(C) and 290.D-5009(D).

6. Testing the magnetar scenario for superluminous supernovae with circular polarimetry

The content of this chapter corresponds to:
Cikota, A., Leloudas, G., Bulla, M., et al.
accepted for publication in the *Monthly Notices of the Royal Astronomical Society*

6.1. Introduction

Superluminous supernovae (SLSNe) may include a few remaining examples of deaths of extremely massive stars that in the early universe may have played an important role for re-ionisation of the Universe, and are therefore an important class of objects to understand. They are extremely bright, as the name would imply, and powering such a luminous display is a challenge. Peak luminosities of SLSNe are greater by a factor of ~5 than peak luminosities of type Ia Supernovae, and ~10-100 times greater than broad-lined type Ic and normal stripped envelope supernovae. They are divided in two classes: the hydrogen poor SLSN-I, which have quite featureless early spectra; and hydrogen-rich SLSN-II, which are thought to occur within a thick hydrogen shell and are therefore difficult to investigate (Gal-Yam, 2012).

Woosley et al. (2007) suggest that collisions between shells of matter ejected by massive stars that undergo an interior instability arising from the production of electron-positron pairs, or a pair-instability explosion of a very massive star (with a core of $\geq 50 M_{\odot}$, e.g. Gal-Yam et al., 2009; Dessart et al., 2013), might explain such luminous SLSNe-I (see also Woosley, 2016). The luminosity may also be produced by interaction between the ejecta and H-poor circumstellar material (Chatzopoulos et al., 2012; Vreeswijk et al., 2017; Sorokina et al., 2016).

Another possibility is that SLSNe-I are powered by an internal engine, such as a magnetar (Kasen & Bildsten, 2010; Inserra et al., 2013; Nicholl et al., 2013; Chen et al., 2015b) or an accreting black hole (Dexter & Kasen, 2013). Kasen & Bildsten (2010) have shown that energy deposited into an expanding supernova remnant by a highly magnetic (B $\sim 5 \times 10^{14}$ G) fast spinning neutron star can substantially contribute to the SLSN luminosity and explain the brightest events ever seen. They calculated that magnetars with initial spin periods < 30 ms can reach a peak luminosity of 10^{42}-10^{45} erg s^{-1} (M_{Bol}=-16.3 to -23.8 mag), because of the rotational energy deposition from magnetar spin-down.

In this work, we first time undertake circular polarimetry of Superluminous Supernovae in the visible part of the spectrum. We aim to test the magnetar scenario using circular polarimetry. Our hypothesis is that if there is a strong magnetic field, we expect to observe circularly polarized light, attributed to the monotonic gray-body magnetoemissivity which has been theoretically predicted by Kemp (1970), and demonstrated in the laboratory. The challenge for the magnetar observations is that the energy from the magnetar is reprocessed by the ejecta so that the bulk of the luminosity is arising from thermal processes (as is manifest in the spectra). In the thermalisation process the polarization of

the original light is destroyed. However, the magnetar's magnetic field will remain.

Circular polarization has already been observed in white dwarfs with strong magnetic fields. For instance, Kemp et al. (1970), and Angel et al. (1972) observed strong circular polarization, 1-3%, in visible light, and 8.5-15% in the infrared (Kemp & Swedlund, 1970) of Grw+70°8247. For this white dwarf they estimate a mean projected B field of 1×10^7 G.

Another possible origin of circularly polarized light may be an electron pitch-angle anisotropy in a relativistic jet, for instance from an accreting black hole, as suggested by Wiersema et al. (2014). They observed circular polarization in the afterglow of Gamma-ray burst 121024A, which are believed to be powered by a collimated relativistic jet from an accreting black hole.

In section § 2 we describe the targets and observations, in § 3 the methods, in § 4 we show the results, which we discuss in § 5, and the summary and conclusions are presented in section § 6.

6.2. Targets and observations

We obtained circular polarimetry of two SLSNe-I in a single epoch: OGLE16dmu at 101.3 days past peak (rest frame), and PS17bek at peak brightness. Additionally, we obtained linear polarimetry of PS17bek at four different epochs ($-4.0, 2.8, 13.4$ and 21.0 days relative to peak brightness in rest frame).

All observations in this study were acquired with the FOcal Reducer and low dispersion Spectrograph (FORS2, Appenzeller, 1967; Appenzeller et al., 1998; ESO, 2015) mounted at the Cassegrain focus of the UT1 Very Large Telescope (VLT), under the ESO program ID 098.D-0532(A), using the MIT CCD chip. The observations were obtained in the imaging polarimetry mode (IPOL). Circular polarimetry was obtained, without any filters, with two different quarter-wave retarder plate (QWP) angles of $\theta = \pm 45°$, but in two different rotations of the instrument (0° and 90°) in order to remove possible cross-talks between linear and circular polarization (Bagnulo et al., 2009).

Linear polarimetry of PS17bek was obtained through the V_HIGH FORS2 standard filter (λ_0 = 555 nm, FWHM = 123.2 nm), at four half-wave retarder plate (HWP) angles ($0, 22.5, 45, 67.5°$).

A observation log is given in Table 6.1.

6.2.1. OGLE16dmu

OGLE16dmu was discovered on September 23, 2016 (MJD 57654.84) (Wyrzykowski et al., 2016), and classified as a SLSN-I. The classification spectrum is shown in Fig. 6.1. It is apparently hostless at a redshift z~0.426 (Prentice et al., 2016). From GROND observations (Chen et al., in preparation), we determined an apparent magnitude at peak of m_r = 19.41 mag in November 11, 2016 (MJD 57698.41). The Galactic reddening at the position of OGLE16dmu is $E(B-V)$ = 0.03 mag (Schlafly & Finkbeiner, 2011), which corresponds to $A_r \sim 0.07$ mag assuming a Fitzpatrick (1999b) extinction law and R_V=3.1. The Galactic reddening-corrected absolute brightness is M_r = -22.2 mag.[1]

From the rest-frame light curve, we estimate the rate of decline in 30 days past maximum (Inserra & Smartt, 2014) to be $DM_{30} \sim 0.22$ mag. Put differently, using the metric described in Nicholl et al. (2015a) (the time to reach from f_{max} to f_{max}/e), we estimate $\tau_{dec} \sim 70.6$ days. Thus, this is a bright and slowly-evolving SLSN-I, similar to PTF12dam or SN 2015bn.

[1] we assume a flat universe with H_0 = 67.8 km s^{-1} Mpc^{-1} and Ω_M = 0.308 (Planck Collaboration et al., 2016).

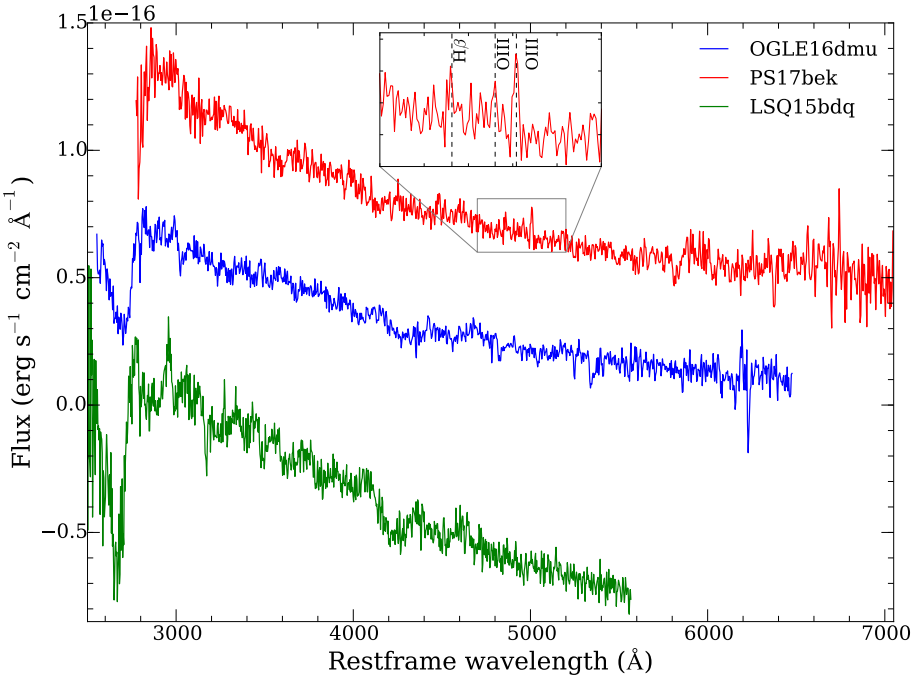

Figure 6.1.: PESSTO classification spectra of OGLE16dmu (middle blue spectrum) and PS17bek (top red spectrum), compared to LSQ14bdq (bottom green spectrum, Nicholl et al. 2015b). The inset shows the [OIII] and Hβ emission lines in the spectrum of PS17bek, used for the redshift determination. PS17bek and LSQ14bdq have been plotted with an constant offset of +4×10^{-17}, and -1×10^{-16} respectively.

6.2.2. PS17bek

PS17bek is a SLSN-I at z=0.30992 ± 0.0003 (see Fig. 6.1, PESSTO classification). It was discovered at α= 10:47:41.90 and δ= +26:50:06.0 and it is possibly associated to the galaxy GALEXMSC J104742.19+265006.8.

This region of sky was observed by Pan-STARRS in response to a possible low significance gravitational wave signal provided to us by LIGO-Virgo (Abbott et al., 2016), but this transient is not considered related to that event.

We determined an apparent magnitude at peak of m_r = 19.8 mag (Cano et al., in preparation) at MJD = 57814.58 days. The Galactic reddening at the position of PS17bek is $E(B-V)$ = 0.03 mag (Schlafly & Finkbeiner, 2011), which corresponds to $A_r \sim 0.07$ mag. Thus, the Galactic reddening-corrected absolute magnitude of PS17bek is $M_r \sim$ -20.7 mag.

For PS17bek we estimate a decline rate of $DM_{30} \sim 1.62$ mag or $t_{dec} \sim 23$ days. Thus, this is a fast-declining SLSN-I, similar to SN 2010gx or SN 2011ke. In fact, the measured decline rate implies that PS17bek is one of the fastest evolving SLSNe-I (see Inserra et al., 2018a). Starting from Gal-Yam (2012), it remains an unsolved issue whether H-poor SLSNe can be divided in more subclasses (e.g., Type I/Type R or fast/slow) and whether this division has physical implications (Inserra et al., 2018a; De Cia et al., 2017; Quimby et al., 2018). Irrespective, it remains an advantage that our experiment probes representative SLSNe from both sub-classes.

Table 6.1.: Observations log

Name	UT Date and Time	Filter	$\lambda/2$-plate angle [°]	$\lambda/4$-plate angle [°]	Wollaston angle [°]	Exposure [s]	Seeing ["]
PS17bek	2017-02-25 05:48:09	None	...	315	0	200	0.61
PS17bek	2017-02-25 05:53:59	None	...	45	0	200	0.62
PS17bek	2017-02-25 06:23:44	None	...	405	90	200	0.67
PS17bek	2017-02-25 06:28:02	None	...	135	90	200	0.61
PS17bek	2017-02-25 06:42:04	v_HIGH	0	...	0	650	0.67
PS17bek	2017-02-25 06:53:37	v_HIGH	45	...	0	650	0.63
PS17bek	2017-02-25 07:05:03	v_HIGH	22.5	...	0	650	0.66
PS17bek	2017-02-25 07:16:35	v_HIGH	67.5	...	0	650	0.55
PS17bek	2017-03-06 05:07:26	v_HIGH	0	...	0	520	0.71
PS17bek	2017-03-06 05:16:48	v_HIGH	45	...	0	700	0.60
PS17bek	2017-03-06 05:29:04	v_HIGH	22.5	...	0	700	0.59
PS17bek	2017-03-06 05:41:26	v_HIGH	67.5	...	0	700	0.50
PS17bek	2017-03-20 01:45:38	v_HIGH	0	...	0	700	0.64
PS17bek	2017-03-20 01:58:02	v_HIGH	45	...	0	700	0.69
PS17bek	2017-03-20 02:10:17	v_HIGH	22.5	...	0	700	0.70
PS17bek	2017-03-20 02:22:40	v_HIGH	67.5	...	0	700	0.86
PS17bek	2017-03-20 02:36:04	v_HIGH	0	...	0	700	0.68
PS17bek	2017-03-20 02:48:27	v_HIGH	45	...	0	700	0.67
PS17bek	2017-03-20 03:00:42	v_HIGH	22.5	...	0	700	0.77
PS17bek	2017-03-20 03:13:05	v_HIGH	67.5	...	0	700	0.81
PS17bek	2017-03-30 02:10:19	v_HIGH	0	...	0	500	0.69
PS17bek	2017-03-30 02:19:23	v_HIGH	45	...	0	500	0.72
PS17bek	2017-03-30 02:28:18	v_HIGH	22.5	...	0	500	0.68
PS17bek	2017-03-30 02:37:21	v_HIGH	67.5	...	0	500	0.56
PS17bek	2017-03-30 02:46:59	v_HIGH	0	...	0	500	0.47
PS17bek	2017-03-30 02:56:02	v_HIGH	45	...	0	500	0.54
PS17bek	2017-03-30 03:04:57	v_HIGH	22.5	...	0	500	0.58
PS17bek	2017-03-30 03:13:60	v_HIGH	67.5	...	0	500	0.81
OGLE16dmu	2017-03-30 23:59:36	None	...	315	0	220	0.74
OGLE16dmu	2017-03-31 00:04:14	None	...	45	0	220	0.85
OGLE16dmu	2017-03-31 00:18:00	None	...	405	90	220	0.84
OGLE16dmu	2017-03-31 00:22:38	None	...	135	90	220	0.75

6.3. Data processing and methods

The data consist of two science frames per exposure: the upper CHIP1 and lower CHIP2, which correspond to two mosaic-parts of the CCD detector. In IPOL mode, the image is split by the Wollaston prism in an ordinary (o) and extra-ordinary (e) beam, and the MOS Slitlets strip mask is inserted to

avoid overlapping of the beams. The observed target is located at the bottom of CHIP1 (upper frame), centered in the optical axis of the telescope. The bottom strip in the upper frame is the extra-ordinary beam. The Wollaston prism is usually aligned with the north celestial meridian except when the instrument is rotated by 90° during the second sequence of circular polarimetry, when it was aligned towards East.

All frames were bias subtracted using the corresponding calibration bias frames. A flat-field correction was not performed because the flat-field effect gets canceled out, because of the redundancy introduced by multiple HWP and QWP angles, for linear and circular polarimetry respectively (ESO, 2015; Patat & Romaniello, 2006).

To determine the polarization of our targets, we undertake aperture photometry of sources in ordinary and extra-ordinary beams using the IRAF's DAOPHOT.PHOT package. An optimal aperture radius of ∼2 FWHM was used.

6.3.1. Circular polarimetry

Following the FORS2 user manual (ESO, 2015), the amount of circular polarization is given as:

$$V = \frac{1}{2}\left[\left(\frac{f^o - f^e}{f^o + f^e}\right)_{\theta=45^\circ} - \left(\frac{f^o - f^e}{f^o + f^e}\right)_{\theta=-45^\circ}\right] \tag{6.1}$$

where f^o and f^e are the measured flux in the ordinary and extra-ordinary beam respectively, for both quarter-wave retarder plate angles of $\theta = \pm 45^\circ$. The circular polarization error was calculated by error propagation of the flux errors.

To minimize a possible linear-to-circular polarization cross talk (Bagnulo et al., 2009), we calculate the average of the Stokes V measured at two instrument position angles, ϕ, and ϕ+90°:

$$P_V = \frac{V_\phi + V_{\phi+90^\circ}}{2}, \tag{6.2}$$

which leads to cancellation of the spurious signal (Bagnulo et al., 2009).

6.3.2. Linear polarimetry

The Stokes Q and U for PS17bek and a number of field stars were derived using the standard approach, as described in Leloudas et al. (2015a); that is via the Fourier transformation of normalized flux differences measured at four half-wave retarder plate angles of 0, 22.5, 45 and 67.5° (see also the FORS2 manual, ESO, 2015).

We correct the polarization position angles of the raw measurements for the half wave plate zero angle chromatic dependence (Table 4.7 in ESO, 2015), and for the instrumental polarization, which increases with distance from the optical axis (Fig. 5 in Patat & Romaniello, 2006). In addition, we used 7 field stars to determine the interstellar polarization (ISP) by calculating their barycenter in the Q–U plane for each epoch (Fig. 6.2). The stars give a stable and self-consistent result with time:
Q_{ISP} = 0.066 ± 0.004 %
U_{ISP} = -0.007 ± 0.018 %.
Thus, P_{ISP} = 0.066 ± 0.004 %. This value is lower than the expected maximum interstellar polarization, $p_{max} = 9.0 \times E(B-V)$, determined by Serkowski et al. (1975), taking the Galactic reddening at the position of PS17bek, $E(B-V)$ = 0.027 ± 0.004 mag (Schlafly & Finkbeiner, 2011).

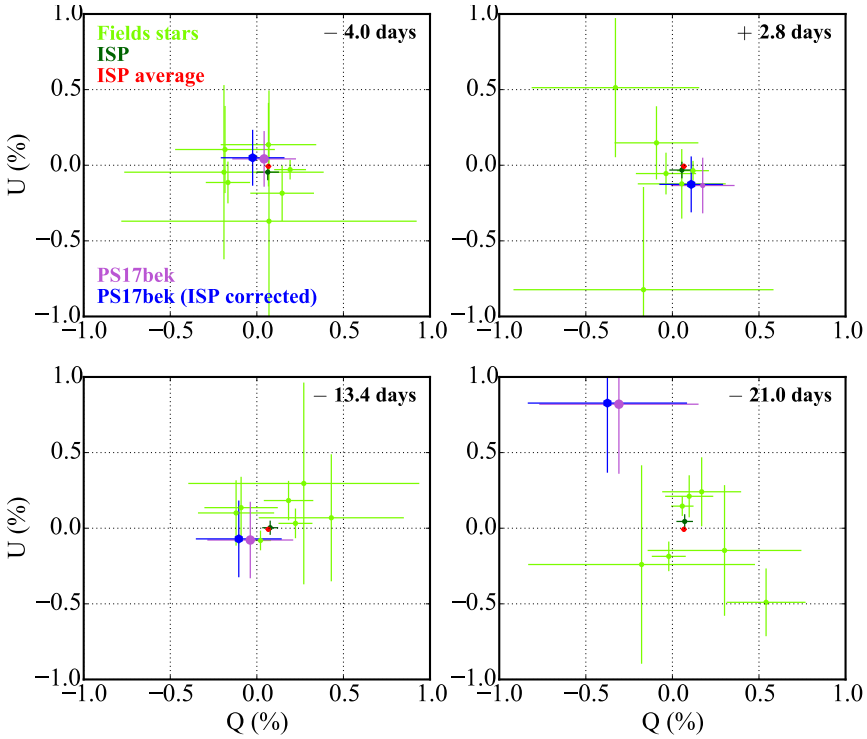

Figure 6.2.: Q–U plane for all 4 epochs of PS17bek. Comparison stars are colored light green. In each panel, a dark green cross indicates the position of the ISP, calculated as the barycenter of the stars in each epoch. The red cross is the ISP averaged over all epochs, which coincides with the dark green cross in the individual epochs. The original measurement of the SN is shown in magenta and the ISP corrected value in blue.

Additionally, we do a polarization bias correction, using the following equation, given in Espinosa et al. (1997):

$$P \sim P_{obs} \sqrt{1 - \left(\frac{\sigma_P}{P_{obs}}\right)^2} \tag{6.3}$$

6.4. Results

We undertook circular polarimetry for two SLSNe-I: OGLE16dmu 101.3 days after peak brightness (in rest frame), and PS17bek 4.0 days before peak brightness.

The circular polarization of both SLSNe is consistent with zero. We measured a circular polarization of P_V=-0.55 ± 1.31 % for OGLE16dmu, and P_V=-0.21 ± 0.18 % for PS17bek. The results are summarized in Table 6.2. The signal-to-noise ratio of PS17bek observed at different instrument rotation angles ϕ of 0 and 90 degrees is S/N~272 and ~172 respectively, while for OGLE16dmu S/N~62 (at ϕ=0 deg) and ~59 (at ϕ=90 deg), which explains the large uncertainties of the calculated polarization[2].

Figure 6.3 shows a section of the FORS2 imaging polarimetry field for OGLE16dmu and PS17bek taken with different instrument position angles. The target is marked with a red circle, and for comparison, other field stars with green circles. The radii of the circles are proportional to the absolute

[2]The absolute error of P is related to the signal-to-noise ratio as $\sigma_P = \frac{1}{\sqrt{N/2}\,SNR}$, where N is the number of waveplate angles used (Patat & Romaniello, 2006).

Table 6.2.: Circular polarimetry results

SLSN	Phase	V_{0° (%)	V_{90° (%)	P_V (%)
PS17bek	-4.0 d	-0.33 ± 0.25	-0.08 ± 0.27	-0.21 ± 0.18
OGLE16dmu	+101.3 d	-0.58 ± 1.30	-0.52 ± 2.28	-0.55 ± 1.31

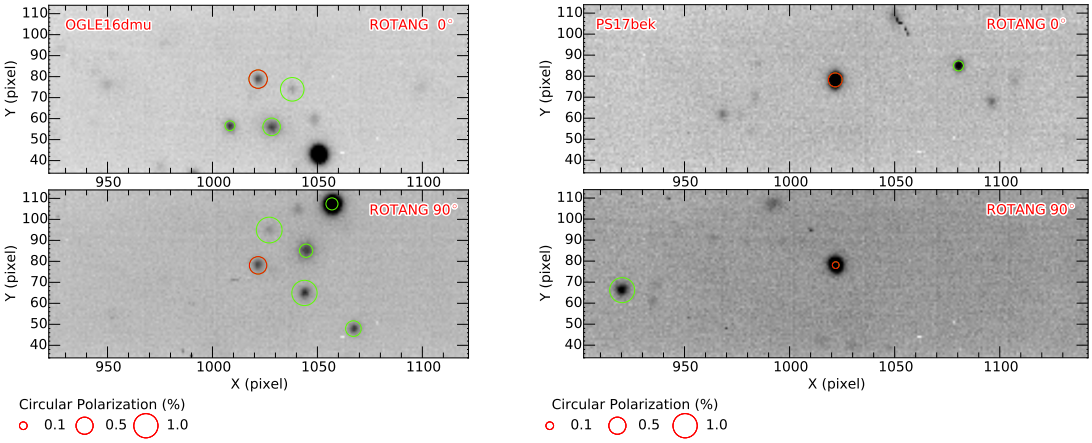

Figure 6.3.: Sections of ordinary beams for single imaging polarimetry exposures for OGLE16dmu (left) and PS17bek (right). The top and bottom panels are exposures taken with 0° and 90° instrument rotation respectively. The red circles mark the targets, while green circles mark comparison stars in the field. The radii of the circles correspond to the absolute circular polarization, as indicated in the legend.

value of circular polarization. It is shown that the measured polarization of our targets is consistent with polarization of field stars which are expected to be unpolarized. Furthermore, the fainter sources with lower S/N have larger polarization values, but also higher uncertainties.

The ISP-corrected linear polarization measurements of PS17bek are given in Table 6.3, and shown in Figure 6.4. At least for the first 3 epochs (-4, 2.8, 13.4 relative to peak brightness), the linear polarization of the SLSN is very similar to the one of the field stars and consistent with zero in Q and U. Thus, there is no significant linear polarization at these phases. The fourth epoch (21.0 days past maximum brightness) might indicate a larger polarization (~0.8 %) but the result is not highly significant. The SNR at the last phase is 154 (the SN has faded), which is significantly lower than at -4 days (SNR~384), 2.8 days (SNR~384) and 13.4 days (SNR~282) relative to peak brightness. Considering that the uncertainty of the last phase is ~0.5%, this is a 2σ result.

Table 6.3.: ISP corrected linear polarimetry results for PS17bek

Phase	Q (%)	U (%)	P^* (%)	ϕ (°)
-4.0	-0.02 ± 0.18	0.05 ± 0.18	0.0 ± 0.18	56.3 ± 97.1
2.8	0.1 ± 0.18	-0.13 ± 0.18	0.0 ± 0.18	-26.5 ± 31.6
13.4	-0.11 ± 0.25	-0.06 ± 0.25	0.0 ± 0.25	-74.6 ± 56.8
21.0	-0.32 ± 0.46	0.85 ± 0.46	0.78 ± 0.46	55.4 ± 14.5

* polarization-bias corrected

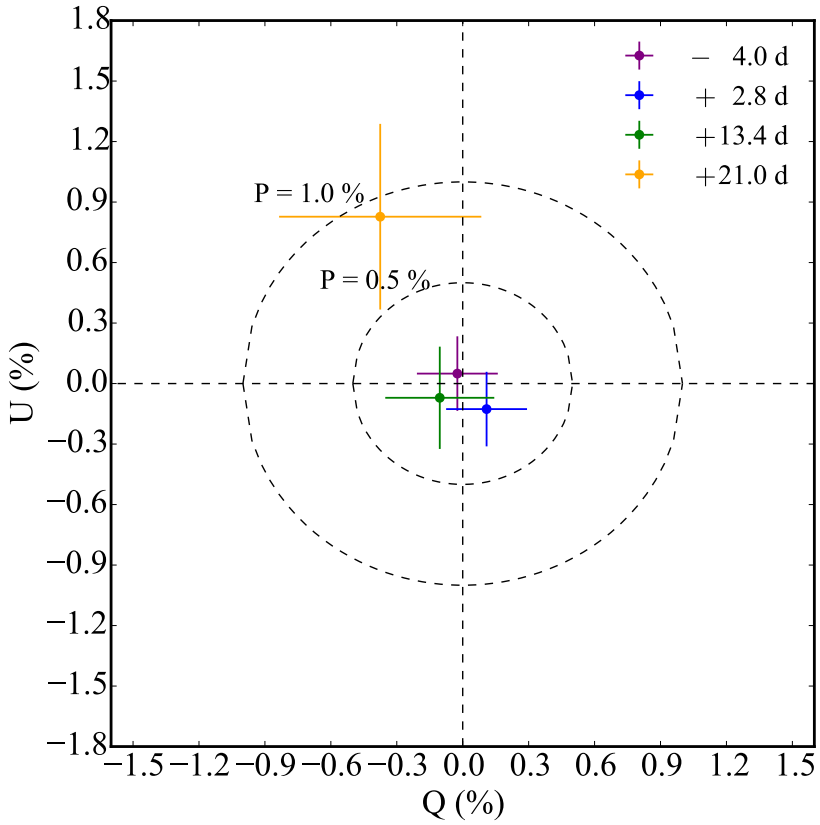

Figure 6.4.: Stokes Q–U plane for PS17bek observed at four epochs. The different colors indicate different epochs: -4.0 (purple), 2.8 (blue), 13.4 (green) and 21.0 (yellow) days relative to peak brightness. The dashed concentric circles of equal polarization have a radius of 0.5 % and 1.0 % respectively.

6.5. Discussion

6.5.1. Circular polarimetry of OGLE16dmu and PS17bek

In the magnetar scenario, a rapidly rotating magnetar is born during a core-collapse SN explosion. The explosion ejects many solar masses of material, which expands while the magnetar spins down. The spin-down injects $\sim 10^{51}$ ergs into the ejected material, that in the meanwhile expanded to a distance of $\sim$100 AU, and heats it up, which then radiates the energy away (Woosley, 2010; Kasen & Bildsten, 2010; Inserra et al., 2013; Vink, 2015).

The idea behind observing a target at early phase was to possibly detect an imprint of the strong magnetic field in the ejected material, while the aim of observing a target at late phase was to observe emitted light of the photosphere which moves inwards with time, closer to the magnetar, as the ejecta expands and becomes transparent.

Kemp (1970) predicted that a "gray-body" model in a magnetic field will emit a fraction of circularly polarized light. The degree of polarization, q, is proportional to the emitting wavelength, λ, and the strength of the magnetic field, B (see Eq. 7 and 16 in Kemp, 1970), and is given by:

$$q(\lambda) \simeq -\frac{\lambda e B}{4\pi m c}, \tag{6.4}$$

where e and m are the electron's charge and mass respectively, and c is speed of light.

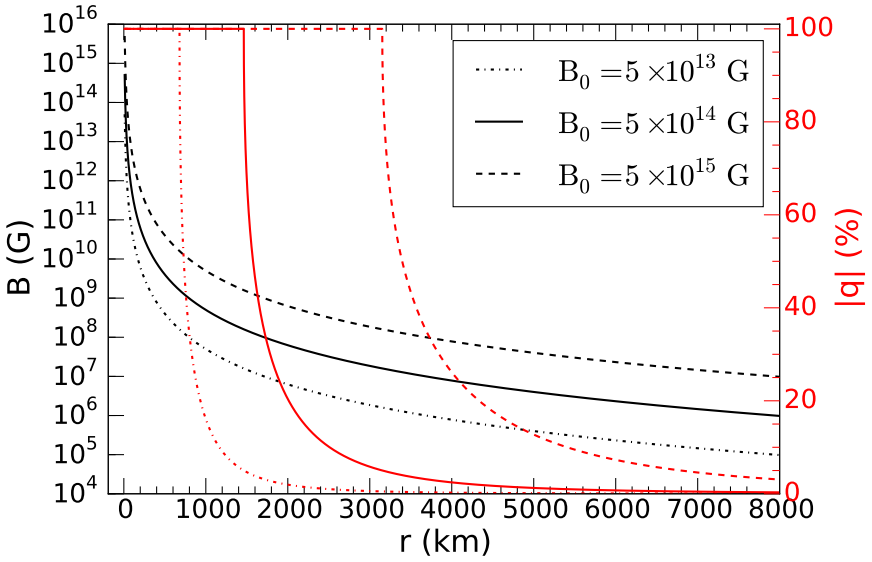

Figure 6.5.: Maximum magnetic field strength (black lines) and absolute circular polarization, q (red lines), in the optical (λ=0.67 μm) as a function of distance, r, for three different initial surface magnetic field strengths, B_0, at R_0=10 km.

However, since the magnetic field is decreasing with distance, proportional to 1/distance^3, the polarization will drop very quickly. Assuming a magnetic field B_0 at the surface of a magnetar with radius R_0, the maximum magnetic field decreases as a function of distance, r, as following:

$$B(r) = B_0 \left(\frac{R_0}{r}\right)^3 . \tag{6.5}$$

Figure 6.5 shows the magnetic field, B, and the circular polarization attributed to gray-body magnetoemissivity, q, as a function of distance, calculated in the optical (λ = 0.67 μm), for three different surface magnetic strengths, B_0, for a magnetar of radius R_0 = 10 km.

For example, assuming a surface magnetic field strength of B_0=5 × 10^{15} G, the magnetic field strength drops to 4×10^4 G at a distance of only 5 ×10^4 km. The degree of polarization produced by gray-body magnetoemissivity at that distance is q~ 0.01 %, which is beyond our detection capabilities.

Furthermore, our observations were taken without any filter in order to achieve a high SNR in a reasonable time, while the absolute degree of circular polarization produced by gray-body magnetoemissivity increases with wavelength (see Eq. 6.4). Therefore, it is generally recommended to observe circular polarization in the infrared wavelengths.

Therefore, despite a non-detection of circular polarization in SLSN-I sightlines, the magnetar scenario can not be excluded as the internal engine of SLSNe, because in order to observe circularly polarized light attributed to gray-body magnetoemissivity, it is necessary that the light is emitted within strong magnetic fields, close to the magnetar, which is not the case in the magnetar scenario as described e.g., by Kasen & Bildsten (2010), in contrast to the observed circular polarization in white dwarfs (e.g. Kemp et al., 1971; Rich & Williams, 1973), where the observed light is emitted from the white dwarf's surface.

Another possibility about the lack of observed circular polarization is that OGLE16dmu and PS17bek are not driven by an internal engine at all. For instance, other possible scenarios that could

explain such a high luminosity is a pair-instability supernova (PISN, e.g. Woosley et al., 2007; Gal-Yam et al., 2009; Dessart et al., 2013; Woosley, 2016), or a normal SN explosion interacting with circumstellar shells (e.g. Chatzopoulos et al., 2012; Vreeswijk et al., 2017; Sorokina et al., 2016). In case of a PISN, which requires high amounts of ^{56}Ni to explain the luminosity, the light curves are expected to evolve slowly, which likely rules out this scenario for PS17bek that has one of the fastest evolving light curves (Chen et al., in preparation). However, it is beyond the scope of this short paper to analyze the light curves for those SLSNe.

6.5.2. Linear polarimetry of PS17bek

Intrinsic linear polarization of SNe is a measure of the supernova's photosphere spherical asymmetry projected on the sky. If the projection of the photosphere is not symmetric, more photons will be scattered by electrons along the photosphere's major axis than along the minor axis, which will produce net-polarization in the continuum (see e.g. Hoflich, 1991; Kasen et al., 2003; Bulla et al., 2015).

Because SLSNe are faint, and thus it is hard to undertake polarimetry which requires high SNR, only a few SLSNe have been studied using polarimetry (Leloudas et al., 2015a; Inserra et al., 2016a, 2018b; Leloudas et al., 2017; Bose et al., 2018).

LSQ14mo, also a fast-declining SLSN-I (as PS17bek), did not show evidence for significant polarization or polarization evolution from −7 and up to +19 days with respect to maximum (Leloudas et al., 2015a). In the contrary, the slowly-evolving SN 2015bn did show an increase in polarization with time, that was attributed to the photosphere receding to inner layers of the explosion that are more asymmetric. Inserra et al. (2016a) obtained the first spectropolarimetric observations of a SLSN-I, at −24 and +28 days, further showing that the geometry was consistent with an axisymmetric configuration (that could be consistent with a magnetar scenario). The polarization increase was confirmed by Leloudas et al. (2017) who obtained multi-epoch imaging polarimetry between −20 and +46 days, showing that the increase was coincident with changes in the optical spectrum.

The result obtained for PS17bek adds up in the small sample and is fairly consistent with the picture obtained from previous events. Similarly to the other SLSNe-I, observed around peak, no significant polarization is detected. Our last observation (at +21 days) could be consistent with an increase in polarization but the significance of this result is below 2σ. Either fast-evolving SLSNe (PS17bek and LSQ14mo) follow a different geometrical evolution than slowly-evolving SLSNe, or simply the available data, due to a combination of low SNR and lack of data at late phases, are not able to significantly detect an increase in polarization.

6.6. Summary and conclusions

In this work, we investigated circular polarization of two hydrogen poor superluminous supernovae for the first time, using FORS2 at the VLT. Our main results can be summarized as follows:

1. OGLE16dmu is a slowly evolving hydrogen poor SLSN. We undertook circular imaging polarimetry at phase 101.3 days past peak (in rest frame r band) and found no evidence of circular polarization.

2. PS17bek is a fast evolving SLSN-I. We undertook circular polarimetry at -4.0 days relative to the peak brightness (in rest frame r band), and found no evidence of circular polarization.

3. Additionally, PS17bek was observed in linear polarimetry mode at four phases (-4.0, 2.8, 13.4 and 21.0 days), and shows no significant linear polarization.

4. We can not exclude the magnetar scenario because of a non-detection of circular polarization, because the strong magnetic field drops with $1/r^3$ with distance r, and thus, the light will be significantly circularly polarized by gray-body magnetoemissivity only at very near distances ($\lesssim$ 5000 km) to the surface of the magnetar.

5. We note that future attempts to measure the strength of magnetic fields using circular polarimetry shall be made in the infrared, where the expected degree of circular polarization produced by gray-body magnetoemissivity is higher.

6. It is not likely that we will observe circular polarization produced by gray-body magnetoemissivity, because (assuming the magnetar scenario) the bulk of the luminosity is arising from thermal processes in the ejecta, which is at large distances from the magnetar, where the magnetic fields are not strong enough to produce significant circular polarization, however, such observations are valuable because it also allows us to probe the existence of relativistic jets.

Acknowledgements

Based on observations made with ESO Telescopes at the Paranal Observatory under programme ID 098.D-0532(A). MB acknowledges support from the Swedish Research Council (Vetenskapsrådet) and the Swedish National Space Board. TWC acknowledgments the funding provided by the Alexander von Humboldt Foundation.

7. Other methods to investigate supernova progenitors: A spatially resolved analysis of superluminous supernovae PTF 11hrq and PTF 12dam host galaxies

The content of this chapter has been published in:
Cikota, A., De Cia, A., Schulze, S., et al.
Monthly Notices of the Royal Astronomical Society, Volume 469, Issue 4, p.4705-4717

7.1. Introduction

Superluminous supernovae (SLSNe) are the most luminous supernovae in the universe. They are found in extreme star-forming galaxies and are probably connected with the death of massive stars (see § 1.3.3). The main difficulty of investigating SLSNe with polarimetry is that they are very distant, and thus faint. Another approach to investigate SLSN progenitors is by studying their host galaxy environments. One hallmark of very massive progenitors would be a tendency to explode in very dense, UV-bright, and blue regions.

In this chapter we investigate the spatially resolved properties, in particular the color and light fraction, of two among the nearest hydrogen-poor SLSNe (SLSNe-I) host galaxies. We focus on the host galaxies of two slowly-decaying hydrogen-poor SLSNe (SLSNe-R, see § 1.3.3), for which we have obtained *HST* multi-band imaging. Furthermore, we obtained integral field spectroscopy of one of the hosts with VLT/MUSE, and additionally investigate the line strength, metallicity and the kinematics at the SN location.

The chapter is organized as following. In Sect. 2 and 3 we describe the targets, and observations and data reduction, respectively. In Sect. 4 the methods and data analysis are presented. We then discuss the results in Sect. 5, and present our conclusions in Sect. 6.

7.2. The targets

The SLSNe-R PTF 11hrq and PTF 12dam were discovered by the Palomar Transient Factory (PTF, Law et al., 2009; Rau et al., 2009). While Perley et al. (2016) and Thöne et al. (2015) included some preliminary commentary on the morphology and properties of host galaxies of PTF 11hrq and PTF 12dam, we will provide a more detailed quantitative and spatially resolved analysis of these systems.

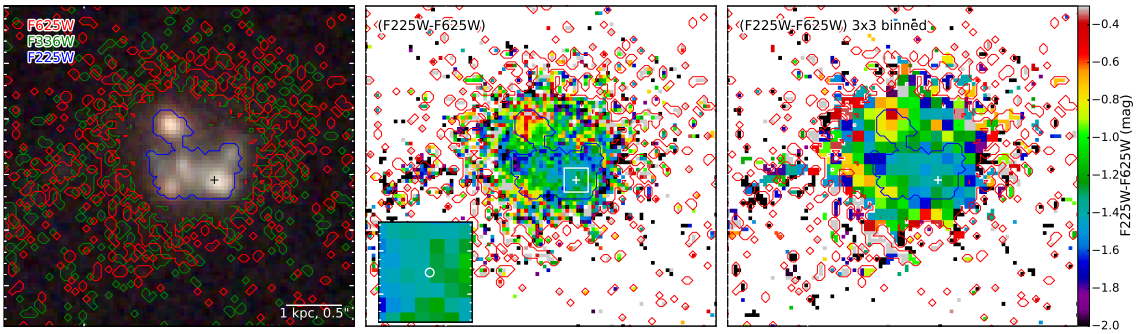

Figure 7.1.: Color maps for the host galaxy of PTF 12dam. Left: A *HST* composite color image. The contours denote the 3σ flux level above noise for *F225W* (blue), *F336W* (green) and *F625W* (red). Middle: *F225W-F625W* color map. The SN position is marked with the white cross. The region inside of the white box is zoomed-in in the subplot. The radius of the white circle in the inset plot corresponds to the position uncertainty of ~ 0.01 arcsec. Right: color map of 3x3 binned data.

7.2.1. PTF 12dam

PTF 12dam is among the most nearby SLSNe-I known, and happened in SDSS J142446.21+461348.6 at a redshift of $z = 0.1073$. The host galaxy of PTF 12dam has also been studied by Thöne et al. (2015), Chen et al. (2015b), and Perley et al. (2016), who found a metallicity of $12 + \log(\mathrm{O/H}) = 8.0$ throughout the galaxy. This metallicity is low, but not the most extreme compared to other SLSNe host (some H-poor SLSNe have $12 + \log(\mathrm{O/H}) \lesssim 7.8$; see e.g. Leloudas et al., 2015b). They also observed an extended asymmetric halo or tidal tail. Furthermore, the host galaxy of PTF 12dam has one of the highest star-formation rates (SFRs) among SLSNe hosts. Thöne et al. (2015) performed partially resolved long-slit spectroscopy probing the kiloparsec environment of the SN site and suggest that the progenitor of PTF 12dam is a > 60 $\mathrm{M}_\odot$ star, formed in a recent starburst.

7.2.2. PTF 11hrq

PTF 11hrq is the nearest among all known SLSNe-I, and is also presented in Perley et al. (2016). It exploded in an uncatalogued galaxy at a redshift of $z = 0.057$. The galaxy might be a disk galaxy, but does not show a clear structure, and is not particularly young or starbursting, as estimated from slit spectroscopy. Perley et al. (2016) determined a metallicity $12 + \log_{10}(\mathrm{O/H}) = 8.15 \pm 0.03$ from emission-line diagnostics, a dust extinction $A_V = 0.29 \pm 0.07$ mag (which corresponds to $E(B-V) \sim 0.07$ mag) from the Balmer-decrement, and a dust-corrected star-formation rate of $0.196 \pm 0.04 M_\odot$ yr^{-1} based on the Hα emission. They measured a rest-frame equivalent width of [OIII]λ5007Å for this galaxy, $EW([OIII]) = 40 \pm 1$Å[1].

7.3. Observations and data reduction

The host galaxies of PTF 12dam and PTF 11hrq were observed with *HST* as part of the programme GO 13858 (PI: De Cia). They were originally selected as host galaxies of SLSNe-R. The two galaxies were observed in Ultraviolet-Visible (UVIS) *F625W*, *F336W* and *F225W* passband filters with the

[1]The quoted error is the statistical uncertainty and is usually underestimated, because it does not include effects such as slit corrections or continuum absorption features.

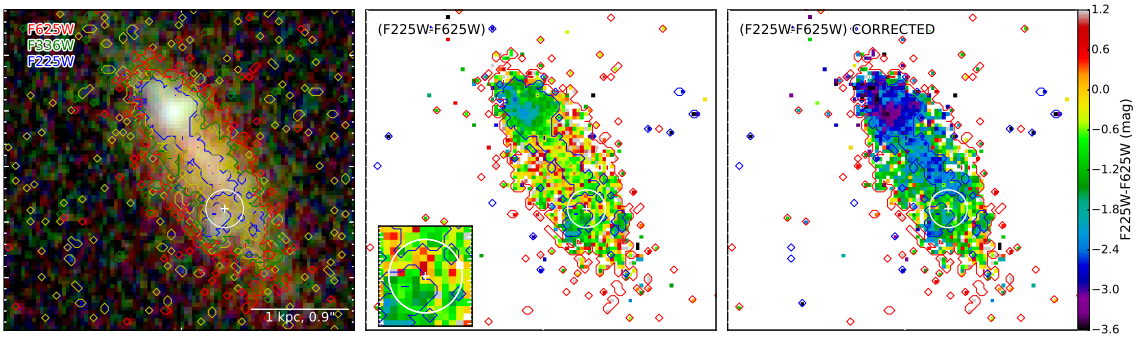

Figure 7.2.: Color maps for the host galaxy of PTF 11hrq. Left: A *HST* composite color image. The contours denote the 3σ flux level above noise for *F225W* (blue), *F336W* (green) and *F625W* (red). The yellow line denotes 2σ flux level above noise for *F225W*. Middle: *F225W-F625W* color map. The SN position is marked with the white cross. The radius of the white circle corresponds to the position uncertainty of ∼ 0.17 arcsec. Right: Color map corrected for dust extinction (see Section § 7.4.5.4).

Table 7.1.: Log of *HST* observations

Host galaxy	Observing date (UT)	Filter	Exp. Time (seconds)
PTF 11hrq	2014-11-14 05:04:49	*F625W*	2×100
PTF 11hrq	2014-11-14 05:14:44	*F336W*	2×460
PTF 11hrq	2014-11-14 06:39:48	*F225W*	400+413
PTF 12dam	2014-10-16 17:59:45	*F625W*	2×100
PTF 12dam	2014-10-16 18:09:40	*F336W*	2×492
PTF 12dam	2014-10-16 18:42:09	*F225W*	2×433

Wide Field Camera 3 (WFC3). A log of the observations is listed in Table 7.1. Two more host galaxies of H-poor SLSNe (initially classified as SLSNe-R), PTF 13dcc (Vreeswijk et al., 2017) and PTF 13ehe (Yan et al., 2015), were observed as well as part of GO 13858, but only in one passband filter, *F625W*, and at an early phase, while the SNe were still bright (Nicholl et al., 2013; Vreeswijk et al., 2017). Thus we do not investigate the host galaxies of PTF 13dcc and PTF 13ehe in this work. The images were processed using standard astrodrizzle tools provided by the Space Telescope Science Institute (STScI), as described in more detail in §3.2 of Perley et al. (2016).

The effective wavelengths of the *F225W*, *F336W* and *F625W* filters are 235.9 nm, 335.5 nm and 624.2 nm respectively, which correspond to restframe wavelengths of 213.0 nm, 303.0 nm and 563.7 nm for PTF 12dam at a redshift of z = 0.1073; and 223.2 nm, 317.4 nm and 590.5 nm for PTF 11hrq (z=0.057).

Additionally, we observed the PTF 11hrq field with the Multi Unit Spectroscopic Explorer (MUSE, Bacon et al., 2010) integral field unit spectrograph mounted at UT4 of ESO's VLT. MUSE has a field-of-view of 60 × 60 arcsec, covered by 24 individual identical integral field units, each supplied with a slicer of 48 mirrors arranged in 4 × 12 stacks. Each spatial element (spaxel) has a size of 0.2 × 0.2 arcsec. This configuration gives a wide spectral range from 4750 to 9350 Å and a spectral resolution ranging from R = 1800 − 3500 across the wavelength domain.

The observation of PTF 11hrq was obtained on October 1st, 2016 as a part of the programme 097.D-1054 (PI: Kim) and consisted of three exposures with an individual integration time of 1200 s. Each integration was dithered by 3 arcsec and rotated by 90°. The full width at half maximum of the reconstructed R-band image (i.e., the seeing) is 0.71 arcsec.

We reduced the data in a standard fashion with the MUSE pipeline package version 1.6.2 that is a part of the ESO Recipe Execution Tool (ESOREX). We removed sky lines with the Zurich Atmosphere Purge (ZAP) software package (Soto et al., 2016) and matched the astrometry to our *HST* images.

7.4. Methods and Data analysis

7.4.1. Morphology of the host galaxies

The *HST* observations reveal a more complex morphology than what was accessible from ground-based imaging, for both host galaxies. In the case of PTF 12dam, the host galaxy has a complex morphology with five bright knots (Fig. 7.1). The extended asymmetric halo observed by Perley et al. (2016) and Thöne et al. (2015) is partly visible in our images, as an extended structure in the west part of the galaxy. The host galaxy of PTF 11hrq has one bright knot in the northern part (Fig. 7.2).

7.4.2. Supernovae position in their host galaxies

7.4.2.1. PTF 12dam position

To locate the exact position of PTF 12dam in our *HST* images, we use an *HST* WFC3/UVIS image of the SN taken before maximum light, on May 26th, 2012 (Proposal ID: 12524, PI: Quimby), through the *F200LP* filter, and our *F625W* image. Using SExtractor (Bertin & Arnouts, 1996) we extract sources on both images. The uncertainty on the barycenter position of the SN is less than a fraction of a pixel (~ 0.002 pixel, or $\sim 1{\times}10^{-5}$ arcsec). We perform relative astrometry, using coordinate lists containing 6 common stars. We compute an image solution for our *HST* data using the images.imcoords.ccmap routine from the PyRAF/STSDAS package. The root-main-square (rms) of the image solution is 0.01 arcsecond for both right ascension and declination. The final estimated position uncertainty of the SN (calculated by taking the square root of the sum of squared rms values) is ~0.01 arcsec, and depends on the SN centroid uncertainty and the *HST* image solution uncertainty. The SN is located between two pixels. Figure 7.1 (left panel) shows a colour and countor-plot image of the host galaxy of PTF 12dam.

7.4.2.2. PTF 11hrq position

We determine the position of the SN in the *HST* images relative to the Palomar Transient Factory (PTF) discovery image, observed on 2011-07-11. Since there are no common stars in the *HST* and PTF field, we use a VLT/FORS2 image observed on 2012-12-17 (Prog ID: 090.D-0440(A), PI: Mazzali) as an intermediate image to transfer the world coordinate system (WCS) from the PTF to the *HST* image. We localize the sources on all images using SExtractor. The uncertainty on the barycenter position of PTF 11hrq in the PTF field is ~ 0.02 pixel, which corresponds to ~ 0.02 arcsecond. To confirm the position, we compared the PTF image from 2011-07-11 to PTF images from July 12, July 13, when the SN was at brightest. There is no discernible difference between the centroids in the images, aligned in WCS. The image from July 13 has a significantly larger PSF (seeing of 4.62 arcsec, compared to 3.46 arcsec on July 12 and 3.15 arcsec on July 11, as recorded in the fits header).

We use 13 common stars in the PTF and FORS2 field, and compute an astrometric solution for the FORS2 field using the images.imcoords.ccmap routine from the PyRAF/STSDAS package. The

rms of the fourth-order polynomial fits is 0.1 arcsecond in both axes, right ascension and declination. There are only three common sources in the FORS2 and *HST* fields, which is not sufficient to obtain an image solution, however, we calculated the rms deviation between the three common sources, and confirmed that the images are well aligned. The rms deviations are 0.12 and 0.13 arcseconds in right ascension and declination respectively. The final estimated position uncertainty (calculated by taking the square root of the sum of squared rms values) of the SN is ~ 0.17 arcsec, and consists of the alignment uncertainty between FORS2 and *HST* image, the astrometry solution uncertainties of the FORS2 image, and the centroid's position uncertainty of the SN in the PTF image. Figure 7.2 (left panel) shows the color image and 3σ contours of the host galaxy of PTF 11hrq.

To align the VLT/MUSE field to the HST astrometry, we use 11 common sources and compute an image solution using the images.imcoords.ccmap routine from the PyRAF/STSDAS package. The rms deviations were 0.18 and 0.16 arcsec in right ascension and declination respectively. The final estimated position uncertainty of the SN in the MUSE field is ~ 0.23 arcsec in right ascension and 0.25 arcsec in declination.

7.4.3. Color maps

We created *F225W* − *F625W* and *F336W* − *F625W* color maps to visualize the bluest regions in the galaxy, which are the regions with the most massive and hottest stars.

For resampling we used SWarp (Bertin et al., 2002), which is a tool that uses the astrometric projection defined in the WCS to resample the images. In order to reduce the impact of noise and possible artifacts introduced during resampling, we also bin the images by 3×3 pixel, calculate the binned color maps and compare the results. The color is calculated as $m_1 - m_2 = -2.5 \log_{10}(f_1/f_2)$, where f_1 and f_2 are flux values in the corresponding filter passband filters. The maps for PTF 12dam and PTF 11hrq are shown in Fig. 7.1 and Fig. 7.2, respectively. Corrections for dust extinction are presented in Sect. 7.4.5.4, and the results are discussed in Sect. 7.5.

7.4.4. Light-distribution analysis

Here we determine the fraction of light of the pixel in which the SN occurred, compared to the host galaxy light distribution. This technique was developed by Fruchter et al. (2006) and allows us to quantify to which extent the SNe trace their host light distribution, regardless of the morphology. However, the light distribution depends on the filter passband and the definition of the galaxy boundaries, i.e., on the choice of which pixels are to be considered as part of the host galaxy.

To operate this choice in an objective way, we calculate the standard deviation of the sky background in two regions around the galaxies, and define a 3σ threshold for each filter (see contours in Fig. 7.1 and Fig. 7.2). The result will strongly depend on the selected threshold. For instance, if the threshold is lower (e.g., 1σ), fainter pixels will be included, and the light fraction of the pixel where the SN occurred will be higher.

We measure the counts at the position of the SN, and calculate the light fractions from the cumulative distribution function. The results, for different thresholds and filters, are given in Table 7.2, and the cumulative distributions for the hosts of PFT 12dam and PTF 11hrq are shown in Fig. 7.3 and Fig. 7.4 respectively.

We also calculate the light fractions using the intersection of the *F225W*, *F336W* and *F625W* 3σ thresholds as an universal threshold for all filters, with the aim to compare the light distribution of the different colors within the same region of the host. However, in the case of the host of PTF 11hrq, this biases the results against the older stellar populations, because part of the *F336W* and *F625W* fluxes

Table 7.2.: Light distribution analysis of host galaxies.

Galaxy	Filter	Threshold	No. of pixel	Light fraction at SN position
PTF 12dam	*F225W*	3σ *F225W*	319	0.984
	F336W	3σ *F336W*	2093	0.998
	F625W	3σ *F625W*	2180	0.993
PTF 12dam	*F225W*	3σ *F225W*$\cap$*F336W*$\cap$*F625W*	319	0.984
	F336W	3σ *F225W*$\cap$*F336W*$\cap$*F625W*	319	0.981
	F625W	3σ *F225W*$\cap$*F336W*$\cap$*F625W*	319	0.953
PTF 11hrq	*F225W*	3σ *F225W*	329	0.0
	F336W	3σ *F336W*	837	0.648
	F625W	3σ *F625W*	1184	0.723
PTF 11hrq	*F225W*	3σ *F225W*$\cap$*F336W*$\cap$*F625W*	286	0.0
	F336W	3σ *F225W*$\cap$*F336W*$\cap$*F625W*	286	0.220
	F625W	3σ *F225W*$\cap$*F336W*$\cap$*F625W*	286	0.311

Notes. *F225W*$\cap$*F336W*$\cap$*F625W* is the intersection between all filters.

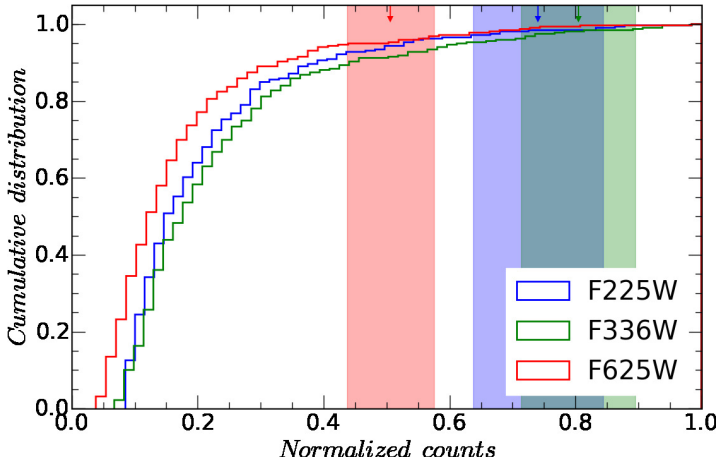

Figure 7.3.: Cumulative histogram of light distribution in the host galaxy PTF 12dam in *F625W* (red), *F336W* (green) and *F225W* (blue line). The arrows indicate the average count between the two pixels at the SN position, while the shaded areas are their standard deviations.

are lost in the regions outside the universal threshold, which is in case of PTF 12dam equivalent to the 3σ *F625W* threshold (Table 7.2).

7.4.5. Analysis of the VLT/MUSE data of the PTF 11hrq host galaxy

7.4.5.1. Metallicity map

We compute the fluxes and equivalent widths (EW) of the Hα, Hβ, [OIII] and [NII] emission lines. Then we compute metallicity maps from both the O3N2 and N2 index, using the Pettini & Pagel

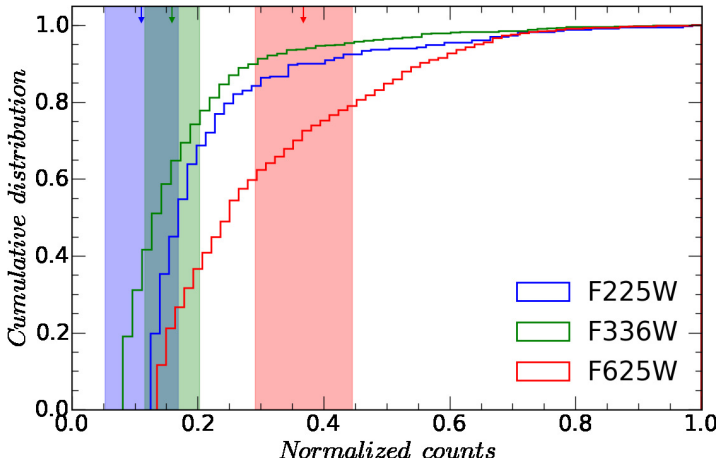

Figure 7.4.: Cumulative histogram of light distribution in the host galaxy PTF 11hrq in *F625W* (red), *F336W* (green) and *F225W* (blue line). The arrows indicate the mean counts within the 1σ position uncertainty of the SN, while the shaded areas are their standard deviations.

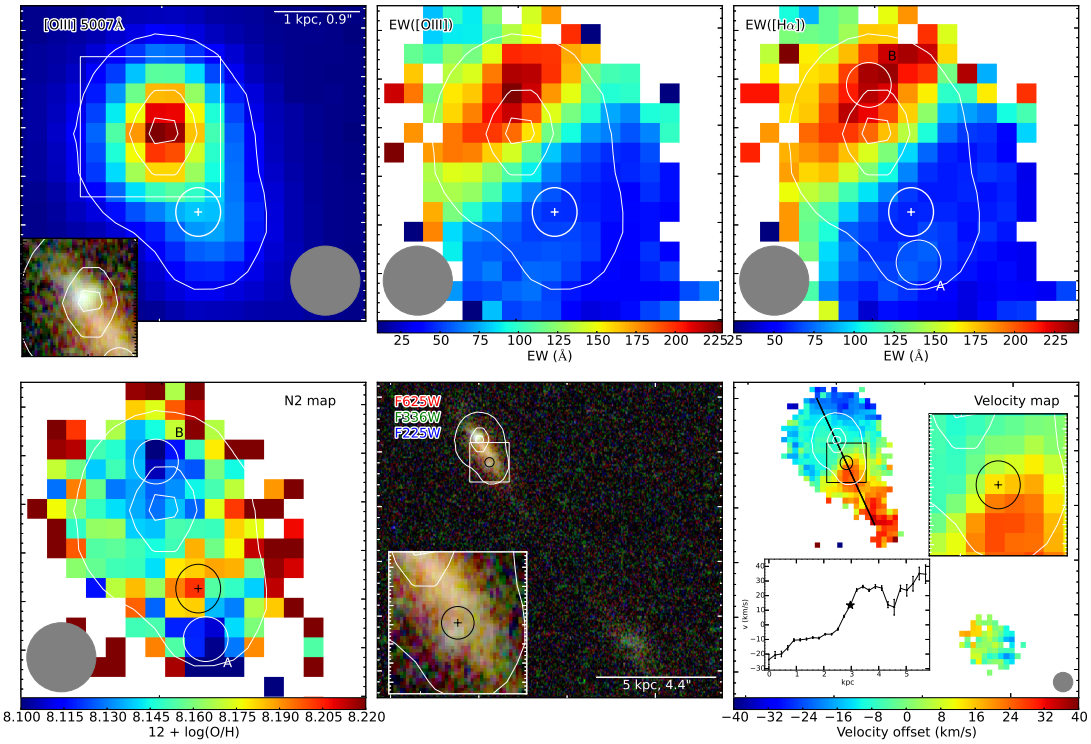

Figure 7.5.: The host galaxy of PTF 11hrq. North is up, east is left. The SN location is marked with the '+' sign, and its position uncertainty is denoted with the circle for the *HST* image and ellipse for MUSE. The seeing (0.71 arcsec) is marked with the gray circle in the bottom corner. Top left: [OIII]5007Å narrow band image. The [OIII] flux level contours are shown to make the comparison with other panels easier. The subframe is an *HST* image with overplotted MUSE contours. Top middle: Equivalent width map of the [OIII]5007Å narrow emission line. Top right: equivalent width (EW) map of Hα. Bottom left: A metallicity map computed in the N2 scale using the Marino et al. (2013) calibration. A and B are regions with lowest metallicities. Bottom middle: *HST* image of the host galaxy. Bottom right: velocity map. The line indicates the position of the cut, shown in the inset frame. The star in the inset frame indicates the position of the SN.

Table 7.3.: Local properties of the host galaxy of PTF 11hrq

Region	PP04 N2	M+13 N2	EW(Hα) [Å]	Stellar Age [Myr]	SFR [$M_\odot$ yr^{-1}]
Galaxy[a]	8.17 ± 0.02	8.15 ± 0.03	130.9 ± 62.7	$10.2^{+1.3}_{-1.0}$	0.174 ± 0.009
SN position	8.19 ± 0.01	8.18 ± 0.02	60.8 ± 2.0	$11.6^{+0.05}_{-0.00}$	0.007 ± 0.001
Region A	8.13 ± 0.01	8.11 ± 0.01	70.7 ± 1.8	$11.5^{+0.02}_{-0.02}$	0.003 ± 0.001
Region B	8.14 ± 0.01	8.12 ± 0.01	226.6 ± 7.2	$8.9^{+0.07}_{-0.1}$	0.016 ± 0.003

[a] Mean within the outer contour in Fig. 7.5.

Notes. The stellar age errors are statistical errors derived from the EW(Hα) - age relation as shown in Fig. B.1. The SFR was converted from Hα luminosity, as described in § 7.4.5.5.

(2004) (hereafter PP04) and the updated Marino et al. (2013) (hereafter M+13) calibrations, where O3N2 ≡ log{([OIII]λ5007/Hβ)/([NII]λ6583/Hα)}^{2} (Alloin et al., 1979) and N2 ≡ log{[NII]λ6583/Hα} (Denicoló et al., 2002).

Despite the stellar absorption being very small and does not affect the metallicities significantly, in this work we use only the N2 scale to estimate the absolute metallicity, because it depends on Hα, which is less affected by stellar absorption than Hβ. A re-reduced stellar absorption corrected metallicity map will be presented and further analyzed in a sample paper of SLSN host galaxies observed with MUSE (Schulze et al., in preparation). Nevertheless, both, the O3N2 and N2 scale can map the relative differences in metallicity throughout the host galaxy.

The results and comparison between the PP04 and M+13 N2 indices are listed in Table 7.3, and the metallicity map is shown in Fig. 7.5. The higher metallicity values at the edges of the galaxy have larger uncertainties, and should be considered with caution. The typical metallicity error is $\lesssim$ 0.15 dex (S/N of Hα $\gtrsim$ 5), and metallicity values with an error ¿ 0.24 dex (S/N $\lesssim$ 2 in Hα) are ignored.

For comparison, also a background-subtracted [OIII] λ5007 Å line flux image is shown in Fig. 7.5. To build the [OIII] image, we defined a narrowband filter with a width of 16 Å and centred it at OIII, and to subtract the continuum, we applied a narrow-band filter with a width of 24 Å to the left and the right of the emission line and computed the mean value.

7.4.5.2. Stellar age

We estimated the age of the youngest ionizing stellar populations from the equivalent width of Hα, assuming a star formation law for an instantaneous burst, i.e., a single stellar population. Leitherer et al. (1999) provide equivalent width of Hα as a function of stellar age in their Starburst99 model. The details of the calculation are presented in Appendix B.1.

The estimated stellar population ages in different regions of the host galaxy and at the SN position (see Fig. 7.5) are given in Table 7.3.

7.4.5.3. Velocity map

For each spatial pixel we fitted up to seven emission lines (Hβ λ4862.68 Å; [OIII] λ4960.295 Å, λ5008.24 Å; Hα λ6564.61 Å; [NII] λ6585.27 Å; [SII] λ6718.29 Å; [SII] λ6732.67 Å) using the MUSE Python Data Analysis Framework (MPDAF, Bacon et al., 2016), and created a redshift map by calculating the weighted average redshift of those lines. The redshifts with a weighted error larger than 3×10^{-5} have been ignored.

The average redshift of the galaxy is $z = 0.0569 \pm 0.0001$. The redshift map is shown in Fig. 7.5. South-west of the host galaxy, a fainter companion galaxy is visible at the same redshift, and at a

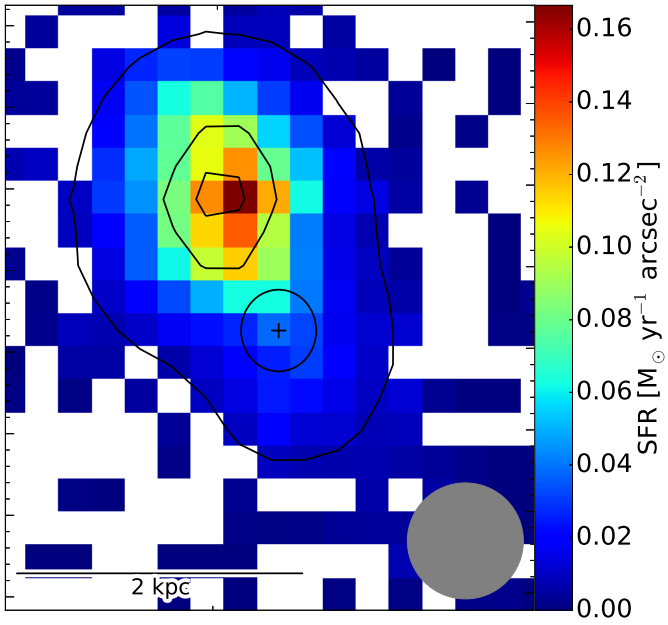

Figure 7.6.: Star formation rate map for the host of PTF 11hrq. The contours are same as in Fig. 7.5. The black ellipse denotes the SN position uncertainty.

projected distance of about 10 kpc. Furthermore, there is a third galaxy at a redshift of z=0.0567, also in the south-west direction at a projected distance of 30 kpc, not visible in Fig. 7.5. This corresponds to a velocity difference of ~45 km s^{-1}. Thus, these galaxies are likely part of the same group.

7.4.5.4. Dust extinction correction

Normally one would expect young star forming regions to be characterized by blue colors. However, often they are the reddest parts of their galaxies, because of the large amounts of dust in which they are embedded. Although we do not expect much dust in low metallicity dwarf galaxies, dust can effectively attenuate UV radiation, and this could significantly affect the observed color.

To correct the color map (Fig. 7.2) for dust extinction, we derived the reddening from the Balmer decrement, and created a color excess map $E(F225W - F625W)$ by adopting an extinction law, which we finally subtract from the observed color map. The typical value of $E(F225W - F625W)_{\rm Host}$ is ~ 0.8 ± 0.8 mag. The calculations are discussed in more detail in Appendix B.2.

7.4.5.5. Star formation rate

We convert the dust-corrected Hα luminosities into star formation rates via the relations presented in Kennicutt (1998), assuming a Chabrier (2003) initial mass function, i.e.:

$$\mathrm{SFR}_{\mathrm{H}\alpha} = 4.61 \times 10^{-42} \mathrm{L}(\mathrm{H}\alpha) \quad (\mathrm{erg\,s^{-1}}) \tag{7.1}$$

The star formation rates (SFR) density map is shown in Fig. 7.6, and SFRs at different locations are listed in Table 7.3. The sum of all values leads to a total SFR in of 0.174 ± 0.009 $M_\odot$ yr^{-1}, which is consistent within the errors with the SFR of 0.196 ± 0.04$M_\odot$ yr^{-1} determined by Perley et al. (2016).

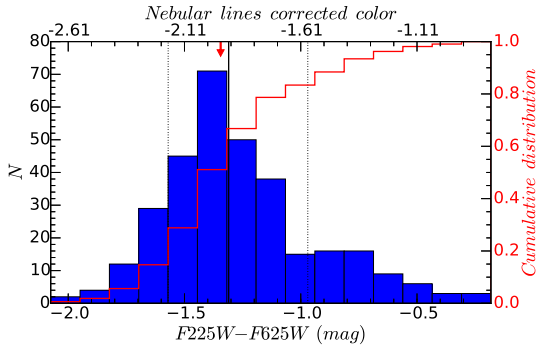

Figure 7.7.: *F225W − F625W* color distribution histogram of the host galaxy of PTF 12dam. Only values within the 3σ contours of the *F225W* and *F625W* image are taken into account. The solid black line is the mean of the distribution and the dotted lines shows its 1σ level deviations. The red arrow indicates the average color at the SN position. The color at the SN position is very close to the average value of the galaxy. The red line denotes the cumulative histogram. The upper x-axis shows the color after the nebular lines subtraction.

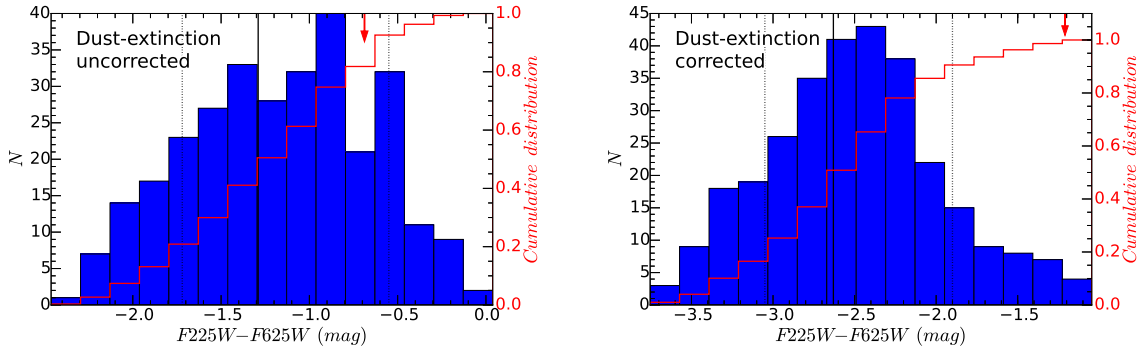

Figure 7.8.: *Left:* dust-extinction uncorrected *F225W − F625W* color distribution histograms of the host galaxy of PTF 11hrq. Only values within the 3σ contours of the *F225W* and *F625W* image are taken into account. The solid black line is the mean of the distribution and the dotted lines are its 1σ levels. The red arrow marks the mean color within the uncertainty of the SN position. The red line denotes the cumulative histogram. 82% of pixels are bluer than the color at the SN position. *Right:* dust-extinction corrected color distribution histogram. 93% of pixels are bluer than the color at the SN position.

7.5. Results and Discussion

We determined the positions of the SLSNe as described in § 7.4.2, calculated *F225W − F625W* and *F336W−F625W* color maps as described in § 7.4.3, and performed a light distribution analysis (§ 7.4.4). For the host galaxy of PTF 11hrq, which was also observed with VLT/MUSE, we investigated the metallicity (§ 7.4.2), color excess $E(\mathrm{H}\beta\text{-}\mathrm{H}\alpha)$ (§ 7.4.5.4), kinematics (§ 7.4.5.3) and determined the stellar age (§ 7.4.5.2).

PTF 12dam occurred in a dwarf galaxy which shows 5 bright knots. The SN position is in between two pixels in the *HST* image (see Fig. 7.1), one pixel away (~ 68 pc)[2] from the brightest pixel in the south-west knot of the galaxy. The light-distribution analysis in individual passband filters shows that

[2]For translating the angular distances into parsecs, we assume a flat universe with $H_0 = 67.8$ km s^{-1} Mpc^{-1} and $\Omega_M = 0.308$ (Planck Collaboration et al., 2016).

Table 7.4.: Colors of host galaxies environments

	PTF 12dam	PTF 11hrq
SN coordinates (J2000)	14:24:46.207 +46:13:48.46[a]	00:51:47.251 -26:25:10.38[b]
SN position uncertainty in *HST* images	$\sim$ 0.01 arcsec	$\sim$ 0.17 arcsec
F225W − *F625W* color at SN position (mag)	-1.40 (left pixel), -1.29 (right pixel)	-0.69[e]
F225W − *F625W* color at SN position, 3x3 binned (mag)	-1.37	-0.73[e]
Mean *F225W* − *F625W* color of galaxy (mag)[c]	-1.31	-1.29
std *F225W* − *F625W* color of galaxy (mag)[c]	$^{+0.34}_{-0.26}$	$^{+0.74}_{-0.43}$
F336W − *F625W* color at SN position (mag)	-0.69 (left pixel), -0.57 (right pixel)	-0.27[e]
F336W − *F625W* color at SN position, 3x3 binned (mag)	-0.67	-0.29[e]
Mean *F336W* − *F625W* color of galaxy (mag)[d]	-0.54	-0.42
std *F336W* − *F625W* color of galaxy (mag)[d]	$^{+0.38}_{-0.28}$	$^{+0.57}_{-0.37}$

[a] In the WCS of the *HST* image taken on 2012-06-26 at 01:52:58.9 UT (Proposal ID: 12524).
[b] In the WCS of the PTF image taken on 2011-07-11 at 11:27:16.5 UT.
[c] Mean color within the intersection of the 3σ *F225W* and *F625W* contours.
[d] Mean color within the intersection of the 3σ *F336W* and *F625W* contours.
[e] Mean within the uncertainty circle with an 0.17 arcsec radius.

the SN happened in one of the brightest pixels, at the 95th percentile (Table 7.2, Fig. 7.3). The average *F225W* − *F625W* color at the SN position is −1.35 mag, while the average color of the galaxy within the 3σ *F225W* contours is $-1.31^{+0.34}_{-0.26}$ mag. This means that the color of the environment (i.e., the integrated color along the line of sight through the galaxy) at the SN position is average, deviating less than 0.35σ from the mean color value of the galaxy. We draw the same conclusions when binning the pixels by 3×3. The color at the SN position is at the 51st percentile, which means that 51% of pixels are bluer compared to the SN location (Fig. 7.7).

A caveat one should bear in mind when considering the color maps is that bright nebular lines can significantly contribute to the flux. The Hα line indeed lies within the *F625W* passband, and the host galaxy of PTF 12dam has strong Hα emission. In Appendix B.3 we estimate the Hα contribution and obtain that the UV-to-optical color is in fact 0.61 mag bluer, over the whole galaxy. The spatial distribution of the Hα, which could influence the relative colors inside the host, is however not known. Despite PTF 12dam exploded in an environment characterized by average colors of its host, this location is rather blue on an absolute scale (*F225W* − *F625W* = −1.98). The color distribution is shown in Fig. 7.7, and the results are also summarized in Table 7.4.

For the host of PTF 12dam, the Galactic extinction is $E(B-V)_{\rm Gal} = 0.0107 \pm 0.0005$ mag (Schlafly & Finkbeiner, 2011). From spectral energy distribution modeling, Schulze et al. (2016) determined a color excess of $E(B-V)_{\rm Host} \sim 0.02$ mag, which is significantly lower than the reddening in the host

of PTF 11hrq.

The host galaxy of PTF 11hrq has a bright peak visible in the *F225W* image, in the northern part. Since the host galaxy is on average not particularly star-bursting (Perley et al., 2016), one might expect that the SN happened in the bluest and brightest star forming region, while it happened far away from this region, with a 5.5σ confidence. However, there is a second fainter blue knot just outside of the $\sim 1\sigma$ uncertainty circle of the SN position (see Fig. 7.2). The mean *F225W* – *F625W* color within the SN position uncertainty circle is −0.69 mag, while the mean color values of the galaxy within the 3σ contours of *F225W* and *F625W* is $-1.29^{+0.74}_{-0.43}$ mag. For comparison, the *F225W* – *F625W* color of the blue knot in the north is $-1.64^{+0.47}_{-0.33}$ mag. As shown in the color-distribution histogram (Fig. 7.8), the SN occurred in the red part of the galaxy. The results are summarized in Table 7.4. However, the observed color is affected by dust reddening. The foreground Galactic reddening is $E(B-V) \sim 0.01$ mag (Schlafly & Finkbeiner, 2011). We derived the host galaxy reddening from the VLT/MUSE data (see §7.4.5.4), $E(\mathrm{H}\beta - \mathrm{H}\alpha)_{Obs} = 0.13 \pm 0.12$ mag (Fig. B.3), which corresponds to $E(B-V) \sim 0.11$ mag, or $E(F225W - F625W)_{Host} = 0.8 \pm 0.8$ mag. After correcting the color map for extinction, the color of the region where the SN occurred is *F225W* – *F625W* ∼ −1.2 mag, at the ∼99th percentile (Fig. 7.8), i.e., among 1% of the reddest pixels.

The light-distribution analysis shows that PTF 11hrq did not happen in a bright pixel (Table 7.2, Fig. 7.4). In the F225W passband, the pixel counts at the position of the SN are below the 3σ threshold, and in F625W, depending on the definition of the threshold (see §7.4.4), ∼ 72% – 31% of the pixels are brighter than the average value at the position of the SN. PTF 11hrq exploded far from the brighter and bluer region in the north part of its host galaxy, and therefore far from the region of likely stronger star formation. However, just outside of the uncertainty circle of the SN position, there is a second fainter blue region, particularly visible after the dust extinction correction, which might be evidence for a nearby star-forming region.

The SLSN PTF 12dam occurred in one of the brightest *F225W*, *F336W* and *F625W* pixels of an already very extreme galaxy. This is coherent with the findings of Thöne et al. (2015). They found that PTF 12dam occurred at a site of recent starburst with a very young stellar population (∼ 3 Myr), superimposed on an old stellar population.

Lunnan et al. (2015) present a light fraction analysis of 16 hydrogen-poor SLSNe host galaxies in the rest-frame UV (∼ 3000Å) using *HST*. PTF 12dam has a light fraction of 0.998 (in *F336W*), which is at the ∼95th percentile compared to their sample (see Fig. 6 in Lunnan et al., 2015), and PTF 11hrq has a light fraction of 0.65 (in *F336W*), which is at the 56th percentile compared to their sample.

SLSNe may be associated with massive stars with zero-age main sequence masses of several hundred solar masses. Massive progenitors for SLSNe may be required to explain the large ejected masses derived from the light curves (M_{ej} of 3–30 $M_{\odot}$, Nicholl et al., 2015a). Therefore, it is expected that their location within the host galaxy is tightly correlated with the UV light. The evidence that both the SLSNe considered here did not explode in the bluest region of their host galaxies, where we would statistically expect them, is therefore surprising. In the case of recent starburst, there is an additional caveat. UV light probes star formation on a time scale of ∼ 100 Myr, while Hα on time scales of ∼6 Myr (Calzetti, 2013). In case of a very young starburst, the region will still not be very UV bright. On the other hand, there is little evidence about the progenitor mass of SLSNe-I. Some models show that it is possible to get the spectral evolution for masses of less than 10 $\mathrm{M}_{\odot}$ (Mazzali et al., 2016).

Given a sample of only two SLSNe, we cannot draw conclusions on the progenitors, based on the color of the environment. The progenitors of PTF 11hrq and PTF 12dam were not born in the most prominent blue regions of recent and massive star formation, but still, both galaxies are in general extreme. In particular, the host of PTF 11hrq has on average very young stellar population and low

metallicity, with little variations between different regions. The host of PTF 12dam also has a young stellar population and a very high star-formation rate (Thöne et al., 2015; Perley et al., 2016). On an absolute scale, the two SN locations, and the two galaxies in general, are UV bright and blue. For instance, the *F225W − F625W* color at the SN locations is -1.21 and −1.98 mag for PTF 11hrq and PTF 12dam, respectively, after the reddening and nebular-lines corrections.

Figure 7.5 shows a comprehensive comparison between the [OIII] λ5007Å line flux image, [OIII] λ5007Å and Hα equivalent width (EW) maps, N2 (Marino et al., 2013) metallicity map, *HST* image, and a velocity map. The peak of the [OIII] narrow band image coincides with the bright blue knot in the *HST* image. The EW([OIII]) and EW(Hα) maps show that the emission lines are stronger in the northern part of the galaxy, far from the SN location. The strongest lines, i.e., lines with largest equivalent widths, are 2–3 pixels north relative to the [OIII] intensity peak, with very high EW values up to $\sim$ 225Å.

From EW(Hα), which comes from O stars exclusively, we estimate the stellar age in different regions of the host galaxy of PTF 11hrq (see § 7.4.5.2). The average age of the galaxy is $\sim$ 10.2 Myr, the youngest region is about 8.9 Myr old (Region B), while the SN occurred in a region of stellar age $\sim$ 11.6 Myr (Fig. B.1), which is not significantly different from the average. Using the CMD 2.8 web interface[3] (Bressan et al., 2012; Chen et al., 2014; Tang et al., 2014; Chen et al., 2015a), from the stellar population age we estimate an upper limit on the stellar mass of $\sim 18 M_{\odot}$ at the SLSN location.

The N2 metallicity in the galaxy ranges from $12 + \log(\mathrm{O/H}) = \sim$ 8.05–8.25, with an average (within the outer contour in Fig. 7.5) of 8.15 and a standard deviation of 0.06. Despite the metallicity range is rather narrow throughout the galaxy, there are two peaks of low metallicity. The minimum metallicity coincides with the region of the strongest emission lines (Region B), and south of the SN (Region A). The metallicity at the SN location is slightly, but clearly higher ($\sim$ 0.03 dex) than the average (see Fig. 7.5). All metallicities are reported in Table 7.3.

Remarkably, in Region A, south from the SN position uncertainty ellipse, just outside of the ellipse, there is a local increase of EW(Hα) and perhaps EW([OIII]), and a decrease in metallicity. Furthermore, the velocity map (bottom right panel of Fig. 7.5) reveals that there is an increase of velocity, with respect to the bulk of the galaxy, at this position. This suggests either locally disturbed kinematics in the galaxy, or a third small companion galaxy. The cut through the velocity map visualizes the galaxy rotation curve with the locally increased velocity near the position of the SN. The SN happened at the edge of the region with disturbed kinematics and is marked with a star in the velocity cut (Fig. 7.5). In summary, Region A, south of the SN uncertainty circle has a local peak in velocity, bluer *F225W − F625W* color than average, stronger Hα and [OIII] emission, and lower metallicity (Table 7.3). These observations indicate likely past or ongoing interaction. This may suggest that local star formation has been triggered by interaction. A more detailed study of the dynamics of the host galaxy is out of the scope of this paper, and will be presented in a paper about a sample of SLSN host galaxies observed with MUSE (Schulze et al., in preparation). The host of PTF 12dam shows irregular morphology with multiple components in the *HST* data, and a tidal tail (see also Thöne et al., 2015; Perley et al., 2016), perhaps hinting at past or ongoing interaction as well.

Intriguingly, the MUSE cube of the PTF 11hrq host galaxy shows that it has two companions in the south-west, at projected distances of $\sim$ 10 kpc and $\sim$ 30 kpc. The nearby companion is at the same redshift as the host (z = 0.0569), with a velocity difference of $\sim$45 km s^{-1}. This suggests possible interaction. Lambas et al. (2003) and Sol Alonso et al. (2006) found, based on analysis of galaxy pairs in the 2dF survey and SDSS, that galaxies with projected distances $r_p < 100h^{-1}$ kpc, and relative velocities $\Delta V < 350$ km s^{-1} have an enhanced star formation activity, induced by interaction. The

[3] http://stev.oapd.inaf.it/cgi-bin/cmd

companions around the host galaxy of PTF 11hrq fulfill those conditions.

Previous studies also suggest that interaction might play an important role in the formation of SLSN progenitors. For instance, Chen et al. (2016a) performed a detailed analysis of LSQ14mo, a type Ic SLSN likely powered by a magnetar spin-down, and its host galaxy system. They measured radial distances and velocities of three bright regions and propose that those are interacting components that have triggered star-formation. On the other hand, Perley et al. (2016) conclude that dynamical interaction or a specific SFR-dependent initial mass function is secondary, given that the majority of SLSNe-I in their sample occurred in host galaxies with SFRs typical of their low metallicity and stellar masses.

Interaction may trigger star formation in certain areas, such as the lower-density outskirts of galaxies, where other star-formation processes are less effective. Based on the velocity map of the host of PTF 11hrq, and the morphology of the host of PTF 12dam, we speculate that the supernovae originated from stars generated during recent star-formation episodes triggered by close interaction. Even though these areas may have overall less vigorous star formation (and appear redder) than other, perhaps denser, parts of these dwarf starbursting hosts, these areas may have specific conditions (for example, lower metallicity) that favor the formation of the massive progenitors of SLSNe.

If SLSNe were associated with the most massive stars, we would statistically expect them to explode in the bluest and brightest starforming regions of their hosts. A larger statistical sample is needed to draw conclusions on the progenitors based on color.

In this work we studied the spatially resolved properties of two nearby SLSN host galaxies, using HST multi-band imaging and VLT/MUSE IFU spectroscopy. These reveal a complexity in morphology and spectral properties that was not accessible from ground-based imaging or slit spectroscopy. The complex morphology of PTF 12dam became evident only thanks to the HST resolution, which allowed a more detailed study of the star-formation regions in terms of color and light fraction. Furthermore, only with HST and MUSE we could appreciate the bright star forming region in the north part of the host of PTF 11hrq, and intensely emitting in Hα and [OIII], as well as the presence of interacting companions. These features were missed, or smoothed away using classical slit spectroscopy. Further complexity in the morphology and spectral properties of more distant SLSN host galaxies in general can therefore be expected.

7.6. Summary and conclusions

We studied the host galaxies of two hydrogen-poor SLSN-I/R, PTF 12dam and PTF 11hrq, obtained with the *Hubble Space Telescope* in *F225W*, *F336W* and *F625W* passband filters, and compared the environment at the position of the SNe with the rest of the galaxy. Additionally, we obtained integral field spectroscopy with VLT/MUSE of the PTF 11hrq host galaxy.

Our results can be summarized as follows:

1. HST observations of PTF 12dam reveal a complex and disturbed morphology with multiple star-forming knots. Combined with deep ground-based images, this complex represents the head of tadpole galaxy. The SN exploded in one of the five star forming knots. The explosion site is among the 5% of brightest pixels in the optical as well as the UV. While the UV-to-optical color appears rather average within the galaxy, it is blue (-1.98 mag, after correcting for nebular lines) and UV-bright on an absolute scale.

2. The host galaxy of PTF 11hrq has a disk-like morphology and is characterized by a large population of evolved stars. HST and IFU observations reveal diverse unexpected features. The

northern part of host contains a vigorously star-forming region with a [OIII] λ5007Å EW of ¿200 Å. Intriguingly, the explosion site does not coincide with this region at $\gtrsim 5.5\sigma$ confidence. The UV-to-optical color of the SLSN location is -1.2 mag, after correction for dust extinction, which is among 1% of the reddest pixels, but nevertheless blue on an absolute scale and similar to PTF 12dam. Within the uncertainties, the SN location includes regions with higher metallicity and weaker [OIII] and Hα emission lines relative to the bright part of the galaxy in the north. South of the SN position, at the edge of 1 sigma circle, there is a fainter blue knot which coincides with a region of locally lower metallicity, stronger Hα emission and more disturbed kinematics.

3. The host galaxy of PTF 11hrq has a nearby ($\sim$ 10 kpc) fainter companion at the same redshift, and possibly another one at a distance of about 30 kpc. The small angular separation and the small radial velocity difference of $\lesssim$ 40 km s^{-1} suggests that they could be part of a galaxy group.

4. Both host galaxies show some evidence for interaction, and for PTF 11hrq this is possibly related to the SN explosion site. We speculate that the SLSN explosions may originate from stars generated in regions of recent or ongoing interaction.

5. The combination of high-resolution imaging and integral-field spectroscopy allowed for examining the conditions of the explosion sites and how star-formation varies across the host galaxies. Larger samples are needed to extract robust constraints on the progenitor population and how their galaxy environments affect the star formation process.

Acknowledgements

We are grateful to Wolfgang Kerzendorf (ESO Garching) for useful discussion and suggestions, in particular related to pixel alignment; and to Eliceth Rojas-Montes (Armagh Observatory) and Giacomo Beccari (ESO) for discussion related to massive stars, wind models and mass-loss rates.

STSDAS and PyRAF are products of the Space Telescope Science Institute, which is operated by AURA for NASA.

Based on observations made with ESO Telescopes at the Paranal Observatory under programme ID 090.D-0440(A) and 097.D-1054.

Based on observations made with the NASA/ESA Hubble Space Telescope, obtained at the Space Telescope Science Institute, which is operated by the Association of Universities for Research in Astronomy, Inc., under NASA contract NAS 5-26555. These observations are associated with program # 13858 and 12524.

This research made use of APLpy, an open-source plotting package for Python hosted at http://aplpy.github.com.

The STARLIGHT project is supported by the Brazilian agencies CNPq, CAPES and FAPESP and by the France-Brazil CAPES/Cofecub program.

8. Summary and conclusions

Supernovae (SNe) enrich galaxies with metals, have influence on births of new stars and the evolution of low mass galaxies, which is mainly driven by feedback from SNe explosions. Therefore they play a crucial role for the development of the universe. This thesis focuses on two important aspects: the progenitor systems of SNe Ia, which are used as standard candles to characterize the expansion of the Universe, and Superluminous Supernovae (SLSNe), which are likely connected to the death of supermassive metal poor stars in pristine environments. The two topics are addressed in this thesis using spectropolarimetry, a powerful, photon-starving technique that became applicable to the SN field relatively recently, thanks to the advent of 8m-class telescopes. As briefly explained in the introductory Chapter 1, spectropolarimetry is a powerful tool that, among other things, enables the study of interstellar and circumstellar dust properties along the lines of sight to SNe (by measuring the continuum polarization), and the SN ejecta asymmetry (by measuring polarization of absorption lines). While for the study of dust and its effects (more specifically reddening) spectropolarimetry provides independent information (with respect to more conventional spectro-photometric techniques), it gives unique insights into the explosion geometry, which no other currently available technique can yield.

The vast majority of the data used in this thesis were obtained using the FOcal Reducer and low dispersion Spectrograph (FORS2), mounted at the Very Large Telescope (VLT). The performance, stability and accuracy of FORS2 are discussed in Chapter 2. For this purpose we analyzed archival observations of 8 unpolarized standard stars observed on 40 epochs, and 6 polarized standard stars (30 epochs). Our analysis confirms that FORS2 can achieve a maximum accuracy of ~0.1% and ~0.3 degrees in polarization degree and angle, respectively. These values, which represent the instrumental limits of this focal reducer, are shown to be stable over timescales of years. We confirm the instrumental wavelength dependent polarization detected by Fossati et al. (2007). The spurious signal steadily grows from the blue to the red, ranging from 0.05% (4000Å) to 0.10% (9000Å). The vectorial correction for P_Q and P_U (see Equation 2.7) can be applied to the observed Stokes parameters. This analysis confirms that FORS2 is indeed suitable for the work presented in this these, being one of the best polarimeters currently in operation.

Understanding the effects of dust extinction on the observed luminosity of SNe Ia is an essential step for accurately measuring the cosmological parameters and the expansion history of the Universe. In addition, studying dust along the sight lines to SNe Ia can give insights on the progenitor systems (whether it is a single-degenerate, or double-degenerate), because different configurations are associated to different circumstellar environments. Intriguingly, a number of studies of the host-galaxy dust extinction observed in SNe Ia yielded values for the total-to-selective extinction ratio that are significantly lower (often $R_V \leq 2$) than the average R_V=3.1 observed for Milky Way dust. In the present study, we have confirmed this result using a statistical approach based on a larger sample, by deriving $E(B-V)$ color excess probabilities as a function of the galacto-centric distance for different galaxy morphological groups, and applying them to a sample of SN Ia $E(B-V)$ observations to determine the average R_V value (Cikota et al., 2016).

This puzzling finding, which still lacks a convincing explanation, was recently addressed in an independent way, using spectropolarimetry. It has been known for more than forty years that, in the

Milky Way, the inter-stellar polarization (ISP) measured along the sightlines to highly reddened stars shows a characteristic wavelength dependency, known as the Serkowski law (Serkowski et al., 1975). The wavelength of the ISP peak (λ_{max}) depends on the dust grain size distribution, in the sense that for an enhanced abundance of small dust grains, λ_{max} moves to shorter wavelengths, whereas for an enhanced abundance of large dust grains it shifts longer wavelengths. In general, Milky Way stars have λ_{max} ~0.55μ. As shown by Patat et al. (2015), highly reddened SNe Ia with low total-to-selective extinction ratios R_V, display peculiar continuum polarization wavelength dependencies, steeply rising towards the blue, with polarization peaks at short wavelengths ($\lambda_{max} \leq 0.4\mu$m), definitely different from what is observed in the Galaxy. It is not clear why SNe Ia sight lines display such peculiar polarization profiles. Possible explanations are that the composition of interstellar dust in SNe Ia host galaxies is different from the dust in our Galaxy, or that there is circumstellar dust, ejected from the progenitor system before the explosion, characterised by an enhanced abundance of small grains. Scattering from CSM dust is also a possibility. This conundrum is addressed in the thesis with two different approaches, discussed in Chapters 3 and 4.

In Chapter 3, we investigated the linear polarization of 17 sightlines to Galactic stars with anomalous extinction and low R_V values, selected from the Mazzei & Barbaro (2011) sample, in order to identify possible similarities to SNe Ia. We found that, despite their anomalous extinction curves, they obey to normal polarization laws (with a mean λ_{max} ~0.53μm). This can be explained in the light of the following considerations. Not all dust that contributes to extinction also contributes to polarization: polarization mainly depends on the dust grain size distribution of silicates, because grain alignment is more efficient for silicates than, for instance, for carbonaceous dust grains (Somerville et al., 1994). On the contrary, R_V is strongly dependent on carbonaceous grains too. We also found that there is no significant $R_V - \lambda_{max}$ relation in our sample (Fig. 3.8). The λ_{max} values in our data set are higher than what is typical for normal stars that follow the empirical $R_V - \lambda_{max}$ relationship described, for instance, by Whittet & van Breda (1978). However, by comparing the R_V values of our sample with those published by Wegner (2002) for a subset of our stars, we find some differences. These are probably due to a different spectral classification and/or luminosity class adopted to derive their extinction curves (see Sect. 3.7.2). The λ_{max} value that we measure and the deviation from the empirical $R_V - \lambda_{max}$ relationship may also suggest a spectral misclassification of some stars by Savage et al. (1985). The Serkowski parameters K and λ_{max} are known to be correlated. However, using our sample we find a slope that is steeper than in the classical empirical relationship presented by Whittet et al. (1992). For better interpreting our results, we adopted a simple dust model that can reproduce the observed sightlines with low R_V values and normal polarization curves. The simulations show that, to reproduce a polarization curve with the normal λ_{max} and low R_V, there must be a population of large interstellar silicate grains of size $a \geq 0.1\mu$m. Moreover, variations in grain alignment and size distribution together are required to reproduce the variation in λ_{max} for a fixed, low, R_V value. However, a change in grain alignment has a greater effect. Interestingly, the $K - \lambda_{max}$ relation appears to be an intrinsic property of dust polarization. The numerical calculations show that for a fixed R_V , the grain alignment function becomes narrower (broader) for a lower (higher) value of λ_{max} and K (see Sect.. 3.7.5). An increase in the Serkowski parameter K and a deviation from the standard value in the $K - \lambda_{max}$ plane can be reproduced by a decreasing contribution of large Si grains (Fig. 3.10).

On the other hand, in Chapter 4 we show that some post-AGB stars (proto-planetary nebulae, PPNe), which also may play an important role in the evolutionary path of some SNe Ia (Jones & Boffin, 2017), have polarization curves that are remarkably similar to those observed in highly reddened SNe Ia. It is a well known fact that, in PPNe, the curves are produced by CS scattering (Oppenheimer et al., 2005). Thus, we suggest that the polarization curves seen in some SN Ia may be produced by CSM dust

scattering (Cikota et al., 2017c). No other sight lines to any normal, known Galactic stars have similar polarization curves: this opens the intriguing possibility that also in the case of SNe Ia scattering may be playing an important role. Furthermore, we speculate that those SNe Ia might have exploded within a PPN, and may provide observational support for the core-degenerate progenitor scenario (Kashi & Soker, 2011), in which a white dwarf merges with the core of a companion AGB star. However, as first pointed out by Patat et al. (2015), the observed alignment along the local magnetic field which characterizes the polarization angle of SNe Ia (see Zelaya et al., 2017b) still needs to be reconciled with the random alignment expected for PPN.

We aim to undertake imaging polarimetry of ∼100 SNe Ia using FORS2 (Proposal ID: 0101.D-0190, PI: Cikota) within the next ∼ 2-3 years to create a statistical sample, with the aim to investigate whether there is a relation between the degree of polarization with galactocentric distance, and therewith answer the question whether the steeply rising polarization curves are produced by host galaxy interstellar dust, or by CSM dust. For instance, high polarization degrees along sightlines towards SNe Ia located far away from the centers of their host galaxies, where we expect low interstellar dust amounts, or in elliptical galaxies, which are known to be dust poor (see Cikota et al., 2016), would provide strong supportive evidence for our hypothesis. On the other hand, if we do not observe high polarization values of SNe Ia in dust poor regions, and elliptical galaxies, that would be evidence against our PPNe hypothesis.

In Chapter 5, we study the ejecta asymetries by examining the polarization of the Si II lines in SNe Ia. We reduced and examined archival spectropolarimetric data of a sample of 35 SNe Ia in a homogeneous way. All the spectra were obtained with FORS1 and FORS2 between 2001 and 2015, at 128 epochs in total. The linear polarization of the prominent Si II λ 6355Å line displays an evolution in time with a variety of peak polarization degrees that range from 0.1% to 1.7%. Maximum polarization is attained at different epochs relative to peak brightness, ranging from −10 to 0 days (Fig. 5.9), at variance with what was assumed in previous studies based on smaller samples (Wang et al., 2007). We populated the Δm$_{15}$-P$_{SiII}$ plane and analyzed the relationship first determined by Wang et al. (2007). Although the overall behaviour is confirmed by our larger sample, the scatter around the best-fit relation is larger. We show that subluminous and transitional objects display lower polarization values, and are located below the Δm$_{15}$-P$_{SiII}$ relationship (Fig. 5.10), likely indicating a different explosion mechanism.

We found a statistically significant linear relationship (ρ ∼0.8) between the degree of linear polarization of Si II line before maximum with the Si II line velocity (Fig. 5.11). We suggest that this relationship, presented here for the first time, along with the Δm$_{15}$-P$_{\rm SiII}$ relationship (Wang et al., 2007) is consistent with the delayed-detonation model. Furthermore, we investigate the evolution of the Si II line in the $Q - U$ plane for a subsample of SNe, which have been observed at multiple epochs, and run simple simulations to explore the effect of clumps on the polarization spectra. In the cases of SN 2005df, SN 2006X, and SN 2002bo, we observe the formation of loops, growth, and shrinking of the loops (see all plots in Appendix C.2), which may be explained by the evolution of the projected silicon ejecta size, from large axisymmetric structures, to large clumps, and finally to small clumps, as the time evolves and the photosphere recedes into the ejecta. Finally, we compared our Si II polarization measurements to numerical predictions for the double-detonation, delayed detonation and violent merger models calculated by Bulla et al. (2016a,b). Our observations are consistent with the predictions for the delayed-detonation and double-detonation models, which have a comparable degree of polarization, while only SN 2004dt has a degree of polarization that is compatible with the predictions for the violent-merger model. We also try to reproduce the Si II polarization-velocity relationship using the simulations (Bulla et al., 2016a,b). Although the calculations show a velocity-

polarization trend, the velocity range produced by the simulations is not sufficient to reliably match the observed relationship. This will be an important test for future, more sophisticated spectral modelling calculations.

Superluminous supernovae (SLSN) are an important class of objects that are ∼10 times more luminous than common SNe. SLSN are divided into H-rich (type-II) and H-poor (type-I) subtypes. While it is believed that SLSNe-II are explosions of massive stars that occur within a thick hydrogen envelope (Gal-Yam, 2012), the hydrogen-poor SLSNe-I that have a quite featureless early spectrum and are poorly understood. Understanding their nature is fundamental, because they may represent rare examples of dying supermassive stars in low-metallicity environments, similar to the conditions that most likely characterized the early Universe. A possible scenario that might explain the observed luminosities is one in which SLSNe-I are powered by an exotic internal engine, such as a magnetar or an accreting black hole. Since strong magnetic fields or collimated jets can circularly polarize light, polarimetry may provide the diagnostics required to distinguish between the two proposed mechanisms. For this purpose, in Chapter 6 we investigate for the first time circular polarization of two H-poor superluminous supernovae, with the final aim of testing the magnetar scenario. The two objects, OGLE16dmu and PS17bek, were discovered during the course of the thesis work. OGLE16dmu is a slowly evolving H-poor SLSN, for which we obtained circular imaging polarimetry with FORS2 at 101.3 days past peak brightness, whilst PS17bek is a fast evolving SLSN-I, which we observed at 4.0 days before maximum light. In both cases, we did not find any evidence (within the noise) of a circular polarization signal. Nevertheless, we can not rule out the magnetar scenario purely based on the non-detection of circular polarization, because the strong magnetic field drops as $1/r^3$ (where r is the distance), and thus the light will be significantly circularly polarized by magneto-emissivity only very close (∼5000 km) to the surface of the magnetar. In other words, while the positive detection of a magnetic field would have strongly supported the magnetar scenario, the non-detection of a polarization signal is not sufficient to rule it out.

The main difficulty of investigating SLSNe with polarimetry is that they are typically very distant, and thus very faint (which makes spectropolarimetry prohibitively expensive in terms of telescope time). This is the reason why we considered an alternative approach to investigate SLSN progenitors, by studying their host galaxy environments. One hallmark of very massive progenitors would be a tendency to explode in very dense, UV-bright and blue regions of the parent galaxy. In Chapter 7 we investigate the spatially resolved host galaxy properties for two nearby H-poor SLSNe, PTF 12dam and PTF 11hrq, using *Hubble Space Telescope* (HST) and VLT/MUSE data. For this purpose, we studied the host galaxies of these two objects using imaging data obtained with HST in the *F225W*, *F336W* and *F625W* passband filters, and compared the environment at the projected explosion position with the rest of the galaxy. Additionally, we obtained integral field spectroscopy with VLT/MUSE of the PTF 11hrq host galaxy. Both hosts show some evidence for interaction, and for PTF 11hrq this is possibly related to the SN explosion site. We speculate that the SLSN explosions may originate from stars generated in regions of recent or ongoing interaction. We demonstrate that the combination of high-resolution imaging and integral-field spectroscopy is very powerful for characterizing the explosion environment. However, larger samples are needed to extract robust constraints on the progenitor population and on how their galaxy environments affect the star formation process.

Bibliography

Abbott B. P., Abbott R., Abbott T. D., Abernathy M. R., Acernese F., Ackley K., Adams C., Adams T., Addesso P., Adhikari R. X., et al.: *Localization and Broadband Follow-up of the Gravitational-wave Transient GW150914.* ApJ **826**, L13 (2016)

Aldering G., Adam G., Antilogus P., Astier P., Bacon R., Bongard S., Bonnaud C., Copin Y., Hardin D., Henault F., et al.: *Overview of the Nearby Supernova Factory.* In: Tyson J. A. & Wolff S. (eds.): *Survey and Other Telescope Technologies and Discoveries.* Proc. SPIE **4836**, 61 (2002)

Alloin D., Collin-Souffrin S., Joly M., & Vigroux L.: *Nitrogen and oxygen abundances in galaxies.* A&A **78**, 200 (1979)

Altavilla G., Fiorentino G., Marconi M., Musella I., Cappellaro E., Barbon R., Benetti S., Pastorello A., Riello M., Turatto M., & Zampieri L.: *Cepheid calibration of Type Ia supernovae and the Hubble constant.* MNRAS **349**, 1344 (2004)

Altavilla G., Stehle M., Ruiz-Lapuente P., Mazzali P., Pignata G., Balastegui A., Benetti S., Blanc G., Canal R., Elias-Rosa N., et al.: *The early spectral evolution of SN 2004dt.* A&A **475**, 585 (2007)

Amanullah R., Lidman C., Rubin D., Aldering G., Astier P., Barbary K., Burns M. S., Conley A., Dawson K. S., Deustua S. E., et al.: *Spectra and Hubble Space Telescope Light Curves of Six Type Ia Supernovae at 0.511* log *T z* log *T 1.12 and the Union2 Compilation.* ApJ **716**, 712 (2010)

Amorín R., Pérez-Montero E., Contini T., Vílchez J. M., Bolzonella M., Tasca L. A. M., Lamareille F., Zamorani G., Maier C., Carollo C. M., et al.: *Extreme emission-line galaxies out to z ˜ 1 in zCOSMOS. I. Sample and characterization of global properties.* A&A **578**, A105 (2015)

Anderson C. M., Weitenbeck A. J., Code A. D., Nordsieck K. H., Meade M. R., Babler B. L., Zellner N. E. B., Bjorkman K. S., Fox G. K., Johnson J. J., et al.: *Ultraviolet Interstellar Polarization of Galactic Starlight.I.Observations by the Wisconsin Ultraviolet Photo Polarimeter Experiment.* AJ **112**, 2726 (1996)

Andersson B.-G., Piirola V., De Buizer J., Clemens D. P., Uomoto A., Charcos-Llorens M., Geballe T. R., Lazarian A., Hoang T., & Vornanen T.: *Evidence for H_2 Formation Driven Dust Grain Alignment in IC 63.* ApJ **775**, 84 (2013)

Andersson B.-G., Lazarian A., & Vaillancourt J. E.: *Interstellar Dust Grain Alignment.* ARA&A **53**, 501 (2015)

Angel J. R. P., Landstreet J. D., & Oke J. B.: *The Spectral Dependence of Circular Polarization in Grw+70°8247.* ApJ **171**, L11 (1972)

Angus C. R., Levan A. J., Perley D. A., Tanvir N. R., Lyman J. D., Stanway E. R., & Fruchter A. S.: *A Hubble Space Telescope survey of the host galaxies of Superluminous Supernovae.* MNRAS **458**, 84 (2016)

Appenzeller I.: *A New Polarimeter for Faint Astronomical Objects.* PASP **79**, 136 (1967)

Appenzeller I., Fricke K., Fürtig W., Gässler W., Häfner R., Harke R., Hess H.-J., Hummel W., Jürgens P., Kudritzki R.-P., et al.: *Successful commissioning of FORS1 - the first optical instrument on the VLT.* The Messenger **94**, 1 (1998)

Arnett W. D.: *A Possible Model of Supernovae: Detonation of ^{12}C.* Ap&SS **5**, 180 (1969)

Asari N. V., Cid Fernandes R., Stasińska G., Torres-Papaqui J. P., Mateus A., Sodré L., Schoenell W., & Gomes J. M.: *The history of star-forming galaxies in the Sloan Digital Sky Survey.* MNRAS **381**, 263 (2007)

Ashall C., Mazzali P., Sasdelli M., & Prentice S. J.: *Luminosity distributions of Type Ia supernovae.* MNRAS **460**, 3529 (2016)

Ashall C., Mazzali P. A., Stritzinger M. D., Hoeflich P., Burns C. R., Gall C., Hsiao E. Y., Phillips M. M., Morrell N., & Foley R. J.: *On the type Ia supernovae 2007on and 2011iv: Evidence for Chandrasekhar-mass explosions at the faint end of the luminosity-width relationship.* MNRAS (2018)

Asplund M., Grevesse N., Sauval A. J., & Scott P.: *The Chemical Composition of the Sun.* ARA&A **47**, 481 (2009)

Bacon R., Accardo M., Adjali L., Anwand H., Bauer S., Biswas I., Blaizot J., Boudon D., Brau-Nogue S., Brinchmann J., et al.: *The MUSE second-generation VLT instrument.* In: *Ground-based and Airborne Instrumentation for Astronomy III.* Proc. SPIE **7735**, 773508 (2010)

Bacon R., Piqueras L., Conseil S., Richard J., & Shepherd M.: *MPDAF: MUSE Python Data Analysis Framework.* Astrophysics Source Code Library (2016)

Bagnulo S., Landolfi M., Landstreet J. D., Landi Degl'Innocenti E., Fossati L., & Sterzik M.: *Stellar Spectropolarimetry with Retarder Waveplate and Beam Splitter Devices.* PASP **121**, 993 (2009)

Bagnulo S., Cox N. L. J., Cikota A., Siebenmorgen R., Voshchinnikov N. V., Patat F., Smith K. T., Smoker J. V., Taubenberger S., Kaper L., et al.: *Large Interstellar Polarisation Survey (LIPS). I. FORS2 spectropolarimetry in the Southern Hemisphere.* A&A **608**, A146 (2017)

Bailey J. & Hough J. H.: *A Simultaneous Infrared / Optical Polarimeter.* PASP **94**, 618 (1982)

Bakker E. J., Waters L. B. F. M., Lamers H. J. G. L. M., Trams N. R., & van der Wolf F. L. A.: *Detection of C_2_, CN, and NaI D absorption in the AGB remnant of HD 56126.* A&A **310**, 893 (1996)

Barber C. B., Dobkin D. P., & Huhdanpaa H.: *The Quickhull algorithm for convex hulls.* ACM TRANSACTIONS ON MATHEMATICAL SOFTWARE **22**, 469 (1996)

Barbon R., Ciatti F., & Rosino L.: *Photometric properties of type II supernovae.* A&A **72**, 287 (1979)

Bertin E. & Arnouts S.: *SExtractor: Software for source extraction.* A&AS **117**, 393 (1996)

Bertin E., Mellier Y., Radovich M., Missonnier G., Didelon P., & Morin B.: *The TERAPIX Pipeline.* In: Bohlender D. A., Durand D., & Handley T. H. (eds.): *Astronomical Data Analysis Software and Systems XI.* Astronomical Society of the Pacific Conference Series **281**, 228 (2002)

Bieging J. H., Schmidt G. D., Smith P. S., & Oppenheimer B. D.: *Optical Spectropolarimetry of Asymptotic Giant Branch and Post-Asymptotic Giant Branch Stars.* ApJ **639**, 1053 (2006)

Blanchard P. K., Berger E., & Fong W.-f.: *The Offset and Host Light Distributions of Long Gamma-Ray Bursts: A New View From HST Observations of Swift Bursts.* ApJ **817**, 144 (2016)

Blöcker T.: *Evolution on the AGB and beyond: on the formation of H-deficient post-AGB stars.* Ap&SS **275**, 1 (2001)

Blondin S., Kirshner R., Challis P., & Calkins M.: *Supernova 2007hj in NGC 7461.* Central Bureau Electronic Telegrams **1048** (2007)

Blondin S. & Tonry J. L.: *Determining the Type, Redshift, and Age of a Supernova Spectrum.* ApJ **666**, 1024 (2007)

Blondin S., Prieto J. L., Patat F., Challis P., Hicken M., Kirshner R. P., Matheson T., & Modjaz M.: *A Second Case of Variable Na I D Lines in a Highly Reddened Type Ia Supernova.* ApJ **693**, 207 (2009)

Blondin S., Matheson T., Kirshner R. P., Mandel K. S., Berlind P., Calkins M., Challis P., Garnavich P. M., Jha S. W., Modjaz M., et al.: *The Spectroscopic Diversity of Type Ia Supernovae.* AJ **143**, 126 (2012)

Bose S., Dong S., Pastorello A., Filippenko A. V., Kochanek C. S., Mauerhan J., Romero-Cañizales C., Brink T. G., Chen P., Prieto J. L., et al.: *Gaia17biu/SN 2017egm in NGC 3191: The Closest Hydrogen-poor Superluminous Supernova to Date Is in a Normal, Massive, Metal-rich Spiral Galaxy.* ApJ **853**, 57 (2018)

Braden B.: *The Surveyor's Area Formula.* The College Mathematics Journal **17**, 326 (1986)

Bressan A., Marigo P., Girardi L., Salasnich B., Dal Cero C., Rubele S., & Nanni A.: *PARSEC: stellar tracks and isochrones with the PAdova and TRieste Stellar Evolution Code.* MNRAS **427**, 127 (2012)

Brindle C., Hough J. H., Bailey J. A., Axon D. J., & Hyland A. R.: *Simultaneous optical and infrared polarization measurements of blazars.* MNRAS **221**, 739 (1986)

Brown P. J., Breeveld A. A., Holland S., Kuin P., & Pritchard T.: *SOUSA: the Swift Optical/Ultraviolet Supernova Archive.* Ap&SS **354**, 89 (2014)

Bruzual G. & Charlot S.: *Stellar population synthesis at the resolution of 2003.* MNRAS **344**, 1000 (2003)

Bufano F., Immler S., Turatto M., Landsman W., Brown P., Benetti S., Cappellaro E., Holland S. T., Mazzali P., Milne P., et al.: *Ultraviolet Spectroscopy of Supernovae: The First Two Years of Swift Observations.* ApJ **700**, 1456 (2009)

Buil C.: *Supernova 2012fr in NGC 1365 = PSN J03333599-3607377.* Central Bureau Electronic Telegrams **3277**, 3 (2012)

Bulla M., Sim S. A., & Kromer M.: *Polarization spectral synthesis for Type Ia supernova explosion models.* MNRAS **450**, 967 (2015)

Bulla M., Sim S. A., Kromer M., Seitenzahl I. R., Fink M., Ciaraldi-Schoolmann F., Röpke F. K., Hillebrandt W., Pakmor R., Ruiter A. J., & Taubenberger S.: *Predicting polarization signatures for double-detonation and delayed-detonation models of Type Ia supernovae.* MNRAS **462**, 1039 (2016a)

Bulla M., Sim S. A., Pakmor R., Kromer M., Taubenberger S., Röpke F. K., Hillebrandt W., & Seitenzahl I. R.: *Type Ia supernovae from violent mergers of carbon-oxygen white dwarfs: polarization signatures.* MNRAS **455**, 1060 (2016b)

Bulla M.: *Polarisation Spectral Synthesis For Type Ia Supernova Explosion Models.* Astrophysics Research Centre, School of Mathematics and Physics, Queen's University Belfast, Belfast BT7 1NN, UK (2017)

Burns C. R., Stritzinger M., Phillips M. M., Kattner S., Persson S. E., Madore B. F., Freedman W. L., Boldt L., Campillay A., Contreras C., et al.: *The Carnegie Supernova Project: Light-curve Fitting with SNooPy.* AJ **141**, 19 (2011)

Burns C. R., Stritzinger M., Phillips M. M., Kattner S., Persson S. E., Madore B. F., Freedman W. L., Boldt L., Campillay A., Contreras C., et al.: *SNooPy: TypeIa supernovae analysis tools.* Astrophysics Source Code Library (2015)

Calzetti D.: *Star Formation Rate Indicators.* In: Falcón-Barroso J. & Knapen J. H. (eds.): *Secular Evolution of Galaxies.* 419 (2013)

Cappellaro E. & Turatto M.: *Supernova Types and Rates.* In: Vanbeveren D. (ed.): *The Influence of Binaries on Stellar Population Studies.* Astrophysics and Space Science Library **264**, 199 (2001)

Cardelli J. A., Clayton G. C., & Mathis J. S.: *The relationship between infrared, optical, and ultraviolet extinction.* ApJ **345**, 245 (1989)

Chabrier G.: *Galactic Stellar and Substellar Initial Mass Function.* PASP **115**, 763 (2003)

Chatzopoulos E., Wheeler J. C., & Vinko J.: *Generalized Semi-analytical Models of Supernova Light Curves.* ApJ **746**, 121 (2012)

Chen T.-W., Smartt S. J., Jerkstrand A., Nicholl M., Bresolin F., Kotak R., Polshaw J., Rest A., Kudritzki R., Zheng Z., et al.: *The host galaxy and late-time evolution of the superluminous supernova PTF12dam.* MNRAS **452**, 1567 (2015b)

Chen T.-W., Nicholl M., Smartt S. J., Mazzali P. A., Yates R. M., Moriya T. J., Inserra C., Langer N., Kruehler T., Pan Y.-C., et al.: *The evolution of superluminous supernova LSQ14mo and its interacting host galaxy system.* ArXiv e-prints **1611.09910** (2016a)

Chen T.-W., Smartt S. J., Yates R. M., Nicholl M., Krühler T., Schady P., Dennefeld M., & Inserra C.: *A sub-solar metallicity is required for superluminous supernova progenitors.* ArXiv e-prints **1605.04925** (2016b)

Chen Y., Girardi L., Bressan A., Marigo P., Barbieri M., & Kong X.: *Improving PARSEC models for very low mass stars.* MNRAS **444**, 2525 (2014)

Chen Y., Bressan A., Girardi L., Marigo P., Kong X., & Lanza A.: *PARSEC evolutionary tracks of massive stars up to 350 $M_{\odot}$ at metallicities 0.0001 ¡ Z ¡ 0.04.* MNRAS **452**, 1068 (2015a)

Chiar J. E., Adamson A. J., Whittet D. C. B., Chrysostomou A., Hough J. H., Kerr T. H., Mason R. E., Roche P. F., & Wright G.: *Spectropolarimetry of the 3.4 μm Feature in the Diffuse ISM toward the Galactic Center Quintuplet Cluster.* ApJ **651**, 268 (2006)

Childress M. J., Scalzo R. A., Sim S. A., Tucker B. E., Yuan F., Schmidt B. P., Cenko S. B., Silverman J. M., Contreras C., Hsiao E. Y., et al.: *Spectroscopic Observations of SN 2012fr: A Luminous, Normal Type Ia Supernova with Early High-velocity Features and a Late Velocity Plateau.* ApJ **770**, 29 (2013)

Childress M. J., Tucker B. E., Yuan F., Scalzo R., Ruiter A., Seitenzahl I., Zhang B., Schmidt B., Anguiano B., Aniyan S., et al.: *The ANU WiFeS SuperNovA Programme (AWSNAP).* PASA **33**, e055 (2016)

Chiosi E., Chiosi C., Trevisan P., Piovan L., & Orio M.: *Exploring an alternative channel of evolution towards SNa Ia explosion.* MNRAS **448**, 2100 (2015)

Chomiuk L., Soderberg A. M., Chevalier R. A., Bruzewski S., Foley R. J., Parrent J., Strader J., Badenes C., Fransson C., Kamble A., et al.: *A Deep Search for Prompt Radio Emission from Thermonuclear Supernovae with the Very Large Array.* ApJ **821**, 119 (2016)

Chornock R., Filippenko A. V., Branch D., Foley R. J., Jha S., & Li W.: *Spectropolarimetry of the Peculiar Type Ia Supernova 2005hk.* PASP **118**, 722 (2006)

Chornock R. & Filippenko A. V.: *Deviations from Axisymmetry Revealed by Line Polarization in the Normal Type Ia Supernova 2004S.* AJ **136**, 2227 (2008)

Cid Fernandes R., Mateus A., Sodré L., Stasińska G., & Gomes J. M.: *Semi-empirical analysis of Sloan Digital Sky Survey galaxies - I. Spectral synthesis method.* MNRAS **358**, 363 (2005)

Cid Fernandes R., Asari N. V., Sodré L., Stasińska G., Mateus A., Torres-Papaqui J. P., & Schoenell W.: *Uncovering the chemical enrichment and mass-assembly histories of star-forming galaxies.* MNRAS **375**, L16 (2007)

Cid Fernandes R., Schoenell W., Gomes J. M., Asari N. V., Schlickmann M., Mateus A., Stasinska G., Sodré L., Jr., Torres-Papaqui J. P., & Seagal Collaboration: *The Star Formation Histories of Galaxies: A tour through the STARLIGHT-SDSS database.* In: Revista Mexicana de Astronomia y Astrofisica Conference Series **35**, 127 (2009)

Cid Fernandes R., Mateus A., Sodré L., Stasinska G., & Gomes J. M.: *STARLIGHT: Spectral Synthesis Code.* Astrophysics Source Code Library (2011)

Cikota A., Deustua S., & Marleau F.: *Determining Type Ia Supernova Host Galaxy Extinction Probabilities and a Statistical Approach to Estimating the Absorption-to-reddening Ratio R_V.* ApJ **819**, 152 (2016)

Cikota A., De Cia A., Schulze S., Vreeswijk P. M., Leloudas G., Gal-Yam A., Perley D. A., Cikota S., Kim S., Patat F., et al.: *Spatially resolved analysis of superluminous supernovae PTF 11hrq and PTF 12dam host galaxies.* MNRAS **469**, 4705 (2017a)

Cikota A., Patat F., Cikota S., & Faran T.: *Linear spectropolarimetry of polarimetric standard stars with VLT/FORS2.* MNRAS **464**, 4146 (2017b)

Cikota A., Patat F., Cikota S., Spyromilio J., & Rau G.: *Common continuum polarization properties: a possible link between proto-planetary nebulae and Type Ia Supernova progenitors.* MNRAS **471**, 2111 (2017c)

Cikota A., Hoang T., Taubenberger S., Patat F., Mazzei P., Cox N. L. J., Zelaya P., Cikota S., Tomasella L., Benetti S., & Rodeghiero G.: *Spectropolarimetry of Galactic stars with anomalous extinction sightlines.* ArXiv e-prints **1803.08043** (2018a)

Cikota A., Leloudas G., Bulla M., Inserra C., Chen T.-W., Spyromilio J., Patat F., Cano Z., Cikota S., Coughlin M. W., et al.: *Testing the magnetar scenario for superluminous supernovae with circular polarimetry.* ArXiv e-prints **1805.00025** (2018b)

Clarke D.: *The Algebra of Polarization.* In: *Stellar Polarimetry.* Wiley-Blackwell47 (2010)

Clayton G. C. & Mathis J. S.: *On the relationship between optical polarization and extinction.* ApJ **327**, 911 (1988)

Clayton G. C., Wolff M. J., Allen R. G., & Lupie O. L.: *Ultraviolet interstellar linear polarization. 2: The wavelength dependence.* ApJ **445**, 947 (1995)

Clayton G. C., Wolff M. J., Sofia U. J., Gordon K. D., & Misselt K. A.: *Dust Grain Size Distributions from MRN to MEM.* ApJ **588**, 871 (2003)

Conley A., Carlberg R. G., Guy J., Howell D. A., Jha S., Riess A. G., & Sullivan M.: *Is There Evidence for a Hubble Bubble? The Nature of Type Ia Supernova Colors and Dust in External Galaxies.* ApJ **664**, L13 (2007)

Contreras C., Hamuy M., Phillips M. M., Folatelli G., Suntzeff N. B., Persson S. E., Stritzinger M., Boldt L., González S., Krzeminski W., et al.: *The Carnegie Supernova Project: First Photometry Data Release of Low-Redshift Type Ia Supernovae.* AJ **139**, 519 (2010)

Cox N. L. J. & Patat F.: *Interstellar atoms, molecules and diffuse bands toward SN2006X in M 100.* A&A **485**, L9 (2008)

Coyne G. V., Gehrels T., & Serkowski K.: *Wavelength dependence of polarization. XXVI. The wavelength of maximum polarization as a characteristic parameter of interstellar grains.* AJ **79**, 581 (1974)

De Cia A., Gal-Yam A., Rubin A., Leloudas G., Vreeswijk P., Perley D. A., Quimby R., Yan L., Sullivan M., Flörs A., et al.: *Light curves of hydrogen-poor Superluminous Supernovae from the Palomar Transient Factory.* ArXiv e-prints **1708.01623** (2017)

Denicoló G., Terlevich R., & Terlevich E.: *New light on the search for low-metallicity galaxies - I. The N2 calibrator.* MNRAS **330**, 69 (2002)

Dessart L., Waldman R., Livne E., Hillier D. J., & Blondin S.: *Radiative properties of pair-instability supernova explosions.* MNRAS **428**, 3227 (2013)

Dexter J. & Kasen D.: *Supernova Light Curves Powered by Fallback Accretion.* ApJ **772**, 30 (2013)

Dhawan S., Leibundgut B., Spyromilio J., & Maguire K.: *Near-infrared light curves of Type Ia supernovae: studying properties of the second maximum.* MNRAS **448**, 1345 (2015)

Domínguez A., Siana B., Henry A. L., Scarlata C., Bedregal A. G., Malkan M., Atek H., Ross N. R., Colbert J. W., Teplitz H. I., et al.: *Dust Extinction from Balmer Decrements of Star-forming Galaxies at 0.75 log T= z log T= 1.5 with Hubble Space Telescope/Wide-Field-Camera 3 Spectroscopy from the WFC3 Infrared Spectroscopic Parallel Survey.* ApJ **763**, 145 (2013)

Draine B. T.: *Interstellar Dust Grains.* ARA&A **41**, 241 (2003)

Draine B. T. & Allaf-Akbari K.: *X-Ray Scattering by Nonspherical Grains. I. Oblate Spheroids.* ApJ **652**, 1318 (2006)

Draine B. T. & Li A.: *Infrared Emission from Interstellar Dust. IV. The Silicate-Graphite-PAH Model in the Post-Spitzer Era.* ApJ **657**, 810 (2007)

Draine B. T. & Fraisse A. A.: *Polarized Far-Infrared and Submillimeter Emission from Interstellar Dust.* ApJ **696**, 1 (2009)

Elias J. H., Matthews K., Neugebauer G., & Persson S. E.: *Type I supernovae in the infrared and their use as distance indicators.* ApJ **296**, 379 (1985)

Elias-Rosa N., Benetti S., Cappellaro E., Turatto M., Mazzali P. A., Patat F., Meikle W. P. S., Stehle M., Pastorello A., Pignata G., et al.: *Anomalous extinction behaviour towards the Type Ia SN 2003cg.* MNRAS **369**, 1880 (2006)

ESO: *FORS2 User Manual, issue 96.0, VLT-MAN-ESO-13100-1543.* European Southern Observatory (2015)

Espinosa J., HERRERO A., & Sánchez F.: *Instrumentation for Large Telescopes.* Cambridge University Press (1997)

Filippenko A. V.: *Supernova 1987K - Type II in youth, type Ib in old age.* AJ **96**, 1941 (1988)

Filippenko A. V., Richmond M. W., Branch D., Gaskell M., Herbst W., Ford C. H., Treffers R. R., Matheson T., Ho L. C., Dey A., et al.: *The subluminous, spectroscopically peculiar type IA supernova 1991bg in the elliptical galaxy NGC 4374.* AJ **104**, 1543 (1992)

Fink M., Röpke F. K., Hillebrandt W., Seitenzahl I. R., Sim S. A., & Kromer M.: *Double-detonation sub-Chandrasekhar supernovae: can minimum helium shell masses detonate the core?* A&A **514**, A53 (2010)

Fitzpatrick E. L.: *Correcting for the Effects of Interstellar Extinction.* PASP **111**, 63 (1999a)

Fitzpatrick E. L.: *Correcting for the Effects of Interstellar Extinction.* PASP **111**, 63 (1999b)

Fitzpatrick E. L. & Massa D.: *An Analysis of the Shapes of Interstellar Extinction Curves. V. The IR-through-UV Curve Morphology.* ApJ **663**, 320 (2007)

Folatelli G., Phillips M. M., Burns C. R., Contreras C., Hamuy M., Freedman W. L., Persson S. E., Stritzinger M., Suntzeff N. B., Krisciunas K., et al.: *The Carnegie Supernova Project: Analysis of the First Sample of Low-Redshift Type-Ia Supernovae.* AJ **139**, 120 (2010)

Folatelli G., Morrell N., Phillips M. M., Hsiao E., Campillay A., Contreras C., Castellón S., Hamuy M., Krzeminski W., Roth M., et al.: *Spectroscopy of Type Ia Supernovae by the Carnegie Supernova Project.* ApJ **773**, 53 (2013)

Foley R. J., Filippenko A. V., & Jha S. W.: *Luminosity Indicators in the Ultraviolet Spectra of Type Ia Supernovae.* ApJ **686**, 117 (2008)

Foley R. J., Kromer M., Howie Marion G., Pignata G., Stritzinger M. D., Taubenberger S., Challis P., Filippenko A. V., Folatelli G., Hillebrandt W., et al.: *The First Maximum-light Ultraviolet through Near-infrared Spectrum of a Type Ia Supernova.* ApJ **753**, L5 (2012a)

Foley R. J., Simon J. D., Burns C. R., Gal-Yam A., Hamuy M., Kirshner R. P., Morrell N. I., Phillips M. M., Shields G. A., & Sternberg A.: *Linking Type Ia Supernova Progenitors and Their Resulting Explosions.* ApJ **752**, 101 (2012b)

Foley R. J., Challis P. J., Chornock R., Ganeshalingam M., Li W., Marion G. H., Morrell N. I., Pignata G., Stritzinger M. D., Silverman J. M., et al.: *Type Iax Supernovae: A New Class of Stellar Explosion.* ApJ **767**, 57 (2013)

Foley R. J., Fox O. D., McCully C., Phillips M. M., Sand D. J., Zheng W., Challis P., Filippenko A. V., Folatelli G., Hillebrandt W., et al.: *Extensive HST ultraviolet spectra and multiwavelength observations of SN 2014J in M82 indicate reddening and circumstellar scattering by typical dust.* MNRAS **443**, 2887 (2014)

Fossati L., Bagnulo S., Mason E., & Landi Degl'Innocenti E.: *Standard Stars for Linear Polarization Observed with FORS1.* In: Sterken C. (ed.): *The Future of Photometric, Spectrophotometric and Polarimetric Standardization.* Astronomical Society of the Pacific Conference Series **364**, 503 (2007)

Fraser M., Inserra C., Jerkstrand A., Kotak R., Pignata G., Benetti S., Botticella M.-T., Bufano F., Childress M., Mattila S., et al.: *SN 2009ip à la PESSTO: no evidence for core collapse yet.* MNRAS **433**, 1312 (2013)

Friedman A. S., Wood-Vasey W. M., Marion G. H., Challis P., Mandel K. S., Bloom J. S., Modjaz M., Narayan G., Hicken M., Foley R. J., et al.: *CfAIR2: Near-infrared Light Curves of 94 Type Ia Supernovae.* ApJS **220**, 9 (2015)

Fruchter A. S., Levan A. J., Strolger L., Vreeswijk P. M., Thorsett S. E., Bersier D., Burud I., Castro Cerón J. M., Castro-Tirado A. J., Conselice C., et al.: *Long γ-ray bursts and core-collapse supernovae have different environments.* Nature **441**, 463 (2006)

Gal-Yam A., Mazzali P., Ofek E. O., Nugent P. E., Kulkarni S. R., Kasliwal M. M., Quimby R. M., Filippenko A. V., Cenko S. B., Chornock R., et al.: *Supernova 2007bi as a pair-instability explosion.* Nature **462**, 624 (2009)

Gal-Yam A.: *Luminous Supernovae.* Science **337**, 927 (2012)

Gal-Yam A.: *Observational and Physical Classification of Supernovae.* ArXiv e-prints **1611.09353** (2016)

Gal-Yam A.: *Observational and Physical Classification of Supernovae.* In: Alsabti A. W. & Murdin P. (eds.): *Handbook of Supernovae.* Springer International Publishing1 (2017)

Gall C., Stritzinger M. D., Ashall C., Baron E., Burns C. R., Hoeflich P., Hsiao E. Y., Mazzali P. A., Phillips M. M., Filippenko A. V., et al.: *Two transitional type˜Ia supernovae located in the Fornax cluster member NGC 1404: SN 2007on and SN 2011iv.* ArXiv e-prints **1707.03823** (2017)

Gall E. E. E., Taubenberger S., Kromer M., Sim S. A., Benetti S., Blanc G., Elias-Rosa N., & Hillebrandt W.: *Interpreting the near-infrared spectra of the 'golden standard' Type Ia supernova 2005cf.* MNRAS **427**, 994 (2012)

Ganeshalingam M., Li W., Filippenko A. V., Anderson C., Foster G., Gates E. L., Griffith C. V., Grigsby B. J., Joubert N., Leja J., et al.: *Results of the Lick Observatory Supernova Search Follow-up Photometry Program: BVRI Light Curves of 165 Type Ia Supernovae.* ApJS **190**, 418 (2010)

Ganeshalingam M., Li W., & Filippenko A. V.: *Constraints on dark energy with the LOSS SN Ia sample.* MNRAS **433**, 2240 (2013)

Garavini G., Nobili S., Taubenberger S., Pastorello A., Elias-Rosa N., Stanishev V., Blanc G., Benetti S., Goobar A., Mazzali P. A., et al.: *ESC observations of SN 2005cf. II. Optical spectroscopy and the high-velocity features.* A&A **471**, 527 (2007)

Giridhar S. & Arellano Ferro A.: *Chemical composition of evolved stars of high galactic latitude.* A&A **443**, 297 (2005)

Goobar A.: *Low R_V from Circumstellar Dust around Supernovae.* ApJ **686**, L103 (2008)

Gordon K. D., Clayton G. C., Misselt K. A., Landolt A. U., & Wolff M. J.: *A Quantitative Comparison of the Small Magellanic Cloud, Large Magellanic Cloud, and Milky Way Ultraviolet to Near-Infrared Extinction Curves.* ApJ **594**, 279 (2003)

Graham M. L., Sand D. J., Valenti S., Howell D. A., Parrent J., Halford M., Zaritsky D., Bianco F., Rest A., & Dilday B.: *Clues to the Nature of SN 2009ip from Photometric and Spectroscopic Evolution to Late Times.* ApJ **787**, 163 (2014)

Guillochon J., Parrent J., Kelley L. Z., & Margutti R.: *An Open Catalog for Supernova Data.* ApJ **835**, 64 (2017)

Gutiérrez C. P., González-Gaitán S., Folatelli G., Pignata G., Anderson J. P., Hamuy M., Morrell N., Stritzinger M., Taubenberger S., Bufano F., et al.: *Supernova 2010ev: A reddened high velocity gradient type Ia supernova.* A&A **590**, A5 (2016)

Harkness R. P., Wheeler J. C., Margon B., Downes R. A., Kirshner R. P., Uomoto A., Barker E. S., Cochran A. L., Dinerstein H. L., Garnett D. R., & Levreault R. M.: *The early spectral phase of type Ib supernovae - Evidence for helium.* ApJ **317**, 355 (1987)

Harrison E. R.: *Thermonuclear and pycnonuclear reactions.* Proceedings of the Physical Society **84**, 213 (1964)

Harutyunyan A. H., Pfahler P., Pastorello A., Taubenberger S., Turatto M., Cappellaro E., Benetti S., Elias-Rosa N., Navasardyan H., Valenti S., et al.: *ESC supernova spectroscopy of non-ESC targets.* A&A **488**, 383 (2008)

Hicken M., Challis P., Jha S., Kirshner R. P., Matheson T., Modjaz M., Rest A., Wood-Vasey W. M., Bakos G., Barton E. J., et al.: *CfA3: 185 Type Ia Supernova Light Curves from the CfA.* ApJ **700**, 331 (2009a)

Hicken M., Wood-Vasey W. M., Blondin S., Challis P., Jha S., Kelly P. L., Rest A., & Kirshner R. P.: *Improved Dark Energy Constraints from ˜100 New CfA Supernova Type Ia Light Curves.* ApJ **700**, 1097 (2009b)

Hicken M., Challis P., Kirshner R. P., Rest A., Cramer C. E., Wood-Vasey W. M., Bakos G., Berlind P., Brown W. R., Caldwell N., et al.: *CfA4: Light Curves for 94 Type Ia Supernovae.* ApJS **200**, 12 (2012)

Hjorth J., Sollerman J., Møller P., Fynbo J. P. U., Woosley S. E., Kouveliotou C., Tanvir N. R., Greiner J., Andersen M. I., Castro-Tirado A. J., et al.: *A very energetic supernova associated with the γ-ray burst of 29 March 2003.* Nature **423**, 847 (2003)

Hoang T., Lazarian A., & Martin P. G.: *Constraint on the Polarization of Electric Dipole Emission from Spinning Dust.* ApJ **779**, 152 (2013)

Hoang T., Lazarian A., & Martin P. G.: *Paramagnetic Alignment of Small Grains: A Novel Method for Measuring Interstellar Magnetic Fields.* ApJ **790**, 6 (2014)

Hoang T. & Lazarian A.: *A Unified Model of Grain Alignment: Radiative Alignment of Interstellar Grains with Magnetic Inclusions.* ApJ **831**, 159 (2016)

Hoang T.: *Properties and Alignment of Interstellar Dust Grains toward Type Ia Supernovae with Anomalous Polarization Curves.* ApJ **836**, 13 (2017a)

Hoang T.: *Properties and Alignment of Interstellar Dust Grains toward Type Ia Supernovae with Anomalous Polarization Curves.* ApJ **836**, 13 (2017b)

Hoflich P.: *Asphericity Effects in Scattering Dominated Photospheres.* A&A **246**, 481 (1991)

Höflich P., Gerardy C. L., Marion H., & Quimby R.: *Signatures of isotopes in thermonuclear supernovae.* New A Rev. **50**, 470 (2006)

Holschneider M., Kronland-Martinet R., Morlet J., & Tchamitchian P.: *A Real-Time Algorithm for Signal Analysis with the Help of the Wavelet Transform.* In: Combes J.-M., Grossmann A., & Tchamitchian P. (eds.): *Wavelets. Time-Frequency Methods and Phase Space.* 286 (1989)

Hong S. S. & Greenberg J. M.: *A unified model of interstellar grains - A connection between alignment efficiency, grain model size, and cosmic abundance.* A&A **88**, 194 (1980)

Hook I. M.: *Supernovae and cosmology with future European facilities.* Philosophical Transactions of the Royal Society of London Series A **371**, 20120282 (2013)

Hough J. H., Bailey J. A., Rouse M. F., & Whittet D. C. B.: *Interstellar polarization in the dust lane of Centaurus A (NGC 5128).* MNRAS **227**, 1P (1987)

Howell D. A., Höflich P., Wang L., & Wheeler J. C.: *Evidence for Asphericity in a Subluminous Type Ia Supernova: Spectropolarimetry of SN 1999by.* ApJ **556**, 302 (2001)

Howell D. A., Sullivan M., Nugent P. E., Ellis R. S., Conley A. J., Le Borgne D., Carlberg R. G., Guy J., Balam D., Basa S., et al.: *The type Ia supernova SNLS-03D3bb from a super-Chandrasekhar-mass white dwarf star.* Nature **443**, 308 (2006)

Hsu J.-C. & Breger M.: *On standard polarized stars.* ApJ **262**, 732 (1982)

Iben I., Jr. & Tutukov A. V.: *Supernovae of type I as end products of the evolution of binaries with components of moderate initial mass (M not greater than about 9 solar masses).* ApJS **54**, 335 (1984)

Inserra C., Smartt S. J., Jerkstrand A., Valenti S., Fraser M., Wright D., Smith K., Chen T.-W., Kotak R., Pastorello A., et al.: *Super-luminous Type Ic Supernovae: Catching a Magnetar by the Tail.* ApJ **770**, 128 (2013)

Inserra C. & Smartt S. J.: *Superluminous Supernovae as Standardizable Candles and High-redshift Distance Probes.* ApJ **796**, 87 (2014)

Inserra C., Bulla M., Sim S. A., & Smartt S. J.: *Spectropolarimetry of Superluminous Supernovae: Insight into Their Geometry.* ApJ **831**, 79 (2016a)

Inserra C., Smartt S. J., Gall E. E. E., Leloudas G., Chen T.-W., Schulze S., Jerkstarnd A., Nicholl M., Anderson J. P., Arcavi I., et al.: *On the nature of Hydrogen-rich Superluminous Supernovae.* ArXiv e-prints **1604.01226** (2016b)

Inserra C., Prajs S., Gutierrez C. P., Angus C., Smith M., & Sullivan M.: *A Statistical Approach to Identify Superluminous Supernovae and Probe Their Diversity.* ApJ **854**, 175 (2018a)

Inserra C., Smartt S. J., Gall E. E. E., Leloudas G., Chen T.-W., Schulze S., Jerkstrand A., Nicholl M., Anderson J. P., Arcavi I., et al.: *On the nature of hydrogen-rich superluminous supernovae.* MNRAS **475**, 1046 (2018b)

Ivanova N., Justham S., Chen X., De Marco O., Fryer C. L., Gaburov E., Ge H., Glebbeek E., Han Z., Li X.-D., et al.: *Common envelope evolution: where we stand and how we can move forward.* A&A Rev. **21**, 59 (2013)

Jerkstrand A., Smartt S. J., & Heger A.: *Nebular spectra of pair-instability supernovae.* MNRAS **455**, 3207 (2016)

Johnson J. J. & Jones T. J.: *From red giant to planetary nebula - Dust, asymmetry, and polarization.* AJ **101**, 1735 (1991)

Jones D. & Boffin H. M. J.: *Binary stars as the key to understanding planetary nebulae.* Nature Astronomy **1**, 0117 (2017)

Kasen D., Nugent P., Wang L., Howell D. A., Wheeler J. C., Höflich P., Baade D., Baron E., & Hauschildt P. H.: *Analysis of the Flux and Polarization Spectra of the Type Ia Supernova SN 2001el: Exploring the Geometry of the High-Velocity Ejecta.* ApJ **593**, 788 (2003)

Kasen D. & Bildsten L.: *Supernova Light Curves Powered by Young Magnetars.* ApJ **717**, 245 (2010)

Kashi A. & Soker N.: *A circumbinary disc in the final stages of common envelope and the core-degenerate scenario for Type Ia supernovae.* MNRAS **417**, 1466 (2011)

Kemp J. C.: *Circular Polarization of Thermal Radiation in a Magnetic Field.* ApJ **162**, 169 (1970)

Kemp J. C. & Swedlund J. B.: *Large Infrared Circular Polarization of Grw+70° 8247.* ApJ **162**, L67 (1970)

Kemp J. C., Swedlund J. B., Landstreet J. D., & Angel J. R. P.: *Discovery of Circularly Polarized Light from a White Dwarf.* ApJ **161**, L77 (1970)

Kemp J. C., Swedlund J. B., & Wolstencroft R. D.: *Confirmation of the Magnetic White Dwarf G-195-19.* ApJ **164**, L17 (1971)

Kennicutt R. C., Jr.: *Star Formation in Galaxies Along the Hubble Sequence.* ARA&A **36**, 189 (1998)

Kessler R., Becker A. C., Cinabro D., Vanderplas J., Frieman J. A., Marriner J., Davis T. M., Dilday B., Holtzman J., Jha S. W., et al.: *First-Year Sloan Digital Sky Survey-II Supernova Results: Hubble Diagram and Cosmological Parameters.* ApJS **185**, 32 (2009)

Khokhlov A. M.: *Delayed detonation model for type IA supernovae.* A&A **245**, 114 (1991)

Kim S.-H. & Martin P. G.: *The size distribution of interstellar dust particles as determined from polarization: Infinite cylinders.* ApJ **431**, 783 (1994)

Kim S.-H. & Martin P. G.: *The size distribution of interstellar dust particles as determined from polarization: Spheroids.* ApJ **444**, 293 (1995)

Kipper T.: *Optical Spectrometry of the Post-Agb Star HD 161796.* Baltic Astronomy **16**, 191 (2007)

Klochkova V. G. & Panchuk V. E.: *The detection of heavy metals in the circumstellar envelopes of post-AGB stars.* Astronomy Reports **60**, 344 (2016)

Kozyreva A., Gilmer M., Hirschi R., Fröhlich C., Blinnikov S., Wollaeger R. T., Noebauer U. M., van Rossum D. R., Heger A., Even W. P., et al.: *Fast evolving pair-instability supernova models: evolution, explosion, light curves.* MNRAS **464**, 2854 (2017)

Krisciunas K., Contreras C., Burns C. R., Phillips M. M., Stritzinger M. D., Morrell N., Hamuy M., Anais J., Boldt L., Busta L., et al.: *The Carnegie Supernova Project. I. Third Photometry Data Release of Low-redshift Type Ia Supernovae and Other White Dwarf Explosions.* AJ **154**, 211 (2017a)

Krisciunas K., Suntzeff N. B., Espinoza J., Gonzalez D., Miranda A., & Sanhueza P.: *Optical and Infrared Photometry of SN 2005df.* Research Notes of the American Astronomical Society **1**, 36 (2017b)

Lambas D. G., Tissera P. B., Alonso M. S., & Coldwell G.: *Galaxy pairs in the 2dF survey - I. Effects of interactions on star formation in the field.* MNRAS **346**, 1189 (2003)

Lampeitl H., Smith M., Nichol R. C., Bassett B., Cinabro D., Dilday B., Foley R. J., Frieman J. A., Garnavich P. M., Goobar A., et al.: *The Effect of Host Galaxies on Type Ia Supernovae in the SDSS-II Supernova Survey.* ApJ **722**, 566 (2010)

Landi Degl'Innocenti E. & Landolfi M. (eds.). *Astrophysics and Space Science Library.* Astrophysics and Space Science Library **307** (2004)

Law N. M., Kulkarni S. R., Dekany R. G., Ofek E. O., Quimby R. M., Nugent P. E., Surace J., Grillmair C. C., Bloom J. S., Kasliwal M. M., et al.: *The Palomar Transient Factory: System Overview, Performance, and First Results.* PASP **121**, 1395 (2009)

Lazarian A., Andersson B.-G., & Hoang T.: *Grain alignment: role of radiative torques and paramagnetic relaxation.* In: Kolokolova L., Hough J., & Levasseur-Regourd A.-C. (eds.): *Polarimetry of stars and planetary systems.* 81 (2015)

Lee H.-W. & Blandford R. D.: *On the polarization of resonantly scattered emission lines - III. Polarization of quasar broad emission lines and broad absorption line troughs.* MNRAS **288**, 19 (1997)

Leibundgut B., Kirshner R. P., Phillips M. M., Wells L. A., Suntzeff N. B., Hamuy M., Schommer R. A., Walker A. R., Gonzalez L., Ugarte P., et al.: *SN 1991bg - A type IA supernova with a difference.* AJ **105**, 301 (1993)

Leitherer C., Schaerer D., Goldader J. D., Delgado R. M. G., Robert C., Kune D. F., de Mello D. F., Devost D., & Heckman T. M.: *Starburst99: Synthesis Models for Galaxies with Active Star Formation.* ApJS **123**, 3 (1999)

Leloudas G., Stritzinger M. D., Sollerman J., Burns C. R., Kozma C., Krisciunas K., Maund J. R., Milne P., Filippenko A. V., Fransson C., et al.: *The normal Type Ia SN 2003hv out to very late phases.* A&A **505**, 265 (2009)

Leloudas G., Patat F., Maund J. R., Hsiao E., Malesani D., Schulze S., Contreras C., de Ugarte Postigo A., Sollerman J., Stritzinger M. D., et al.: *Polarimetry of the Superluminous Supernova LSQ14mo: No Evidence for Significant Deviations from Spherical Symmetry.* ApJ **815**, L10 (2015a)

Leloudas G., Schulze S., Krühler T., Gorosabel J., Christensen L., Mehner A., de Ugarte Postigo A., Amorín R., Thöne C. C., Anderson J. P., et al.: *Spectroscopy of superluminous supernova host galaxies. A preference of hydrogen-poor events for extreme emission line galaxies.* MNRAS **449**, 917 (2015b)

Leloudas G., Maund J. R., Gal-Yam A., Pursimo T., Hsiao E., Malesani D., Patat F., de Ugarte Postigo A., Sollerman J., Stritzinger M. D., & Wheeler J. C.: *Time-resolved Polarimetry of the Superluminous SN 2015bn with the Nordic Optical Telescope.* ApJ **837**, L14 (2017)

Leonard D. C., Li W., Filippenko A. V., Foley R. J., & Chornock R.: *Evidence for Spectropolarimetric Diversity in Type Ia Supernovae.* ApJ **632**, 450 (2005)

Leonini S. & Brimacombe J.: *Possible supernova in NGC 1954.* Central Bureau Electronic Telegrams **2569**, 1 (2010)

Livio M. & Riess A. G.: *Have the Elusive Progenitors of Type Ia Supernovae Been Discovered?* ApJ **594**, L93 (2003)

Livio M. & Mazzali P.: *On the Progenitors of Type Ia Supernovae.* ArXiv e-prints **1802.03125** (2018)

Lü G., Zhu C., & Podsiadlowski P.: *Dust Formation in the Ejecta of Common Envelope Systems.* ApJ **768**, 193 (2013)

Lunnan R., Chornock R., Berger E., Laskar T., Fong W., Rest A., Sanders N. E., Challis P. M., Drout M. R., Foley R. J., et al.: *Hydrogen-poor Superluminous Supernovae and Long-duration Gamma-Ray Bursts Have Similar Host Galaxies.* ApJ **787**, 138 (2014)

Lunnan R., Chornock R., Berger E., Rest A., Fong W., Scolnic D., Jones D. O., Soderberg A. M., Challis P. M., Drout M. R., et al.: *Zooming In on the Progenitors of Superluminous Supernovae With the HST.* ApJ **804**, 90 (2015)

Lunnan R., Chornock R., Berger E., Milisavljevic D., Jones D. O., Rest A., Fong W., Fransson C., Margutti R., Drout M. R., et al.: *PS1-14bj: A Hydrogen-poor Superluminous Supernova With a Long Rise and Slow Decay.* ApJ **831**, 144 (2016)

Ma X., Hopkins P. F., Faucher-Giguère C.-A., Zolman N., Muratov A. L., Kereš D., & Quataert E.: *The origin and evolution of the galaxy mass-metallicity relation.* MNRAS **456**, 2140 (2016)

Maercker M., Mohamed S., Vlemmings W. H. T., Ramstedt S., Groenewegen M. A. T., Humphreys E., Kerschbaum F., Lindqvist M., Olofsson H., Paladini C., et al.: *Unexpectedly large mass loss during the thermal pulse cycle of the red giant star R Sculptoris.* Nature **490**, 232 (2012)

Mandel K. S., Narayan G., & Kirshner R. P.: *Type Ia Supernova Light Curve Inference: Hierarchical Models in the Optical and Near-infrared.* ApJ **731**, 120 (2011)

Margutti R., Milisavljevic D., Soderberg A. M., Chornock R., Zauderer B. A., Murase K., Guidorzi C., Sanders N. E., Kuin P., Fransson C., et al.: *A Panchromatic View of the Restless SN 2009ip Reveals the Explosive Ejection of a Massive Star Envelope.* ApJ **780**, 21 (2014)

Marigo P., Bressan A., Nanni A., Girardi L., & Pumo M. L.: *Evolution of thermally pulsing asymptotic giant branch stars - I. The COLIBRI code.* MNRAS **434**, 488 (2013)

Marigo P., Girardi L., Bressan A., Rosenfield P., Aringer B., Chen Y., Dussin M., Nanni A., Pastorelli G., Rodrigues T. S., et al.: *A New Generation of PARSEC-COLIBRI Stellar Isochrones Including the TP-AGB Phase.* ApJ **835**, 77 (2017)

Marino R. A., Rosales-Ortega F. F., Sánchez S. F., Gil de Paz A., Vílchez J., Miralles-Caballero D., Kehrig C., Pérez-Montero E., Stanishev V., Iglesias-Páramo J., et al.: *The O3N2 and N2 abundance indicators revisited: improved calibrations based on CALIFA and T_e-based literature data.* A&A **559**, A114 (2013)

Martin P. G.: *Interstellar polarization from a medium with changing grain alignment.* ApJ **187**, 461 (1974)

Martin P. G., Clayton G. C., & Wolff M. J.: *Ultraviolet Interstellar Linear Polarization. V. Analysis of the Final Data Set.* ApJ **510**, 905 (1999)

Masiero J., Hodapp K., Harrington D., & Lin H.: *Commissioning of the Dual-Beam Imaging Polarimeter for the University of Hawaii 88 inch Telescope.* PASP **119**, 1126 (2007)

Mateus A., Sodré L., Cid Fernandes R., Stasińska G., Schoenell W., & Gomes J. M.: *Semi-empirical analysis of Sloan Digital Sky Survey galaxies - II. The bimodality of the galaxy population revisited.* MNRAS **370**, 721 (2006)

Mateus A., Sodré L., Cid Fernandes R., & Stasińska G.: *Semi-empirical analysis of Sloan Digital Sky Survey galaxies - IV. A nature via nurture scenario for galaxy evolution.* MNRAS **374**, 1457 (2007)

Matheson T., Challis P., Kirshner R., & Calkins M.: *Supernovae 2003ef, 2003eg, 2003eh, 2003ei, 2003ej, 2003ek.* IAU Circ. **8134** (2003)

Matheson T., Kirshner R. P., Challis P., Jha S., Garnavich P. M., Berlind P., Calkins M. L., Blondin S., Balog Z., Bragg A. E., et al.: *Optical Spectroscopy of Type ia Supernovae.* AJ **135**, 1598 (2008)

Mathis J. S., Rumpl W., & Nordsieck K. H.: *The size distribution of interstellar grains.* ApJ **217**, 425 (1977)

Maund J. R., Wheeler J. C., Wang L., Baade D., Clocchiatti A., Patat F., Höflich P., Quinn J., & Zelaya P.: *A Spectropolarimetric View on the Nature of the Peculiar Type I SN 2005hk.* ApJ **722**, 1162 (2010)

Mazzali P. A., Benetti S., Altavilla G., Blanc G., Cappellaro E., Elias-Rosa N., Garavini G., Goobar A., Harutyunyan A., Kotak R., et al.: *High-Velocity Features: A Ubiquitous Property of Type Ia Supernovae.* ApJ **623**, L37 (2005)

Mazzali P. A., Sullivan M., Pian E., Greiner J., & Kann D. A.: *Spectrum formation in superluminous supernovae (Type I).* MNRAS **458**, 3455 (2016)

Mazzali P. A., Ashall C., Pian E., Stritzinger M. D., Gall C., Phillips M. M., Höflich P., & Hsiao E.: *The nebular spectra of the transitional Type Ia Supernovae 2007on and 2011iv: broad, multiple components indicate aspherical explosion cores.* MNRAS **476**, 2905 (2018)

Mazzei P. & Barbaro G.: *Dust properties along anomalous extinction sightlines.* MNRAS **390**, 706 (2008)

Mazzei P. & Barbaro G.: *Dust properties along anomalous extinction sightlines. II. Studying extinction curves with dust models.* A&A **527**, A34 (2011)

Minkowski R.: *Spectra of Supernovae.* PASP **53**, 224 (1941)

Misra K., Sahu D. K., Anupama G. C., & Pandey K.: *Photometric and spectroscopic study of a highly reddened type Ia supernova SN 2003hx in NGC 2076.* MNRAS **389**, 706 (2008)

Neill J. D., Sullivan M., Gal-Yam A., Quimby R., Ofek E., Wyder T. K., Howell D. A., Nugent P., Seibert M., Martin D. C., et al.: *The Extreme Hosts of Extreme Supernovae.* ApJ **727**, 15 (2011)

Nicholl M., Smartt S. J., Jerkstrand A., Inserra C., McCrum M., Kotak R., Fraser M., Wright D., Chen T.-W., Smith K., et al.: *Slowly fading super-luminous supernovae that are not pair-instability explosions.* Nature **502**, 346 (2013)

Nicholl M., Smartt S. J., Jerkstrand A., Inserra C., Sim S. A., Chen T.-W., Benetti S., Fraser M., Gal-Yam A., Kankare E., et al.: *On the diversity of superluminous supernovae: ejected mass as the dominant factor.* MNRAS **452**, 3869 (2015a)

Nicholl M., Smartt S. J., Jerkstrand A., Sim S. A., Inserra C., Anderson J. P., Baltay C., Benetti S., Chambers K., Chen T.-W., et al.: *LSQ14bdq: A Type Ic Super-luminous Supernova with a Double-peaked Light Curve.* ApJ **807**, L18 (2015b)

Nobili S. & Goobar A.: *The colour-lightcurve shape relation of type Ia supernovae and the reddening law.* A&A **487**, 19 (2008)

Nomoto K.: *Accreting white dwarf models for type I supernovae. I - Presupernova evolution and triggering mechanisms.* ApJ **253**, 798 (1982)

Nomoto K., Thielemann F.-K., & Yokoi K.: *Accreting white dwarf models of Type I supernovae. III - Carbon deflagration supernovae.* ApJ **286**, 644 (1984)

Nordhaus J. & Blackman E. G.: *Low-mass binary-induced outflows from asymptotic giant branch stars.* MNRAS **370**, 2004 (2006)

Ofek E. O., Arcavi I., Tal D., Sullivan M., Gal-Yam A., Kulkarni S. R., Nugent P. E., Ben-Ami S., Bersier D., Cao Y., et al.: *Interaction-powered Supernovae: Rise-time versus Peak-luminosity Correlation and the Shock-breakout Velocity.* ApJ **788**, 154 (2014)

Oliva E.: *Wedged double Wollaston, a device for single shot polarimetric measurements.* A&AS **123** (1997)

Oppenheimer B. D., Bieging J. H., Schmidt G. D., Gordon K. D., Misselt K. A., & Smith P. S.: *Spectropolarimetry and Radiative Transfer Modeling of Three Proto-Planetary Nebulae.* ApJ **624**, 957 (2005)

Osterbrock D. E.: *Astrophysics of gaseous nebulae and active galactic nuclei.* (1989)

Osterbrock D. E. & Ferland G. J.: *Astrophysics of gaseous nebulae and active galactic nuclei.* (2006)

Pakmor R., Kromer M., Taubenberger S., Sim S. A., Röpke F. K., & Hillebrandt W.: *Normal Type Ia Supernovae from Violent Mergers of White Dwarf Binaries.* ApJ **747**, L10 (2012)

Pastorello A., Mazzali P. A., Pignata G., Benetti S., Cappellaro E., Filippenko A. V., Li W., Meikle W. P. S., Arkharov A. A., Blanc G., et al.: *ESC and KAIT observations of the transitional Type Ia SN 2004eo.* Monthly Notices of the Royal Astronomical Society **377**, 1531 (2007)

Pastorello A., Mazzali P. A., Pignata G., Benetti S., Cappellaro E., Filippenko A. V., Li W., Meikle W. P. S., Arkharov A. A., Blanc G., et al.: *ESC and KAIT observations of the transitional Type Ia SN 2004eo.* MNRAS **377**, 1531 (2007)

Patat F.: *Reflections on reflexions - I. Light echoes in Type Ia supernovae.* MNRAS **357**, 1161 (2005)

Patat F., Benetti S., Cappellaro E., & Turatto M.: *Reflections on reflexions - II. Effects of light echoes on the luminosity and spectra of Type Ia supernovae.* MNRAS **369**, 1949 (2006)

Patat F. & Romaniello M.: *Error Analysis for Dual-Beam Optical Linear Polarimetry.* PASP **118**, 146 (2006)

Patat F., Chandra P., Chevalier R., Justham S., Podsiadlowski P., Wolf C., Gal-Yam A., Pasquini L., Crawford I. A., Mazzali P. A., et al.: *Detection of Circumstellar Material in a Normal Type Ia Supernova.* Science **317**, 924 (2007)

Patat F., Baade D., Höflich P., Maund J. R., Wang L., & Wheeler J. C.: *VLT spectropolarimetry of the fast expanding type Ia SN 2006X.* A&A **508**, 229 (2009)

Patat F., Maund J. R., Benetti S., Botticella M. T., Cappellaro E., Harutyunyan A., & Turatto M.: *VLT spectropolarimetry of the optical transient in NGC 300. Evidence of asymmetry in the circumstellar dust.* A&A **510**, A108 (2010)

Patat F. & Taubenberger S.: *Characterisation of the CAFOS linear spectropolarimeter.* A&A **529**, A57 (2011)

Patat F., Höflich P., Baade D., Maund J. R., Wang L., & Wheeler J. C.: *VLT Spectropolarimetry of the Type Ia SN 2005ke. A step towards understanding subluminous events.* A&A **545**, A7 (2012)

Patat F., Taubenberger S., Cox N. L. J., Baade D., Clocchiatti A., Höflich P., Maund J. R., Reilly E., Spyromilio J., Wang L., et al.: *Properties of extragalactic dust inferred from linear polarimetry of Type Ia Supernovae.* A&A **577**, A53 (2015)

Patat F.: *Introduction to Supernova Polarimetry.* In: Alsabti A. W. & Murdin P. (eds.): *Handbook of Supernovae.* Springer International Publishing1017 (2017)

Perley D. A., Quimby R. M., Yan L., Vreeswijk P. M., De Cia A., Lunnan R., Gal-Yam A., Yaron O., Filippenko A. V., Graham M. L., et al.: *Host-galaxy Properties of 32 Low-redshift Superluminous Supernovae from the Palomar Transient Factory.* ApJ **830**, 13 (2016)

Perlmutter S., Aldering G., Goldhaber G., Knop R. A., Nugent P., Castro P. G., Deustua S., Fabbro S., Goobar A., Groom D. E., et al.: *Measurements of Ω and Λ from 42 High-Redshift Supernovae.* ApJ **517**, 565 (1999)

Pettini M. & Pagel B. E. J.: *[OIII]/[NII] as an abundance indicator at high redshift.* MNRAS **348**, L59 (2004)

Phillips M. M.: *The absolute magnitudes of Type IA supernovae.* ApJ **413**, L105 (1993)

Phillips M. M., Lira P., Suntzeff N. B., Schommer R. A., Hamuy M., & Maza J.: *The Reddening-Free Decline Rate Versus Luminosity Relationship for Type IA Supernovae.* AJ **118**, 1766 (1999)

Phillips M. M., Li W., Frieman J. A., Blinnikov S. I., DePoy D., Prieto J. L., Milne P., Contreras C., Folatelli G., Morrell N., et al.: *The Peculiar SN 2005hk: Do Some Type Ia Supernovae Explode as Deflagrations?1,.* PASP **119**, 360 (2007)

Phillips M. M., Simon J. D., Morrell N., Burns C. R., Cox N. L. J., Foley R. J., Karakas A. I., Patat F., Sternberg A., Williams R. E., et al.: *On the Source of the Dust Extinction in Type Ia Supernovae and the Discovery of Anomalously Strong Na I Absorption.* ApJ **779**, 38 (2013)

Pignata G., Maza J., Hamuy M., Antezana R., Gonzalez L., Gonzalez P., Lopez P., Silva S., Folatelli G., Iturra D., et al.: *Supernova 2008fl in NGC 6805.* Central Bureau Electronic Telegrams **1498** (2008)

Pinto P. A. & Eastman R. G.: *The Physics of Type IA Supernova Light Curves. II. Opacity and Diffusion.* ApJ **530**, 757 (2000)

Planck Collaboration, Ade P. A. R., Aghanim N., Arnaud M., Ashdown M., Aumont J., Baccigalupi C., Banday A. J., Barreiro R. B., Bartlett J. G., et al.: *Planck 2015 results. XIII. Cosmological parameters.* A&A **594**, A13 (2016)

Porter A. L., Leising M. D., Williams G. G., Milne P., Smith P., Smith N., Bilinski C., Hoffman J. L., Huk L., & Leonard D. C.: *Asymmetries in SN 2014J near Maximum Light Revealed through Spectropolarimetry.* ApJ **828**, 24 (2016)

Pourbaix D., Tokovinin A. A., Batten A. H., Fekel F. C., Hartkopf W. I., Levato H., Morrell N. I., Torres G., & Udry S.: *$S_{B⁹}$: The ninth catalogue of spectroscopic binary orbits.* A&A **424**, 727 (2004)

Prentice S., James P., Anderson J., Short L., Galbany L., Taubenberger S., Inserra C., Kankare E., Maguire K., Smartt S. J., et al.: *PESSTO spectroscopic classification of optical transients.* The Astronomer's Telegram **9542** (2016)

Prieto J. L., Rest A., & Suntzeff N. B.: *A New Method to Calibrate the Magnitudes of Type Ia Supernovae at Maximum Light.* ApJ **647**, 501 (2006)

Prieto J. L., Stanek K. Z., & Beacom J. F.: *Characterizing Supernova Progenitors via the Metallicities of their Host Galaxies, from Poor Dwarfs to Rich Spirals.* ApJ **673**, 999 (2008)

Quimby R. M., Kulkarni S. R., Kasliwal M. M., Gal-Yam A., Arcavi I., Sullivan M., Nugent P., Thomas R., Howell D. A., Nakar E., et al.: *Hydrogen-poor superluminous stellar explosions.* Nature **474**, 487 (2011)

Quimby R. M., De Cia A., Gal-Yam A., Leloudas G., Lunnan R., Perley D. A., Vreeswijk P. M., Yan L., Bloom J. S., Cenko S. B., et al.: *Spectra of Hydrogen-poor Superluminous Supernovae from the Palomar Transient Factory.* ApJ **855**, 2 (2018)

Rasio F. A. & Shapiro S. L.: *Hydrodynamics of binary coalescence. 1: Polytropes with stiff equations of state.* ApJ **432**, 242 (1994)

Rau A., Kulkarni S. R., Law N. M., Bloom J. S., Ciardi D., Djorgovski G. S., Fox D. B., Gal-Yam A., Grillmair C. C., Kasliwal M. M., et al.: *Exploring the Optical Transient Sky with the Palomar Transient Factory.* PASP **121**, 1334 (2009)

Rau G., Paladini C., Hron J., Aringer B., Groenewegen M. A. T., & Nowotny W.: *Modelling the atmosphere of the carbon-rich Mira RU Virginis.* A&A **583**, A106 (2015)

Rau G., Hron J., Paladini C., Aringer B., Eriksson K., Marigo P., Nowotny W., & Grellmann R.: *The adventure of carbon stars. Observations and modeling of a set of C-rich AGB stars.* A&A **600**, A92 (2017)

Reindl B., Tammann G. A., Sandage A., & Saha A.: *Reddening, Absorption, and Decline Rate Corrections for a Complete Sample of Type Ia Supernovae Leading to a Fully Corrected Hubble Diagram to $v < 30{,}000$ km s^{-1}.* ApJ **624**, 532 (2005)

Rich A. & Williams W. L.: *A Search for Optical Circular Polarization in White Dwarfs and Late-Type Stars with Circumstellar Shells.* ApJ **180**, L123 (1973)

Richardson D., Thomas R. C., Casebeer D., Blankenship Z., Ratowt S., Baron E., & Branch D.: *SUSPECT - The Online Supernova Spectrum Database.* In: *American Astronomical Society Meeting Abstracts.* Bulletin of the American Astronomical Society **33**, 1428 (2001)

Richmond M. W., Treffers R. R., Filippenko A. V., Paik Y., Leibundgut B., Schulman E., & Cox C. V.: *UBVRI photometry of SN 1993J in M81: The first 120 days.* AJ **107**, 1022 (1994)

Riess A. G., Press W. H., & Kirshner R. P.: *Is the Dust Obscuring Supernovae in Distant Galaxies the Same as Dust in the Milky Way?* ApJ **473**, 588 (1996)

Riess A. G., Filippenko A. V., Challis P., Clocchiatti A., Diercks A., Garnavich P. M., Gilliland R. L., Hogan C. J., Jha S., Kirshner R. P., et al.: *Observational Evidence from Supernovae for an Accelerating Universe and a Cosmological Constant.* AJ **116**, 1009 (1998)

Riess A. G. & Livio M.: *The First Type Ia Supernovae: An Empirical Approach to Taming Evolutionary Effects in Dark Energy Surveys from SNe Ia at z>2.* ApJ **648**, 884 (2006)

Rosswog S., Kasen D., Guillochon J., & Ramirez-Ruiz E.: *Collisions of White Dwarfs as a New Progenitor Channel for Type Ia Supernovae.* ApJ **705**, L128 (2009)

Ruiz-Lapuente P., Cappellaro E., Turatto M., Gouiffes C., Danziger I. J., della Valle M., & Lucy L. B.: *Modeling the iron-dominated spectra of the type IA supernova SN 1991T at premaximum.* ApJ **387**, L33 (1992)

Sahu D. K., Tanaka M., Anupama G. C., Kawabata K. S., Maeda K., Tominaga N., Nomoto K., Mazzali P. A., & Prabhu T. P.: *The Evolution of the Peculiar Type Ia Supernova SN 2005hk over 400 Days.* ApJ **680**, 580 (2008)

Sato Y., Nakasato N., Tanikawa A., Nomoto K., Maeda K., & Hachisu I.: *A Systematic Study of Carbon-Oxygen White Dwarf Mergers: Mass Combinations for Type Ia Supernovae.* ApJ **807**, 105 (2015)

Savage B. D., Massa D., Meade M., & Wesselius P. R.: *A catalog of ultraviolet interstellar extinction excesses for 1415 stars.* ApJS **59**, 397 (1985)

Scalzo R. A., Aldering G., Antilogus P., Aragon C., Bailey S., Baltay C., Bongard S., Buton C., Childress M., Chotard N., et al.: *Nearby Supernova Factory Observations of SN 2007if: First Total Mass Measurement of a Super-Chandrasekhar-Mass Progenitor.* ApJ **713**, 1073 (2010)

Scalzo R., Aldering G., Antilogus P., Aragon C., Bailey S., Baltay C., Bongard S., Buton C., Cellier-Holzem F., Childress M., et al.: *Type Ia supernova bolometric light curves and ejected mass estimates from the Nearby Supernova Factory.* MNRAS **440**, 1498 (2014)

Scarrott S. M.: *Optical Polarization and Magnetic Fields in Spiral Galaxies.* QJRAS **37**, 297 (1996)

Scarrott S. M., Foley N. B., Gledhill T. M., & Wolstencroft R. D.: *BVRI imaging polarimetric studies of the galaxy NGC 5128.* MNRAS **282**, 252 (1996)

Schlafly E. F. & Finkbeiner D. P.: *Measuring Reddening with Sloan Digital Sky Survey Stellar Spectra and Recalibrating SFD.* ApJ **737**, 103 (2011)

Schlafly E. F., Peek J. E. G., Finkbeiner D. P., & Green G. M.: *Mapping the Extinction Curve in 3D: Structure on Kiloparsec Scales.* ApJ **838**, 36 (2017)

Schlegel E. M.: *A new subclass of Type II supernovae?* MNRAS **244**, 269 (1990)

Schmidt G. D., Elston R., & Lupie O. L.: *The Hubble Space Telescope Northern-Hemisphere grid of stellar polarimetric standards.* AJ **104**, 1563 (1992)

Schulze S., Krühler T., Leloudas G., Gorosabel J., Mehner A., Buchner J., Kim S., Ibar E., Amorín R., Herrero-Illana R., et al.: *Cosmic evolution and metal aversion in super-luminous supernova host galaxies.* ArXiv e-prints **1612.05978** (2016)

Scovacricchi D., Nichol R. C., Bacon D., Sullivan M., & Prajs S.: *Cosmology with superluminous supernovae.* MNRAS **456**, 1700 (2016)

Seitenzahl I. R., Ciaraldi-Schoolmann F., Röpke F. K., Fink M., Hillebrandt W., Kromer M., Pakmor R., Ruiter A. J., Sim S. A., & Taubenberger S.: *Three-dimensional delayed-detonation models with nucleosynthesis for Type Ia supernovae.* MNRAS **429**, 1156 (2013)

Serkowski K., Mathewson D. S., & Ford V. L.: *Wavelength dependence of interstellar polarization and ratio of total to selective extinction.* ApJ **196**, 261 (1975)

Shapiro P. R.: *Interstellar polarization - Magnetite dust.* ApJ **201**, 151 (1975)

Silverman J. M., Foley R. J., Filippenko A. V., Ganeshalingam M., Barth A. J., Chornock R., Griffith C. V., Kong J. J., Lee N., Leonard D. C., et al.: *Berkeley Supernova Ia Program - I. Observations, data reduction and spectroscopic sample of 582 low-redshift Type Ia supernovae.* MNRAS **425**, 1789 (2012)

Silverman J. M., Nugent P. E., Gal-Yam A., Sullivan M., Howell D. A., Filippenko A. V., Arcavi I., Ben-Ami S., Bloom J. S., Cenko S. B., et al.: *Type Ia Supernovae Strongly Interacting with Their Circumstellar Medium.* ApJS **207**, 3 (2013)

Simon J. D., Gal-Yam A., Gnat O., Quimby R. M., Ganeshalingam M., Silverman J. M., Blondin S., Li W., Filippenko A. V., Wheeler J. C., et al.: *Variable Sodium Absorption in a Low-extinction Type Ia Supernova.* ApJ **702**, 1157 (2009)

Skilling J.: *Nested Sampling.* In: Fischer R., Preuss R., & Toussaint U. V. (eds.). American Institute of Physics Conference Series **735**, 395 (2004)

Sol Alonso M., Lambas D. G., Tissera P., & Coldwell G.: *Effects of galaxy interactions in different environments.* MNRAS **367**, 1029 (2006)

Somerville W. B., Allen R. G., Carnochan D. J., He L., McNally D., Martin P. G., Morgan D. H., Nandy K., Walsh J. R., Whittet D. C. B., et al.: *Ultraviolet interstellar polarization observed with the Hubble Space Telescope.* ApJ **427**, L47 (1994)

Sorokina E., Blinnikov S., Nomoto K., Quimby R., & Tolstov A.: *Type I Superluminous Supernovae as Explosions inside Non-hydrogen Circumstellar Envelopes.* ApJ **829**, 17 (2016)

Soto K. T., Lilly S. J., Bacon R., Richard J., & Conseil S.: *ZAP - enhanced PCA sky subtraction for integral field spectroscopy.* MNRAS **458**, 3210 (2016)

Sternberg A., Gal-Yam A., Simon J. D., Leonard D. C., Quimby R. M., Phillips M. M., Morrell N., Thompson I. B., Ivans I., Marshall J. L., et al.: *Circumstellar Material in Type Ia Supernovae via Sodium Absorption Features.* Science **333**, 856 (2011)

Stokes G.: *On the Composition and Resolution of Streams of Polarized Light from Different Sources.* Cambridge Philosophical Society (1852)

Stritzinger M., Leibundgut B., Walch S., & Contardo G.: *Constraints on the progenitor systems of type Ia supernovae.* A&A **450**, 241 (2006)

Tan T. G.: *Supernova 2008ff in Pgc 64319.* Central Bureau Electronic Telegrams **1488** (2008)

Tanaka M., Maeda K., Mazzali P. A., Kawabata K. S., & Nomoto K.: *Three-dimensional Explosion Geometry of Stripped-envelope Core-collapse Supernovae. II. Modeling of Polarization.* ApJ **837**, 105 (2017)

Tang J., Bressan A., Rosenfield P., Slemer A., Marigo P., Girardi L., & Bianchi L.: *New PARSEC evolutionary tracks of massive stars at low metallicity: testing canonical stellar evolution in nearby star-forming dwarf galaxies.* MNRAS **445**, 4287 (2014)

Taubenberger S.: *The Extremes of Thermonuclear Supernovae.* ArXiv e-prints **1703.00528** (2017)

Thöne C. C., de Ugarte Postigo A., García-Benito R., Leloudas G., Schulze S., & Amorín R.: *A young stellar environment for the superluminous supernova PTF12dam.* MNRAS **451**, L65 (2015)

Trujillo-Bueno J., Moreno-Insertis F., & Sanchez Martinez F.: *Astrophysical Spectropolarimetry.* (2002)

Ueta T., Meixner M., & Bobrowsky M.: *A Hubble Space Telescope Snapshot Survey of Proto-Planetary Nebula Candidates: Two Types of Axisymmetric Reflection Nebulosities.* ApJ **528**, 861 (2000)

van de Hulst H. C.: *Light Scattering by Small Particles.* (1957)

van Kerkwijk M. H., Chang P., & Justham S.: *Sub-Chandrasekhar White Dwarf Mergers as the Progenitors of Type Ia Supernovae.* ApJ **722**, L157 (2010)

van Winckel H.: *Post-AGB Stars.* ARA&A **41**, 391 (2003)

Vink J. S. (ed.): *Very Massive Stars in the Local Universe.* Astrophysics and Space Science Library **412** (2015)

Vinkó J., Bíró I. B., Csák B., Csizmadia S., Derekas A., Furész G., Heiner Z., Sárneczky K., Sipocz B., Szabó G., et al.: *The Type Ia Supernova 2001V in NGC 3987.* A&A **397**, 115 (2003)

Voshchinnikov N. V.: *Interstellar extinction and interstellar polarization: Old and new models.* J. Quant. Spec. Radiat. Transf. **113**, 2334 (2012)

Vreeswijk P. M., Savaglio S., Gal-Yam A., De Cia A., Quimby R. M., Sullivan M., Cenko S. B., Perley D. A., Filippenko A. V., Clubb K. I., et al.: *The Hydrogen-poor Superluminous Supernova iPTF 13ajg and its Host Galaxy in Absorption and Emission.* ApJ **797**, 24 (2014)

Vreeswijk P. M., Leloudas G., Gal-Yam A., De Cia A., Perley D. A., Quimby R. M., Waldman R., Sullivan M., Yan L., Ofek E. O., et al.: *On the Early-time Excess Emission in Hydrogen-poor Superluminous Supernovae.* ApJ **835**, 58 (2017)

Wagers A., Wang L., & Asztalos S.: *Quantifying Spectral Features of Type Ia Supernovae.* ApJ **711**, 711 (2010)

Wang L., Wheeler J. C., & Höflich P.: *Polarimetry of the Type IA Supernova SN 1996X.* ApJ **476**, L27 (1997)

Wang L., Baade D., Höflich P., Khokhlov A., Wheeler J. C., Kasen D., Nugent P. E., Perlmutter S., Fransson C., & Lundqvist P.: *Spectropolarimetry of SN 2001el in NGC 1448: Asphericity of a Normal Type Ia Supernova.* ApJ **591**, 1110 (2003)

Wang L.: *Dust around Type Ia Supernovae.* ApJ **635**, L33 (2005)

Wang L., Baade D., Höflich P., Wheeler J. C., Kawabata K., Khokhlov A., Nomoto K., & Patat F.: *Premaximum Spectropolarimetry of the Type Ia SN 2004dt.* ApJ **653**, 490 (2006a)

Wang L., Baade D., & Patat F.: *Spectropolarimetric Diagnostics of Thermonuclear Supernova Explosions.* Science **315**, 212 (2007)

Wang L. & Wheeler J. C.: *Spectropolarimetry of Supernovae.* ARA&A **46**, 433 (2008)

Wang X., Wang L., Pain R., Zhou X., & Li Z.: *Determination of the Hubble Constant, the Intrinsic Scatter of Luminosities of Type Ia Supernovae, and Evidence for Nonstandard Dust in Other Galaxies.* ApJ **645**, 488 (2006b)

Wang X., Li W., Filippenko A. V., Foley R. J., Smith N., & Wang L.: *The Detection of a Light Echo from the Type Ia Supernova 2006X in M100.* ApJ **677**, 1060 (2008a)

Wang X., Li W., Filippenko A. V., Krisciunas K., Suntzeff N. B., Li J., Zhang T., Deng J., Foley R. J., Ganeshalingam M., et al.: *Optical and Near-Infrared Observations of the Highly Reddened, Rapidly Expanding Type Ia Supernova SN 2006X in M100.* ApJ **675**, 626 (2008b)

Wang X., Li W., Filippenko A. V., Foley R. J., Kirshner R. P., Modjaz M., Bloom J., Brown P. J., Carter D., Friedman A. S., et al.: *The Golden Standard Type Ia Supernova 2005cf: Observations from the Ultraviolet to the Near-Infrared Wavebands.* ApJ **697**, 380 (2009)

Webbink R. F.: *Double white dwarfs as progenitors of R Coronae Borealis stars and Type I supernovae.* ApJ **277**, 355 (1984)

Wegner W.: *Atlas of Interstellar Extinction Curves of OB Stars Covering the Whole Available Wavelength Range.* Baltic Astronomy **11**, 1 (2002)

Weingartner J. C. & Draine B. T.: *Dust Grain-Size Distributions and Extinction in the Milky Way, Large Magellanic Cloud, and Small Magellanic Cloud.* ApJ **548**, 296 (2001)

Wesselius P. R., van Duinen R. J., de Jonge A. R. W., Aalders J. W. G., Luinge W., & Wildeman K. J.: *ANS ultraviolet photometry, catalogue of point sources.* A&AS **49**, 427 (1982)

Wheeler J. C. & Harkness R. P.: *Type I supernovae.* Reports on Progress in Physics **53**, 1467 (1990)

Whelan J. & Iben I., Jr.: *Binaries and Supernovae of Type I.* ApJ **186**, 1007 (1973)

Whittet D. C. B. & van Breda I. G.: *The correlation of the interstellar extinction law with the wavelength of maximum polarization.* A&A **66**, 57 (1978)

Whittet D. C. B., Martin P. G., Hough J. H., Rouse M. F., Bailey J. A., & Axon D. J.: *Systematic variations in the wavelength dependence of interstellar linear polarization.* ApJ **386**, 562 (1992)

Whittet D. C. B., Gerakines P. A., Carkner A. L., Hough J. H., Martin P. G., Prusti T., & Kilkenny D.: *A Study of the Chamaeleon-I Dark Cloud and T-Association - Part Six - Interstellar Polarization Grain Alignment and Magnetic Field.* MNRAS **268**, 1 (1994)

Whittet D. C. B., Gerakines P. A., Hough J. H., & Shenoy S. S.: *Interstellar Extinction and Polarization in the Taurus Dark Clouds: The Optical Properties of Dust near the Diffuse/Dense Cloud Interface.* ApJ **547**, 872 (2001)

Wiersema K., Covino S., Toma K., van der Horst A. J., Varela K., Min M., Greiner J., Starling R. L. C., Tanvir N. R., Wijers R. A. M. J., et al.: *Circular polarization in the optical afterglow of GRB 121024A.* Nature **509**, 201 (2014)

Wilking B. A., Lebofsky M. J., Kemp J. C., Martin P. G., & Rieke G. H.: *The wavelength dependence of interstellar linear polarization.* ApJ **235**, 905 (1980)

Wilking B. A., Lebofsky M. J., & Rieke G. H.: *The wavelength dependence of interstellar linear polarization - Stars with extreme values of lambda/max/.* AJ **87**, 695 (1982)

Wolff M. J., Nordsieck K. H., & Nook M. A.: *A Medium-Resolution Search for Polarmetric Structure: Moderate Y Reddening Sightlines.* AJ **111**, 856 (1996)

Woosley S. E. & Bloom J. S.: *The Supernova Gamma-Ray Burst Connection.* ARA&A **44**, 507 (2006)

Woosley S. E., Blinnikov S., & Heger A.: *Pulsational pair instability as an explanation for the most luminous supernovae.* Nature **450**, 390 (2007)

Woosley S. E.: *Bright Supernovae from Magnetar Birth.* ApJ **719**, L204 (2010)

Woosley S. E.: *Pulsational Pair-Instability Supernovae.* ArXiv e-prints **1608.08939** (2016)

Wyrzykowski L., Hamanowicz A., Kostrzewa-Rutkowska Z., Klencki J., Sitek M., Udalski A., Kozlowski S., Ulaczyk K., Soszynski I., & Mroz P.: *OGLE-IV Transient Search report 24 September 2016.* The Astronomer's Telegram **9543** (2016)

Yamanaka M., Naito H., Kinugasa K., Takanashi N., Tanaka M., Kawabata K. S., Ozaki S., Narusawa S.-Y., & Sadakane Kozo: *Early Spectral Evolution of the Rapidly Expanding Type Ia Supernova 2006X.* PASJ **61**, 713 (2009)

Yan L., Quimby R., Ofek E., Gal-Yam A., Mazzali P., Perley D., Vreeswijk P. M., Leloudas G., de Cia A., Masci F., et al.: *Detection of Broad Hα Emission Lines in the Late-time Spectra of a Hydrogen-poor Superluminous Supernova.* ApJ **814**, 108 (2015)

Yang Y., Wang L., Baade D., Brown P. J., Cracraft M., Höflich P. A., Maund J., Patat F., Sparks W. B., Spyromilio J., et al.: *Interstellar-medium Mapping in M82 through Light Echoes around Supernova 2014J.* ApJ **834**, 60 (2017)

Yaron O. & Gal-Yam A.: *WISeREP - An Interactive Supernova Data Repository.* PASP **124**, 668 (2012)

Yoon S.-C. & Langer N.: *On the evolution of rapidly rotating massive white dwarfs towards supernovae or collapses.* A&A **435**, 967 (2005)

Yoon S.-C., Podsiadlowski P., & Rosswog S.: *Remnant evolution after a carbon-oxygen white dwarf merger.* MNRAS **380**, 933 (2007)

Zelaya P., Clocchiatti A., Baade D., Höflich P., Maund J., Patat F., Quinn J. R., Reilly E., Wang L., Wheeler J. C., et al.: *Continuum Foreground Polarization and Na I Absorption in Type Ia SNe.* ApJ **836**, 88 (2017a)

Zelaya P., Clocchiatti A., Baade D., Höflich P., Maund J., Patat F., Quinn J. R., Reilly E., Wang L., Wheeler J. C., et al.: *Continuum Foreground Polarization and Na I Absorption in Type Ia SNe.* ApJ **836**, 88 (2017b)

Zhang J.-J., Wang X.-F., Bai J.-M., Zhang T.-M., Wang B., Liu Z.-W., Zhao X.-L., & Chen J.-C.: *Optical and Ultraviolet Observations of the Narrow-lined Type Ia SN 2012fr in NGC 1365.* AJ **148**, 1 (2014)

A. Appendix 1

A.1. Standard stars

A.1.1. Standard stars with CAFOS

Two unpolarized standard stars were observed with CAFOS: HD 144579 (2 epochs), and HD 90508 (1 epoch); and two polarized standard stars, each at two epochs: HD 154445 and HD 43384.

We use the unpolarized standard stars to investigate possible instrumental effects. The observations have been binned in 200Å bins, and the Stokes parameters, the polarization degree and polarization angle were calculated as described in Sect. 3.3.3. Figure A.1 shows the derived Stokes parameters and polarization of the two unpolarized standard stars at three epochs, compared to the instrumental polarization determined in Patat & Taubenberger (2011). Our measurements show consistent values between the three epochs, with average Q and U vales of 0.07 % and 0.004 % respectively, in a wavelength range 3850-8650Å, leading to an average polarization of $P \approx 0.10\,\%$. The standard deviations are $\sigma_Q \approx 0.06$ %, $\sigma_U \approx 0.11$ % and $\sigma_P \approx 0.07$ %. The average uncertainty per 200Å bin is ∼0.03 %. Our values are more consistent with zero than the values determined in Patat & Taubenberger (2011). They analyzed observations of the unpolarized star HD 14069 observed at 16 half-wave plate angle, and claimed average values of the instrumental Stokes parameters in a wavelength range above 4000Å of $\langle Q_{ins} \rangle$ = 0.25 ± 0.03% and $\langle U_{ins} \rangle$ = -0.13 ± 0.03%, leading to an average polarization P_{ins} = 0.28 ± 0.03%.

There were two polarized standard stars observed with CAFOS, each at two epochs: HD 154445 and HD 43384. The calculated polarization spectra of HD 43384 are consistent to each other with an RMS of ∼ 0.04 %. Our Serkowski parameters (see Table A.3) are fully consistent with $p_{\max}$ = 3.01 ± 0.04 % and $\lambda_{\max}$ = 0.531 ± 0.011 μm, determined in Hsu & Breger (1982). The wavelength dependent phase retardance variation of the half-wave plate deployed in CAFOS was quantified in Patat & Taubenberger (2011). HD 43384 has a variable (+0.6 °/100 yr), and slightly wavelength dependent (+2.5±1.3 °/μm) polarization position angle (Hsu & Breger, 1982). Therefore it is not the best standard star for HWP chromatism investigation. However, for comparison reasons, we use $\chi_0(V)$= 169.8 ± 0.7 degrees to compute the phase retardance variance and find that it is consistent with Patat & Taubenberger (2011) (see Fig. A.2). The average deviation of our phase retardance variation compared to Patat & Taubenberger (2011) is ∼ +0.3 degrees, which is within the errors of χ_0.

Also, both observed polarization spectra of HD 154445 are consistent to each other with an RMS of 0.07 %. The average $\lambda_{\max}$=5579 ± 11 Å and $p_{\max}$= 3.64 ± 0.01 % matches with the literature values $p_{\max}$ = 3.66± 0.01 % and $\lambda_{\max}$=5690 ± 10 Å (Wolff et al., 1996). Our average θ after the HWP chromatism correction is 89.2 ± 0.4 degree, which is similar to the literature values of θ_V = 88.8 ± 0.1 (Schmidt et al., 1992), θ_V = 90.1 ± 0.1 and $\theta_{\max}$=88.3 ± 0.1 degrees (Hsu & Breger, 1982).

A.1.2. Standard stars with AFOSC

Because of lack of space in AFOSC, for polarimetry purposes, the Wollaston prism gets inserted into the filter wheel in place of a filter. Therefore, during each observing run it is necessary to calibrate the instrument's zero point rotation angle using polarized standard stars.

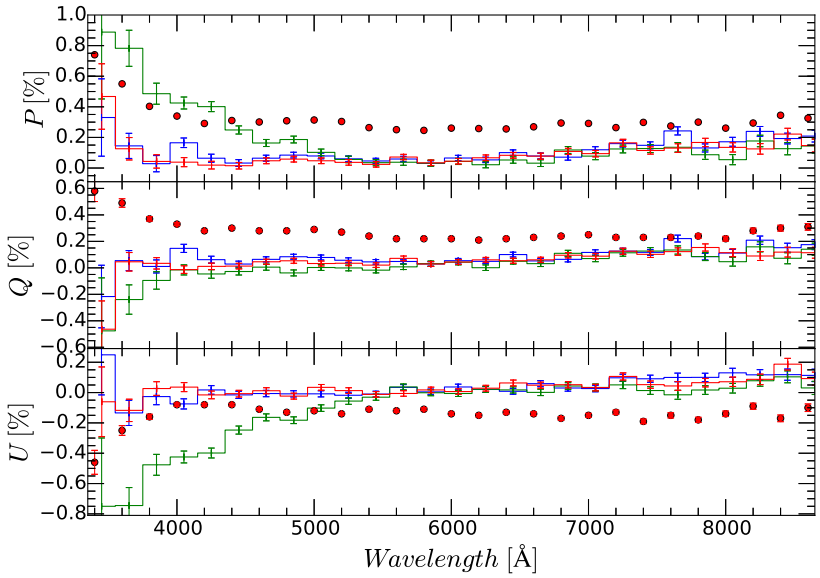

Figure A.1.: Unpolarized standard stars observed with CAFOS. HD 144579 was observed at two epochs, on 2015-04-30 at 00:51 UT (blue line) and 04:22 UT (green line). The red line indicates HD 90508 observed on 2015-04-29 at 21:28 UT. For comparison, the red dots indicate the instrumental polarization determined in Patat & Taubenberger (2011).

We use observations of 3 unpolarized standard stars observed from 2015-02-09 to 2015-03-11 to investigate possible instrumental polarization of AFOSC: HD 90508 (2 epochs), HD 39587 (2 epochs) and HD 144579 (1 epoch). They have all been observed at 4 rotation angles of the adapter (-45, 0, 45 and 90 degrees), except for one epoch of HD 90508 which has been observed at only 2 rotation angles (0 and 90 degree). Figure A.3 shows the derived Stokes parameters Q and U, and the polarization for all unpolarized standard stars. The black lines indicate the epochs observed at 4 rotation angles, and the blue line indicates HD 90508 observed at 2 rotation angles. The average stokes parameters at a wavelength range above 3600 Å, excluding the range from 7500-7700Å, which is contaminated by the strong telluric 7605.0 Å O_2 line, are 0.03 % and -0.002 % for Q and U respectively, leading to a polarization of 0.05 %, with a standard deviation of 0.05 %.

When ignoring the observations performed with the adapter rotation angles of -45 and 45 degrees, and calculating the polarization using only the adapter rotation angles of 0 and 90 degrees for all 5 epochs of the 3 standard stars, the average stokes parameters, are 0.05 % and -0.04 % for Q and U respectively, leading to a polarization of 0.08 %, with a standard deviation of 0.10 %.

Also HD 185395, observed on 2016-08-02, is consistent with zero, with an average polarization above 3600 Å, excluding the range from 7500-7700Å, of 0.08 % and an RMS of 0.06 %.

There were three polarized standard stars observed with AFOSC: HD 43384 (3 epochs at two different runs), HD 21291 (1 epoch), and HD 198478 (1 epoch), all at 4 rotation angles of the adapter. However, because most of the science data was taken only with two rotation angles, to be consistent, we use only two rotation angles.

Figure A.4 shows HD 43384 at 3 different epochs. Although the shapes of the polarization spectra are similar, i.e., $\lambda_{\rm max}$ and K of the Serkowski fit are similar to each other, the peak polarization values, $p_{\rm max}$, are not consistent and range from ~2.92% to ~3.19% (see Table A.4), while the literature value is $p_{\rm max}$ = 3.01 ± 0.04 % (Hsu & Breger, 1982).

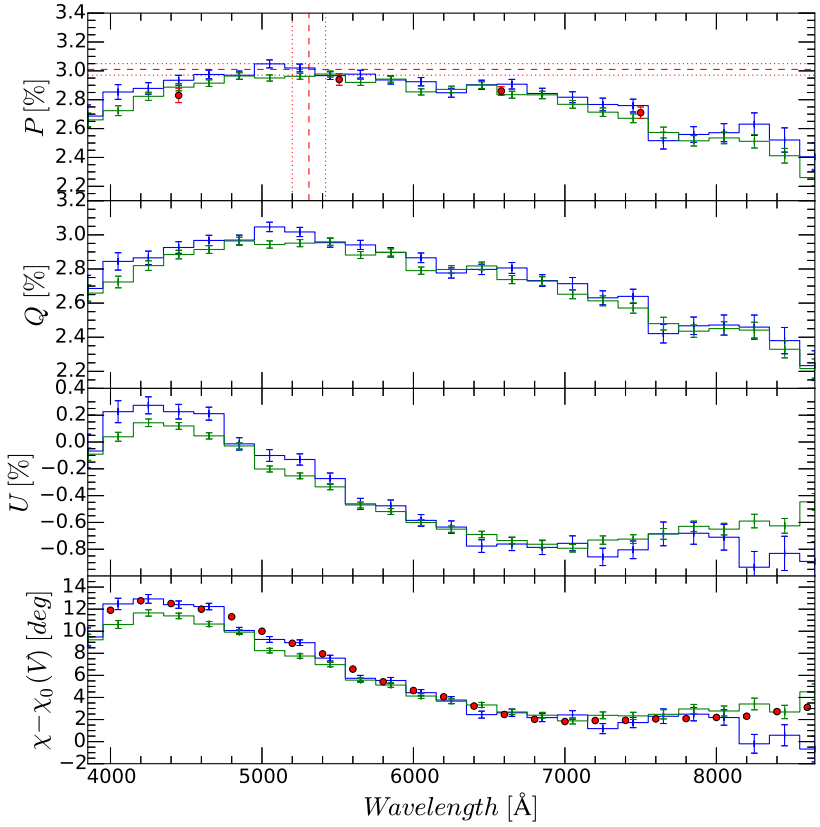

Figure A.2.: Polarized standard star HD 43384 observed with CAFOS at two epochs, on 2015-04-29 at 20:14 UT (green line) and 21:14 UT (blue line). Both epochs are consistent to each other with a RMS of ~ 0.04 %. The red dashed lines in the polarization panel indicate $p_{\max}$ and $\lambda_{\max}$ and their errors (dotted line) determined by Hsu & Breger (1982), and the red dots are their individual measurements. The red dots in the χ - $\chi_0(V)$ panel indicate the phase retardance variance determined in Patat & Taubenberger (2011).

For HD 21291 our determined peak polarization value is lower than the literature value. By fitting the Serkowski curve, we find $\lambda_{\max}$ = 5166 ± 27, $p_{\max}$ = 2.95 ± 0.01 %, while the literature values are $p_{\max}$ ~ 3.53 ± 0.02 % and $\lambda_{\max}$ = 5210 ± 30 Å (Hsu & Breger, 1982).

HD 198478 was observed on 2016-08-02. Our determined peak polarization value is almost consistent with the literature value. By fitting the Serkowski curve, we find $\lambda_{\max}$ = 5132 ± 42, $p_{\max}$ = 2.76 ± 0.01 %, while the literature values are $p_{\max}$ ~ 2.72 ± 0.02 % and $\lambda_{\max}$ = 5220 ± 80 Å (Hsu & Breger, 1982).

We use polarized standard stars to determine the correction of the instrument's rotation angle zero point for each of the three runs separately.

During the first run (2015-02-09) two stars have been observed: HD 43384 (2 epochs) and HD 21291 (1 epoch). Using the literature values of χ_V = 169.8 ± 0.7 degrees for HD 43384, and χ_V = 116.6 ± 0.2 degrees for HD 21291, we calculated an weighted average of the offset $\Delta\theta_V$ = 136.4 ± 0.3 degrees.

During the second run (2015-03-09), HD 43384 was observed at one epoch, from which we calculated the instrument's rotation angle zero point offset $\Delta\theta_V$ = 134.0 ± 0.8 degrees.

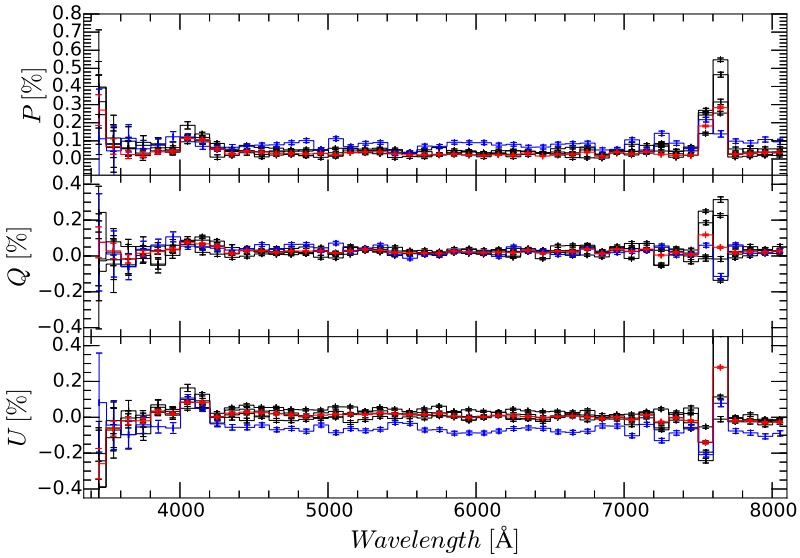

Figure A.3.: Unpolarized standard stars observed with AFOSC. The black lines indicates observations observed at 4 rotation angles, and the blue lines indicates HD 90508 observed at two rotation angles only. The red line is the average of all measurements.

Finally, from HD 198478 observed during the third run (2016-08-02), we calculated $\Delta\theta_V$ = 138.3 ± 0.4 degrees.

A.2. Serkowski fit to SNe Ia

We determine the Serkowski parameters of the sodium sample in Zelaya et al. (2017a) by fitting Eq. (4.1) to the data shown in their Fig. 1. The polarized lines have been excluded from the wavelength range. The results are given in Table A.1.

Table A.1.: Serkowski paramaters of the SNe Ia Sodium-sample (Zelaya et al. 2017)

SN Name	$\lambda_{\max}$ (Å)	$p_{\max}$ (%)	K
SN 2007le	3967 ± 494	1.93 ± 0.09	1.73 ± 0.87
SN 2010ev	4408 ± 114	1.88 ± 0.02	1.89 ± 0.23
SN 2007fb	3821 ± 447	0.76 ± 0.03	1.13 ± 0.46
SN 2003W	3996 ± 371	0.78 ± 0.04	2.56 ± 1.03
SN 2007af	7409 ± 537	0.64 ± 0.01	1.24 ± 0.35
SN 2002fk	4403 ± 460	0.40 ± 0.01	0.57 ± 0.35
SN 2002bo	3525 ± 137	1.11 ± 0.05	3.95 ± 0.49
SN 2011ae	4256 ± 295	0.33 ± 0.01	3.56 ± 1.87
SN 2005hk[a]	6731 ± 2116	0.17 ± 0.02	-1.36 ± 1.51

[a] Because of a low polarization degree and low signal to noise, a good fit with the Serkowski curve was not possible.

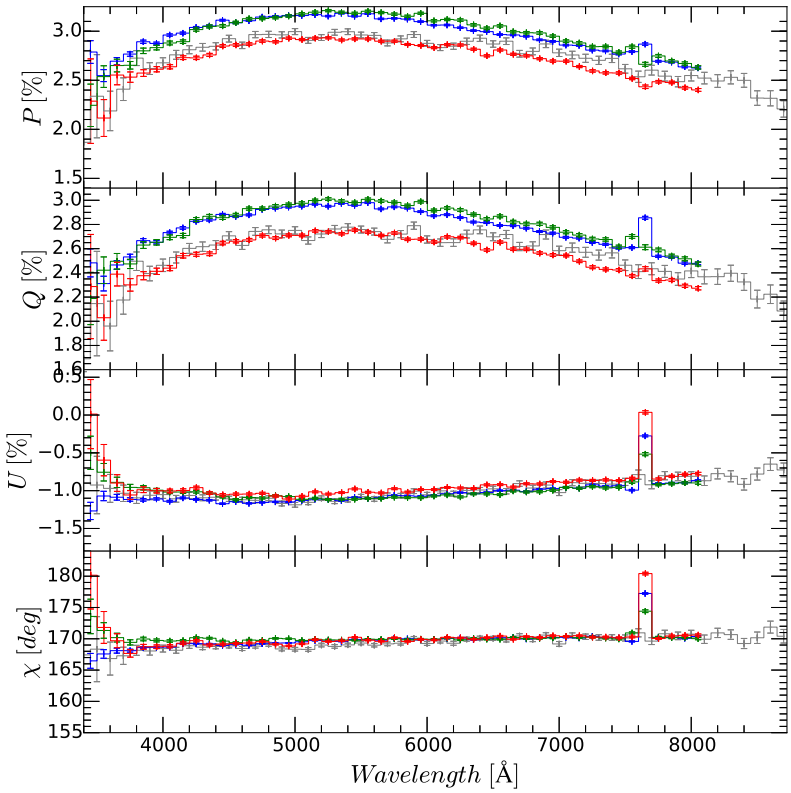

Figure A.4.: Polarized standard star HD 43384 observed at three different nights with AFOSC. The peak polarization values, $p_{\max}$, are not fully consistent and range from ~2.92% to ~3.19%. For reference, the gray line indicates HD 43384 observed with CAFOS.

A.3. Individual observations

Table A.2.: Individual epochs with FORS2

								Serkowski curve		
Name	Filter	Epoch	Passband	P (%)	P_Q (%)	P_U (%)	θ(°)	$\lambda_{\max}$ (Å)	$P_{\max}$ (%)	K
HD 141318	free	2014-10-10 00:23:57						5827 ± 40	2.43 ± 0.01	1.11 ± 0.06
			B	2.28 ± 0.02	-0.41 ± 0.01	2.24 ± 0.02	50.2 ± 0.2			
			V	2.43 ± 0.01	-0.52 ± 0.01	2.38 ± 0.01	51.2 ± 0.2			
			R	2.40 ± 0.01	-0.55 ± 0.01	2.34 ± 0.01	51.7 ± 0.1			
			I	2.18 ± 0.01	-0.50 ± 0.01	2.12 ± 0.01	51.7 ± 0.1			
HD 141318	free	2014-10-10 00:27:27						5770 ± 23	2.46 ± 0.01	1.29 ± 0.04
			B	2.30 ± 0.01	-0.40 ± 0.01	2.26 ± 0.01	50.0 ± 0.1			
			V	2.46 ± 0.01	-0.52 ± 0.01	2.40 ± 0.01	51.1 ± 0.1			
			R	2.41 ± 0.01	-0.55 ± 0.01	2.35 ± 0.01	51.6 ± 0.1			
			I	2.15 ± 0.01	-0.48 ± 0.01	2.10 ± 0.01	51.4 ± 0.1			
HD 141318	GG435	2014-10-10 00:37:56						5544 ± 57	2.43 ± 0.01	1.24 ± 0.08
			B	2.35 ± 0.02	-0.49 ± 0.02	2.30 ± 0.02	51.0 ± 0.2			
			V	2.44 ± 0.01	-0.50 ± 0.01	2.39 ± 0.01	50.9 ± 0.1			
			R	2.36 ± 0.01	-0.50 ± 0.01	2.31 ± 0.01	51.1 ± 0.1			
			I	2.06 ± 0.01	-0.39 ± 0.01	2.02 ± 0.01	50.6 ± 0.1			
HD 141318	GG435	2014-10-10 00:46:02						5851 ± 79	2.38 ± 0.01	0.81 ± 0.08
			B	2.33 ± 0.02	-0.46 ± 0.02	2.28 ± 0.02	50.7 ± 0.2			
			V	2.40 ± 0.01	-0.44 ± 0.01	2.36 ± 0.01	50.3 ± 0.1			
			R	2.37 ± 0.01	-0.46 ± 0.01	2.32 ± 0.01	50.6 ± 0.1			
			I	2.20 ± 0.01	-0.46 ± 0.01	2.15 ± 0.01	51.0 ± 0.1			
HD 152245	free	2014-10-13 00:22:31						6360 ± 63	0.93 ± 0.01	1.32 ± 0.12
			B	0.80 ± 0.01	-0.10 ± 0.01	0.79 ± 0.01	48.4 ± 0.4			
			V	0.91 ± 0.01	-0.10 ± 0.01	0.90 ± 0.01	48.3 ± 0.3			
			R	0.92 ± 0.01	-0.10 ± 0.01	0.92 ± 0.01	48.2 ± 0.2			
			I	0.84 ± 0.01	-0.06 ± 0.01	0.84 ± 0.01	47.2 ± 0.2			
HD 152245	GG435	2015-02-06 08:26:24						6174 ± 64	1.01 ± 0.01	1.25 ± 0.12
			B	0.92 ± 0.01	0.18 ± 0.01	0.90 ± 0.01	39.3 ± 0.4			
			V	0.98 ± 0.01	0.24 ± 0.01	0.95 ± 0.01	38.0 ± 0.2			
			R	0.98 ± 0.01	0.25 ± 0.01	0.94 ± 0.01	37.6 ± 0.1			
			I	0.88 ± 0.01	0.26 ± 0.01	0.84 ± 0.01	36.4 ± 0.2			
HD 152245	GG435	2015-02-06 08:31:36.880						6465 ± 66	1.0 ± 0.01	1.13 ± 0.11
			B	0.88 ± 0.01	0.22 ± 0.01	0.85 ± 0.01	37.9 ± 0.5			
			V	0.95 ± 0.01	0.28 ± 0.01	0.91 ± 0.01	36.4 ± 0.2			
			R	0.97 ± 0.01	0.30 ± 0.01	0.92 ± 0.01	36.1 ± 0.1			
			I	0.91 ± 0.01	0.30 ± 0.01	0.85 ± 0.01	35.3 ± 0.2			
HD 54439	free	2014-10-27T05:39:01						4802 ± 196	0.8 ± 0.01	0.82 ± 0.13
			B	0.76 ± 0.01	0.04 ± 0.01	-0.76 ± 0.01	136.6 ± 0.5			
			V	0.76 ± 0.01	0.09 ± 0.01	-0.76 ± 0.01	138.2 ± 0.4			
			R	0.72 ± 0.01	0.11 ± 0.01	-0.71 ± 0.01	139.3 ± 0.2			
			I	0.64 ± 0.01	0.07 ± 0.01	-0.64 ± 0.01	138.2 ± 0.4			
HD 54439	GG435	2014-10-27 05:50:15						4756 ± 268	0.79 ± 0.01	1.11 ± 0.22
			B	0.74 ± 0.02	0.10 ± 0.02	-0.73 ± 0.02	139.0 ± 0.7			

Table A.2.: continued.

Name	Filter	Epoch	Passband	P (%)	P_Q (%)	P_U (%)	θ(°)	Serkowski curve		
								$\lambda_{\max}$ (Å)	$P_{\max}$ (%)	K
			V	0.75 ± 0.01	0.11 ± 0.01	-0.74 ± 0.01	139.3 ± 0.4			
			R	0.69 ± 0.01	0.15 ± 0.01	-0.68 ± 0.01	141.2 ± 0.3			
			I	0.58 ± 0.01	0.15 ± 0.01	-0.56 ± 0.01	142.4 ± 0.4			
HD 73420	free	2014-10-27 06:04:31						6756 ± 323	0.55 ± 0.01	0.65 ± 0.23
			B	0.35 ± 0.01	0.35 ± 0.01	-0.04 ± 0.02	176.4 ± 1.0			
			V	0.37 ± 0.01	0.36 ± 0.01	-0.10 ± 0.01	172.5 ± 0.7			
			R	0.36 ± 0.01	0.35 ± 0.01	-0.08 ± 0.01	173.4 ± 0.4			
			I	0.33 ± 0.01	0.32 ± 0.01	-0.08 ± 0.01	172.5 ± 0.6			
HD 73420	GG435	2014-10-27 06:41:43						6482 ± 150	0.42 ± 0.01	1.22 ± 0.28
			B	0.35 ± 0.02	0.34 ± 0.02	-0.08 ± 0.02	173.3 ± 1.3			
			V	0.38 ± 0.01	0.35 ± 0.01	-0.15 ± 0.01	168.4 ± 0.6			
			R	0.38 ± 0.01	0.36 ± 0.01	-0.14 ± 0.01	169.2 ± 0.4			
			I	0.30 ± 0.01	0.28 ± 0.01	-0.11 ± 0.01	168.8 ± 0.6			
HD 78785	free	2014-11-14 07:04:31						5771 ± 10	3.96 ± 0.01	1.22 ± 0.02
			B	3.64 ± 0.01	3.39 ± 0.01	1.30 ± 0.01	10.5 ± 0.1			
			V	3.88 ± 0.01	3.63 ± 0.01	1.37 ± 0.01	10.3 ± 0.1			
			R	3.80 ± 0.01	3.53 ± 0.01	1.39 ± 0.01	10.8 ± 0.1			
			I	3.40 ± 0.01	3.16 ± 0.01	1.26 ± 0.01	10.9 ± 0.1			
HD 78785	GG435	2014-11-14 06:54:19						5766 ± 16	3.97 ± 0.01	1.18 ± 0.02
			B	3.73 ± 0.02	3.48 ± 0.02	1.35 ± 0.02	10.6 ± 0.1			
			V	3.89 ± 0.01	3.65 ± 0.01	1.34 ± 0.01	10.0 ± 0.1			
			R	3.81 ± 0.01	3.55 ± 0.01	1.38 ± 0.01	10.6 ± 0.1			
			I	3.41 ± 0.01	3.18 ± 0.01	1.24 ± 0.01	10.6 ± 0.1			
HD 78785	GG435	2014-11-14 07:13:33						5754 ± 17	3.94 ± 0.01	1.18 ± 0.02
			B	3.71 ± 0.02	3.45 ± 0.02	1.37 ± 0.02	10.8 ± 0.1			
			V	3.86 ± 0.01	3.62 ± 0.01	1.34 ± 0.01	10.2 ± 0.1			
			R	3.78 ± 0.01	3.52 ± 0.01	1.38 ± 0.01	10.7 ± 0.1			
			I	3.38 ± 0.01	3.15 ± 0.01	1.24 ± 0.01	10.8 ± 0.1			
HD 96042	free	2014-12-21 08:14:55						4816 ± 255	0.58 ± 0.01	0.93 ± 0.19
			B	0.59 ± 0.01	-0.38 ± 0.01	-0.45 ± 0.01	115.1 ± 0.5			
			V	0.60 ± 0.01	-0.40 ± 0.01	-0.45 ± 0.01	114.0 ± 0.4			
			R	0.57 ± 0.01	-0.38 ± 0.01	-0.42 ± 0.01	114.0 ± 0.3			
			I	0.51 ± 0.01	-0.34 ± 0.01	-0.38 ± 0.01	114.2 ± 0.4			
HD 96042	free	2014-12-21 08:22:47						4850 ± 245	0.60 ± 0.01	0.90 ± 0.18
			B	0.60 ± 0.01	-0.39 ± 0.01	-0.46 ± 0.01	114.7 ± 0.5			
			V	0.62 ± 0.01	-0.41 ± 0.01	-0.46 ± 0.01	114.1 ± 0.4			
			R	0.59 ± 0.01	-0.39 ± 0.01	-0.44 ± 0.01	114.2 ± 0.3			
			I	0.54 ± 0.01	-0.36 ± 0.01	-0.40 ± 0.01	114.1 ± 0.4			
HD 96042	GG435	2015-01-02 07:25:12						3494 ± 955	0.64 ± 0.05	0.51 ± 0.24
			B	0.62 ± 0.02	-0.34 ± 0.02	-0.52 ± 0.02	118.5 ± 0.8			
			V	0.60 ± 0.01	-0.36 ± 0.01	-0.49 ± 0.01	116.9 ± 0.5			
			R	0.56 ± 0.01	-0.33 ± 0.01	-0.46 ± 0.01	117.2 ± 0.3			

Table A.2.: continued.

Name	Filter	Epoch	Passband	P (%)	P_Q (%)	P_U (%)	θ(°)	Serkowski curve		
								$\lambda_{\max}$ (Å)	$P_{\max}$ (%)	K
			I	0.51 ± 0.01	-0.32 ± 0.01	-0.40 ± 0.01	115.8 ± 0.5			
HD 96042	GG435	2015-01-02 07:29:02						5116 ± 242	0.59 ± 0.01	1.43 ± 0.30
			B	0.59 ± 0.02	-0.35 ± 0.02	-0.48 ± 0.02	117.0 ± 1.0			
			V	0.62 ± 0.01	-0.39 ± 0.01	-0.47 ± 0.01	115.1 ± 0.5			
			R	0.58 ± 0.01	-0.36 ± 0.01	-0.45 ± 0.01	115.4 ± 0.3			
			I	0.49 ± 0.01	-0.31 ± 0.01	-0.37 ± 0.01	115.0 ± 0.5			
HD 152853	free	2015-02-03 07:45:45						5804 ± 75	1.78 ± 0.02	1.35 ± 0.14
			B	1.57 ± 0.01	1.19 ± 0.01	1.02 ± 0.01	20.3 ± 0.2			
			V	1.71 ± 0.01	1.29 ± 0.01	1.13 ± 0.01	20.6 ± 0.2			
			R	1.71 ± 0.01	1.26 ± 0.01	1.15 ± 0.01	21.1 ± 0.1			
			I	1.42 ± 0.01	1.04 ± 0.01	0.97 ± 0.01	21.5 ± 0.2			
HD 152853	GG435	2015-02-03 08:03:39						5619 ± 67	1.69 ± 0.01	1.11 ± 0.08
			B	1.59 ± 0.02	1.18 ± 0.02	1.06 ± 0.02	21.0 ± 0.3			
			V	1.64 ± 0.01	1.21 ± 0.01	1.10 ± 0.01	21.2 ± 0.2			
			R	1.60 ± 0.01	1.14 ± 0.01	1.12 ± 0.01	22.3 ± 0.1			
			I	1.41 ± 0.01	0.98 ± 0.01	1.00 ± 0.01	22.8 ± 0.1			
HD 137569[a,b]	free	2015-02-03 08:31:58						…	…	…
			B	0.11 ± 0.01	-0.09 ± 0.01	0.05 ± 0.01	…			
			V	0.13 ± 0.01	-0.11 ± 0.01	0.07 ± 0.01	…			
			R	0.11 ± 0.01	-0.10 ± 0.01	0.06 ± 0.01	…			
			I	0.09 ± 0.01	-0.08 ± 0.01	0.05 ± 0.01	…			
HD 137569[a,b]	free	2015-02-03T08:43:51						…	…	…
			B	0.11 ± 0.01	-0.11 ± 0.01	0.04 ± 0.01	…			
			V	0.12 ± 0.01	-0.12 ± 0.01	0.04 ± 0.01	…			
			R	0.11 ± 0.01	-0.10 ± 0.01	0.05 ± 0.01	…			
			I	0.09 ± 0.01	-0.06 ± 0.01	0.06 ± 0.01	…			
HD 137569[a,b]	GG435	2015-02-06 07:58:28						…	…	…
			B	0.10 ± 0.03	0.08 ± 0.03	0.06 ± 0.03	…			
			V	0.07 ± 0.02	0.07 ± 0.02	0.02 ± 0.02	…			
			R	0.11 ± 0.01	0.10 ± 0.01	0.03 ± 0.01	…			
			I	0.13 ± 0.01	0.11 ± 0.01	0.06 ± 0.01	…			
HD 137569[a,b]	GG435	2015-02-06 08:45:46						…	…	…
			B	0.47 ± 0.02	-0.21 ± 0.02	0.42 ± 0.02	…			
			V	0.39 ± 0.01	-0.15 ± 0.01	0.36 ± 0.01	…			
			R	0.31 ± 0.01	-0.14 ± 0.01	0.27 ± 0.01	…			
			I	0.19 ± 0.01	-0.12 ± 0.01	0.15 ± 0.01	…			
HD 137569[a,b]	GG435	2015-02-06 08:49:35						…	…	…
			B	0.09 ± 0.02	-0.09 ± 0.02	0.02 ± 0.02	…			
			V	0.06 ± 0.01	-0.04 ± 0.01	0.04 ± 0.01	…			
			R	0.04 ± 0.01	-0.02 ± 0.01	0.03 ± 0.01	…			
			I	0.03 ± 0.01	0.02 ± 0.01	0.03 ± 0.01	…			
HD 137569[a,b]	GG435	2015-02-06 08:58:20						…	…	…

Table A.2.: continued.

Name	Filter	Epoch	Passband	P (%)	P_Q (%)	P_U (%)	θ(°)	Serkowski curve λ_{max} (Å)	Serkowski curve P_{max} (%)	Serkowski curve K
			B	0.47 ± 0.02	-0.21 ± 0.02	-0.42 ± 0.02	...			
			V	0.40 ± 0.01	-0.18 ± 0.01	-0.36 ± 0.01	...			
			R	0.34 ± 0.01	-0.11 ± 0.01	-0.32 ± 0.01	...			
			I	0.30 ± 0.01	-0.05 ± 0.01	-0.29 ± 0.01	...			

The errors in this table are statistical only, while the root-mean-square of the Stokes Q and U is ~ 0.05%.
[a] The constant polarization curve of this star could not be fitted well with a Serkowski curve.
[b] The polarization angle could not be determined due to low polarization degree.

Table A.3.: Individual epochs with CAFOS

Name	Filter	Epoch	Passband	P (%)	P_Q (%)	P_U (%)	θ(°)	Serkowski curve λ_{max} (Å)	Serkowski curve P_{max} (%)	Serkowski curve K
BD+23d3762	free	2015-04-30 03:09:40						4964.8 ± 60.9	2.23 ± 0.01	0.92 ± 0.06
			B	2.20 ± 0.01	1.83 ± 0.01	1.21 ± 0.02	16.7 ± 0.2			
			V	2.19 ± 0.01	1.76 ± 0.01	1.31 ± 0.02	18.3 ± 0.2			
			R	2.07 ± 0.01	1.62 ± 0.01	1.28 ± 0.01	19.2 ± 0.1			
BD+45d3341	free	2015-04-30 02:06:40						5046.5 ± 72.6	3.09 ± 0.01	0.83 ± 0.08
			B	3.02 ± 0.02	-0.19 ± 0.01	3.02 ± 0.02	46.8 ± 0.2			
			V	3.06 ± 0.02	-0.31 ± 0.01	3.04 ± 0.02	47.9 ± 0.1			
			R	2.90 ± 0.01	-0.31 ± 0.01	2.88 ± 0.01	48.0 ± 0.1			
BD+45d3341	free	2015-04-30 02:34:01						5192.5 ± 34.0	3.01 ± 0.01	1.09 ± 0.06
			B	2.93 ± 0.01	-0.20 ± 0.01	2.92 ± 0.01	47.0 ± 0.1			
			V	2.97 ± 0.01	-0.30 ± 0.01	2.96 ± 0.01	47.9 ± 0.1			
			R	2.87 ± 0.01	-0.30 ± 0.01	2.85 ± 0.01	48.0 ± 0.1			
HD1337[a]	free	2015-04-30 03:47:04						...	...	...
			B	0.56 ± 0.03	0.04 ± 0.02	0.56 ± 0.03	42.8 ± 1.7			
			V	0.54 ± 0.02	-0.04 ± 0.02	0.54 ± 0.02	47.1 ± 1.3			
			R	0.55 ± 0.01	-0.03 ± 0.01	0.55 ± 0.01	46.6 ± 0.7			
HD1337[a]	free	2015-04-30 03:55:09						...	...	...
			B	0.54 ± 0.01	-0.02 ± 0.01	0.54 ± 0.01	46.3 ± 0.5			
			V	0.56 ± 0.01	-0.04 ± 0.01	0.56 ± 0.01	47.2 ± 0.5			
			R	0.55 ± 0.01	-0.04 ± 0.01	0.55 ± 0.01	47.1 ± 0.3			
HD1337[a]	free	2015-04-30 04:09:15						...	...	...
			B	0.58 ± 0.01	-0.04 ± 0.01	0.57 ± 0.01	47.0 ± 0.6			
			V	0.58 ± 0.01	-0.05 ± 0.01	0.57 ± 0.01	47.6 ± 0.6			
			R	0.56 ± 0.01	-0.04 ± 0.01	0.56 ± 0.01	46.8 ± 0.4			
HD137569[a,b]	free	2015-04-29T23:40:10						...	...	...
			B	0.19 ± 0.03	-0.19 ± 0.03	-0.04 ± 0.03	...			
			V	0.34 ± 0.05	-0.29 ± 0.05	-0.18 ± 0.05	...			
			R	0.21 ± 0.03	-0.21 ± 0.03	-0.04 ± 0.03	...			
HD137569[a,b]	free	2015-04-30T00:08:05						...	...	...

Table A.3.: continued.

							Serkowski curve		
Name	Filter	Epoch	Passband	P (%)	P_Q (%)	P_U (%)	θ(°)	$\lambda_{\max}$ (Å)	$P_{\max}$ (%)	K
			B	0.20 ± 0.02	-0.14 ± 0.03	-0.15 ± 0.02	...			
			V	0.18 ± 0.04	-0.11 ± 0.04	-0.14 ± 0.04	...			
			R	0.16 ± 0.03	-0.15 ± 0.03	-0.06 ± 0.02	...			
HD154445	free	2015-04-30 00:39:26						5550.8 ± 13.8	3.67 ± 0.01	1.50 ± 0.04
			B	3.37 ± 0.01	-3.36 ± 0.01	0.19 ± 0.01	88.4 ± 0.1			
			V	3.63 ± 0.01	-3.63 ± 0.01	0.07 ± 0.01	89.4 ± 0.1			
			R	3.53 ± 0.01	-3.53 ± 0.01	0.02 ± 0.01	89.9 ± 0.1			
HD154445	free	2015-04-30 04:33:46						5640.8 ± 20.5	3.61 ± 0.01	1.85 ± 0.07
			B	3.23 ± 0.01	-3.22 ± 0.01	0.13 ± 0.01	88.9 ± 0.1			
			V	3.57 ± 0.01	-3.57 ± 0.01	0.05 ± 0.01	89.6 ± 0.1			
			R	3.48 ± 0.01	-3.48 ± 0.01	-0.01 ± 0.01	90.1 ± 0.1			
HD194092	free	2015-04-30 01:21:46						5727.8 ± 235.1	0.64 ± 0.01	1.46 ± 0.47
			B	0.51 ± 0.01	-0.39 ± 0.01	0.32 ± 0.01	70.6 ± 0.5			
			V	0.61 ± 0.01	-0.52 ± 0.01	0.31 ± 0.02	74.5 ± 0.6			
			R	0.61 ± 0.01	-0.50 ± 0.01	0.34 ± 0.01	72.9 ± 0.4			
HD28446	free	2015-04-29 20:44:12						4835.7 ± 117.9	2.12 ± 0.01	1.08 ± 0.16
			B	2.13 ± 0.02	1.16 ± 0.02	-1.79 ± 0.02	151.4 ± 0.2			
			V	2.07 ± 0.01	1.13 ± 0.01	-1.74 ± 0.01	151.6 ± 0.2			
			R	1.98 ± 0.01	1.12 ± 0.01	-1.63 ± 0.01	152.3 ± 0.1			
HD28446	free	2015-04-29 20:52:17						4887.0 ± 100.4	2.07 ± 0.01	0.60 ± 0.08
			B	2.03 ± 0.01	1.12 ± 0.01	-1.69 ± 0.01	151.8 ± 0.1			
			V	2.03 ± 0.01	1.10 ± 0.01	-1.70 ± 0.01	151.5 ± 0.1			
			R	1.96 ± 0.01	1.09 ± 0.01	-1.63 ± 0.01	151.8 ± 0.1			
HD43384	free	2015-04-29 20:14:24						5342.5 ± 42.8	2.96 ± 0.01	0.96 ± 0.06
			B	2.88 ± 0.01	2.62 ± 0.01	-1.19 ± 0.01	167.8 ± 0.1			
			V	2.94 ± 0.01	2.73 ± 0.01	-1.08 ± 0.01	169.2 ± 0.1			
			R	2.85 ± 0.01	2.70 ± 0.01	-0.92 ± 0.01	170.6 ± 0.1			
HD43384	free	2015-04-29 21:14:04						5215.5 ± 75.8	3.00 ± 0.01	0.80 ± 0.08
			B	2.93 ± 0.02	2.72 ± 0.02	-1.08 ± 0.03	169.2 ± 0.2			
			V	2.97 ± 0.02	2.79 ± 0.01	-1.02 ± 0.02	170.0 ± 0.2			
			R	2.87 ± 0.01	2.72 ± 0.01	-0.91 ± 0.01	170.8 ± 0.1			

The errors in this table are statistical only, while the root-mean-square of the Stokes Q and U is ~ 0.04%.
[a] The constant polarization curve of this star could not be fitted well with a Serkowski curve.
[b] The polarization angle could not be determined due to low polarization degree.

Table A.4.: Individual epochs with AFOSC

							Serkowski curve		
Name	Filter	Epoch	Passband	P (%)	P_Q (%)	P_U (%)	θ(°)	$\lambda_{\max}$ (Å)	$P_{\max}$ (%)	K
HD 28446	free	2015-02-09 19:43:28						4722 ± 49	2.00 ± 0.01	0.72 ± 0.04
			B	1.99 ± 0.01	1.16 ± 0.01	-1.62 ± 0.01	152.8 ± 0.1			

Table A.4.: continued.

Name	Filter	Epoch	Passband	P (%)	P_Q (%)	P_U (%)	θ(°)	Serkowski curve		
								λ_{max} (Å)	P_{max} (%)	K
			V	1.96 ± 0.01	1.12 ± 0.01	-1.61 ± 0.01	152.3 ± 0.1			
			R	1.85 ± 0.01	1.04 ± 0.01	-1.53 ± 0.01	152.1 ± 0.1			
HD 43384	free	2015-02-09 20:03:30						5201 ± 17	3.16 ± 0.01	1.03 ± 0.02
			B	3.08 ± 0.01	2.92 ± 0.01	-0.96 ± 0.01	170.9 ± 0.1			
			V	3.14 ± 0.01	3.01 ± 0.01	-0.92 ± 0.01	171.5 ± 0.1			
			R	2.99 ± 0.01	2.87 ± 0.01	-0.84 ± 0.01	171.9 ± 0.1			
HD 43384	free	2015-02-10 17:53:17						5371 ± 14	3.19 ± 0.01	1.21 ± 0.03
			B	3.04 ± 0.01	2.91 ± 0.01	-0.89 ± 0.01	171.5 ± 0.1			
			V	3.17 ± 0.01	3.04 ± 0.01	-0.92 ± 0.01	171.6 ± 0.1			
			R	3.03 ± 0.01	2.91 ± 0.01	-0.86 ± 0.01	171.8 ± 0.1			
HD 43384	free	2015-03-09 21:06:00						5317 ± 20	2.92 ± 0.01	1.14 ± 0.03
			B	2.82 ± 0.01	2.62 ± 0.01	-1.04 ± 0.01	169.2 ± 0.1			
			V	2.90 ± 0.01	2.71 ± 0.01	-1.02 ± 0.01	169.7 ± 0.1			
			R	2.76 ± 0.01	2.60 ± 0.01	-0.93 ± 0.01	170.2 ± 0.1			
HD 1337 [a]	free	2015-02-09 18:40:10						…	…	…
			B	0.51 ± 0.01	-0.12 ± 0.01	0.49 ± 0.01	52.1 ± 0.2			
			V	0.50 ± 0.01	-0.14 ± 0.01	0.48 ± 0.01	53.2 ± 0.2			
			R	0.54 ± 0.01	-0.19 ± 0.01	0.51 ± 0.01	55.2 ± 0.1			
HD 1337 [a]	free	2015-03-10 18:06:42						…	…	…
			B	0.65 ± 0.01	-0.07 ± 0.01	0.64 ± 0.01	48.0 ± 0.2			
			V	0.61 ± 0.01	-0.08 ± 0.01	0.60 ± 0.01	48.6 ± 0.2			
			R	0.61 ± 0.01	-0.11 ± 0.01	0.60 ± 0.01	49.9 ± 0.1			
HD 54439	free	2015-02-10 20:48:43						5138 ± 114	0.69 ± 0.01	1.28 ± 0.22
			B	0.66 ± 0.01	-0.03 ± 0.01	-0.66 ± 0.01	133.8 ± 0.2			
			V	0.69 ± 0.01	0.08 ± 0.01	-0.68 ± 0.01	138.4 ± 0.1			
			R	0.63 ± 0.01	0.03 ± 0.01	-0.63 ± 0.01	136.5 ± 0.1			
HD 21291	free	2015-02-10 17:23:13						5166 ± 27	2.95 ± 0.01	1.05 ± 0.04
			B	2.87 ± 0.01	-1.73 ± 0.01	-2.29 ± 0.01	116.4 ± 0.1			
			V	2.92 ± 0.01	-1.81 ± 0.01	-2.29 ± 0.01	115.9 ± 0.1			
			R	2.77 ± 0.01	-1.74 ± 0.01	-2.16 ± 0.01	115.6 ± 0.1			
HD 137569 [a,b]	free	2015-02-11 03:51:49						…	…	…
			B	0.22 ± 0.01	-0.22 ± 0.01	-0.02 ± 0.01	…			
			V	0.19 ± 0.01	-0.19 ± 0.01	-0.00 ± 0.01	…			
			R	0.19 ± 0.01	-0.19 ± 0.01	0.01 ± 0.01	…			
HD 137569 [a,b]	free	2015-03-10 02:41:10						…	…	…
			B	0.20 ± 0.01	-0.18 ± 0.01	0.10 ± 0.01	…			
			V	0.18 ± 0.01	-0.17 ± 0.01	0.07 ± 0.01	…			
			R	0.22 ± 0.01	-0.20 ± 0.01	0.10 ± 0.01	…			
HD 198478	free	2016-08-02 21:00:02						5132 ± 41	2.77 ± 0.01	0.99 ± 0.06
			B	2.70 ± 0.01	2.69 ± 0.01	0.25 ± 0.01	2.6 ± 0.1			
			V	2.73 ± 0.01	2.72 ± 0.01	0.30 ± 0.01	3.2 ± 0.1			
			R	2.61 ± 0.01	2.59 ± 0.01	0.30 ± 0.01	3.3 ± 0.1			

Table A.4.: continued.

							Serkowski curve		
Name	Filter	Epoch	Passband	$P\,(\%)$	$P_Q\,(\%)$	$P_U\,(\%)$	$\theta(^\circ)$	$\lambda_{\max}$ (Å)	$P_{\max}\,(\%)$	K
HD 194092	free	2016-08-02 20:22:18						5884 ± 107	0.74 ± 0.01	1.09 ± 0.18
			B	0.69 ± 0.01	-0.67 ± 0.01	0.16 ± 0.01	83.1 ± 0.3			
			V	0.75 ± 0.01	-0.72 ± 0.01	0.20 ± 0.01	82.4 ± 0.2			
			R	0.73 ± 0.01	-0.70 ± 0.01	0.17 ± 0.01	83.1 ± 0.1			

The errors in this table are statistical only, while the root-mean-square of the Stokes Q and U is ~ 0.05%.

[a] The constant polarization curve of this star could not be fitted well with a Serkowski curve.

[b] The polarization angle could not be determined due to low polarization degree.

B. Appendix 2

B.1. Stellar age estimate

We use the relation between EW(Hα) and stellar age of Leitherer et al. (1999), based of Starburst99 models. The EW-age relation depends on the assumed metallicity, Z, and on the initial mass function (IMF). They offer three choices of the IMF, which are similar to each other for EW(Hα) $\lesssim$ 150 Å, and different metallicities, Z = 0.04, 0.02, 0.008, 0.004 and 0.001. The reference model is a power law with index α = 2.35 between low-mass and high-mass (M_{up}) cutoff masses of 1 and 100 $M_{\odot}$. We determined the average gas-phase oxygen abundance of the host galaxy of PTF 11hrq, 12 + log(O/H) $\sim$ 8.15 (see Table 7.3). To calculate the gas-phase metallicity, Z_{gas}, we adopt the gas-phase oxygen abundance 12 + log(O/H) versus gas-phase metallicity Z_{gas} relationship, given in Ma et al. (2016):

$$12 + \log(\mathrm{O/H}) = \log(Z_{\mathrm{gas}}/Z_{\odot}) + 9.0 \tag{B.1}$$

where $Z_{\odot}$=0.02 is the solar gas-phase metallicity. Thus, the average gas-phase metallicity of the host galaxy of PTF 11hrq is $Z \sim 0.003$.

For comparison, if we use the solar abundance of oxygen in the log scale, 12 + log(O/H)$_{\odot}$=8.69 (e.g., Asplund et al. (2009)) instead of 9.0, the result does not change significantly. We derive an average gas-phase metallicity of the host galaxy of PTF 11hrq $Z \sim 0.006$.

Therefore, we use the Starburst99 model for the gas-phase metallicity Z = 0.004, and estimate the stellar population age in regions A, B, and at the SN position (see Fig. 7.5). The results are summarized in Table 7.3, and shown in Fig. B.1.

B.2. Dust extinction estimate

We derive the dust extinction for the host galaxy of PTF 11hrq from the Balmer decrement:

$$R_{\mathrm{Balmer}} = \frac{(\mathrm{H}\alpha/\mathrm{H}\beta)_{\mathrm{obs}}}{(\mathrm{H}\alpha/\mathrm{H}\beta)_{\mathrm{int}}}, \tag{B.2}$$

where (Hα/Hβ)$_{\mathrm{obs}}$ is the observed, and (Hα/Hβ)$_{\mathrm{int}}$ the intrinsic Hα/Hβ ratio. The (Hα/Hβ)$_{\mathrm{int}}$ does not strongly depend on the temperature and electron density. For example, at a fixed temperature of T=10^4 K, (Hα/Hβ)$_{\mathrm{int}}$ = 2.86, 2.85 and 2.81 for n_e = 10^2, 10^4, and 10^5 cm^{-3}, respectively; and at a fixed electron density of n_e = 10^4 cm^{-3}, (Hα/Hβ)$_{\mathrm{int}}$=3.00, 2.85 and 2.74 for T=5000, 10000 and 20000 K respectively (see Table 4.4. in Osterbrock & Ferland, 2006).

We assume (Hα/Hβ)$_{int}$ = 2.86, which is a standard choice for star forming galaxies (Osterbrock, 1989; Osterbrock & Ferland, 2006; Domínguez et al., 2013). It corresponds to T = 10^4 K and electron density n_e = 10^2 cm^{-3}.

Because stellar absorption may be affecting the underlying continuum of the emission lines, Hα and in particular Hβ, the Balmer decrement and the extinction might be overestimated. Figure B.2 shows the Hβ line close to the SN explosion site, where the stellar absorption is small, but not negligible. Therefore, we use the spectral synthesis code STARLIGHT (Cid Fernandes et al., 2005, 2009, 2011;

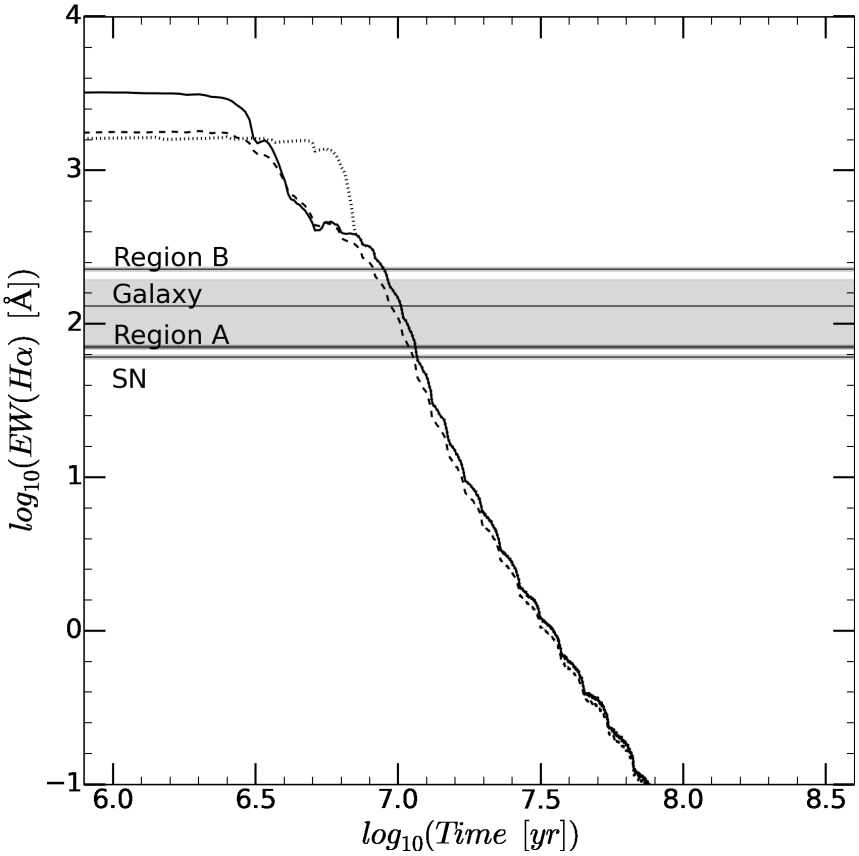

Figure B.1.: EW(Hα)-age relation for PTF 11hrq. The lines denote the Starburst99 model instantaneous star formation law with α=2.35, M_{up} = 100 $M_\odot$ (solid line); α=3.30, M_{up} = 100 $M_\odot$ (dashed line); and α=2.35, M_{up} = 30 $M_\odot$ (dotted line). The horizontal lines mark the average equivalent widths of the whole host galaxy, at the position of the SN and of region A and B. The gray shaded area denotes standard deviations of the average equivalent widths.

Asari et al., 2007; Mateus et al., 2007) to best-fit subtract the synthetic continuum before we measure the Hα and Hβ fluxes. STARLIGHT is a code that fits observed spectra (after masking the regions of known nebular emission lines, telluric absorptions, and strong night-sky emission lines) with a linear combination of a pre-defined set of single stellar populations (SSP) base spectra of different ages and metallicities. As the base, we use 150 Bruzual & Charlot (2003, , BC03) SSP spectra of 6 metallicities (Z=0.0001, 0.0004, 0.004, 0.008, 0.02, 0.05) and 25 different ages ($10^6 > age_{SSP} > 18 \times 10^9$ years), which was also used in Mateus et al. (2006); Cid Fernandes et al. (2007); Asari et al. (2007).

The color excess can be expressed as following:

$$E(\mathrm{H}\beta - \mathrm{H}\alpha) = A(\mathrm{H}\beta) - A(\mathrm{H}\alpha) = -2.5 \times \log\left[\frac{(\mathrm{H}\alpha/\mathrm{H}\beta)_{\mathrm{int}}}{(\mathrm{H}\alpha/\mathrm{H}\beta)_{\mathrm{obs}}}\right]. \tag{B.3}$$

The $E(\mathrm{H}\beta - \mathrm{H}\alpha)$ map is shown in Fig. B.3.

This color excess can be related to color excess in other passband filters, e.g., $E(B-V)$, or $E(F225W - F625W)$ via an extinction law.

We adopt the Cardelli, Clayton, & Mathis (1989) extinction law (hereafter, CCM) and calculate the

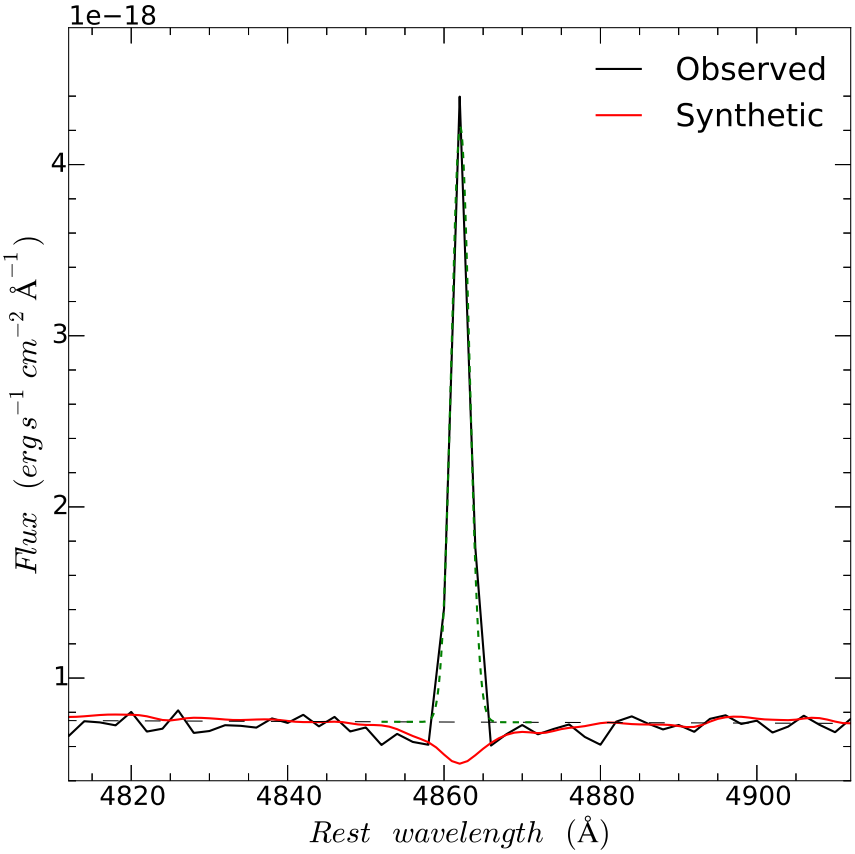

Figure B.2.: Hβ line (black line) at the explosion region, and a Gaussian fit (green line) with respect to the synthetic best-fit continuum using the STARLIGHT code (red line), compared to the polynomial fit continuum (dashed line). The stellar absorption typically deducts 5-20% of the line flux.

ratios $E(B-V)/E(\mathrm{H}\alpha/\mathrm{H}\beta)$ and $E(\mathrm{H}\beta-\mathrm{H}\alpha)/E(\mathrm{H}\alpha/\mathrm{H}\beta)$, e.g.:

$$\frac{E(B-V)}{E(\mathrm{H}\beta-\mathrm{H}\alpha)} = \frac{a(\frac{1}{\lambda_B}) + b(\frac{1}{\lambda_B})/R_V - a(\frac{1}{\lambda_V}) + b(\frac{1}{\lambda_V})/R_V}{a(\frac{1}{\lambda_{\mathrm{H}\beta}}) + b(\frac{1}{\lambda_{\mathrm{H}\beta}})/R_V - a(\frac{1}{\lambda_{\mathrm{H}\alpha}}) + b(\frac{1}{\lambda_{\mathrm{H}\alpha}})/R_V}, \tag{B.4}$$

where a and b are the wavelength dependent polynomials given in CCM, and R_V is the total-to-selective extinction ratio, which we assume to be $R_V = 3.1$. We obtain $\frac{E(B-V)}{E(\mathrm{H}\beta-\mathrm{H}\alpha)} = 0.93$ and $\frac{E(F225W-F625W)}{E(\mathrm{H}\beta-\mathrm{H}\alpha)} = 6.39$.

The CCM law is comparable to other extinction laws in the linear regime, at wavelengths $\lambda \gtrsim 0.25$ μm (see Gordon et al., 2003). As a sanity check, we also calculate the color excess ratios using an average extinction curve for the Small Magellanic Cloud (SMC) Wing sample (Gordon et al., 2003), with $R_V = 2.74$, and obtain $\frac{E(B-V)}{E(\mathrm{H}\beta-\mathrm{H}\alpha)} = 0.83$ and $\frac{E(F225W-F625W)}{E(\mathrm{H}\beta-\mathrm{H}\alpha)} = 5.80$. The color excess ratios calculated using the CCM extinction law are ~ 1.1 times larger than with the SMC law, indicating a possible overestimation of the dust reddening with this method.

The Galactic reddening at the position of PTF 11hrq is $E(B-V)_{\mathrm{Gal}} = 0.0119 \pm 0.0005$ mag (Schlafly & Finkbeiner, 2011), which corresponds to $E(F225W-F625W)_{Gal} \simeq 0.082$ mag (assuming CCM, and $R_V = 3.1$).

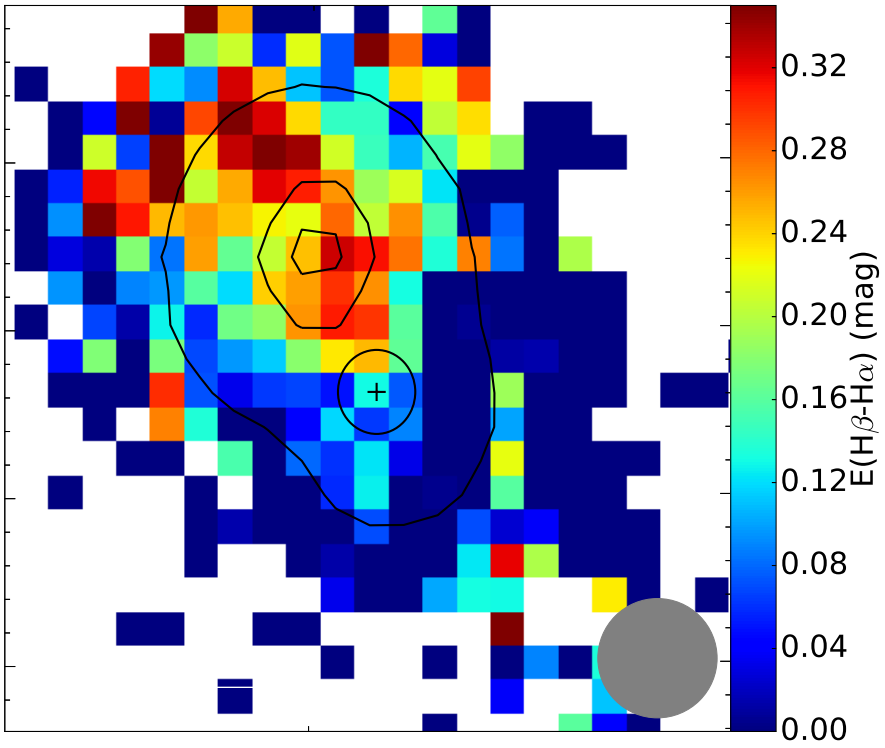

Figure B.3.: Color excess E(Hβ-Hα) map for the host galaxy of PTF 11hrq. The contours are same as in Fig. 7.5. The black ellipse denotes the SN position uncertainty.

To calculate the reddening due to dust in the host galaxy, we subtract the Galactic reddening from the observed (total) reddening:

$$E(F225W - F625W)_{\rm Host} = E(F225W - F625W)_{\rm obs} - E(F225W - F625W)_{\rm Gal}. \quad \text{(B.5)}$$

The typical value of $E(F225W - F625W)_{Obs}$ is 0.83 ± 0.77 mag, and $E(F225W - F625W)_{\rm Host} \sim 0.8$ ± 0.8 mag.

Finally, we calculate the corrected color map after resampling the E($F225W$-$F625W$)$_{host}$ map using SWarp:

$$(F225W - F625W)_{\rm corrected} = (F225W - F625W)_{\rm obs} - E(F225W - F625W)_{\rm host}. \quad \text{(B.6)}$$

The corrected color map is shown in Fig. 7.2.

B.3. Impact of emission lines on broad-band photometry

Studies of extreme emission-line galaxies have shown that emission lines can significantly increase the brightness in broadband filters (e.g. Amorín et al., 2015). This could also affect the reported UV-to-optical colors of PTF 11hrq and PTF 12dam. In the following, we quantify the contribution of emission lines to the *HST* broad-band photometry of PTF 12dam which is also the SLSN host galaxy with the strongest emission lines in the sample known today.

The blue empty symbols in the top panel of Fig. B.4 display the photometry presented in Schulze et al. (2016) after correcting for Galactic reddening. The new *HST* photometry is shown in a darker

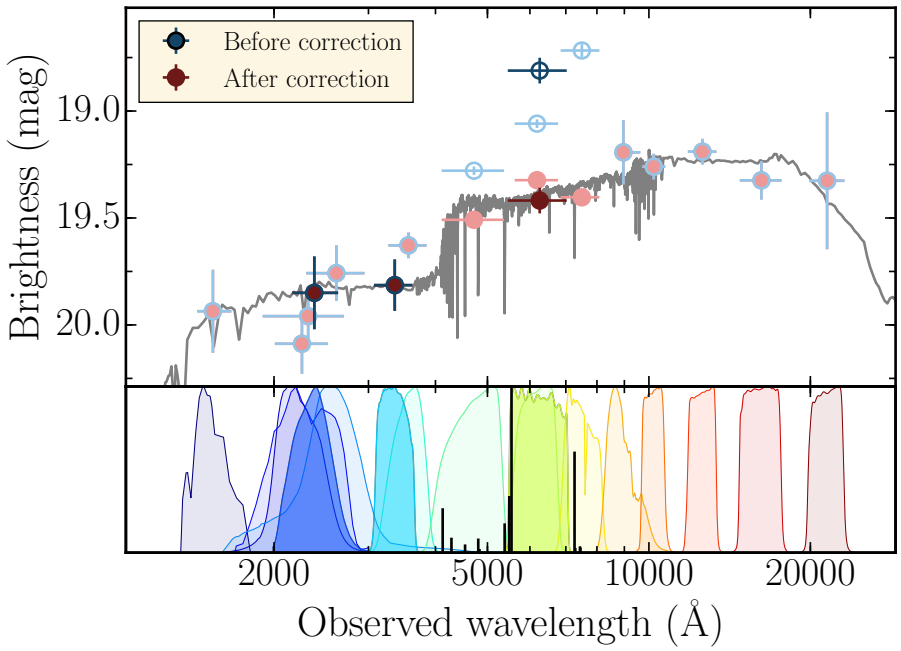

Figure B.4.: The broadband spectral energy-distribution of PTF 12dam. *Top:* The empty symbols displays the photometry before the emission-line subtracting, whereas the filled symbols display the photometry after subtracting nebular emission lines. Our *HST* measurements are shown in a darker shade. The gray line displays the best-fit of the SED after subtracting emission lines with a single-age stellar population (for details see Schulze et al. 2016). *Bottom:* Synthetic emission-line spectrum built from the equivalent measurements reported in (Leloudas et al., 2015b). The shaded regions represent the transmission functions of the broad-band filters. The *HST* filters are displayed in a darker tone.

tone. While the broad-band spectral energy distribution shows a relatively smooth evolution, the data between 4000 and 10000 Å in particular the F625W photometry, show a significant excess with respect to the emission from the stellar emission (gray line in the fit). The bottom panel shows a synthetic emission-line spectrum built from the equivalent measurements in Leloudas et al. (2015b) and the filter bandpasses corresponding to each measurement. Although [OIII]$\lambda\lambda$4959,5007 fall on the edge of the F625W bandpass, they still contribute > 63% to the total flux.

After removing the line contribution (red data points), the broad-band spectral energy distribution is adequately fitted with a single-age stellar population (gray curve; fit taken from Schulze et al. 2016). This stark change in the photometry also translates into a significant bluer UV-to-optical color of −1.98 mag. The emission-lines of PTF 11hrq's host have significantly smaller equivalent widths resulting in a significantly smaller correction.

We note that uncertainties in the wings of the F625W filter response function could alter this correction. Furthermore, the line measurement were obtained with a long-slit observation. Spatial variations of the emission-line fluxes would manifest in a non-uniform color correction.

C. Appendix 3

C.1. Supplementary tables the statistical analysis of the Si II line polarization

Table C.1.: Observing log

SN name	Epoch (UT)	RA (deg)	DEC (deg)	Filter	HWP angle (deg)	Exposure (s)	ProgID
2001dm	2001-08-13 07:57:37	28.919141	-29.92281	GG435	0.0	900	67.D-0517(A)
2001dm	2001-08-13 08:14:32	28.919141	-29.92281	GG435	22.5	900	67.D-0517(A)
2001dm	2001-08-13 08:31:27	28.919141	-29.92281	GG435	45.0	900	67.D-0517(A)
2001dm	2001-08-13 08:48:22	28.919141	-29.92281	GG435	67.5	900	67.D-0517(A)
2001V	2001-02-22 04:19:37	179.353546	25.20317	GG435	0.0	1200	66.D-0328(A)
2001V	2001-02-22 04:41:33	179.353546	25.20317	GG435	22.5	1200	66.D-0328(A)
2001V	2001-02-22 05:03:28	179.353546	25.20317	GG435	45.0	1200	66.D-0328(A)
2001V	2001-02-22 05:40:31	179.353546	25.20317	GG435	67.5	1200	66.D-0328(A)
2001V	2001-02-26 04:32:32	179.353717	25.20306	GG435	0.0	1200	66.D-0328(A)
2001V	2001-02-26 04:54:29	179.353717	25.20306	GG435	22.5	1200	66.D-0328(A)
2001V	2001-02-26 05:16:25	179.353717	25.20306	GG435	45.0	1200	66.D-0328(A)
2001V	2001-02-26 05:38:21	179.353717	25.20306	GG435	67.5	1200	66.D-0328(A)
2001V	2001-03-22 02:53:44	179.353575	25.20296	GG435	0.0	1200	66.D-0328(A)
2001V	2001-03-22 03:15:40	179.353575	25.20296	GG435	22.5	1200	66.D-0328(A)
2001V	2001-03-22 03:37:37	179.353575	25.20296	GG435	45.0	1200	66.D-0328(A)
2001V	2001-03-22 03:59:32	179.353575	25.20296	GG435	67.5	1200	66.D-0328(A)
2001V	2001-04-04 03:58:20	179.353748	25.20298	GG435	0.0	1200	66.D-0328(A)
2001V	2001-04-04 04:20:15	179.353748	25.20298	GG435	22.5	1200	66.D-0328(A)
2001V	2001-04-04 04:42:10	179.353748	25.20298	GG435	45.0	1200	66.D-0328(A)
2001V	2001-04-04 05:04:05	179.353748	25.20298	GG435	67.5	1200	66.D-0328(A)
2001el	2001-09-26 06:49:05	56.127732	-44.63969	GG435	0.0	60	67.D-0517(A)
2001el	2001-09-26 06:52:07	56.127732	-44.63969	GG435	45.0	60	67.D-0517(A)
2001el	2001-09-26 06:55:03	56.127732	-44.63969	GG435	22.5	60	67.D-0517(A)
2001el	2001-09-26 06:58:06	56.127732	-44.63969	GG435	67.5	60	67.D-0517(A)
2001el	2001-09-26 07:07:31	56.127758	-44.63971	GG435	0.0	480	67.D-0517(A)
2001el	2001-09-26 07:17:34	56.127758	-44.63971	GG435	45.0	480	67.D-0517(A)
2001el	2001-09-26 07:27:29	56.127758	-44.63971	GG435	22.5	480	67.D-0517(A)
2001el	2001-09-26 07:37:31	56.127758	-44.63971	GG435	67.5	480	67.D-0517(A)
2001el	2001-10-01 04:55:08	56.127365	-44.63955	GG435	0.0	500	68.D-0571(A)
2001el	2001-10-01 05:05:24	56.127365	-44.63955	GG435	22.5	500	68.D-0571(A)
2001el	2001-10-01 05:15:40	56.127365	-44.63955	GG435	45.0	500	68.D-0571(A)

Table C.1.: continued.

SN name	Epoch (UT)	RA (deg)	DEC (deg)	Filter	HWP angle (deg)	Exposure (s)	ProgID
2001el	2001-10-01 05:35:22	56.127365	-44.63955	GG435	67.5	300	68.D-0571(A)
2001el	2001-10-09 05:50:04	56.12778	-44.6397	free	0.0	240	68.D-0571(A)
2001el	2001-10-09 05:56:06	56.12778	-44.6397	free	45.0	240	68.D-0571(A)
2001el	2001-10-09 06:02:02	56.12778	-44.6397	free	22.5	240	68.D-0571(A)
2001el	2001-10-09 06:08:05	56.12778	-44.6397	free	67.5	240	68.D-0571(A)
2001el	2001-10-09 06:16:41	56.12778	-44.6397	GG435	0.0	400	68.D-0571(A)
2001el	2001-10-09 06:25:25	56.12778	-44.6397	GG435	45.0	400	68.D-0571(A)
2001el	2001-10-09 06:34:01	56.12778	-44.6397	GG435	22.5	400	68.D-0571(A)
2001el	2001-10-09 06:42:44	56.12778	-44.6397	GG435	67.5	400	68.D-0571(A)
2001el	2001-10-18 03:51:08	56.127844	-44.63968	GG435	0.0	500	68.D-0571(A)
2001el	2001-10-18 04:01:31	56.127844	-44.63968	GG435	45.0	500	68.D-0571(A)
2001el	2001-10-18 04:11:47	56.127844	-44.63968	GG435	22.5	500	68.D-0571(A)
2001el	2001-10-18 04:22:10	56.127844	-44.63968	GG435	67.5	500	68.D-0571(A)
2001el	2001-10-18 04:35:31	56.127844	-44.63968	free	0.0	500	68.D-0571(A)
2001el	2001-10-18 04:45:54	56.127844	-44.63968	free	45.0	500	68.D-0571(A)
2001el	2001-10-18 04:56:10	56.127844	-44.63968	free	22.5	500	68.D-0571(A)
2001el	2001-10-18 05:06:33	56.127844	-44.63968	free	67.5	500	68.D-0571(A)
2001el	2001-11-09 02:25:35	56.1278	-44.63976	free	0.0	1200	68.D-0571(A)
2001el	2001-11-09 02:47:38	56.1278	-44.63976	free	45.0	1200	68.D-0571(A)
2001el	2001-11-09 03:09:33	56.1278	-44.63976	free	22.5	1200	68.D-0571(A)
2001el	2001-11-09 03:31:37	56.1278	-44.63976	free	67.5	1200	68.D-0571(A)
2002bo	2002-03-12 03:05:10	154.527193	21.82838	free	0.0	600	68.D-0571(A)
2002bo	2002-03-12 03:17:30	154.527193	21.82838	free	45.0	600	68.D-0571(A)
2002bo	2002-03-12 03:29:31	154.527193	21.82838	free	22.5	600	68.D-0571(A)
2002bo	2002-03-12 03:41:36	154.527193	21.82838	free	67.5	600	68.D-0571(A)
2002bo	2002-03-12 04:53:49	154.527197	21.82836	GG435	45.0	600	68.D-0571(A)
2002bo	2002-03-12 05:05:46	154.527197	21.82836	GG435	22.5	600	68.D-0571(A)
2002bo	2002-03-12 05:17:54	154.527197	21.82836	GG435	67.5	600	68.D-0571(A)
2002bo	2002-03-12 05:31:59	154.527197	21.82836	GG435	0.0	600	68.D-0571(A)
2002bo	2002-03-16 02:50:27	154.527331	21.82832	free	0.0	600	68.D-0571(A)
2002bo	2002-03-16 03:02:31	154.527331	21.82832	free	45.0	600	68.D-0571(A)
2002bo	2002-03-16 03:14:27	154.527331	21.82832	free	22.5	600	68.D-0571(A)
2002bo	2002-03-16 03:26:31	154.527331	21.82832	free	67.5	600	68.D-0571(A)
2002bo	2002-03-16 03:41:43	154.527331	21.82832	GG435	0.0	600	68.D-0571(A)
2002bo	2002-03-16 03:53:47	154.527331	21.82832	GG435	45.0	600	68.D-0571(A)
2002bo	2002-03-16 04:05:44	154.527331	21.82832	GG435	22.5	600	68.D-0571(A)
2002bo	2002-03-16 04:17:48	154.527331	21.82832	GG435	67.5	600	68.D-0571(A)
2002bo	2002-03-17 01:39:01	154.52733	21.82819	GG435	0.0	600	68.D-0571(A)
2002bo	2002-03-17 01:51:05	154.52733	21.82819	GG435	45.0	600	68.D-0571(A)
2002bo	2002-03-17 02:03:01	154.52733	21.82819	GG435	22.5	600	68.D-0571(A)
2002bo	2002-03-17 02:15:05	154.52733	21.82819	GG435	67.5	600	68.D-0571(A)
2002bo	2002-03-19 01:07:41	154.526989	21.8286	GG435	0.0	600	68.D-0571(A)

Table C.1.: continued.

SN name	Epoch (UT)	RA (deg)	DEC (deg)	Filter	HWP angle (deg)	Exposure (s)	ProgID
2002bo	2002-03-19 01:19:48	154.526989	21.8286	GG435	45.0	600	68.D-0571(A)
2002bo	2002-03-19 01:33:08	154.526989	21.8286	GG435	22.5	600	68.D-0571(A)
2002bo	2002-03-19 01:45:14	154.526989	21.8286	GG435	67.5	600	68.D-0571(A)
2002bo	2002-03-19 02:05:49	154.526838	21.82867	free	0.0	600	68.D-0571(A)
2002bo	2002-03-19 02:17:57	154.526838	21.82867	free	45.0	600	68.D-0571(A)
2002bo	2002-03-19 02:30:09	154.526838	21.82867	free	22.5	600	68.D-0571(A)
2002bo	2002-03-19 02:42:16	154.526838	21.82867	free	67.5	600	68.D-0571(A)
2002bo	2002-03-22 01:29:41	154.526898	21.82853	free	0.0	600	68.D-0571(A)
2002bo	2002-03-22 01:41:51	154.526898	21.82853	free	45.0	600	68.D-0571(A)
2002bo	2002-03-22 01:53:51	154.526898	21.82853	free	22.5	600	68.D-0571(A)
2002bo	2002-03-22 02:07:06	154.526898	21.82853	free	67.5	600	68.D-0571(A)
2002bo	2002-04-02 02:19:10	154.527455	21.82839	free	0.0	587	69.D-0438(A)
2002bo	2002-04-02 02:30:59	154.527455	21.82839	free	45.0	600	69.D-0438(A)
2002bo	2002-04-02 02:44:52	154.527455	21.82839	free	22.5	600	69.D-0438(A)
2002bo	2002-04-02 02:56:54	154.527455	21.82839	free	67.5	600	69.D-0438(A)
2002bo	2002-04-05 01:19:01	154.527171	21.82841	free	0.0	600	69.D-0438(A)
2002bo	2002-04-05 01:31:09	154.527171	21.82841	free	45.0	600	69.D-0438(A)
2002bo	2002-04-05 01:43:07	154.527171	21.82841	free	22.5	600	69.D-0438(A)
2002bo	2002-04-05 01:55:21	154.527171	21.82841	free	67.5	600	69.D-0438(A)
2002el	2002-08-14 03:44:59	314.125344	-18.55974	free	0.0	1200	69.D-0438(A)
2002el	2002-08-14 04:07:03	314.125344	-18.55974	free	45.0	1200	69.D-0438(A)
2002el	2002-08-14 04:29:00	314.125344	-18.55974	free	22.5	1200	69.D-0438(A)
2002el	2002-08-14 04:51:10	314.125415	-18.55971	free	67.5	1200	69.D-0438(A)
2002el	2002-08-15 04:32:08	314.125362	-18.55992	free	0.0	1200	69.D-0438(A)
2002el	2002-08-15 04:54:16	314.125362	-18.55992	free	45.0	1200	69.D-0438(A)
2002el	2002-08-15 05:18:22	314.125362	-18.55992	free	22.5	1200	69.D-0438(A)
2002el	2002-08-15 05:40:55	314.125362	-18.55992	free	67.5	1200	69.D-0438(A)
2002fk	2002-10-01 07:15:19	50.522792	-15.40125	free	0.0	477	69.D-0438(A)
2002fk	2002-10-01 07:25:20	50.522792	-15.40125	free	45.0	720	69.D-0438(A)
2002fk	2002-10-01 07:39:17	50.522792	-15.40125	free	22.5	720	69.D-0438(A)
2002fk	2002-10-01 07:53:21	50.522792	-15.40125	free	67.5	720	69.D-0438(A)
2002fk	2002-10-05 07:12:19	50.523972	-15.40102	free	0.0	720	70.D-0111(A)
2002fk	2002-10-05 07:26:36	50.523972	-15.40102	free	45.0	720	70.D-0111(A)
2002fk	2002-10-05 07:40:34	50.523972	-15.40102	free	22.5	720	70.D-0111(A)
2002fk	2002-10-05 07:54:41	50.523972	-15.40102	free	67.5	720	70.D-0111(A)
2002fk	2002-10-14 08:14:40	50.522672	-15.40127	free	0.0	900	70.D-0111(A)
2002fk	2002-10-14 08:31:45	50.522672	-15.40127	free	45.0	600	70.D-0111(A)
2002fk	2002-10-14 08:43:42	50.522672	-15.40127	free	22.5	600	70.D-0111(A)
2002fk	2002-10-14 08:55:46	50.522672	-15.40127	free	67.5	600	70.D-0111(A)
2003eh	2003-05-23 00:22:33	167.101306	3.49663	free	0.0	1500	71.D-0141(A)

Table C.1.: continued.

SN name	Epoch (UT)	RA (deg)	DEC (deg)	Filter	HWP angle (deg)	Exposure (s)	ProgID
2003eh	2003-05-23 00:49:38	167.101306	3.49663	free	45.0	1500	71.D-0141(A)
2003eh	2003-05-23 01:16:39	167.101306	3.49663	free	22.5	1500	71.D-0141(A)
2003eh	2003-05-23 01:43:48	167.101306	3.49663	free	67.5	1500	71.D-0141(A)
2003eh	2003-06-03 23:15:39	167.097231	3.49701	free	0.0	1500	71.D-0141(A)
2003eh	2003-06-03 23:42:47	167.097231	3.49701	free	45.0	1500	71.D-0141(A)
2003eh	2003-06-04 00:09:56	167.097231	3.49701	free	22.5	1500	71.D-0141(A)
2003eh	2003-06-04 00:37:03	167.097231	3.49701	free	67.5	1500	71.D-0141(A)
2003hv	2003-09-15 07:16:50	46.038263	-26.08524	free	88.7	240	71.D-0141(A)
2003hv	2003-09-15 07:22:55	46.038263	-26.08524	free	133.7	240	71.D-0141(A)
2003hv	2003-09-15 07:28:52	46.038263	-26.08524	free	111.2	240	71.D-0141(A)
2003hv	2003-09-15 07:34:58	46.038263	-26.08524	free	156.2	240	71.D-0141(A)
2003hv	2003-09-15 09:39:40	46.038723	-26.08522	free	272.0	100	71.D-0141(A)
2003hv	2003-09-15 09:43:25	46.038723	-26.08522	free	317.0	100	71.D-0141(A)
2003hv	2003-09-15 09:47:01	46.038723	-26.08522	free	294.5	100	71.D-0141(A)
2003hv	2003-09-15 09:50:46	46.038723	-26.08522	free	339.5	100	71.D-0141(A)
2003hx	2003-09-15 07:56:24	86.69584	-16.78331	free	108.7	500	71.D-0141(A)
2003hx	2003-09-15 08:06:49	86.69584	-16.78331	free	153.7	500	71.D-0141(A)
2003hx	2003-09-15 08:17:06	86.69584	-16.78331	free	131.2	500	71.D-0141(A)
2003hx	2003-09-15 08:27:32	86.69584	-16.78331	free	176.2	500	71.D-0141(A)
2003hx	2003-09-15 08:38:29	86.69584	-16.78331	free	108.7	500	71.D-0141(A)
2003hx	2003-09-15 08:48:54	86.69584	-16.78331	free	153.7	500	71.D-0141(A)
2003hx	2003-09-15 08:59:11	86.69584	-16.78331	free	131.2	500	71.D-0141(A)
2003hx	2003-09-15 09:09:37	86.69584	-16.78331	free	176.2	500	71.D-0141(A)
2003hx	2003-09-27 08:16:09	86.696019	-16.78307	free	0.0	420	71.D-0141(A)
2003hx	2003-09-27 08:25:13	86.696019	-16.78307	free	45.0	420	71.D-0141(A)
2003hx	2003-09-27 08:34:09	86.696019	-16.78307	free	22.5	420	71.D-0141(A)
2003hx	2003-09-27 08:43:13	86.696019	-16.78307	free	67.5	420	71.D-0141(A)
2003hx	2003-09-29 08:10:37	86.69607	-16.78303	free	0.0	300	71.D-0141(A)
2003hx	2003-09-29 08:17:42	86.69607	-16.78303	free	45.0	300	71.D-0141(A)
2003hx	2003-09-29 08:24:38	86.69607	-16.78303	free	22.5	300	71.D-0141(A)
2003hx	2003-09-29 08:31:41	86.69607	-16.78303	free	67.5	300	71.D-0141(A)
2003W	2003-02-01 05:53:52	146.707401	16.04423	free	0.0	1200	70.D-0111(A)
2003W	2003-02-01 06:15:57	146.707401	16.04423	free	45.0	1200	70.D-0111(A)
2003W	2003-02-01 06:37:54	146.707401	16.04423	free	22.5	1200	70.D-0111(A)
2003W	2003-02-01 06:59:59	146.707401	16.04423	free	67.5	1200	70.D-0111(A)
2003W	2003-02-03 05:49:55	146.707409	16.0441	free	0.0	1200	70.D-0111(A)
2003W	2003-02-03 06:22:14	146.706077	16.04407	free	45.0	1200	70.D-0111(A)
2003W	2003-02-03 06:44:11	146.706077	16.04407	free	22.5	1200	70.D-0111(A)
2003W	2003-02-03 07:06:15	146.706077	16.04407	free	67.5	1200	70.D-0111(A)
2003W	2003-02-26 01:28:41	146.706318	16.0437	free	0.0	1800	70.D-0111(A)
2003W	2003-02-26 02:00:44	146.706318	16.0437	free	45.0	1800	70.D-0111(A)

Table C.1.: continued.

SN name	Epoch (UT)	RA (deg)	DEC (deg)	Filter	HWP angle (deg)	Exposure (s)	ProgID
2003W	2003-02-26 02:32:41	146.706318	16.0437	free	22.5	1800	70.D-0111(A)
2003W	2003-02-26 03:04:45	146.706318	16.0437	free	67.5	1800	70.D-0111(A)
2004br	2004-05-19 00:46:29	187.781843	0.61661	free	0.0	900	073.D-0771(A)
2004br	2004-05-19 01:03:55	187.781843	0.61661	free	45.0	900	073.D-0771(A)
2004br	2004-05-19 01:21:13	187.781843	0.61661	free	22.5	900	073.D-0771(A)
2004br	2004-05-19 01:38:39	187.781843	0.61661	free	67.5	900	073.D-0771(A)
2004dt	2004-08-13 07:02:28	30.552855	-0.0974	free	0.0	900	073.D-0771(A)
2004dt	2004-08-13 07:19:53	30.552855	-0.0974	free	45.0	900	073.D-0771(A)
2004dt	2004-08-13 07:37:11	30.552855	-0.0974	free	22.5	900	073.D-0771(A)
2004dt	2004-08-13 07:54:36	30.552855	-0.0974	free	67.5	900	073.D-0771(A)
2004dt	2004-08-27 08:42:20	30.55283	-0.09737	free	0.0	450	073.D-0771(A)
2004dt	2004-08-27 08:52:16	30.55283	-0.09737	free	45.0	450	073.D-0771(A)
2004dt	2004-08-27 09:02:04	30.55283	-0.09737	free	22.5	450	073.D-0771(A)
2004dt	2004-08-27 09:12:00	30.55283	-0.09737	free	67.5	450	073.D-0771(A)
2004dt	2004-08-28 05:31:18	30.552893	-0.09747	free	0.0	450	073.D-0565(A)
2004dt	2004-08-28 05:41:14	30.552893	-0.09747	free	45.0	450	073.D-0565(A)
2004dt	2004-08-28 05:51:02	30.552893	-0.09747	free	22.5	450	073.D-0565(A)
2004dt	2004-08-28 06:00:57	30.552893	-0.09747	free	67.5	450	073.D-0565(A)
2004dt	2004-08-28 06:15:56	30.552883	-0.09738	free	0.0	450	073.D-0565(A)
2004dt	2004-08-28 06:25:52	30.552883	-0.09738	free	45.0	450	073.D-0565(A)
2004dt	2004-08-28 06:35:41	30.552883	-0.09738	free	22.5	450	073.D-0565(A)
2004dt	2004-08-28 06:45:37	30.552883	-0.09738	free	67.5	450	073.D-0565(A)
2004dt	2004-09-02 06:58:06	30.552873	-0.09738	free	0.0	1800	073.D-0771(A)
2004dt	2004-09-02 07:30:33	30.552873	-0.09738	free	45.0	1800	073.D-0771(A)
2004dt	2004-09-02 08:02:53	30.552873	-0.09738	free	22.5	1800	073.D-0771(A)
2004dt	2004-09-02 08:35:19	30.552873	-0.09738	free	67.5	1800	073.D-0771(A)
2004dt	2004-09-25 03:58:37	30.553182	-0.09764	free	0.0	600	073.D-0771(A)
2004dt	2004-09-25 04:11:02	30.553182	-0.09764	free	45.0	600	073.D-0771(A)
2004dt	2004-09-25 04:23:20	30.553182	-0.09764	free	22.5	600	073.D-0771(A)
2004dt	2004-09-25 04:35:46	30.553182	-0.09764	free	67.5	600	073.D-0771(A)
2004ef	2004-09-11 03:31:41	340.541795	19.99436	free	0.0	2400	073.D-0771(A)
2004ef	2004-09-11 04:17:14	340.541795	19.99436	free	45.0	1500	073.D-0771(A)
2004ef	2004-09-11 04:44:40	340.541795	19.99436	free	22.5	1500	073.D-0771(A)
2004ef	2004-09-11 05:12:08	340.541795	19.99436	free	67.5	1500	073.D-0771(A)
2004eo	2004-09-20 02:27:17	308.226037	9.92862	free	0.0	900	073.D-0771(A)
2004eo	2004-09-20 02:44:41	308.226037	9.92862	free	45.0	900	073.D-0771(A)
2004eo	2004-09-20 03:01:59	308.226037	9.92862	free	22.5	900	073.D-0771(A)
2004eo	2004-09-20 03:19:24	308.226037	9.92862	free	67.5	900	073.D-0771(A)
2005cf	2005-06-01 01:09:35	230.384609	-7.41274	free	0.0	750	075.D-0628(A)
2005cf	2005-06-01 01:24:30	230.384609	-7.41274	free	45.0	750	075.D-0628(A)

Table C.1.: continued.

SN name	Epoch (UT)	RA (deg)	DEC (deg)	Filter	HWP angle (deg)	Exposure (s)	ProgID
2005cf	2005-06-01 01:39:18	230.384609	-7.41274	free	22.5	750	075.D-0628(A)
2005cf	2005-06-01 01:54:13	230.384609	-7.41274	free	67.5	750	075.D-0628(A)
2005cf	2005-06-07 03:58:50	230.384584	-7.41277	free	0.0	750	075.D-0628(A)
2005cf	2005-06-07 04:13:45	230.384584	-7.41277	free	45.0	750	075.D-0628(A)
2005cf	2005-06-07 04:28:33	230.384584	-7.41277	free	22.5	750	075.D-0628(A)
2005cf	2005-06-07 04:43:28	230.384584	-7.41277	free	67.5	750	075.D-0628(A)
2005de	2005-08-06 00:14:14	270.597499	26.05203	free	0.0	1200	075.D-0213(A)
2005de	2005-08-06 00:36:39	270.597499	26.05203	free	45.0	1200	075.D-0213(A)
2005de	2005-08-06 00:58:57	270.597499	26.05203	free	22.5	1200	075.D-0213(A)
2005de	2005-08-06 01:21:22	270.597499	26.05203	free	67.5	1200	075.D-0213(A)
2005de	2005-08-12 00:07:19	270.597471	26.05202	free	0.0	1200	075.D-0628(A)
2005de	2005-08-12 00:29:45	270.597471	26.05202	free	45.0	1200	075.D-0628(A)
2005de	2005-08-12 00:52:03	270.597471	26.05202	free	22.5	1200	075.D-0628(A)
2005de	2005-08-12 01:14:30	270.597471	26.05202	free	67.5	1200	075.D-0628(A)
2005df	2005-08-06 09:01:11	64.407611	-62.76932	free	0.0	300	075.D-0213(A)
2005df	2005-08-06 09:08:36	64.407611	-62.76932	free	45.0	300	075.D-0213(A)
2005df	2005-08-06 09:15:54	64.407611	-62.76932	free	22.5	300	075.D-0213(A)
2005df	2005-08-06 09:23:20	64.407611	-62.76932	free	67.5	300	075.D-0213(A)
2005df	2005-08-08 09:11:48	64.407707	-62.76931	free	0.0	200	075.D-0213(A)
2005df	2005-08-08 09:17:33	64.407707	-62.76931	free	45.0	200	075.D-0213(A)
2005df	2005-08-08 09:23:11	64.407707	-62.76931	free	22.5	200	075.D-0213(A)
2005df	2005-08-08 09:28:56	64.407707	-62.76931	free	67.5	200	075.D-0213(A)
2005df	2005-08-09 09:33:29	64.407662	-62.7693	free	0.0	200	075.D-0628(A)
2005df	2005-08-09 09:39:16	64.407662	-62.7693	free	45.0	200	075.D-0628(A)
2005df	2005-08-09 09:44:55	64.407662	-62.7693	free	22.5	200	075.D-0628(A)
2005df	2005-08-09 09:50:40	64.407662	-62.7693	free	67.5	200	075.D-0628(A)
2005df	2005-08-10 09:04:12	64.407988	-62.76923	GG435	0.0	180	075.D-0628(A)
2005df	2005-08-10 09:09:38	64.407988	-62.76923	GG435	45.0	180	075.D-0628(A)
2005df	2005-08-10 09:14:57	64.407988	-62.76923	GG435	22.5	180	075.D-0628(A)
2005df	2005-08-10 09:20:23	64.407988	-62.76923	GG435	67.5	180	075.D-0628(A)
2005df	2005-08-14 09:35:46	64.407867	-62.76935	free	0.0	360	075.D-0628(A)
2005df	2005-08-14 09:44:14	64.407867	-62.76935	free	45.0	360	075.D-0628(A)
2005df	2005-08-14 09:52:43	64.407867	-62.76935	free	22.5	300	075.D-0628(A)
2005df	2005-08-14 10:00:14	64.407867	-62.76935	free	67.5	300	075.D-0628(A)
2005df	2005-08-17 09:19:31	64.407498	-62.76929	free	0.0	240	075.D-0628(A)
2005df	2005-08-17 09:25:56	64.407498	-62.76929	free	45.0	240	075.D-0628(A)
2005df	2005-08-17 09:32:15	64.407498	-62.76929	free	22.5	240	075.D-0628(A)
2005df	2005-08-17 09:38:40	64.407498	-62.76929	free	67.5	240	075.D-0628(A)
2005df	2005-08-21 09:47:05	64.408332	-62.76942	free	0.0	200	075.D-0628(A)

Table C.1.: continued.

SN name	Epoch (UT)	RA (deg)	DEC (deg)	Filter	HWP angle (deg)	Exposure (s)	ProgID
2005df	2005-08-21 09:52:50	64.408332	-62.76942	free	45.0	200	075.D-0628(A)
2005df	2005-08-21 09:58:28	64.408332	-62.76942	free	22.5	200	075.D-0628(A)
2005df	2005-08-21 10:04:13	64.408332	-62.76942	free	67.5	200	075.D-0628(A)
2005df	2005-08-22 09:24:20	64.407707	-62.76929	free	45.0	360	075.D-0628(A)
2005df	2005-08-22 09:32:38	64.407707	-62.76929	free	22.5	360	075.D-0628(A)
2005df	2005-08-22 09:41:03	64.407707	-62.76929	free	67.5	360	075.D-0628(A)
2005df	2005-08-22 09:49:54	64.407707	-62.76929	free	0.0	360	075.D-0628(A)
2005df	2005-08-25 08:53:42	64.407656	-62.76931	free	0.0	150	075.D-0628(A)
2005df	2005-08-25 08:58:38	64.407656	-62.76931	free	45.0	150	075.D-0628(A)
2005df	2005-08-25 09:03:26	64.407656	-62.76931	free	22.5	150	075.D-0628(A)
2005df	2005-08-25 09:08:22	64.407656	-62.76931	free	67.5	150	075.D-0628(A)
2005df	2005-08-26 07:53:25	64.407883	-62.76931	free	0.0	300	075.D-0628(A)
2005df	2005-08-26 08:00:51	64.407883	-62.76931	free	45.0	400	075.D-0628(A)
2005df	2005-08-26 08:09:48	64.407883	-62.76931	free	22.5	400	075.D-0628(A)
2005df	2005-08-26 08:18:54	64.407883	-62.76931	free	67.5	400	075.D-0628(A)
2005df	2005-09-15 08:48:26	64.407621	-62.76947	free	0.0	500	075.D-0628(A)
2005df	2005-09-15 08:59:12	64.407621	-62.76947	free	45.0	500	075.D-0628(A)
2005df	2005-09-15 09:09:50	64.407621	-62.76947	free	22.5	500	075.D-0628(A)
2005df	2005-09-15 09:20:35	64.407621	-62.76947	free	67.5	500	075.D-0628(A)
2005df	2005-09-28 07:17:35	64.407849	-62.76936	free	0.0	700	075.D-0213(A)
2005df	2005-09-28 07:31:46	64.407849	-62.76936	free	45.0	700	075.D-0213(A)
2005df	2005-09-28 07:45:50	64.407849	-62.76936	free	22.5	700	075.D-0213(A)
2005df	2005-09-28 07:59:58	64.407849	-62.76936	free	67.5	700	075.D-0213(A)
2005df	2005-09-28 08:14:19	64.407849	-62.76936	free	0.0	700	075.D-0213(A)
2005df	2005-09-28 08:28:27	64.407849	-62.76936	free	45.0	700	075.D-0213(A)
2005df	2005-09-28 08:42:28	64.407849	-62.76936	free	22.5	700	075.D-0213(A)
2005df	2005-09-28 08:56:37	64.407849	-62.76936	free	67.5	700	075.D-0213(A)
2005el	2005-10-01 08:15:50	77.953137	5.19421	free	0.0	300	075.D-0628(A)
2005el	2005-10-01 08:23:15	77.953137	5.19421	free	45.0	300	075.D-0628(A)
2005el	2005-10-01 08:30:33	77.953137	5.19421	free	22.5	300	075.D-0628(A)
2005el	2005-10-01 08:37:58	77.953137	5.19421	free	67.5	300	075.D-0628(A)
2005hk	2005-11-09 03:28:29	6.962075	-1.19806	free	22.5	900	076.D-0178(A)
2005hk	2005-11-09 03:45:54	6.962075	-1.19806	free	67.5	900	076.D-0178(A)
2005hk	2005-11-09 04:03:52	6.962075	-1.19806	free	0.0	900	076.D-0178(A)
2005hk	2005-11-09 04:21:18	6.962075	-1.19806	free	45.0	900	076.D-0178(A)
2005hk	2005-11-23 01:51:22	6.961921	-1.19811	free	0.0	900	076.D-0178(A)
2005hk	2005-11-23 02:08:47	6.961921	-1.19811	free	45.0	900	076.D-0178(A)
2005hk	2005-11-23 02:26:05	6.961921	-1.19811	free	22.5	900	076.D-0178(A)
2005hk	2005-11-23 02:43:31	6.961921	-1.19811	free	67.5	900	076.D-0178(A)
2005ke	2005-11-16 02:29:45	53.768126	-24.94442	free	0.0	300	076.D-0177(A)

Table C.1.: continued.

SN name	Epoch (UT)	RA (deg)	DEC (deg)	Filter	HWP angle (deg)	Exposure (s)	ProgID
2005ke	2005-11-16 02:37:10	53.768126	-24.94442	free	45.0	300	076.D-0177(A)
2005ke	2005-11-16 02:44:28	53.768126	-24.94442	free	22.5	300	076.D-0177(A)
2005ke	2005-11-16 02:51:53	53.768126	-24.94442	free	67.5	300	076.D-0177(A)
2005ke	2005-11-17 01:57:43	53.768095	-24.94443	free	0.0	300	076.D-0178(A)
2005ke	2005-11-17 02:05:08	53.768095	-24.94443	free	45.0	300	076.D-0178(A)
2005ke	2005-11-17 02:12:25	53.768095	-24.94443	free	22.5	300	076.D-0178(A)
2005ke	2005-11-17 02:19:51	53.768095	-24.94443	free	67.5	300	076.D-0178(A)
2005ke	2005-11-17 02:29:53	53.768095	-24.94443	free	0.0	600	076.D-0178(A)
2005ke	2005-11-17 02:42:18	53.768095	-24.94443	free	45.0	600	076.D-0178(A)
2005ke	2005-11-17 02:54:37	53.768095	-24.94443	free	22.5	600	076.D-0178(A)
2005ke	2005-11-17 03:07:03	53.768095	-24.94443	free	67.5	600	076.D-0178(A)
2005ke	2006-02-09 01:20:21	53.767981	-24.94421	free	0.0	900	076.D-0178(A)
2005ke	2006-02-09 01:37:52	53.767981	-24.94421	free	45.0	900	076.D-0178(A)
2005ke	2006-02-09 01:55:15	53.767981	-24.94421	free	22.5	900	076.D-0178(A)
2005ke	2006-02-09 02:12:46	53.767981	-24.94421	free	67.5	900	076.D-0178(A)
2006X	2006-02-09 08:37:54	185.72459	15.8088	free	0.0	300	076.D-0177(A)
2006X	2006-02-09 08:45:25	185.72459	15.8088	free	45.0	300	076.D-0177(A)
2006X	2006-02-09 08:52:47	185.72459	15.8088	free	22.5	300	076.D-0177(A)
2006X	2006-02-09 09:00:17	185.72459	15.8088	free	67.5	300	076.D-0177(A)
2006X	2006-02-11 06:12:09	185.724599	15.80877	free	0.0	300	076.D-0178(A)
2006X	2006-02-11 06:19:40	185.724599	15.80877	free	45.0	300	076.D-0178(A)
2006X	2006-02-11 06:27:02	185.724599	15.80877	free	22.5	300	076.D-0178(A)
2006X	2006-02-11 06:34:33	185.724599	15.80877	free	67.5	300	076.D-0178(A)
2006X	2006-02-11 08:48:50	185.724808	15.8088	free	0.0	300	076.D-0178(A)
2006X	2006-02-11 08:56:21	185.724808	15.8088	free	45.0	300	076.D-0178(A)
2006X	2006-02-11 09:03:44	185.724808	15.8088	free	22.5	300	076.D-0178(A)
2006X	2006-02-11 09:11:14	185.724808	15.8088	free	67.5	300	076.D-0178(A)
2006X	2006-02-12 04:59:11	185.724606	15.80875	free	0.0	600	076.D-0178(A)
2006X	2006-02-12 05:11:42	185.724606	15.80875	free	45.0	600	076.D-0178(A)
2006X	2006-02-12 05:24:05	185.724606	15.80875	free	22.5	600	076.D-0178(A)
2006X	2006-02-12 05:36:36	185.724606	15.80875	free	67.5	600	076.D-0178(A)
2006X	2006-02-12 08:08:56	185.724635	15.80875	free	0.0	600	076.D-0178(A)
2006X	2006-02-12 08:21:26	185.724635	15.80875	free	45.0	600	076.D-0178(A)
2006X	2006-02-12 08:33:49	185.724635	15.80875	free	22.5	600	076.D-0178(A)
2006X	2006-02-12 08:46:20	185.724635	15.80875	free	67.5	600	076.D-0178(A)
2006X	2006-02-13 04:51:00	185.724618	15.80875	free	0.0	600	076.D-0178(A)
2006X	2006-02-13 05:03:30	185.724618	15.80875	free	45.0	600	076.D-0178(A)
2006X	2006-02-13 05:15:53	185.724618	15.80875	free	22.5	600	076.D-0178(A)
2006X	2006-02-13 05:28:24	185.724618	15.80875	free	67.5	600	076.D-0178(A)
2006X	2006-02-16 07:55:04	185.724622	15.80875	free	0.0	600	076.D-0178(A)
2006X	2006-02-16 08:07:35	185.724622	15.80875	free	45.0	600	076.D-0178(A)
2006X	2006-02-16 08:19:59	185.724622	15.80875	free	22.5	600	076.D-0178(A)

Table C.1.: continued.

SN name	Epoch (UT)	RA (deg)	DEC (deg)	Filter	HWP angle (deg)	Exposure (s)	ProgID
2006X	2006-02-16 08:32:29	185.724622	15.80875	free	67.5	600	076.D-0178(A)
2006X	2006-02-16 08:51:22	185.724637	15.80874	free	0.0	420	076.D-0178(A)
2006X	2006-02-16 09:00:53	185.724637	15.80874	free	45.0	420	076.D-0178(A)
2006X	2006-02-16 09:10:17	185.724637	15.80874	free	22.5	420	076.D-0178(A)
2006X	2006-02-16 09:19:47	185.724637	15.80874	free	67.5	420	076.D-0178(A)
2006X	2006-02-17 06:04:36	185.724615	15.80877	free	0.0	600	076.D-0178(A)
2006X	2006-02-17 06:17:07	185.724615	15.80877	free	45.0	600	076.D-0178(A)
2006X	2006-02-17 06:29:30	185.724615	15.80877	free	22.5	600	076.D-0178(A)
2006X	2006-02-17 06:42:01	185.724615	15.80877	free	67.5	600	076.D-0178(A)
2006X	2006-02-17 08:19:50	185.724622	15.80876	free	0.0	600	076.D-0178(A)
2006X	2006-02-17 08:32:20	185.724622	15.80876	free	45.0	600	076.D-0178(A)
2006X	2006-02-17 08:44:43	185.724622	15.80876	free	22.5	600	076.D-0178(A)
2006X	2006-02-17 08:57:14	185.724622	15.80876	free	67.5	600	076.D-0178(A)
2006X	2006-02-18 08:58:31	185.724655	15.80873	free	0.0	480	076.D-0178(A)
2006X	2006-02-18 09:09:02	185.724655	15.80873	free	45.0	480	076.D-0178(A)
2006X	2006-02-18 09:19:25	185.724655	15.80873	free	22.5	480	076.D-0178(A)
2006X	2006-02-18 09:30:08	185.724655	15.80873	free	67.5	480	076.D-0178(A)
2006X	2006-03-30 03:50:01	185.724748	15.80874	free	0.0	900	076.D-0177(A)
2006X	2006-03-30 04:07:31	185.724748	15.80874	free	45.0	900	076.D-0177(A)
2006X	2006-03-30 04:24:54	185.724748	15.80874	free	22.5	900	076.D-0177(A)
2006X	2006-03-30 04:42:24	185.724748	15.80874	free	67.5	900	076.D-0177(A)
2006X	2006-03-30 05:00:14	185.724748	15.80874	free	0.0	900	076.D-0177(A)
2006X	2006-03-30 05:17:44	185.724748	15.80874	free	45.0	900	076.D-0177(A)
2006X	2006-03-30 05:35:07	185.724748	15.80874	free	22.5	900	076.D-0177(A)
2006X	2006-03-30 05:52:38	185.724748	15.80874	free	67.5	900	076.D-0177(A)
2006X	2006-03-31 03:47:41	185.724601	15.80882	free	0.0	900	076.D-0177(A)
2006X	2006-03-31 04:05:12	185.724601	15.80882	free	45.0	900	076.D-0177(A)
2006X	2006-03-31 04:22:35	185.724601	15.80882	free	22.5	900	076.D-0177(A)
2006X	2006-03-31 04:40:05	185.724601	15.80882	free	67.5	900	076.D-0177(A)
2006X	2006-03-31 04:58:15	185.724601	15.80882	free	0.0	900	076.D-0177(A)
2006X	2006-03-31 05:15:46	185.724601	15.80882	free	45.0	900	076.D-0177(A)
2006X	2006-03-31 05:33:09	185.724601	15.80882	free	22.5	900	076.D-0177(A)
2006X	2006-03-31 05:50:40	185.724601	15.80882	free	67.5	900	076.D-0177(A)
2007fb	2007-07-10 08:49:06	359.218434	5.50883	free	0.0	300	079.D-0090(A)
2007fb	2007-07-10 08:55:08	359.218434	5.50883	free	45.0	300	079.D-0090(A)
2007fb	2007-07-10 09:01:01	359.218434	5.50883	free	22.5	300	079.D-0090(A)
2007fb	2007-07-10 09:07:01	359.218434	5.50883	free	67.5	300	079.D-0090(A)
2007fb	2007-07-10 09:13:54	359.218434	5.50883	free	0.0	300	079.D-0090(A)
2007fb	2007-07-10 09:19:54	359.218434	5.50883	free	45.0	300	079.D-0090(A)
2007fb	2007-07-10 09:25:47	359.218434	5.50883	free	22.5	300	079.D-0090(A)
2007fb	2007-07-10 09:31:47	359.218434	5.50883	free	67.5	300	079.D-0090(A)
2007fb	2007-07-13 08:51:23	359.218529	5.50607	free	0.0	300	079.D-0090(A)
2007fb	2007-07-13 08:57:26	359.218529	5.50607	free	45.0	300	079.D-0090(A)

Table C.1.: continued.

SN name	Epoch (UT)	RA (deg)	DEC (deg)	Filter	HWP angle (deg)	Exposure (s)	ProgID
2007fb	2007-07-13 09:03:20	359.218529	5.50607	free	22.5	300	079.D-0090(A)
2007fb	2007-07-13 09:09:23	359.218529	5.50607	free	67.5	300	079.D-0090(A)
2007fb	2007-07-14 07:23:11	359.218546	5.50869	free	0.0	750	079.D-0090(A)
2007fb	2007-07-14 07:36:43	359.218546	5.50869	free	45.0	750	079.D-0090(A)
2007fb	2007-07-14 07:50:08	359.218546	5.50869	free	22.5	750	079.D-0090(A)
2007fb	2007-07-14 08:03:41	359.218546	5.50869	free	67.5	750	079.D-0090(A)
2007fb	2007-07-14 09:31:32	359.218534	5.50869	GG435	0.0	750	079.D-0090(A)
2007fb	2007-07-14 09:45:06	359.218534	5.50869	GG435	45.0	750	079.D-0090(A)
2007fb	2007-07-14 09:58:31	359.218534	5.50869	GG435	22.5	750	079.D-0090(A)
2007fb	2007-07-14 10:12:04	359.218534	5.50869	GG435	67.5	750	079.D-0090(A)
2007fb	2007-07-17 07:27:20	359.218535	5.50867	free	0.0	750	079.D-0090(A)
2007fb	2007-07-17 07:40:52	359.218535	5.50867	free	45.0	750	079.D-0090(A)
2007fb	2007-07-17 07:54:16	359.218535	5.50867	free	22.5	750	079.D-0090(A)
2007fb	2007-07-17 08:07:48	359.218535	5.50867	free	67.5	750	079.D-0090(A)
2007fb	2007-07-17 08:24:24	359.218535	5.50867	free	0.0	750	079.D-0090(A)
2007fb	2007-07-17 08:37:55	359.218535	5.50867	free	45.0	750	079.D-0090(A)
2007fb	2007-07-17 08:51:18	359.218535	5.50867	free	22.5	750	079.D-0090(A)
2007fb	2007-07-17 09:04:50	359.218535	5.50867	free	67.5	750	079.D-0090(A)
2007hj	2007-09-06 03:33:23	345.449463	15.58654	GG435	0.0	600	079.D-0090(A)
2007hj	2007-09-06 03:44:23	345.449463	15.58654	GG435	45.0	800	079.D-0090(A)
2007hj	2007-09-06 03:58:37	345.449463	15.58654	GG435	22.5	800	079.D-0090(A)
2007hj	2007-09-06 04:12:57	345.449463	15.58654	GG435	67.5	700	079.D-0090(A)
2007hj	2007-09-12 03:04:59	345.449457	15.58662	GG435	0.0	900	079.D-0090(A)
2007hj	2007-09-12 03:21:03	345.449457	15.58662	GG435	45.0	900	079.D-0090(A)
2007hj	2007-09-12 03:36:57	345.449457	15.58662	GG435	22.5	900	079.D-0090(A)
2007hj	2007-09-12 03:52:59	345.449457	15.58662	GG435	67.5	900	079.D-0090(A)
2007hj	2007-09-18 02:37:01	345.449448	15.58656	GG435	0.0	1700	079.D-0090(A)
2007hj	2007-09-18 03:06:21	345.449448	15.58656	GG435	45.0	1700	079.D-0090(A)
2007hj	2007-09-18 03:45:57	345.449448	15.58656	GG435	22.5	1700	079.D-0090(A)
2007hj	2007-09-18 04:18:14	345.449448	15.58656	GG435	67.5	1700	079.D-0090(A)
2007if	2007-09-13 03:54:26	17.714385	15.46108	GG435	0.0	1500	079.D-0090(A)
2007if	2007-09-13 04:20:24	17.714385	15.46108	GG435	45.0	1500	079.D-0090(A)
2007if	2007-09-13 04:46:15	17.714385	15.46108	GG435	22.5	1500	079.D-0090(A)
2007if	2007-09-13 05:12:15	17.714385	15.46108	GG435	67.5	1500	079.D-0090(A)
2007if	2007-09-13 05:45:05	17.714265	15.46113	GG435	0.0	1500	079.D-0090(A)
2007if	2007-09-13 06:12:08	17.714265	15.46113	GG435	45.0	1500	079.D-0090(A)
2007if	2007-09-13 06:38:01	17.714265	15.46113	GG435	22.5	1500	079.D-0090(A)
2007if	2007-09-13 07:11:25	17.714232	15.46112	GG435	67.5	1500	079.D-0090(A)
2007if	2007-09-20 03:39:08	17.714353	15.46089	GG435	0.0	1500	079.D-0090(A)
2007if	2007-09-20 04:05:33	17.714353	15.46089	GG435	45.0	1500	079.D-0090(A)
2007if	2007-09-20 04:31:24	17.714353	15.46089	GG435	22.5	1500	079.D-0090(A)
2007if	2007-09-20 04:57:23	17.714353	15.46089	GG435	67.5	1500	079.D-0090(A)

Table C.1.: continued.

SN name	Epoch (UT)	RA (deg)	DEC (deg)	Filter	HWP angle (deg)	Exposure (s)	ProgID
2007if	2007-09-20 05:28:28	17.714428	15.46098	GG435	0.0	1500	079.D-0090(A)
2007if	2007-09-20 05:54:27	17.714428	15.46098	GG435	45.0	1500	079.D-0090(A)
2007if	2007-09-20 06:20:19	17.714428	15.46098	GG435	22.5	1500	079.D-0090(A)
2007if	2007-09-20 06:46:17	17.714428	15.46098	GG435	67.5	1500	079.D-0090(A)
2007if	2007-10-15 01:56:54	17.714292	15.46099	GG435	0.0	1800	080.D-0108(A)
2007if	2007-10-15 02:27:56	17.714292	15.46099	GG435	45.0	1800	080.D-0108(A)
2007if	2007-10-15 02:58:51	17.714292	15.46099	GG435	22.5	1800	080.D-0108(A)
2007if	2007-10-15 03:32:00	17.714292	15.46099	GG435	67.5	1800	080.D-0108(A)
2007if	2007-10-15 04:04:13	17.714292	15.46099	GG435	0.0	1800	080.D-0108(A)
2007if	2007-10-15 04:35:17	17.714292	15.46099	GG435	45.0	1800	080.D-0108(A)
2007if	2007-10-15 05:07:39	17.714292	15.46099	GG435	22.5	1800	080.D-0108(A)
2007if	2007-10-15 05:38:40	17.714292	15.46099	GG435	67.5	1800	080.D-0108(A)
2007if	2007-10-16 02:36:51	17.714093	15.46107	GG435	0.0	1800	080.D-0108(A)
2007if	2007-10-16 03:07:51	17.714093	15.46107	GG435	45.0	1800	080.D-0108(A)
2007if	2007-10-16 03:39:47	17.714093	15.46107	GG435	22.5	1800	080.D-0108(A)
2007if	2007-10-16 04:13:03	17.714093	15.46107	GG435	67.5	1800	080.D-0108(A)
2007le	2007-10-16 00:04:50	354.702038	-6.5226	GG435	0.0	1200	080.D-0108(A)
2007le	2007-10-16 00:25:50	354.702038	-6.5226	GG435	45.0	1000	080.D-0108(A)
2007le	2007-10-16 00:43:21	354.702038	-6.5226	GG435	22.5	1000	080.D-0108(A)
2007le	2007-10-16 01:01:01	354.702038	-6.5226	GG435	67.5	1000	080.D-0108(A)
2007le	2007-10-21 05:27:49	354.70214	-6.52258	GG435	45.0	300	080.D-0108(A)
2007le	2007-10-21 05:33:34	354.70214	-6.52258	GG435	22.5	300	080.D-0108(A)
2007le	2007-10-21 05:39:27	354.70214	-6.52258	GG435	67.5	300	080.D-0108(A)
2007le	2007-10-21 05:53:07	354.70214	-6.52258	GG435	0.0	300	080.D-0108(A)
2007le	2007-12-06 00:54:48	354.702006	-6.5226	GG435	0.0	675	080.D-0108(A)
2007le	2007-12-06 01:07:05	354.702006	-6.5226	GG435	45.0	675	080.D-0108(A)
2007le	2007-12-06 01:19:14	354.702006	-6.5226	GG435	22.5	675	080.D-0108(A)
2007le	2007-12-06 01:31:32	354.702006	-6.5226	GG435	67.5	675	080.D-0108(A)
2007sr	2008-02-15 06:00:17	180.471133	-18.97267	free	0.0	600	080.D-0108(A)
2007sr	2008-02-15 06:11:10	180.471133	-18.97267	free	45.0	600	080.D-0108(A)
2007sr	2008-02-15 06:21:54	180.471133	-18.97267	free	22.5	600	080.D-0108(A)
2007sr	2008-02-15 06:32:47	180.471133	-18.97267	free	67.5	600	080.D-0108(A)
2007sr	2008-02-15 06:44:16	180.471133	-18.97267	free	0.0	600	080.D-0108(A)
2007sr	2008-02-15 06:55:09	180.471133	-18.97267	free	45.0	600	080.D-0108(A)
2007sr	2008-02-15 07:05:53	180.471133	-18.97267	free	22.5	600	080.D-0108(A)
2007sr	2008-02-15 07:16:46	180.471133	-18.97267	free	67.5	600	080.D-0108(A)
2008ff	2008-09-26 04:10:19	303.499275	-44.3515	GG435	0.0	750	081.D-0557(A)
2008ff	2008-09-26 04:23:41	303.499275	-44.3515	GG435	45.0	750	081.D-0557(A)
2008ff	2008-09-26 04:36:56	303.499275	-44.3515	GG435	22.5	750	081.D-0557(A)
2008ff	2008-09-26 04:50:18	303.499275	-44.3515	GG435	67.5	750	081.D-0557(A)
2008fl	2008-09-14 00:18:04	294.186502	-37.55124	GG435	0.0	750	081.D-0558(A)

Table C.1.: continued.

SN name	Epoch (UT)	RA (deg)	DEC (deg)	Filter	HWP angle (deg)	Exposure (s)	ProgID
2008fl	2008-09-14 00:31:26	294.186502	-37.55124	GG435	45.0	750	081.D-0558(A)
2008fl	2008-09-14 00:44:40	294.186502	-37.55124	GG435	22.5	750	081.D-0558(A)
2008fl	2008-09-14 00:58:02	294.186502	-37.55124	GG435	67.5	750	081.D-0558(A)
2008fl	2008-09-20 01:38:13	294.186779	-37.55111	GG435	0.0	1200	081.D-0558(A)
2008fl	2008-09-20 01:59:10	294.186779	-37.55111	GG435	45.0	1200	081.D-0558(A)
2008fl	2008-09-20 02:19:58	294.186779	-37.55111	GG435	22.5	1200	081.D-0558(A)
2008fl	2008-09-20 02:40:55	294.186779	-37.55111	GG435	67.5	1200	081.D-0558(A)
2008fl	2008-09-21 00:29:57	294.186518	-37.55121	GG435	0.0	750	081.D-0558(A)
2008fl	2008-09-21 00:43:19	294.186518	-37.55121	GG435	45.0	750	081.D-0558(A)
2008fl	2008-09-21 00:56:34	294.186518	-37.55121	GG435	22.5	750	081.D-0558(A)
2008fl	2008-09-21 01:09:56	294.186518	-37.55121	GG435	67.5	750	081.D-0558(A)
2008fl	2008-09-23 02:31:10	294.186515	-37.5512	GG435	0.0	750	081.D-0558(A)
2008fl	2008-09-23 02:44:31	294.186515	-37.5512	GG435	45.0	750	081.D-0558(A)
2008fl	2008-09-23 02:57:46	294.186515	-37.5512	GG435	22.5	750	081.D-0558(A)
2008fl	2008-09-23 03:11:08	294.186515	-37.5512	GG435	67.5	750	081.D-0558(A)
2008fl	2008-09-27 02:51:43	294.186452	-37.55121	GG435	0.0	1000	081.D-0558(A)
2008fl	2008-09-27 03:09:16	294.186452	-37.55121	GG435	45.0	1000	081.D-0558(A)
2008fl	2008-09-27 03:26:40	294.186452	-37.55121	GG435	22.5	1000	081.D-0558(A)
2008fl	2008-09-27 03:44:12	294.186452	-37.55121	GG435	67.5	1000	081.D-0558(A)
2008fp	2008-09-16 08:19:42	109.134968	-29.32481	GG435	45.0	500	081.D-0558(A)
2008fp	2008-09-16 08:28:46	109.134968	-29.32481	GG435	22.5	500	081.D-0558(A)
2008fp	2008-09-16 08:37:58	109.134968	-29.32481	GG435	67.5	500	081.D-0558(A)
2008fp	2008-09-16 08:47:48	109.134968	-29.32481	GG435	0.0	500	081.D-0558(A)
2008fp	2008-09-21 08:39:08	109.134896	-29.3248	GG435	0.0	500	081.D-0557(A)
2008fp	2008-09-21 08:48:21	109.134896	-29.3248	GG435	45.0	400	081.D-0557(A)
2008fp	2008-09-21 08:55:45	109.134896	-29.3248	GG435	22.5	400	081.D-0557(A)
2008fp	2008-09-21 09:03:17	109.134896	-29.3248	GG435	67.5	350	081.D-0557(A)
2008fp	2008-09-23 07:24:13	109.134796	-29.32483	GG435	0.0	300	081.D-0557(A)
2008fp	2008-09-23 07:30:05	109.134796	-29.32483	GG435	45.0	300	081.D-0557(A)
2008fp	2008-09-23 07:35:49	109.134796	-29.32483	GG435	22.5	300	081.D-0557(A)
2008fp	2008-09-23 07:41:41	109.134796	-29.32483	GG435	67.5	300	081.D-0557(A)
2008fp	2008-09-27 08:00:19	109.13594	-29.32553	GG435	0.0	500	081.D-0557(A)
2008fp	2008-09-27 08:09:31	109.13594	-29.32553	GG435	45.0	500	081.D-0557(A)
2008fp	2008-09-27 08:18:37	109.13594	-29.32553	GG435	22.5	500	081.D-0557(A)
2008fp	2008-09-27 08:27:49	109.13594	-29.32553	GG435	67.5	500	081.D-0557(A)
2010ev	2010-07-06 23:55:18	156.370965	-39.83113	free	0.0	120	085.D-0731(A)
2010ev	2010-07-06 23:58:03	156.370965	-39.83113	free	22.5	120	085.D-0731(A)
2010ev	2010-07-07 00:00:49	156.370965	-39.83113	free	45.0	120	085.D-0731(A)
2010ev	2010-07-07 00:03:36	156.370965	-39.83113	free	67.5	120	085.D-0731(A)
2010ev	2010-07-07 00:07:02	156.370965	-39.83113	free	0.0	240	085.D-0731(A)

Table C.1.: continued.

SN name	Epoch (UT)	RA (deg)	DEC (deg)	Filter	HWP angle (deg)	Exposure (s)	ProgID
2010ev	2010-07-07 00:11:47	156.370965	-39.83113	free	22.5	240	085.D-0731(A)
2010ev	2010-07-07 00:16:33	156.370965	-39.83113	free	45.0	240	085.D-0731(A)
2010ev	2010-07-07 00:21:18	156.370965	-39.83113	free	67.5	240	085.D-0731(A)
2010ev	2010-07-10 23:37:56	156.37107	-39.83113	free	0.0	300	085.D-0731(A)
2010ev	2010-07-10 23:43:42	156.37107	-39.83113	free	22.5	300	085.D-0731(A)
2010ev	2010-07-10 23:49:27	156.37107	-39.83113	free	45.0	300	085.D-0731(A)
2010ev	2010-07-10 23:55:12	156.37107	-39.83113	free	67.5	300	085.D-0731(A)
2010ev	2010-07-19 23:38:03	156.371013	-39.83114	free	0.0	600	085.D-0731(A)
2010ev	2010-07-19 23:48:49	156.371013	-39.83114	free	22.5	900	085.D-0731(A)
2010ev	2010-07-20 00:04:35	156.371013	-39.83114	free	45.0	900	085.D-0731(A)
2010ev	2010-07-20 00:20:21	156.371013	-39.83114	free	67.5	900	085.D-0731(A)
2010ko	2010-12-08 02:48:51	83.20753	-14.09762	GG435	0.0	110	086.D-0262(A)
2010ko	2010-12-08 02:51:26	83.20753	-14.09762	GG435	22.5	110	086.D-0262(A)
2010ko	2010-12-08 02:54:01	83.20753	-14.09762	GG435	45.0	110	086.D-0262(A)
2010ko	2010-12-08 02:56:36	83.20753	-14.09762	GG435	67.5	110	086.D-0262(A)
2010ko	2010-12-08 03:01:53	83.20753	-14.09762	free	0.0	110	086.D-0262(A)
2010ko	2010-12-08 03:04:28	83.20753	-14.09762	free	22.5	110	086.D-0262(A)
2010ko	2010-12-08 03:07:03	83.20753	-14.09762	free	45.0	110	086.D-0262(A)
2010ko	2010-12-08 03:09:38	83.20753	-14.09762	free	67.5	110	086.D-0262(A)
2010ko	2010-12-09 04:39:23	83.207608	-14.09763	free	0.0	400	086.D-0262(A)
2010ko	2010-12-09 04:46:55	83.207608	-14.09763	free	45.0	400	086.D-0262(A)
2010ko	2010-12-09 04:54:20	83.207608	-14.09763	free	22.5	400	086.D-0262(A)
2010ko	2010-12-09 05:01:53	83.207608	-14.09763	free	67.5	400	086.D-0262(A)
2010ko	2010-12-09 05:10:34	83.207608	-14.09763	free	0.0	900	086.D-0262(A)
2010ko	2010-12-09 05:26:28	83.207608	-14.09763	free	45.0	900	086.D-0262(A)
2010ko	2010-12-09 05:42:13	83.207608	-14.09763	free	22.5	900	086.D-0262(A)
2010ko	2010-12-09 05:58:06	83.207608	-14.09763	free	67.5	900	086.D-0262(A)
2010ko	2010-12-13 05:07:52	83.207545	-14.09761	free	0.0	350	086.D-0262(A)
2010ko	2010-12-13 05:14:35	83.207545	-14.09761	free	45.0	350	086.D-0262(A)
2010ko	2010-12-13 05:21:11	83.207545	-14.09761	free	22.5	350	086.D-0262(A)
2010ko	2010-12-13 05:27:54	83.207545	-14.09761	free	67.5	350	086.D-0262(A)
2010ko	2010-12-13 05:40:52	83.207545	-14.09761	free	0.0	350	086.D-0262(A)
2010ko	2010-12-13 05:47:35	83.207545	-14.09761	free	45.0	350	086.D-0262(A)
2010ko	2010-12-13 05:54:11	83.207545	-14.09761	free	22.5	350	086.D-0262(A)
2010ko	2010-12-13 06:00:54	83.207545	-14.09761	free	67.5	350	086.D-0262(A)
2010ko	2010-12-13 06:07:55	83.207545	-14.09761	free	0.0	350	086.D-0262(A)
2010ko	2010-12-13 06:14:37	83.207545	-14.09761	free	45.0	350	086.D-0262(A)
2010ko	2010-12-13 06:21:13	83.207545	-14.09761	free	22.5	350	086.D-0262(A)
2010ko	2010-12-13 06:27:55	83.207545	-14.09761	free	67.5	350	086.D-0262(A)
2010ko	2010-12-14 01:52:32	83.207511	-14.0974	free	0.0	500	086.D-0262(A)
2010ko	2010-12-14 02:28:33	83.207511	-14.0974	free	45.0	500	086.D-0262(A)
2010ko	2010-12-14 03:04:27	83.207511	-14.0974	free	22.5	500	086.D-0262(A)
2010ko	2010-12-14 03:40:28	83.207511	-14.0974	free	67.5	500	086.D-0262(A)

Table C.1.: continued.

SN name	Epoch (UT)	RA (deg)	DEC (deg)	Filter	HWP angle (deg)	Exposure (s)	ProgID
2010ko	2010-12-14 02:01:28	83.207511	-14.0974	free	0.0	500	086.D-0262(A)
2010ko	2010-12-14 02:37:29	83.207511	-14.0974	free	45.0	500	086.D-0262(A)
2010ko	2010-12-14 03:13:23	83.207511	-14.0974	free	22.5	500	086.D-0262(A)
2010ko	2010-12-14 03:49:24	83.207511	-14.0974	free	67.5	500	086.D-0262(A)
2010ko	2010-12-14 02:10:24	83.207511	-14.0974	free	0.0	500	086.D-0262(A)
2010ko	2010-12-14 02:46:25	83.207511	-14.0974	free	45.0	500	086.D-0262(A)
2010ko	2010-12-14 03:22:19	83.207511	-14.0974	free	22.5	500	086.D-0262(A)
2010ko	2010-12-14 03:58:21	83.207511	-14.0974	free	67.5	500	086.D-0262(A)
2010ko	2010-12-14 02:19:20	83.207511	-14.0974	free	0.0	500	086.D-0262(A)
2010ko	2010-12-14 02:55:22	83.207511	-14.0974	free	45.0	500	086.D-0262(A)
2010ko	2010-12-14 03:31:15	83.207511	-14.0974	free	22.5	500	086.D-0262(A)
2010ko	2010-12-14 04:07:16	83.207511	-14.0974	free	67.5	500	086.D-0262(A)
2010ko	2010-12-17 03:43:20	83.207544	-14.09773	free	0.0	650	086.D-0262(A)
2010ko	2010-12-17 03:54:56	83.207544	-14.09773	free	22.5	650	086.D-0262(A)
2010ko	2010-12-17 04:06:31	83.207544	-14.09773	free	45.0	650	086.D-0262(A)
2010ko	2010-12-17 04:18:06	83.207544	-14.09773	free	67.5	650	086.D-0262(A)
2010ko	2010-12-19 03:18:26	83.20751	-14.09744	free	0.0	800	086.D-0262(A)
2010ko	2010-12-19 03:32:31	83.20751	-14.09744	free	22.5	800	086.D-0262(A)
2010ko	2010-12-19 03:46:36	83.20751	-14.09744	free	45.0	800	086.D-0262(A)
2010ko	2010-12-19 04:00:41	83.20751	-14.09744	free	67.5	800	086.D-0262(A)
2010ko	2010-12-19 04:28:26	83.207679	-14.09759	free	0.0	800	086.D-0262(A)
2010ko	2010-12-19 04:42:32	83.207679	-14.09759	free	22.5	800	086.D-0262(A)
2010ko	2010-12-19 04:56:37	83.207679	-14.09759	free	45.0	800	086.D-0262(A)
2010ko	2010-12-19 05:10:43	83.207679	-14.09759	free	67.5	800	086.D-0262(A)
2010ko	2010-12-26 03:17:26	83.207559	-14.09762	free	0.0	900	086.D-0262(B)
2010ko	2010-12-26 03:33:18	83.207559	-14.09762	free	45.0	1000	086.D-0262(B)
2010ko	2010-12-26 03:50:44	83.207559	-14.09762	free	22.5	1000	086.D-0262(B)
2010ko	2010-12-26 04:08:16	83.207559	-14.09762	free	67.5	1000	086.D-0262(B)
2010ko	2010-12-26 04:26:18	83.207559	-14.09762	free	0.0	1000	086.D-0262(B)
2010ko	2010-12-26 04:43:51	83.207559	-14.09762	free	45.0	1000	086.D-0262(B)
2010ko	2010-12-26 05:01:17	83.207559	-14.09762	free	22.5	1000	086.D-0262(B)
2010ko	2010-12-26 05:18:49	83.207559	-14.09762	free	67.5	1000	086.D-0262(B)
2010ko	2010-12-31 02:45:35	83.207515	-14.09764	free	0.0	900	086.D-0262(A)
2010ko	2010-12-31 03:48:17	83.207515	-14.09764	free	45.0	900	086.D-0262(A)
2010ko	2010-12-31 04:50:51	83.207515	-14.09764	free	22.5	900	086.D-0262(A)
2010ko	2010-12-31 05:53:34	83.207515	-14.09764	free	67.5	900	086.D-0262(A)
2010ko	2010-12-31 03:01:11	83.207515	-14.09764	free	0.0	900	086.D-0262(A)
2010ko	2010-12-31 04:03:53	83.207515	-14.09764	free	45.0	900	086.D-0262(A)
2010ko	2010-12-31 05:06:27	83.207515	-14.09764	free	22.5	900	086.D-0262(A)
2010ko	2010-12-31 06:09:10	83.207515	-14.09764	free	67.5	900	086.D-0262(A)
2010ko	2010-12-31 03:16:47	83.207515	-14.09764	free	0.0	900	086.D-0262(A)
2010ko	2010-12-31 04:19:29	83.207515	-14.09764	free	45.0	900	086.D-0262(A)
2010ko	2010-12-31 05:22:04	83.207515	-14.09764	free	22.5	900	086.D-0262(A)
2010ko	2010-12-31 06:24:47	83.207515	-14.09764	free	67.5	900	086.D-0262(A)
2010ko	2010-12-31 03:32:23	83.207515	-14.09764	free	0.0	900	086.D-0262(A)

Table C.1.: continued.

SN name	Epoch (UT)	RA (deg)	DEC (deg)	Filter	HWP angle (deg)	Exposure (s)	ProgID
2010ko	2010-12-31 04:35:06	83.207515	-14.09764	free	45.0	900	086.D-0262(A)
2010ko	2010-12-31 05:37:40	83.207515	-14.09764	free	22.5	900	086.D-0262(A)
2010ko	2010-12-31 06:40:24	83.207515	-14.09764	free	67.5	900	086.D-0262(A)
2010ko	2011-02-04 02:29:03	83.207569	-14.09756	free	0.0	900	086.D-0262(B)
2010ko	2011-02-04 02:44:49	83.207569	-14.09756	free	22.5	900	086.D-0262(B)
2010ko	2011-02-04 03:00:34	83.207569	-14.09756	free	45.0	900	086.D-0262(B)
2010ko	2011-02-04 03:16:19	83.207569	-14.09756	free	67.5	900	086.D-0262(B)
2010ko	2011-02-04 03:40:55	83.207428	-14.09761	free	0.0	900	086.D-0262(B)
2010ko	2011-02-04 03:56:41	83.207428	-14.09761	free	22.5	900	086.D-0262(B)
2010ko	2011-02-04 04:12:25	83.207428	-14.09761	free	45.0	900	086.D-0262(B)
2010ko	2011-02-04 04:28:11	83.207428	-14.09761	free	67.5	900	086.D-0262(B)
2010ko	2011-02-05 00:50:31	83.207548	-14.09763	free	0.0	900	086.D-0262(B)
2010ko	2011-02-05 01:06:16	83.207548	-14.09763	free	22.5	900	086.D-0262(B)
2010ko	2011-02-05 01:22:02	83.207548	-14.09763	free	45.0	900	086.D-0262(B)
2010ko	2011-02-05 01:37:47	83.207548	-14.09763	free	67.5	900	086.D-0262(B)
2010ko	2011-02-11 00:48:14	83.20751	-14.09758	free	0.0	60	086.D-0262(B)
2010ko	2011-02-11 00:49:59	83.20751	-14.09758	free	22.5	60	086.D-0262(B)
2010ko	2011-02-11 00:51:44	83.20751	-14.09758	free	45.0	60	086.D-0262(B)
2010ko	2011-02-11 00:53:30	83.20751	-14.09758	free	67.5	60	086.D-0262(B)
2010ko	2011-02-11 00:55:57	83.20751	-14.09758	free	0.0	900	086.D-0262(B)
2010ko	2011-02-11 01:11:42	83.20751	-14.09758	free	22.5	900	086.D-0262(B)
2010ko	2011-02-11 01:27:27	83.20751	-14.09758	free	45.0	900	086.D-0262(B)
2010ko	2011-02-11 01:43:12	83.20751	-14.09758	free	67.5	900	086.D-0262(B)
2010ko	2011-02-11 02:01:56	83.20751	-14.09758	free	0.0	900	086.D-0262(B)
2010ko	2011-02-11 02:17:41	83.20751	-14.09758	free	22.5	900	086.D-0262(B)
2010ko	2011-02-11 02:33:26	83.20751	-14.09758	free	45.0	900	086.D-0262(B)
2010ko	2011-02-11 02:49:11	83.20751	-14.09758	free	67.5	900	086.D-0262(B)
2010ko	2011-02-11 03:09:49	83.20761	-14.09758	free	0.0	900	086.D-0262(B)
2010ko	2011-02-11 03:25:34	83.20761	-14.09758	free	22.5	900	086.D-0262(B)
2010ko	2011-02-11 03:41:19	83.20761	-14.09758	free	45.0	900	086.D-0262(B)
2010ko	2011-02-11 03:57:04	83.20761	-14.09758	free	67.5	900	086.D-0262(B)
2010ko	2011-02-12 00:30:55	83.20749	-14.09757	free	0.0	900	086.D-0262(A)
2010ko	2011-02-12 00:46:40	83.20749	-14.09757	free	22.5	900	086.D-0262(A)
2010ko	2011-02-12 01:02:25	83.20749	-14.09757	free	45.0	900	086.D-0262(A)
2010ko	2011-02-12 01:18:11	83.20749	-14.09757	free	67.5	900	086.D-0262(A)
2010ko	2011-02-12 01:37:17	83.20749	-14.09757	free	0.0	900	086.D-0262(A)
2010ko	2011-02-12 01:53:02	83.20749	-14.09757	free	22.5	900	086.D-0262(A)
2010ko	2011-02-12 02:08:48	83.20749	-14.09757	free	45.0	900	086.D-0262(A)
2010ko	2011-02-12 02:24:33	83.20749	-14.09757	free	67.5	900	086.D-0262(A)
2010ko	2011-02-12 02:43:32	83.20749	-14.09757	free	0.0	900	086.D-0262(A)
2010ko	2011-02-12 02:59:17	83.20749	-14.09757	free	22.5	900	086.D-0262(A)
2010ko	2011-02-12 03:15:03	83.20749	-14.09757	free	45.0	900	086.D-0262(A)
2010ko	2011-02-12 03:30:48	83.20749	-14.09757	free	67.5	900	086.D-0262(A)
2010ko	2011-02-13 00:16:14	83.207543	-14.09759	free	0.0	900	086.D-0262(B)

Table C.1.: continued.

SN name	Epoch (UT)	RA (deg)	DEC (deg)	Filter	HWP angle (deg)	Exposure (s)	ProgID
2010ko	2011-02-13 00:31:58	83.207543	-14.09759	free	22.5	900	086.D-0262(B)
2010ko	2011-02-13 00:47:44	83.207543	-14.09759	free	45.0	900	086.D-0262(B)
2010ko	2011-02-13 01:03:29	83.207543	-14.09759	free	67.5	900	086.D-0262(B)
2010ko	2011-02-13 01:21:20	83.207543	-14.09759	free	0.0	900	086.D-0262(B)
2010ko	2011-02-13 01:37:05	83.207543	-14.09759	free	22.5	900	086.D-0262(B)
2010ko	2011-02-13 01:52:51	83.207543	-14.09759	free	45.0	900	086.D-0262(B)
2010ko	2011-02-13 02:08:36	83.207543	-14.09759	free	67.5	900	086.D-0262(B)
2010ko	2011-02-13 02:26:43	83.207543	-14.09759	free	0.0	900	086.D-0262(B)
2010ko	2011-02-13 02:42:28	83.207543	-14.09759	free	22.5	900	086.D-0262(B)
2010ko	2011-02-13 02:58:14	83.207543	-14.09759	free	45.0	900	086.D-0262(B)
2010ko	2011-02-13 03:13:59	83.207543	-14.09759	free	67.5	900	086.D-0262(B)
2011ae	2011-03-04 04:27:14	178.705294	-16.8629	free	0.0	250	086.D-0262(A)
2011ae	2011-03-04 04:32:16	178.705294	-16.8629	free	45.0	250	086.D-0262(A)
2011ae	2011-03-04 04:37:12	178.705294	-16.8629	free	22.5	250	086.D-0262(A)
2011ae	2011-03-04 04:42:14	178.705294	-16.8629	free	67.5	250	086.D-0262(A)
2011ae	2011-03-04 04:49:24	178.705294	-16.8629	free	0.0	250	086.D-0262(A)
2011ae	2011-03-04 04:54:27	178.705294	-16.8629	free	45.0	250	086.D-0262(A)
2011ae	2011-03-04 04:59:24	178.705294	-16.8629	free	22.5	250	086.D-0262(A)
2011ae	2011-03-04 05:04:27	178.705294	-16.8629	free	67.5	250	086.D-0262(A)
2011ae	2011-03-16 05:03:44	178.705333	-16.86285	free	0.0	310	086.D-0262(A)
2011ae	2011-03-16 05:09:40	178.705333	-16.86285	free	22.5	310	086.D-0262(A)
2011ae	2011-03-16 05:15:36	178.705333	-16.86285	free	45.0	310	086.D-0262(A)
2011ae	2011-03-16 05:21:32	178.705333	-16.86285	free	67.5	310	086.D-0262(A)
2011ae	2011-03-16 05:39:22	178.705402	-16.86285	free	0.0	310	086.D-0262(A)
2011ae	2011-03-16 05:45:17	178.705402	-16.86285	free	22.5	310	086.D-0262(A)
2011ae	2011-03-16 05:51:14	178.705402	-16.86285	free	45.0	310	086.D-0262(A)
2011ae	2011-03-16 05:57:08	178.705402	-16.86285	free	67.5	310	086.D-0262(A)
2011iv	2011-12-10 03:41:21	54.713468	-35.59261	free	0.0	65	088.D-0502(A)
2011iv	2011-12-10 03:43:19	54.713468	-35.59261	free	45.0	65	088.D-0502(A)
2011iv	2011-12-10 03:45:09	54.713468	-35.59261	free	22.5	65	088.D-0502(A)
2011iv	2011-12-10 03:47:07	54.713468	-35.59261	free	67.5	65	088.D-0502(A)
2011iv	2011-12-10 03:49:29	54.713468	-35.59261	free	0.0	60	088.D-0502(A)
2011iv	2011-12-10 03:51:22	54.713468	-35.59261	free	45.0	60	088.D-0502(A)
2011iv	2011-12-10 03:53:08	54.713468	-35.59261	free	22.5	60	088.D-0502(A)
2011iv	2011-12-10 03:55:01	54.713468	-35.59261	free	67.5	60	088.D-0502(A)
2011iv	2011-12-10 03:57:24	54.713468	-35.59261	free	0.0	65	088.D-0502(A)
2011iv	2011-12-10 03:59:22	54.713468	-35.59261	free	45.0	65	088.D-0502(A)
2011iv	2011-12-10 04:01:12	54.713468	-35.59261	free	22.5	65	088.D-0502(A)
2011iv	2011-12-10 04:03:11	54.713468	-35.59261	free	67.5	65	088.D-0502(A)
2011iv	2011-12-13 03:45:55	54.713852	-35.59244	free	45.0	70	088.D-0502(A)
2011iv	2011-12-13 03:47:50	54.713852	-35.59244	free	22.5	70	088.D-0502(A)
2011iv	2011-12-13 03:49:54	54.713852	-35.59244	free	67.5	70	088.D-0502(A)
2011iv	2011-12-13 03:52:35	54.713852	-35.59244	free	0.0	70	088.D-0502(A)
2011iv	2011-12-13 03:54:38	54.713852	-35.59244	free	45.0	70	088.D-0502(A)
2011iv	2011-12-13 03:56:33	54.713852	-35.59244	free	22.5	70	088.D-0502(A)

Table C.1.: continued.

SN name	Epoch (UT)	RA (deg)	DEC (deg)	Filter	HWP angle (deg)	Exposure (s)	ProgID
2011iv	2011-12-13 03:58:37	54.713852	-35.59244	free	67.5	70	088.D-0502(A)
2011iv	2011-12-13 04:01:05	54.713852	-35.59244	free	0.0	70	088.D-0502(A)
2011iv	2011-12-13 04:03:09	54.713852	-35.59244	free	45.0	70	088.D-0502(A)
2011iv	2011-12-13 04:05:04	54.713852	-35.59244	free	22.5	70	088.D-0502(A)
2011iv	2011-12-13 04:07:08	54.713852	-35.59244	free	67.5	70	088.D-0502(A)
2011iv	2011-12-13 04:09:48	54.713852	-35.59244	free	0.0	70	088.D-0502(A)
2011iv	2011-12-16 03:40:03	54.713799	-35.59241	free	0.0	65	088.D-0502(A)
2011iv	2011-12-16 03:42:01	54.713799	-35.59241	free	45.0	65	088.D-0502(A)
2011iv	2011-12-16 03:43:53	54.713799	-35.59241	free	22.5	65	088.D-0502(A)
2011iv	2011-12-16 03:45:52	54.713799	-35.59241	free	67.5	65	088.D-0502(A)
2011iv	2011-12-16 03:48:23	54.713799	-35.59241	free	0.0	72	088.D-0502(A)
2011iv	2011-12-16 03:50:29	54.713799	-35.59241	free	45.0	65	088.D-0502(A)
2011iv	2011-12-16 03:52:19	54.713799	-35.59241	free	22.5	72	088.D-0502(A)
2011iv	2011-12-16 03:54:24	54.713799	-35.59241	free	67.5	72	088.D-0502(A)
2011iv	2011-12-16 03:56:59	54.713799	-35.59241	free	0.0	70	088.D-0502(A)
2011iv	2011-12-16 03:59:02	54.713799	-35.59241	free	45.0	70	088.D-0502(A)
2011iv	2011-12-16 04:00:58	54.713799	-35.59241	free	22.5	70	088.D-0502(A)
2011iv	2011-12-16 04:03:01	54.713799	-35.59241	free	67.5	70	088.D-0502(A)
2011iv	2011-12-16 04:05:32	54.713799	-35.59241	free	0.0	65	088.D-0502(A)
2011iv	2011-12-16 04:07:30	54.713799	-35.59241	free	45.0	65	088.D-0502(A)
2011iv	2011-12-16 04:09:21	54.713799	-35.59241	free	22.5	65	088.D-0502(A)
2011iv	2011-12-16 04:11:19	54.713799	-35.59241	free	67.5	65	088.D-0502(A)
2011iv	2011-12-22 03:27:37	54.713288	-35.59268	free	0.0	150	088.D-0502(A)
2011iv	2011-12-22 03:31:01	54.713288	-35.59268	free	45.0	150	088.D-0502(A)
2011iv	2011-12-22 03:34:16	54.713288	-35.59268	free	22.5	150	088.D-0502(A)
2011iv	2011-12-22 03:37:40	54.713288	-35.59268	free	67.5	150	088.D-0502(A)
2011iv	2011-12-22 03:41:48	54.713288	-35.59268	free	0.0	120	088.D-0502(A)
2011iv	2011-12-22 03:44:41	54.713288	-35.59268	free	45.0	120	088.D-0502(A)
2011iv	2011-12-22 03:47:26	54.713288	-35.59268	free	22.5	120	088.D-0502(A)
2011iv	2011-12-22 03:50:21	54.713288	-35.59268	free	67.5	120	088.D-0502(A)
2011iv	2011-12-22 03:58:55	54.713288	-35.59268	free	0.0	150	088.D-0502(A)
2011iv	2011-12-22 04:02:19	54.713288	-35.59268	free	45.0	150	088.D-0502(A)
2011iv	2011-12-22 04:05:35	54.713288	-35.59268	free	22.5	150	088.D-0502(A)
2011iv	2011-12-22 04:08:58	54.713288	-35.59268	free	67.5	150	088.D-0502(A)
2011iv	2011-12-23 02:34:32	54.713376	-35.59241	free	0.0	160	088.D-0502(A)
2011iv	2011-12-23 02:38:05	54.713376	-35.59241	free	45.0	160	088.D-0502(A)
2011iv	2011-12-23 02:41:30	54.713376	-35.59241	free	22.5	160	088.D-0502(A)
2011iv	2011-12-23 02:45:03	54.713376	-35.59241	free	67.5	160	088.D-0502(A)
2011iv	2011-12-23 02:54:44	54.713376	-35.59241	free	0.0	220	088.D-0502(A)
2011iv	2011-12-23 02:59:17	54.713376	-35.59241	free	45.0	220	088.D-0502(A)
2011iv	2011-12-23 03:03:43	54.713376	-35.59241	free	22.5	220	088.D-0502(A)
2011iv	2011-12-23 03:08:16	54.713376	-35.59241	free	67.5	220	088.D-0502(A)
2011iv	2011-12-23 03:18:54	54.713376	-35.59241	free	0.0	180	088.D-0502(A)
2011iv	2011-12-23 03:22:48	54.713376	-35.59241	free	45.0	180	088.D-0502(A)
2011iv	2011-12-23 03:26:35	54.713376	-35.59241	free	22.5	180	088.D-0502(A)
2011iv	2011-12-23 03:30:29	54.713376	-35.59241	free	67.5	180	088.D-0502(A)

Table C.1.: continued.

SN name	Epoch (UT)	RA (deg)	DEC (deg)	Filter	HWP angle (deg)	Exposure (s)	ProgID
2011iv	2011-12-30 01:13:13	54.713782	-35.59245	free	0.0	160	088.D-0502(A)
2011iv	2011-12-30 01:16:47	54.713782	-35.59245	free	45.0	160	088.D-0502(A)
2011iv	2011-12-30 01:20:12	54.713782	-35.59245	free	22.5	160	088.D-0502(A)
2011iv	2011-12-30 01:23:46	54.713782	-35.59245	free	67.5	160	088.D-0502(A)
2011iv	2011-12-30 01:39:22	54.713782	-35.59245	free	0.0	110	088.D-0502(A)
2011iv	2011-12-30 01:42:05	54.713782	-35.59245	free	45.0	110	088.D-0502(A)
2011iv	2011-12-30 01:44:40	54.713782	-35.59245	free	22.5	110	088.D-0502(A)
2011iv	2011-12-30 01:47:24	54.713782	-35.59245	free	67.5	110	088.D-0502(A)
2011iv	2011-12-30 01:50:45	54.713782	-35.59245	free	0.0	120	088.D-0502(A)
2011iv	2011-12-30 01:53:40	54.713782	-35.59245	free	45.0	120	088.D-0502(A)
2011iv	2011-12-30 01:56:26	54.713782	-35.59245	free	22.5	120	088.D-0502(A)
2011iv	2011-12-30 01:59:20	54.713782	-35.59245	free	67.5	120	088.D-0502(A)
2012fr	2012-11-01 01:21:34	53.401119	-36.12653	GG435	0.0	170	290.D-5009(A)
2012fr	2012-11-01 01:25:10	53.401119	-36.12653	GG435	22.5	170	290.D-5009(A)
2012fr	2012-11-01 01:28:46	53.401119	-36.12653	GG435	45.0	170	290.D-5009(A)
2012fr	2012-11-01 01:32:22	53.401119	-36.12653	GG435	67.5	170	290.D-5009(A)
2012fr	2012-11-01 01:36:27	53.401119	-36.12653	GG435	0.0	170	290.D-5009(A)
2012fr	2012-11-01 01:40:02	53.401119	-36.12653	GG435	22.5	170	290.D-5009(A)
2012fr	2012-11-01 01:43:37	53.401119	-36.12653	GG435	45.0	170	290.D-5009(A)
2012fr	2012-11-01 01:47:13	53.401119	-36.12653	GG435	67.5	170	290.D-5009(A)
2012fr	2012-11-01 01:51:22	53.401119	-36.12653	GG435	0.0	170	290.D-5009(A)
2012fr	2012-11-01 01:54:57	53.401119	-36.12653	GG435	22.5	170	290.D-5009(A)
2012fr	2012-11-01 01:58:32	53.401119	-36.12653	GG435	45.0	170	290.D-5009(A)
2012fr	2012-11-01 02:02:08	53.401119	-36.12653	GG435	67.5	170	290.D-5009(A)
2012fr	2012-11-06 05:45:25	53.401033	-36.12657	GG435	0.0	100	290.D-5009(B)
2012fr	2012-11-06 05:47:51	53.401033	-36.12657	GG435	22.5	100	290.D-5009(B)
2012fr	2012-11-06 05:50:17	53.401033	-36.12657	GG435	45.0	100	290.D-5009(B)
2012fr	2012-11-06 05:52:42	53.401033	-36.12657	GG435	67.5	100	290.D-5009(B)
2012fr	2012-11-06 05:55:34	53.401033	-36.12657	GG435	0.0	100	290.D-5009(B)
2012fr	2012-11-06 05:58:00	53.401033	-36.12657	GG435	22.5	100	290.D-5009(B)
2012fr	2012-11-06 06:00:26	53.401033	-36.12657	GG435	45.0	100	290.D-5009(B)
2012fr	2012-11-06 06:02:52	53.401033	-36.12657	GG435	67.5	100	290.D-5009(B)
2012fr	2012-11-14 05:12:14	53.401081	-36.12656	GG435	0.0	100	290.D-5009(C)
2012fr	2012-11-14 05:14:39	53.401081	-36.12656	GG435	22.5	100	290.D-5009(C)
2012fr	2012-11-14 05:17:05	53.401081	-36.12656	GG435	45.0	100	290.D-5009(C)
2012fr	2012-11-14 05:19:31	53.401081	-36.12656	GG435	67.5	100	290.D-5009(C)
2012fr	2012-11-14 05:22:35	53.401081	-36.12656	GG435	0.0	80	290.D-5009(C)
2012fr	2012-11-14 05:24:41	53.401081	-36.12656	GG435	22.5	80	290.D-5009(C)
2012fr	2012-11-14 05:26:46	53.401081	-36.12656	GG435	45.0	80	290.D-5009(C)
2012fr	2012-11-14 05:28:52	53.401081	-36.12656	GG435	67.5	80	290.D-5009(C)
2012fr	2012-12-06 07:27:56	53.401104	-36.12651	GG435	0.0	125	290.D-5009(D)
2012fr	2012-12-06 07:30:47	53.401104	-36.12651	GG435	22.5	125	290.D-5009(D)
2012fr	2012-12-06 07:33:37	53.401104	-36.12651	GG435	45.0	125	290.D-5009(D)
2012fr	2012-12-06 07:36:27	53.401104	-36.12651	GG435	67.5	125	290.D-5009(D)

Table C.1.: continued.

SN name	Epoch (UT)	RA (deg)	DEC (deg)	Filter	HWP angle (deg)	Exposure (s)	ProgID
2012fr	2012-12-06 07:39:43	53.401104	-36.12651	GG435	0.0	125	290.D-5009(D)
2012fr	2012-12-06 07:42:34	53.401104	-36.12651	GG435	22.5	125	290.D-5009(D)
2012fr	2012-12-06 07:45:24	53.401104	-36.12651	GG435	45.0	125	290.D-5009(D)
2012fr	2012-12-06 07:48:14	53.401104	-36.12651	GG435	67.5	125	290.D-5009(D)
2012fr	2012-12-06 07:51:37	53.401104	-36.12651	GG435	0.0	125	290.D-5009(D)
2012fr	2012-12-06 07:54:27	53.401104	-36.12651	GG435	22.5	125	290.D-5009(D)
2012fr	2012-12-06 07:57:17	53.401104	-36.12651	GG435	45.0	125	290.D-5009(D)
2012fr	2012-12-06 08:00:08	53.401104	-36.12651	GG435	67.5	125	290.D-5009(D)
2012fr	2012-12-06 08:03:24	53.401104	-36.12651	GG435	0.0	125	290.D-5009(D)
2012fr	2012-12-06 08:06:14	53.401104	-36.12651	GG435	22.5	125	290.D-5009(D)
2012fr	2012-12-06 08:09:04	53.401104	-36.12651	GG435	45.0	125	290.D-5009(D)
2012fr	2012-12-06 08:11:55	53.401104	-36.12651	GG435	67.5	125	290.D-5009(D)
2015ak	2015-08-21 01:08:17	333.831432	-65.54816	GG435	0.0	1500	095.D-0848(A)
2015ak	2015-08-21 01:34:03	333.831432	-65.54816	GG435	22.5	1500	095.D-0848(A)
2015ak	2015-08-21 01:59:49	333.831432	-65.54816	GG435	45.0	1500	095.D-0848(A)
2015ak	2015-08-21 02:25:35	333.831432	-65.54816	GG435	67.5	1500	095.D-0848(A)
2015ak	2015-09-08 01:41:19	333.831573	-65.54818	GG435	0.0	500	095.D-0848(B)
2015ak	2015-09-08 01:50:25	333.831573	-65.54818	GG435	22.5	500	095.D-0848(B)
2015ak	2015-09-08 01:59:31	333.831573	-65.54818	GG435	45.0	500	095.D-0848(B)
2015ak	2015-09-08 02:08:37	333.831573	-65.54818	GG435	67.5	500	095.D-0848(B)
2015ak	2015-09-10 00:17:07	333.831521	-65.54815	GG435	0.0	500	095.D-0848(B)
2015ak	2015-09-10 00:26:13	333.831521	-65.54815	GG435	22.5	500	095.D-0848(B)
2015ak	2015-09-10 00:35:19	333.831521	-65.54815	GG435	45.0	500	095.D-0848(B)
2015ak	2015-09-10 00:44:25	333.831521	-65.54815	GG435	67.5	500	095.D-0848(B)
2015ak	2015-09-27 00:17:11	333.831609	-65.54816	GG435	0.0	1700	095.D-0848(B)
2015ak	2015-09-27 00:46:17	333.831609	-65.54816	GG435	22.5	1700	095.D-0848(B)
2015ak	2015-09-27 01:15:23	333.831609	-65.54816	GG435	45.0	1700	095.D-0848(B)
2015ak	2015-09-27 01:44:29	333.831609	-65.54816	GG435	67.5	1700	095.D-0848(B)

Table C.5.: Si II line polarization measured at different binnings

Name	Epoch	100Å binning P_{SiII} (%)	50Å binning P_{SiII} (%)	25Å binning P_{SiII} (%)
2001dm	6.3	0.24 ± 0.1	0.32 ± 0.21	0.42 ± 0.29
2001el	-4.2	0.15 ± 0.03	0.21 ± 0.05	0.23 ± 0.07
2001el	0.7	0.16 ± 0.03	0.22 ± 0.04	0.24 ± 0.06
2001el	8.7	0.09 ± 0.03	0.12 ± 0.04	0.11 ± 0.07
2001el	17.7	0.08 ± 0.03	0.12 ± 0.04	0.13 ± 0.06
2001el	39.6	0.03 ± 0.04	0.05 ± 0.06	0.09 ± 0.08
2001V	-10.4	0.12 ± 0.09	0.16 ± 0.14	0.21 ± 0.22
2001V	-6.4	0.14 ± 0.06	0.16 ± 0.09	0.17 ± 0.13
2001V	17.5	0.19 ± 0.06	0.28 ± 0.09	0.34 ± 0.13
2001V	30.6	0.15 ± 0.08	0.23 ± 0.11	0.35 ± 0.16
2002bo	-11.4	0.21 ± 0.08	0.19 ± 0.1	0.19 ± 0.14
2002bo	-7.4	0.47 ± 0.04	0.54 ± 0.07	0.6 ± 0.09

Table C.5.: continued.

Name	Epoch	100Å binning P_{SiII} (%)	50Å binning P_{SiII} (%)	25Å binning P_{SiII} (%)
2002bo	-6.4	0.47 ± 0.06	0.61 ± 0.09	0.65 ± 0.12
2002bo	-4.5	0.42 ± 0.03	0.67 ± 0.05	0.68 ± 0.07
2002bo	-1.4	0.28 ± 0.04	0.6 ± 0.09	0.63 ± 0.12
2002bo	9.6	0.38 ± 0.05	0.46 ± 0.08	0.49 ± 0.12
2002bo	12.6	0.27 ± 0.06	0.33 ± 0.1	0.32 ± 0.14
2002el	-8.6	0.23 ± 0.2	0.29 ± 0.28	0.39 ± 0.39
2002el	-7.6	0.37 ± 0.12	0.57 ± 0.19	0.53 ± 0.29
2002fk	0.4	0.11 ± 0.04	0.19 ± 0.06	0.19 ± 0.08
2002fk	4.4	0.15 ± 0.04	0.43 ± 0.06	0.47 ± 0.08
2002fk	13.4	0.06 ± 0.05	0.13 ± 0.09	0.16 ± 0.12
2003eh	0.0	0.78 ± 0.27	0.96 ± 0.28	1.74 ± 0.74
2003eh	12.0	0.8 ± 0.2	1.55 ± 0.33	2.15 ± 0.51
2003hv	6.1	0.06 ± 0.04	0.1 ± 0.06	0.1 ± 0.08
2003hx	4.8	0.2 ± 0.06	0.45 ± 0.11	0.53 ± 0.17
2003hx	16.8	0.24 ± 0.08	0.32 ± 0.12	0.46 ± 0.17
2003hx	18.8	0.33 ± 0.14	0.66 ± 0.2	0.75 ± 0.28
2003W	-8.7	0.71 ± 0.13	0.82 ± 0.2	0.93 ± 0.28
2003W	-6.7	0.4 ± 0.11	0.54 ± 0.16	0.53 ± 0.22
2003W	16.1	0.91 ± 0.14	1.26 ± 0.22	1.33 ± 0.32
2004br	-3.9	0.09 ± 0.11	0.19 ± 0.17	0.13 ± 0.2
2004dt	-9.7	1.34 ± 0.14	1.67 ± 0.19	1.68 ± 0.28
2004dt	4.4	1.37 ± 0.22	2.42 ± 0.36	3.01 ± 0.51
2004dt	5.2	1.3 ± 0.11	1.81 ± 0.18	1.99 ± 0.26
2004dt	10.3	0.64 ± 0.07	1.09 ± 0.16	1.34 ± 0.24
2004dt	33.2	0.58 ± 0.18	0.71 ± 0.26	0.65 ± 0.36
2004ef	-5.3	0.32 ± 0.25	0.83 ± 0.4	1.04 ± 0.49
2004eo	-10.3	0.3 ± 0.1	0.32 ± 0.14	0.37 ± 0.18
2005cf	-11.9	0.16 ± 0.08	0.25 ± 0.11	0.28 ± 0.15
2005cf	-5.8	0.16 ± 0.03	0.21 ± 0.05	0.25 ± 0.08
2005de	-10.9	0.34 ± 0.14	0.39 ± 0.21	0.38 ± 0.29
2005de	-4.9	0.12 ± 0.09	0.12 ± 0.09	0.14 ± 0.13
2005df	-10.8	0.22 ± 0.04	0.3 ± 0.07	0.33 ± 0.1
2005df	-8.8	0.29 ± 0.06	0.41 ± 0.08	0.4 ± 0.11
2005df	-7.8	0.22 ± 0.04	0.26 ± 0.06	0.28 ± 0.09
2005df	-6.8	0.26 ± 0.05	0.37 ± 0.08	0.4 ± 0.1
2005df	-2.8	0.31 ± 0.03	0.37 ± 0.05	0.39 ± 0.07
2005df	0.2	0.29 ± 0.04	0.51 ± 0.06	0.54 ± 0.09
2005df	4.2	0.29 ± 0.04	0.54 ± 0.06	0.54 ± 0.09
2005df	5.2	0.29 ± 0.03	0.45 ± 0.05	0.46 ± 0.07
2005df	8.2	0.24 ± 0.05	0.36 ± 0.08	0.36 ± 0.11
2005df	9.1	0.19 ± 0.03	0.3 ± 0.06	0.35 ± 0.08
2005df	29.2	0.09 ± 0.04	0.13 ± 0.06	0.13 ± 0.08
2005df	42.1	0.03 ± 0.03	0.04 ± 0.05	0.06 ± 0.07
2005el	-2.7	0.47 ± 0.16	0.63 ± 0.24	0.86 ± 0.35
2005hk	-2.3	-0.0 ± 0.09	0.19 ± 0.13	0.26 ± 0.19
2005hk	11.7	0.07 ± 0.07	0.07 ± 0.1	0.11 ± 0.16
2005ke	-9.1	0.16 ± 0.12	0.41 ± 0.19	0.54 ± 0.28
2005ke	-8.1	0.09 ± 0.06	0.12 ± 0.09	0.11 ± 0.13
2005ke	75.9	0.43 ± 0.29	0.8 ± 0.4	0.91 ± 0.5

Table C.5.: continued.

Name	Epoch	100Å binning P_{SiII} (%)	50Å binning P_{SiII} (%)	25Å binning P_{SiII} (%)
2006X	-10.9	0.19 ± 0.13	0.22 ± 0.14	0.2 ± 0.19
2006X	-9.0	0.32 ± 0.08	0.5 ± 0.12	0.68 ± 0.19
2006X	-8.1	0.24 ± 0.05	0.32 ± 0.08	0.33 ± 0.12
2006X	-7.1	0.5 ± 0.07	0.85 ± 0.13	1.02 ± 0.19
2006X	-4.0	0.61 ± 0.06	0.81 ± 0.08	0.85 ± 0.12
2006X	-3.0	0.63 ± 0.05	0.85 ± 0.07	0.85 ± 0.09
2006X	-1.9	0.57 ± 0.07	0.7 ± 0.1	0.7 ± 0.14
2006X	37.9	0.06 ± 0.05	0.05 ± 0.07	0.07 ± 0.09
2006X	38.9	0.07 ± 0.04	0.13 ± 0.07	0.14 ± 0.1
2007fb	3.0	0.24 ± 0.05	0.33 ± 0.09	0.35 ± 0.12
2007fb	6.0	0.58 ± 0.15	0.8 ± 0.21	0.85 ± 0.3
2007fb	6.9	0.21 ± 0.04	0.3 ± 0.07	0.3 ± 0.08
2007fb	9.9	0.21 ± 0.07	0.34 ± 0.1	0.34 ± 0.13
2007hj	-1.1	0.59 ± 0.06	0.77 ± 0.1	0.77 ± 0.15
2007hj	4.9	0.32 ± 0.05	0.37 ± 0.09	0.45 ± 0.11
2007hj	10.9	0.09 ± 0.05	0.09 ± 0.1	0.15 ± 0.14
2007if	13.1	0.13 ± 0.08	0.12 ± 0.13	0.2 ± 0.18
2007if	20.1	0.17 ± 0.08	0.29 ± 0.11	0.34 ± 0.15
2007if	45.0	0.06 ± 0.12	0.16 ± 0.17	0.13 ± 0.24
2007if	46.0	0.43 ± 0.18	0.75 ± 0.26	0.76 ± 0.43
2007le	-10.3	0.28 ± 0.03	0.28 ± 0.04	0.3 ± 0.08
2007le	-5.1	0.45 ± 0.04	0.53 ± 0.06	0.56 ± 0.09
2007le	40.7	0.08 ± 0.05	0.09 ± 0.07	0.07 ± 0.09
2008ff	31.0	0.09 ± 0.07	0.18 ± 0.14	0.23 ± 0.2
2008fl	2.2	0.12 ± 0.06	0.13 ± 0.17	0.2 ± 0.26
2008fl	8.3	0.2 ± 0.12	0.34 ± 0.2	0.3 ± 0.32
2008fl	9.2	0.11 ± 0.06	0.28 ± 0.1	0.3 ± 0.14
2008fl	11.3	0.15 ± 0.07	0.23 ± 0.11	0.27 ± 0.16
2008fl	15.3	0.15 ± 0.09	0.27 ± 0.11	0.29 ± 0.18
2008fp	-5.6	0.15 ± 0.03	0.21 ± 0.04	0.23 ± 0.06
2008fp	-0.5	0.22 ± 0.03	0.24 ± 0.04	0.24 ± 0.06
2008fp	1.4	0.24 ± 0.03	0.31 ± 0.05	0.34 ± 0.06
2008fp	5.4	0.2 ± 0.03	0.21 ± 0.04	0.2 ± 0.05
2010ev	-1.1	0.45 ± 0.06	0.53 ± 0.11	0.56 ± 0.14
2010ev	2.9	0.24 ± 0.06	0.25 ± 0.1	0.3 ± 0.11
2010ev	11.9	0.37 ± 0.05	0.51 ± 0.07	0.54 ± 0.12
2010ko	-7.1	0.34 ± 0.15	0.29 ± 0.2	0.36 ± 0.3
2010ko	-6.0	0.57 ± 0.05	0.69 ± 0.08	0.68 ± 0.12
2010ko	-2.0	0.26 ± 0.04	0.32 ± 0.08	0.36 ± 0.11
2010ko	-1.2	0.23 ± 0.04	0.34 ± 0.06	0.36 ± 0.09
2010ko	1.9	0.22 ± 0.06	0.37 ± 0.11	0.34 ± 0.16
2010ko	3.9	0.18 ± 0.03	0.25 ± 0.06	0.25 ± 0.08
2010ko	10.9	0.25 ± 0.04	0.3 ± 0.07	0.29 ± 0.1
2010ko	15.9	0.17 ± 0.03	0.21 ± 0.04	0.24 ± 0.05
2010ko	50.9	0.36 ± 0.15	0.58 ± 0.21	0.65 ± 0.3
2010ko	51.8	0.16 ± 0.17	0.4 ± 0.26	0.32 ± 0.41
2010ko	57.8	0.14 ± 0.1	0.2 ± 0.15	0.24 ± 0.22
2010ko	58.8	0.13 ± 0.12	0.24 ± 0.17	0.28 ± 0.24
2010ko	59.8	0.43 ± 0.13	0.48 ± 0.2	0.46 ± 0.27

Table C.5.: continued.

Name	Epoch	100Å binning P_{SiII} (%)	50Å binning P_{SiII} (%)	25Å binning P_{SiII} (%)
2011ae	4.0	0.24 ± 0.03	0.36 ± 0.04	0.38 ± 0.06
2011ae	16.0	0.2 ± 0.02	0.27 ± 0.04	0.58 ± 0.05
2011iv	-0.4	0.04 ± 0.02	0.13 ± 0.03	0.13 ± 0.05
2011iv	-0.4	0.11 ± 0.02	0.13 ± 0.03	0.13 ± 0.05
2011iv	2.6	0.02 ± 0.02	0.08 ± 0.04	0.17 ± 0.06
2011iv	2.6	0.06 ± 0.02	0.08 ± 0.04	0.17 ± 0.06
2011iv	5.6	0.04 ± 0.02	0.08 ± 0.02	0.1 ± 0.03
2011iv	5.6	0.07 ± 0.02	0.08 ± 0.02	0.1 ± 0.03
2011iv	11.5	0.07 ± 0.02	0.11 ± 0.03	0.12 ± 0.04
2011iv	11.5	0.11 ± 0.02	0.11 ± 0.03	0.12 ± 0.04
2011iv	12.5	0.02 ± 0.02	0.06 ± 0.03	0.07 ± 0.04
2011iv	12.5	0.05 ± 0.02	0.06 ± 0.03	0.07 ± 0.04
2011iv	19.5	-0.0 ± 0.02	0.07 ± 0.04	0.05 ± 0.06
2011iv	19.5	0.04 ± 0.03	0.07 ± 0.04	0.05 ± 0.06
2012fr	-12.1	0.09 ± 0.02	0.11 ± 0.03	0.11 ± 0.04
2012fr	-6.9	0.16 ± 0.02	0.25 ± 0.04	0.25 ± 0.05
2012fr	1.0	0.18 ± 0.03	0.38 ± 0.04	0.42 ± 0.06
2012fr	23.1	0.06 ± 0.02	0.09 ± 0.03	0.12 ± 0.04
2015ak	-13.1	0.12 ± 0.06	0.15 ± 0.08	0.2 ± 0.11
2015ak	4.9	0.34 ± 0.06	0.43 ± 0.08	0.49 ± 0.13
2015ak	6.9	0.22 ± 0.07	0.38 ± 0.1	0.38 ± 0.15
2015ak	23.9	0.25 ± 0.06	0.28 ± 0.08	0.35 ± 0.12

Table C.2.: SN Ia light curves from the Open Supernova Catalog

Name	No. of epochs per pass-band	References
SN 2001V	69 V, 60 B	1, 2, 3, 4
SN 2002el	22 B, 25 V	5, 4
SN 2003W	45 B, 41 V	5, 4, 6
SN 2004br	18 B, 19 V	5, 4
SN 2004dt	85 B, 86 V, 45 g, 44 i, 45 r, 44 u	5, 4, 7
SN 2005cf	86 V, 83 B, 17 H, 17 J	1, 3, 4, 8, 9
SN 2005de	37 B, 39 V	5, 4
SN 2005df	12 B, 10 H, 10 J, 13 V, 10 Y	10, 8
SN 2005hk	70 V, 65 B, 25 H, 25 J	1, 8, 11, 9
SN 2005ke	100 V, 91 B, 39 g, 39 i, 39 r, 36 u, 62 H, 65 J, 30 Y	12, 6, 7, 9
SN 2007fb	28 B, 29 V, 2 H, 2 J	13, 9
SN 2007hj	56 B, 62 V	5, 4, 14
SN 2007sr	95 B, 81 V, 32 H, 30 J	1, 3, 4, 8, 9
SN 2010ev	13 B, 13 V	12
SN 2010ko	14 V, 14 B	12
SN 2011ae	32 H, 32 J	15
SN 2012fr	104 B, 118 V	12, 16
SN 2015ak	13 V, 13 B	17

References. 1: Hicken et al. (2009a); 2: Vinkó et al. (2003); 3: Silverman et al. (2012); 4: Ganeshalingam et al. (2010); 5: Silverman et al. (2012); 6: Hicken et al. (2009a); 7: Contreras et al. (2010); 8: Brown et al. (2014); 9: Friedman et al. (2015); 10: Krisciunas et al. (2017b); 11: Sahu et al. (2008); 12: Brown et al. (2014); 13: Hicken et al. (2012); 14: Hicken et al. (2012); 15: Friedman et al. (2015); 16: Zhang et al. (2014); 17: Brown et al. (2014)

Table C.3.: SN Ia spectra from the Open Supernova Catalog

Name	Epochs	References
SN 2001dm	16.0	1
SN 2001el	-4.5, 0.5, 8.5, 17.5, 29.1, 37.1, 39.5	2, 3, 4, 5
SN 2001V	-13.6, -13.2, -12.6, -12.3, -11.6, -11.2, -10.6, -10.1, -9.6, -9.2, -7.6, -7.3, -6.6, -6.3, -5.6, -5.2, -3.6, -3.1, 9.4, 9.9, 10.4, 10.9, 11.4, 11.7, 12.4, 12.9, 13.4, 13.9, 16.4, 18.4, 18.7, 19.4, 19.6, 20.4, 20.6, 20.8, 21.4, 21.7, 21.9, 22.4, 22.7, 23.4, 23.7, 24.4, 24.7, 25.4, 27.4, 27.6, 28.4, 28.6	6, 7, 5
SN 2002el	11.2, 21.2, 39.2	1
SN 2002fk	-3.4, -1.5, 2.6, 4.5, 6.6, 7.1, 7.5, 8.5, 9.5, 30.4, 33.5, 37.4, 39.1	8, 9, 5
SN 2003eh	-1.8, -0.9, 0.2, 3.2, 5.2, 9.2	8, 9
SN 2003hv	0.8, 5.8, 8.8, 16.8, 19.4, 23.3	10, 11, 12, 5
SN 2003hx	22.0	1
SN 2003W	-11.6, -10.7, -9.6, -8.6, -7.7, -6.6, -6.0, -5.7, -3.7, -2.6, -0.6, 0.4, 18.0, 21.4, 25.3, 28.3, 30.3	8, 9, 5
SN 2004br	4.4, 21.3, 28.1	1
SN 2004dt	-11.0, -10.0, -8.0, -7.0, -6.6, -5.0, -4.0, -3.0, -2.0, 1.0, 2.0, 3.0, 9.0, 13.0, 16.0, 16.5, 18.4, 19.4, 20.0, 22.2, 23.5, 27.3, 28.2, 32.4, 36.0, 39.0	13, 12, 3, 5, 14, 7, 9, 15
SN 2004ef	-9.2, -9.1, -8.2, -8.0, -7.2, -7.1, -6.2, -6.1, -5.1, -4.1, -2.3, -2.2, -1.1, -0.1, 0.9, 1.9, 2.7, 3.7, 5.8, 7.9, 19.8, 25.7, 27.0, 31.6, 33.8, 37.7	16, 7, 9, 5
SN 2004eo	-11.4, -10.4, -6.4, -6.2, -3.4, 1.6, 6.6, 10.6, 12.6, 12.9, 13.6, 20.6, 21.6, 23.6, 24.6, 29.6	17, 3, 15, 5
SN 2005cf	-12.9, -12.7, -11.9, -11.7, -11.5, -10.9, -10.7, -9.9, -9.6, -8.9, -7.9, -6.9, -5.9, -5.7, -4.9, -4.7, -3.9, -3.7, -2.9, -2.6, -1.9, -1.7, -1.6, -0.9, -0.6, 0.1, 0.4, 1.1, 1.4, 2.1, 2.3, 3.1, 3.3, 4.1, 4.3, 5.1, 6.1, 8.1, 9.1, 11.1, 13.1, 14.1, 15.1, 16.1, 16.4, 18.1, 18.3, 21.3, 23.1, 23.3, 24.1, 24.2, 25.1, 25.3, 26.1, 26.3, 27.1, 27.3, 28.1, 28.3, 29.1, 29.2, 31.1, 36.1	18, 3, 19, 7, 9, 20, 12, 5, 21
SN 2005de	-10.9, -1.6, 9.4, 25.3	22, 12, 5
SN 2005df	-6.2, -3.2, -0.2, 3.8	12
SN 2005el	-7.7, -7.5, -6.7, -6.5, -5.5, -4.5, 0.5, 1.4, 1.5, 3.5, 7.5, 14.3, 14.4, 22.5, 29.4	16, 5, 7, 9
SN 2005hk	-10.2, -9.4, -9.2, -8.4, -8.2, -7.4, -7.2, -6.4, -6.2, -5.4, -5.2, -5.1, -4.4, -4.2, -3.2, -2.2, 2.6, 11.6, 13.6, 13.8, 19.8, 21.4, 22.6, 22.7, 22.9, 25.6, 26.7, 36.6, 38.6	8, 9, 24, 3, 5, 25
SN 2005ke	-1.9, -0.9, -0.1, 0.0, 0.1, 2.1, 6.1, 7.1, 8.1, 9.2, 10.1, 11.1, 12.9, 13.1, 14.2, 23.1, 26.0, 26.1, 28.0, 29.1, 31.0	16, 7, 9, 5
SN 2006X	-11.3, -8.3, -7.3, -7.0, -6.9, -1.3, 0.7, 1.1, 2.1, 2.7, 4.1, 4.7, 5.1, 6.0, 6.7, 7.0, 7.1, 8.0, 10.2, 10.7, 11.1, 11.7, 12.2, 13.0, 13.2, 14.1, 14.7, 15.7, 16.1, 17.0, 23.0, 23.1, 26.7, 28.7, 29.0, 30.1, 30.9, 31.1, 31.7, 31.9, 32.0, 33.2, 34.0, 38.0, 38.7, 39.1, 39.7	26, 3, 15, 27, 7, 9, 5
SN 2007fb	0.0, 0.1, 4.0, 9.0, 11.1, 12.1, 13.0, 31.1, 38.1	8, 9, 5
SN 2007hj	-4.0, -2.9, -2.0, -1.9, 0.1, 1.1, 2.1, 3.1, 5.0, 5.1, 6.1, 7.0, 11.0, 11.1, 12.0, 13.0, 25.9, 32.0, 36.0, 38.1	8, 9, 5, 15
SN 2007if	-4.6, 10.4, 11.2, 11.3, 12.2, 12.4, 13.3, 15.4, 20.3, 20.4, 22.4, 30.3, 32.4, 35.4	28, 29, 7, 9
SN 2007le	-11.0, -10.1, -9.0, -8.1, -7.1, -5.2, 1.8, 2.8, 2.9, 3.8, 3.9, 4.9, 6.8, 6.9, 7.9, 9.0, 9.8, 9.9, 10.8, 11.9, 12.9, 13.9, 14.9, 15.8, 15.9, 16.9, 17.8, 18.9, 19.9, 20.8, 21.8, 22.9, 23.8, 34.8, 35.8, 37.8, 38.8, 39.8	8, 9, 5, 30, 15
SN 2007sr	13.5, 15.7, 16.7, 17.7, 18.7, 20.5, 20.7, 22.5, 28.7, 32.8, 34.5, 34.6	16, 7, 9, 5
SN 2008fp	-4.9, -4.6, -0.5, 0.5, 6.5, 22.5, 28.4, 35.5	31, 15
SN 2009ip	-41.6, -14.6, -13.6, -11.6, -10.6, -9.6, -8.6, -7.6, -6.6, -5.6, -4.6, -3.6, -2.6, -1.6, -0.6, 1.4, 2.4, 3.4, 4.4, 5.4, 6.4, 7.4, 8.4, 9.4, 10.4, 13.4, 14.4, 15.4, 16.4, 17.4, 18.4, 19.4, 20.4, 22.4, 23.4, 24.4, 26.4, 28.4, 29.4, 30.4, 31.4, 32.4, 34.4, 36.4, 37.4, 38.4, 39.4	32, 12, 33, 34, 35
SN 2010ev	-3.1, 2.9	12
SN 2011iv	0.4	36, 12
SN 2012fr	-16.2, -15.2, -14.2, -13.2, -12.2, -11.2, -10.2, -9.2, -8.2, -7.2, -6.2, -5.2, -4.2, -3.2, -2.2, -1.2, -0.2, 0.8, 1.8, 2.8, 3.8, 4.8, 5.8, 6.8, 7.8, 8.8, 9.8, 10.8, 14.8, 15.8, 16.8, 20.8, 21.8, 24.8, 27.8, 28.8, 31.8, 32.8, 33.8, 34.8, 37.8, 38.8	37, 12, 38

References. 1: Silverman et al. (2012); 2: Wang et al. (2003); 3: Richardson et al. (2001); 4: Foley et al. (2008); 5: Silverman et al. (2012); 6: Matheson et al. (2008); 7: Blondin et al. (2012); 8: Blondin et al. (2012); 9: Matheson et al. (2008); 10: Richardson et al. (2001); 11: Leloudas et al. (2009); 12: Yaron & Gal-Yam (2012); 13: Altavilla et al. (2007); 14: Leonard et al. (2005); 15: Folatelli et al. (2013); 16: Folatelli et al. (2013); 17: Pastorello et al. (2007); 18: Garavini et al. (2007); 19: Wang et al. (2009); 20: Gall et al. (2012); 21: Bufano et al. (2009); 22: Harutyunyan et al. (2008); 24: Phillips et al. (2007); 25: Chornock et al. (2006); 26: Yamanaka et al. (2009); 27: Wang et al. (2008b); 28: Scalzo et al. (2010); 29: Aldering et al. (2002); 30: Simon et al. (2009); 31: Yaron & Gal-Yam (2012); 32: Margutti et al. (2014); 33: Graham et al. (2014); 34: Fraser et al. (2013); 35: Childress et al. (2016); 36: Foley et al. (2012a); 37: Childress et al. (2013); 38: Zhang et al. (2014)

Table C.4.: Si II λ6355Å blueshift velocity at -5 days relative to peak brightness.

Name	v (km s^{-1})
SN 2001dm	9497 ± 500[a]
SN 2001el	9746 ± 109
SN 2001V	11388 ± 39
SN 2002bo	13586 ± 66
SN 2002el	10612 ± 187
SN 2002fk	10080 ± 97
SN 2003eh	10069 ± 452
SN 2003hv	10900 ± 139
SN 2003hx	12030 ± 134
SN 2003W	16412 ± 781
SN 2004br	8969 ± 500[a]
SN 2004dt	14874 ± 138
SN 2004ef	12031 ± 152
SN 2004eo	10908 ± 285
SN 2005cf	10556 ± 64
SN 2005de	10752 ± 71
SN 2005df	9819 ± 58
SN 2005el	10907 ± 193
SN 2005hk	6695 ± 351
SN 2005ke	11094 ± 234
SN 2006X	17041 ± 90
SN 2007fb	11651 ± 85
SN 2007hj	12075 ± 67
SN 2007if	10704 ± 1243
SN 2007le	12550 ± 52
SN 2008ff	...
SN 2008fl	11674 ± 461
SN 2008fp	11313 ± 24
SN 2010ev	14500 ± 69
SN 2010ko	10835 ± 102
SN 2011ae	10978 ± 500[a]
SN 2011iv	10665 ± 76
SN 2012fr	12091 ± 64
SN 2015ak	13310 ± 259

[a] There are only two observations available. We estimate the error to 500 km s^{-1}. For SN 2008ff, we have only one velocity measurement.

C.2. Polarization of Si II λ6355Å line figures

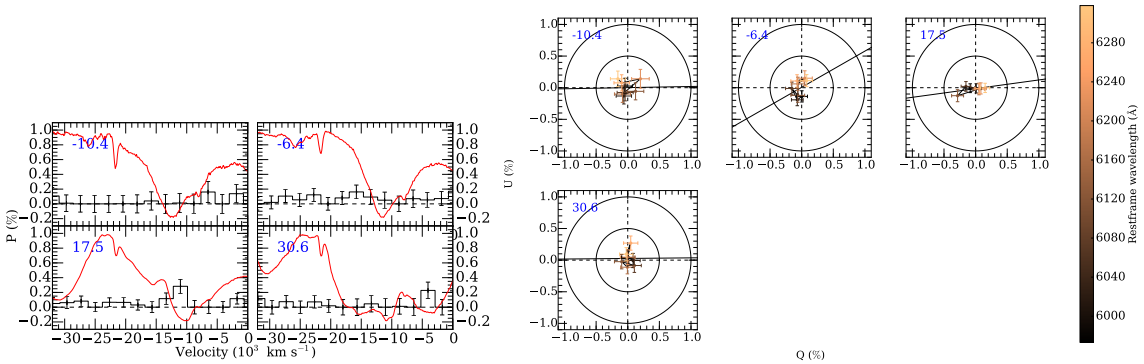

Figure C.1.: SN 2001V. *Left:* Polarization of the Si II λ6355Å line at different epochs relative to peak brightness (black bins). The flux spectrum is shown in red. *Right:* Polarization in the Q–U plane. The color indicates the wavelength.

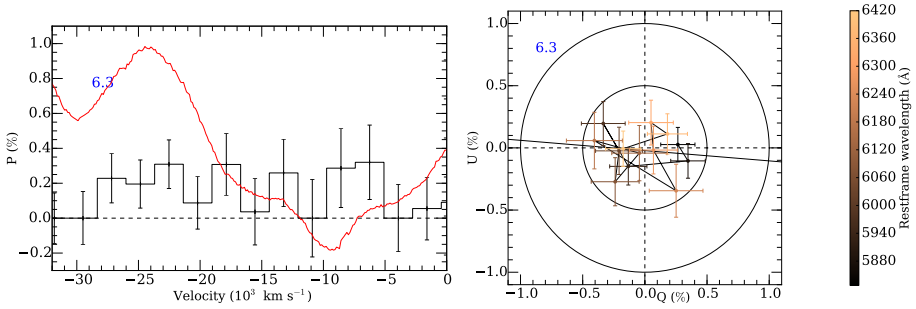

Figure C.2.: SN 2001dm. *Left:* Polarization of the Si II λ6355Å line at different epochs relative to peak brightness (black bins). The flux spectrum is shown in red. *Right:* Polarization in the Q–U plane. The color indicates the wavelength.

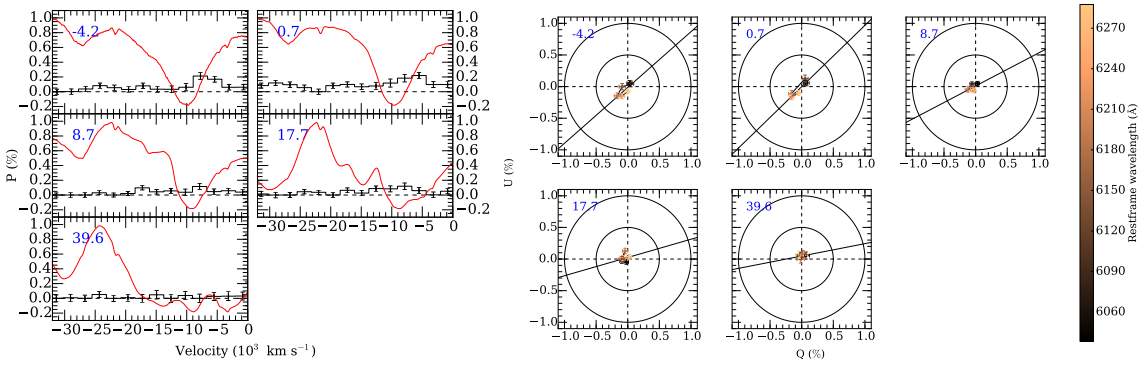

Figure C.3.: SN 2001el. *Left:* Polarization of the Si II λ6355Å line at different epochs relative to peak brightness (black bins). The flux spectrum is shown in red. *Right:* Polarization in the Q–U plane. The color indicates the wavelength.

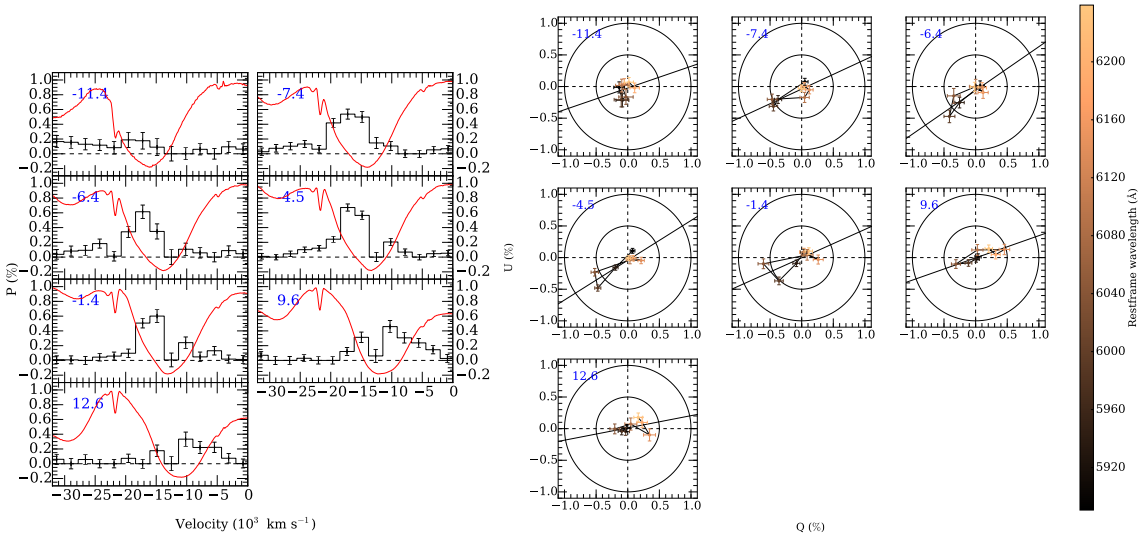

Figure C.4.: SN 2002bo. *Left:* Polarization of the Si II λ6355Å line at different epochs relative to peak brightness (black bins). The flux spectrum is shown in red. *Right:* Polarization in the Q–U plane. The color indicates the wavelength.

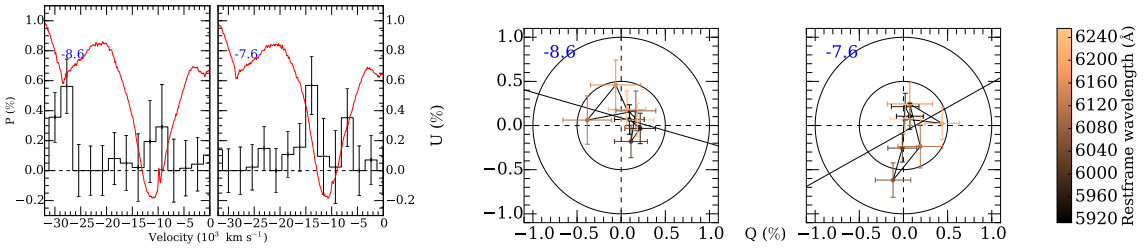

Figure C.5.: SN 2002el. *Left:* Polarization of the Si II λ6355Å line at different epochs relative to peak brightness (black bins). The flux spectrum is shown in red. *Right:* Polarization in the Q–U plane. The color indicates the wavelength.

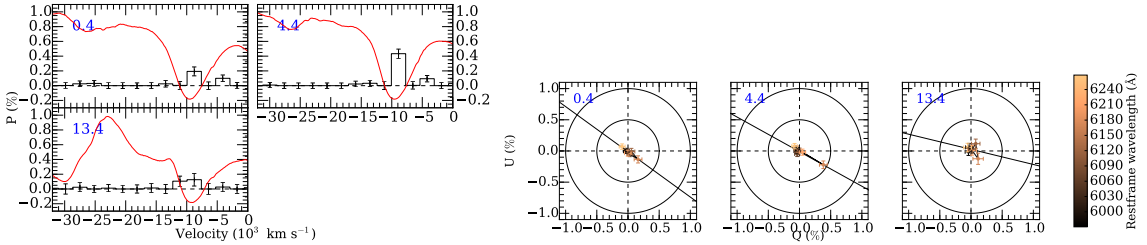

Figure C.6.: SN 2002fk. *Left:* Polarization of the Si II λ6355Å line at different epochs relative to peak brightness (black bins). The flux spectrum is shown in red. *Right:* Polarization in the Q–U plane. The color indicates the wavelength.

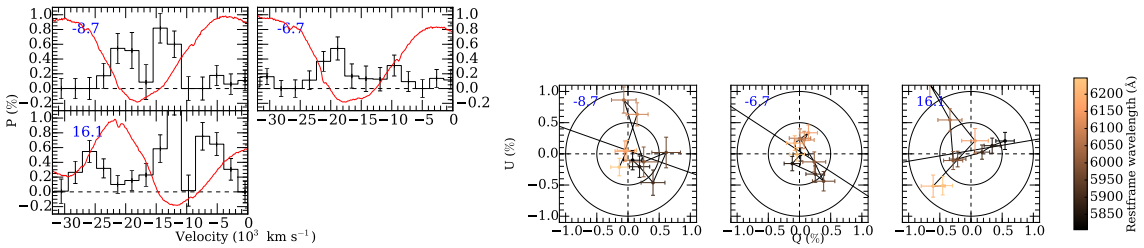

Figure C.7.: SN 2003W. *Left:* Polarization of the Si II λ6355Å line at different epochs relative to peak brightness (black bins). The flux spectrum is shown in red. *Right:* Polarization in the Q–U plane. The color indicates the wavelength.

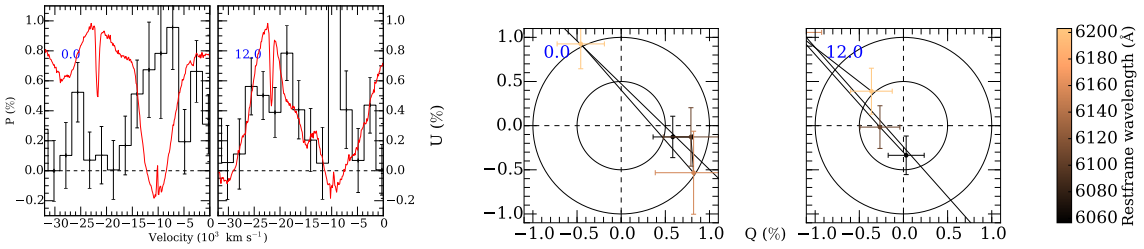

Figure C.8.: SN 2003eh. *Left:* Polarization of the Si II λ6355Å line at different epochs relative to peak brightness (black bins). The flux spectrum is shown in red. *Right:* Polarization in the Q–U plane. The color indicates the wavelength.

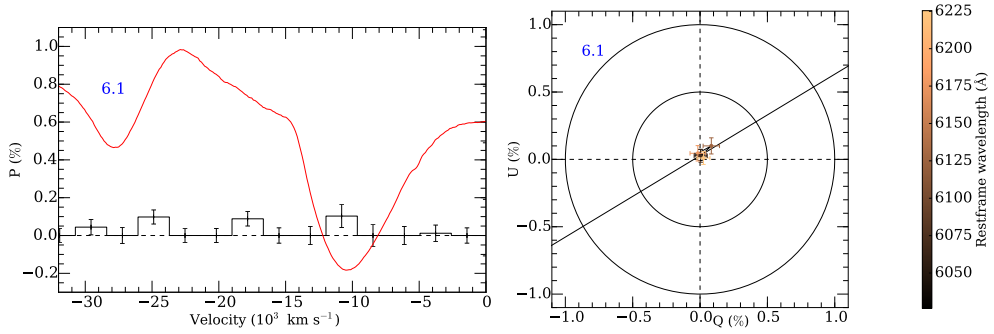

Figure C.9.: SN 2003hv. *Left:* Polarization of the Si II λ6355Å line at different epochs relative to peak brightness (black bins). The flux spectrum is shown in red. *Right:* Polarization in the Q–U plane. The color indicates the wavelength.

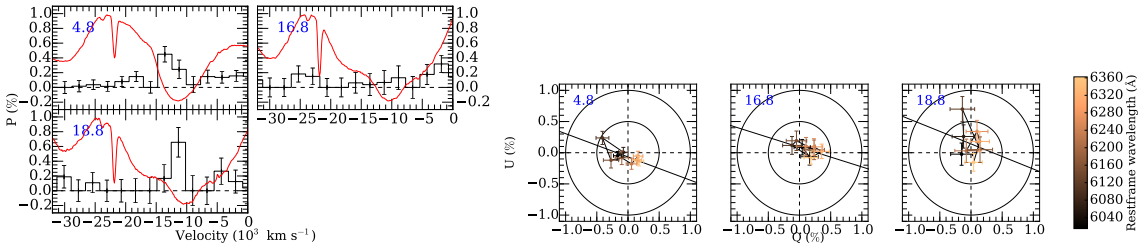

Figure C.10.: SN 2003hx. *Left:* Polarization of the Si II λ6355Å line at different epochs relative to peak brightness (black bins). The flux spectrum is shown in red. *Right:* Polarization in the Q–U plane. The color indicates the wavelength.

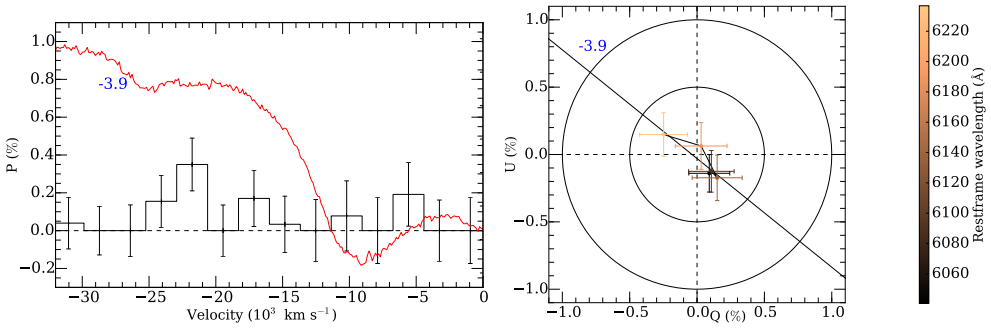

Figure C.11.: SN 2004br. *Left:* Polarization of the Si II λ6355Å line at different epochs relative to peak brightness (black bins). The flux spectrum is shown in red. *Right:* Polarization in the Q–U plane. The color indicates the wavelength.

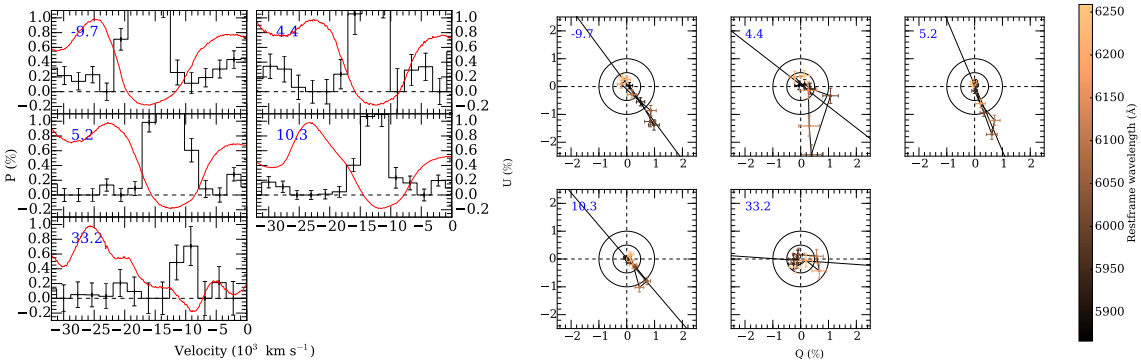

Figure C.12.: SN 2004dt. *Left:* Polarization of the Si II λ6355Å line at different epochs relative to peak brightness (black bins). The flux spectrum is shown in red. *Right:* Polarization in the Q–U plane. The color indicates the wavelength.

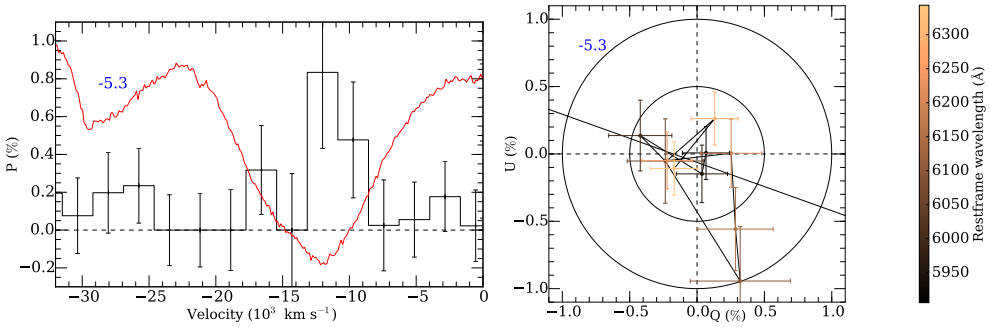

Figure C.13.: SN 2004ef. *Left:* Polarization of the Si II λ6355Å line at different epochs relative to peak brightness (black bins). The flux spectrum is shown in red. *Right:* Polarization in the Q–U plane. The color indicates the wavelength.

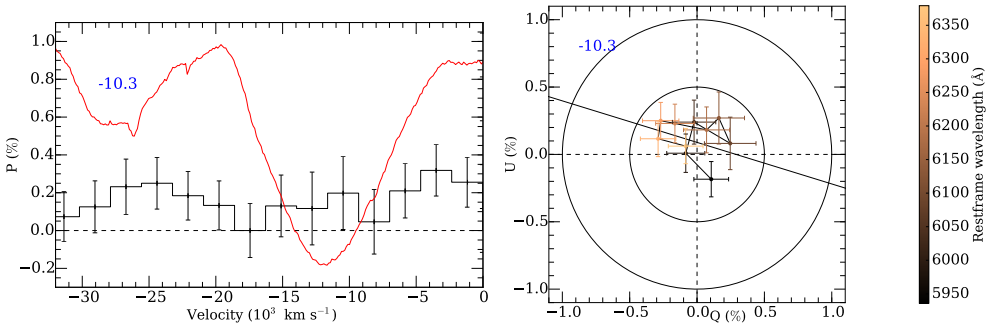

Figure C.14.: SN 2004eo. *Left:* Polarization of the Si II λ6355Å line at different epochs relative to peak brightness (black bins). The flux spectrum is shown in red. *Right:* Polarization in the Q–U plane. The color indicates the wavelength.

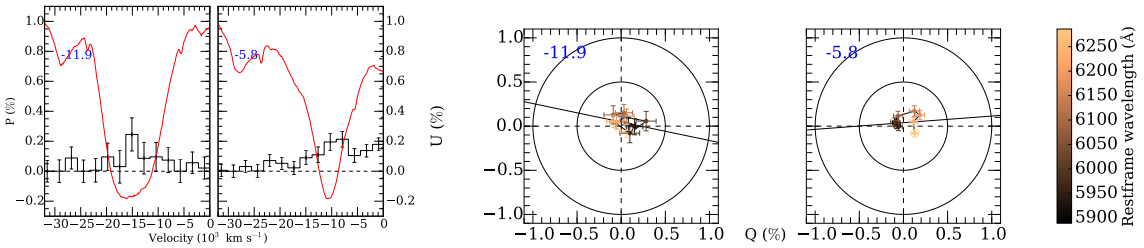

Figure C.15.: SN 2005cf. *Left:* Polarization of the Si II λ6355Å line at different epochs relative to peak brightness (black bins). The flux spectrum is shown in red. *Right:* Polarization in the Q–U plane. The color indicates the wavelength.

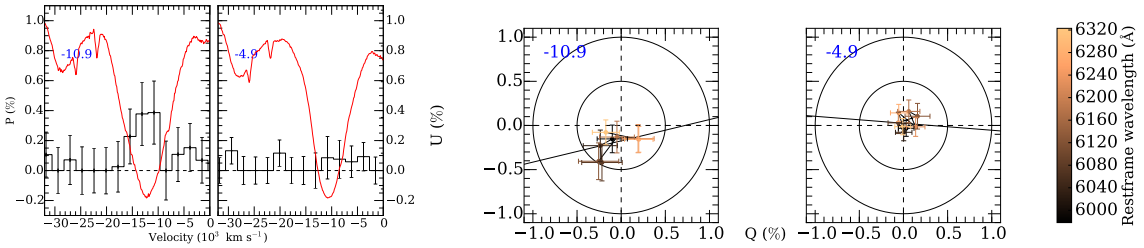

Figure C.16.: SN 2005de. *Left:* Polarization of the Si II λ6355Å line at different epochs relative to peak brightness (black bins). The flux spectrum is shown in red. *Right:* Polarization in the Q–U plane. The color indicates the wavelength.

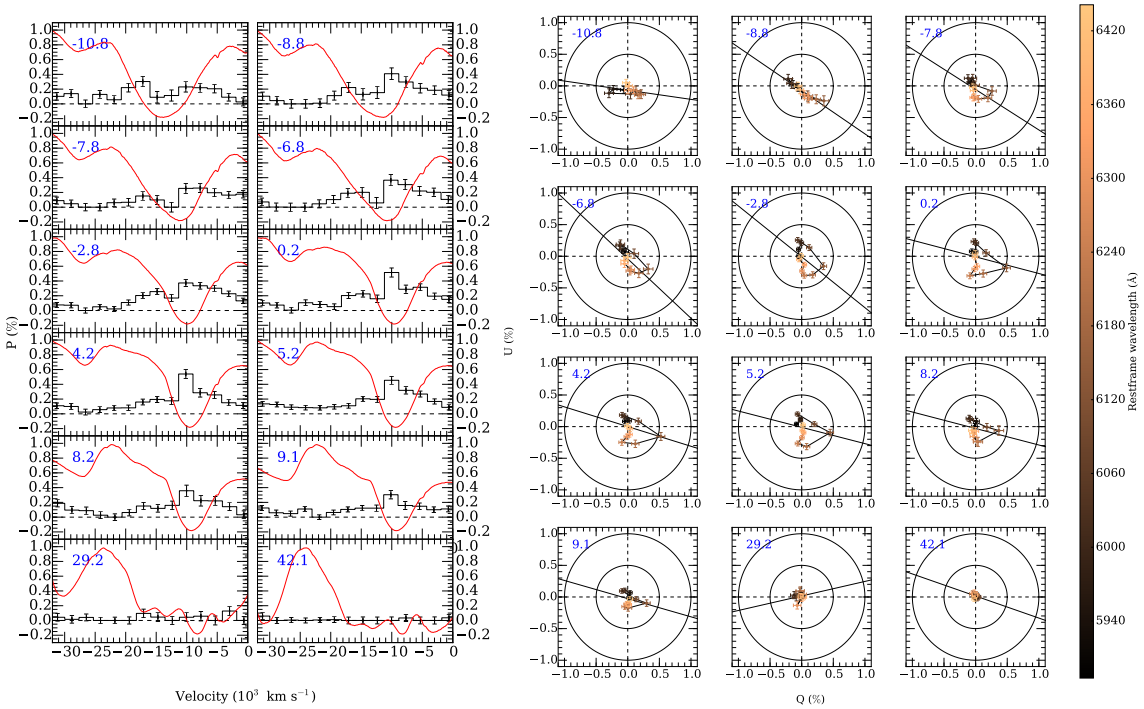

Figure C.17.: SN 2005df. *Left:* Polarization of the Si II λ6355Å line at different epochs relative to peak brightness (black bins). The flux spectrum is shown in red. *Right:* Polarization in the Q–U plane. The color indicates the wavelength.

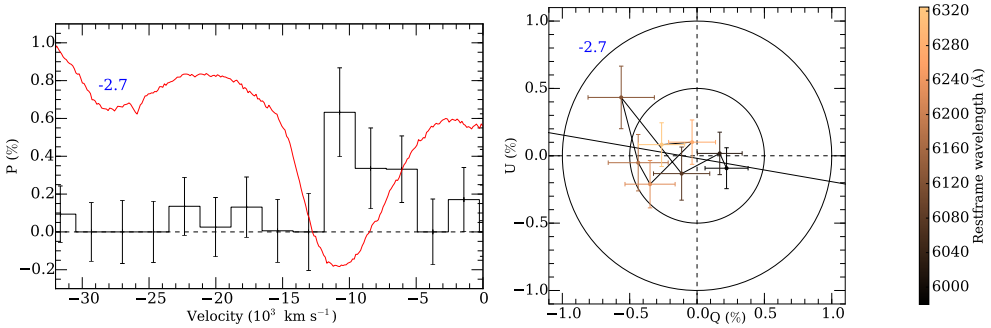

Figure C.18.: SN 2005el. *Left:* Polarization of the Si II λ6355Å line at different epochs relative to peak brightness (black bins). The flux spectrum is shown in red. *Right:* Polarization in the Q–U plane. The color indicates the wavelength.

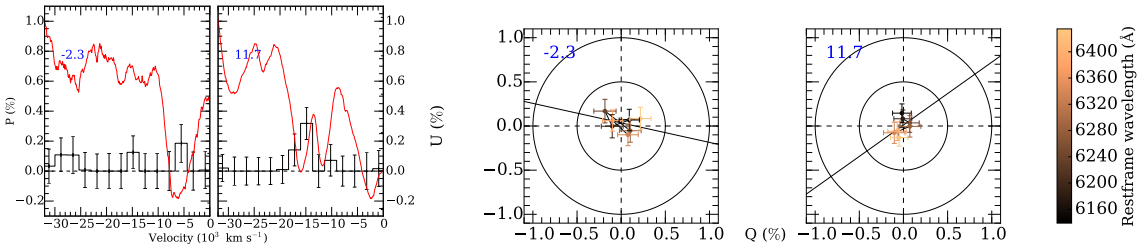

Figure C.19.: SN 2005hk. *Left:* Polarization of the Si II λ6355Å line at different epochs relative to peak brightness (black bins). The flux spectrum is shown in red. *Right:* Polarization in the Q–U plane. The color indicates the wavelength.

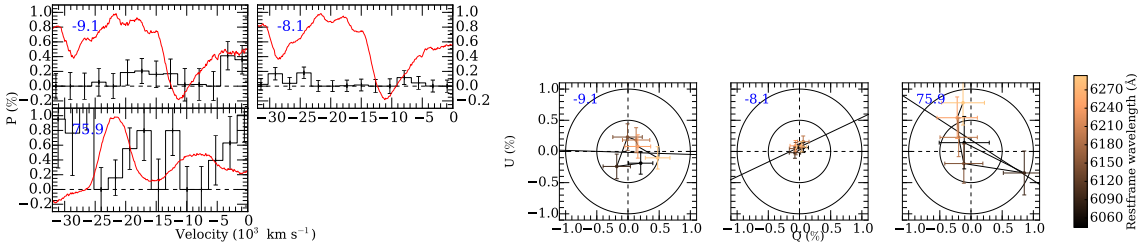

Figure C.20.: SN 2005ke. *Left:* Polarization of the Si II λ6355Å line at different epochs relative to peak brightness (black bins). The flux spectrum is shown in red. *Right:* Polarization in the Q–U plane. The color indicates the wavelength.

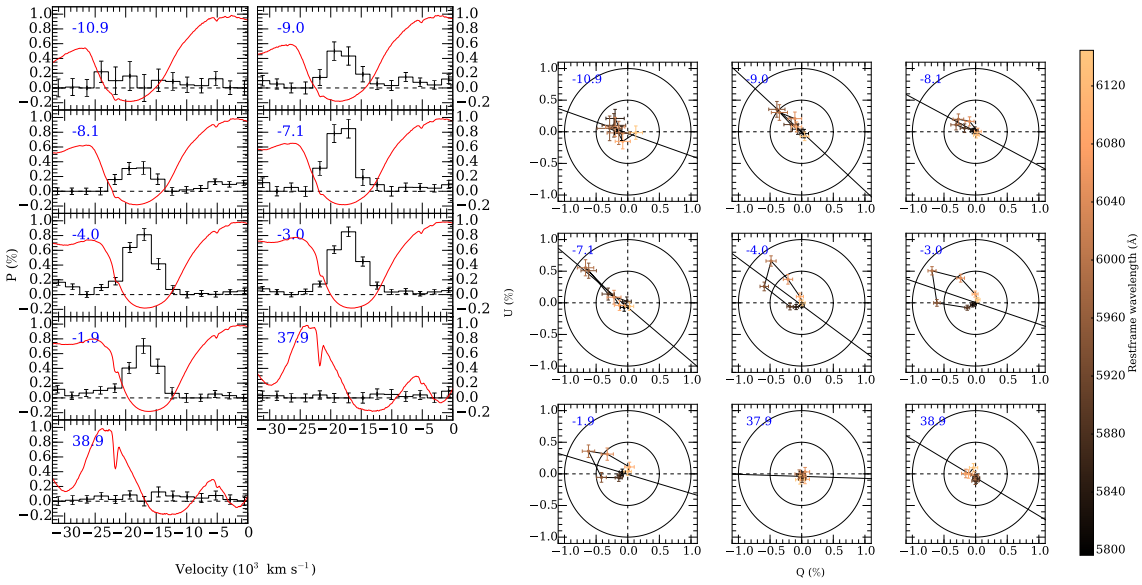

Figure C.21.: SN 2006X. *Left:* Polarization of the Si II λ6355Å line at different epochs relative to peak brightness (black bins). The flux spectrum is shown in red. *Right:* Polarization in the Q–U plane. The color indicates the wavelength.

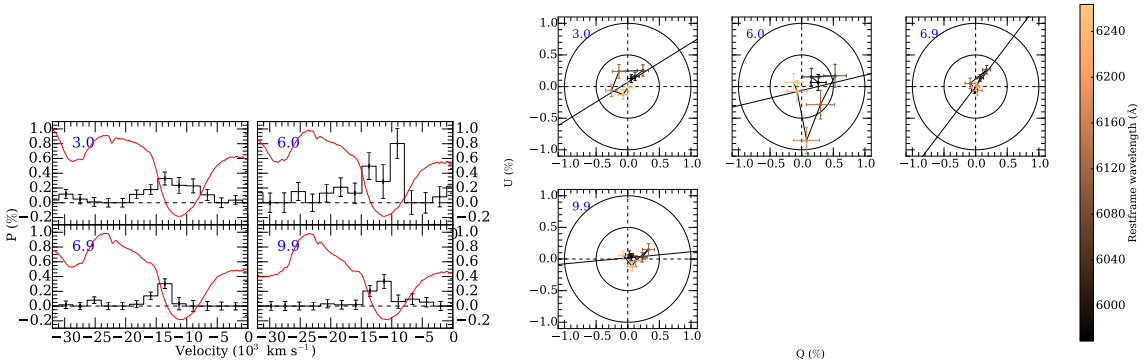

Figure C.22.: SN 2007fb. *Left:* Polarization of the Si II λ6355Å line at different epochs relative to peak brightness (black bins). The flux spectrum is shown in red. *Right:* Polarization in the Q–U plane. The color indicates the wavelength.

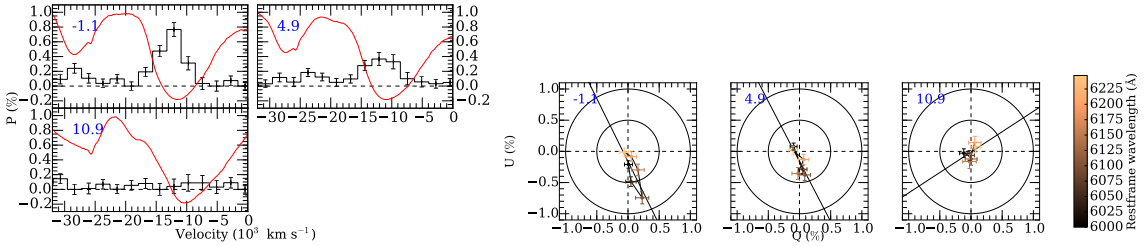

Figure C.23.: SN 2007hj. *Left:* Polarization of the Si II λ6355Å line at different epochs relative to peak brightness (black bins). The flux spectrum is shown in red. *Right:* Polarization in the Q–U plane. The color indicates the wavelength.

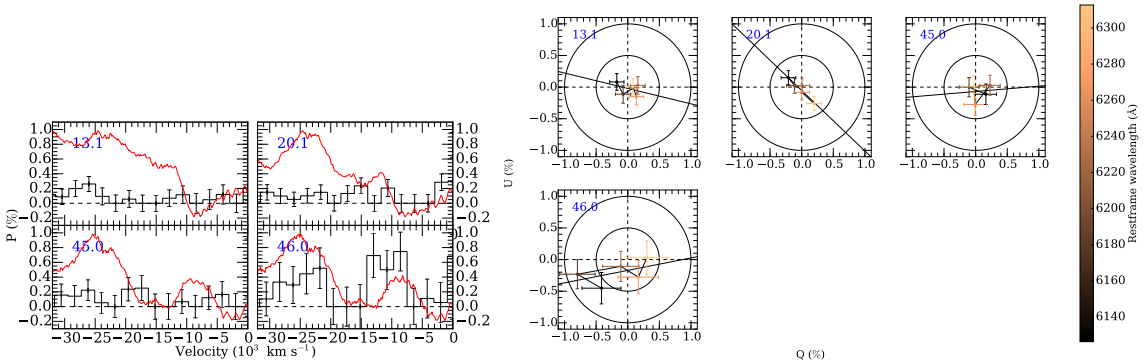

Figure C.24.: SN 2007if. *Left:* Polarization of the Si II λ6355Å line at different epochs relative to peak brightness (black bins). The flux spectrum is shown in red. *Right:* Polarization in the Q–U plane. The color indicates the wavelength.

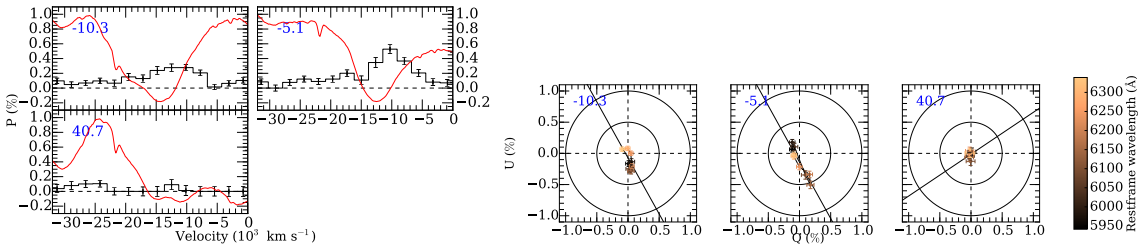

Figure C.25.: SN 2007le. *Left:* Polarization of the Si II λ6355Å line at different epochs relative to peak brightness (black bins). The flux spectrum is shown in red. *Right:* Polarization in the Q–U plane. The color indicates the wavelength.

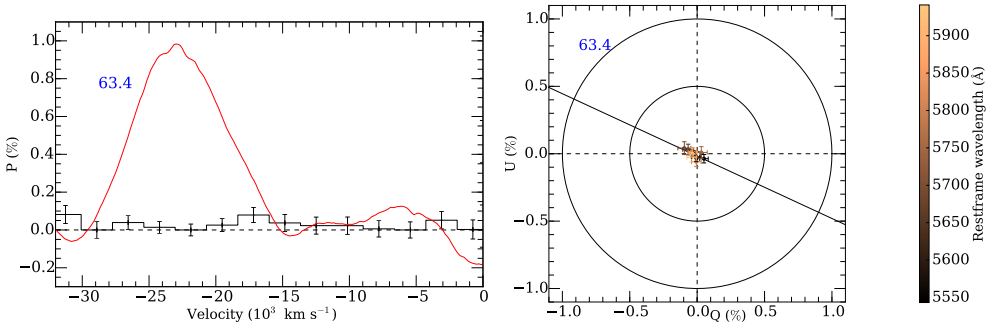

Figure C.26.: SN 2007sr. *Left:* Polarization of the Si II λ6355Å line at different epochs relative to peak brightness (black bins). The flux spectrum is shown in red. *Right:* Polarization in the Q–U plane. The color indicates the wavelength.

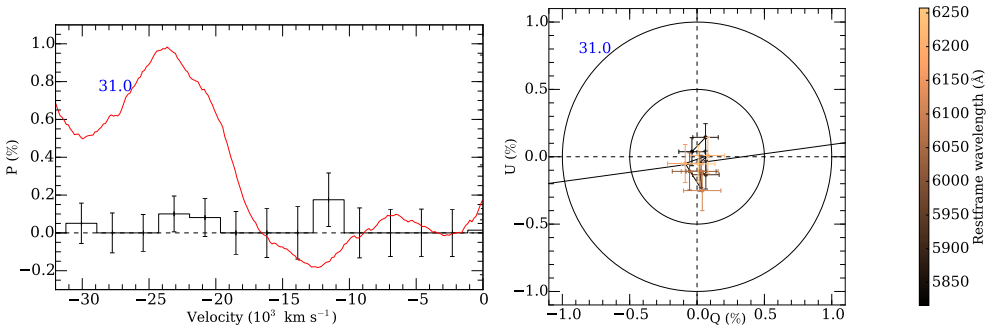

Figure C.27.: SN 2008ff. *Left:* Polarization of the Si II λ6355Å line at different epochs relative to peak brightness (black bins). The flux spectrum is shown in red. *Right:* Polarization in the Q–U plane. The color indicates the wavelength.

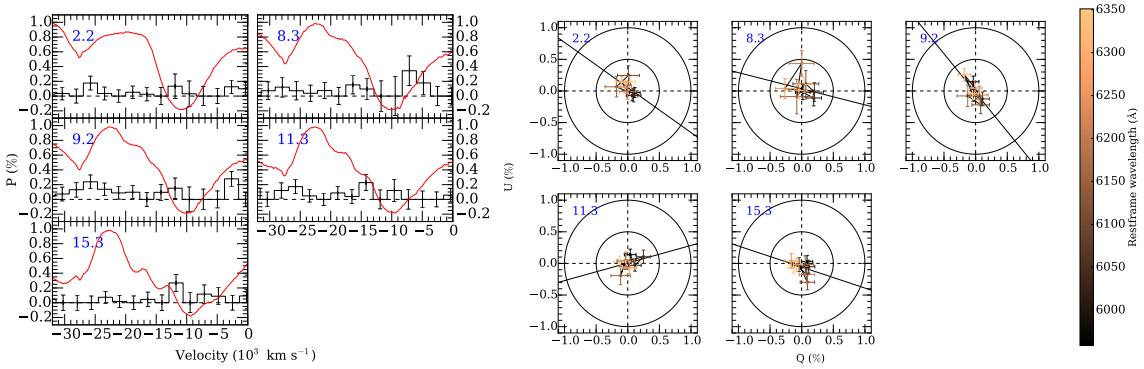

Figure C.28.: SN 2008fl. *Left:* Polarization of the Si II λ6355Å line at different epochs relative to peak brightness (black bins). The flux spectrum is shown in red. *Right:* Polarization in the Q–U plane. The color indicates the wavelength.

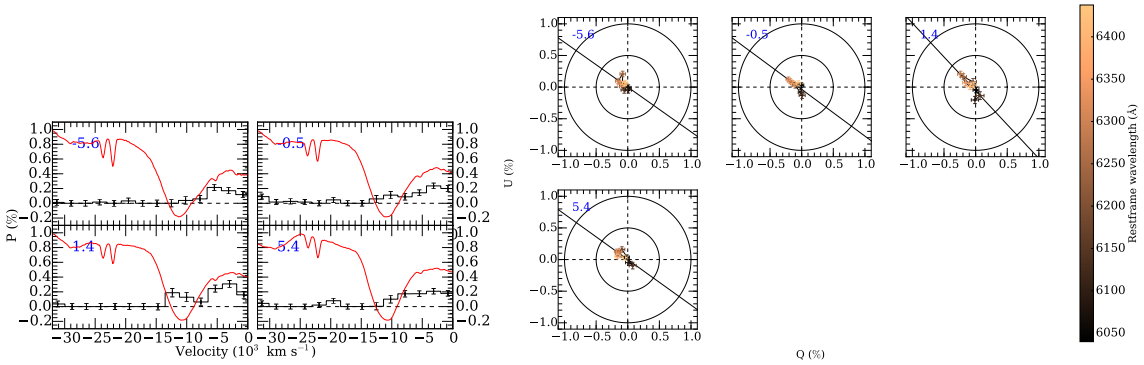

Figure C.29.: SN 2008fp. *Left:* Polarization of the Si II λ6355Å line at different epochs relative to peak brightness (black bins). The flux spectrum is shown in red. *Right:* Polarization in the Q–U plane. The color indicates the wavelength.

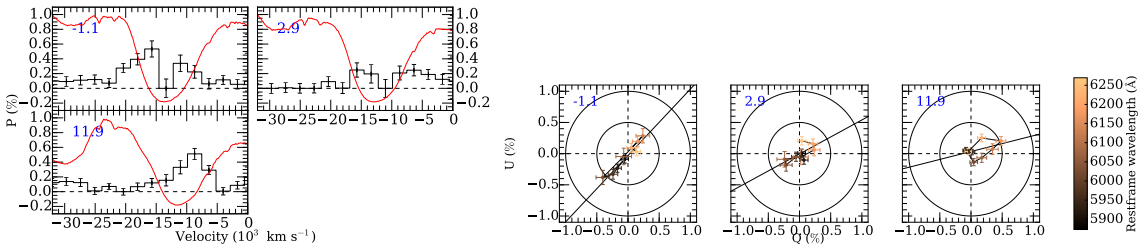

Figure C.30.: SN 2010ev. *Left:* Polarization of the Si II λ6355Å line at different epochs relative to peak brightness (black bins). The flux spectrum is shown in red. *Right:* Polarization in the Q–U plane. The color indicates the wavelength.

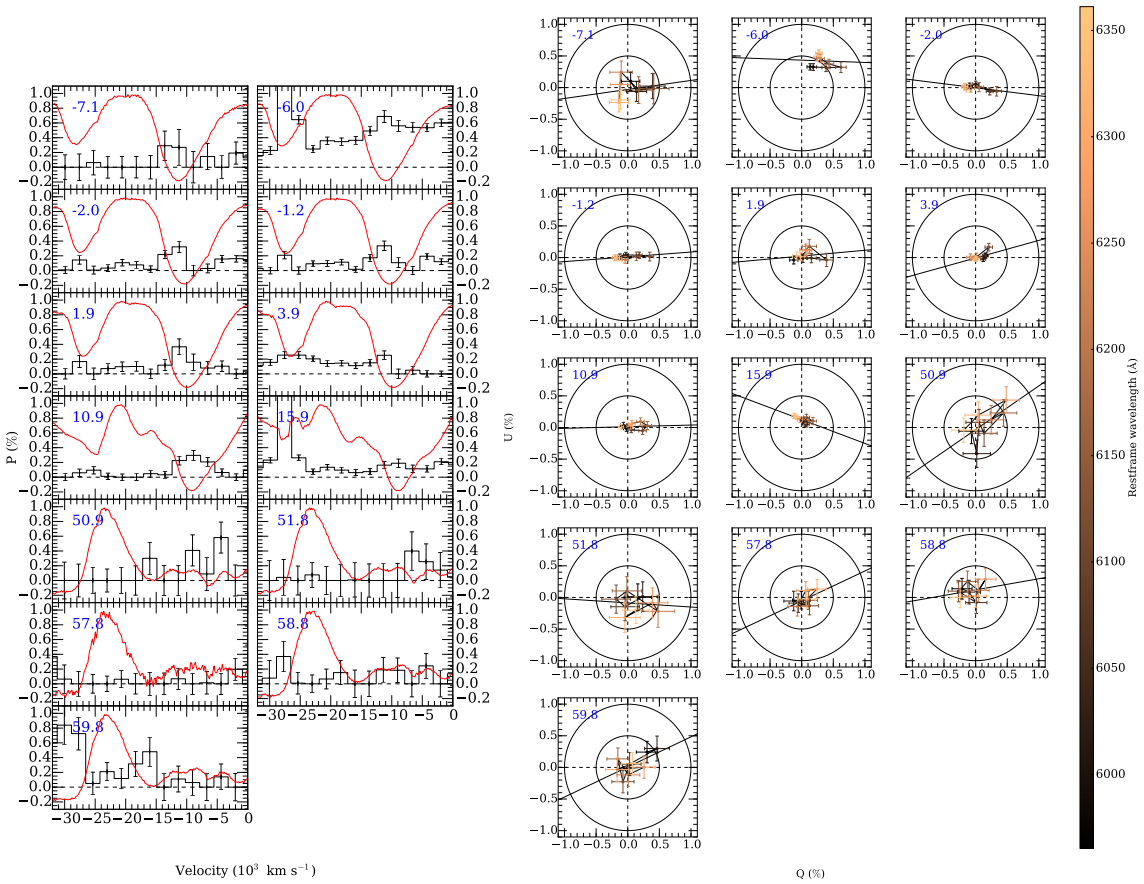

Figure C.31.: SN 2010ko. *Left:* Polarization of the Si II λ6355Å line at different epochs relative to peak brightness (black bins). The flux spectrum is shown in red. *Right:* Polarization in the Q–U plane. The color indicates the wavelength.

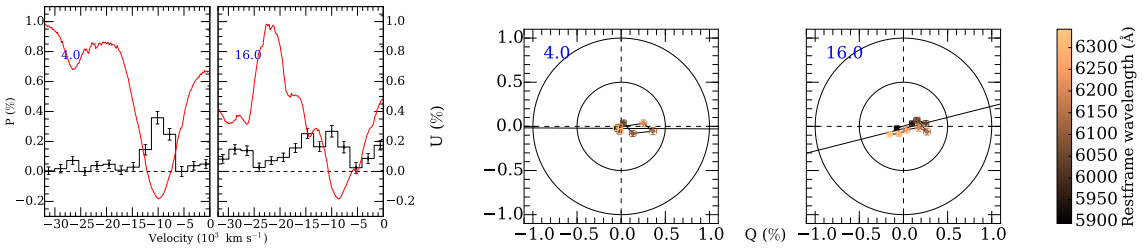

Figure C.32.: SN 2011ae. *Left:* Polarization of the Si II λ6355Å line at different epochs relative to peak brightness (black bins). The flux spectrum is shown in red. *Right:* Polarization in the Q–U plane. The color indicates the wavelength.

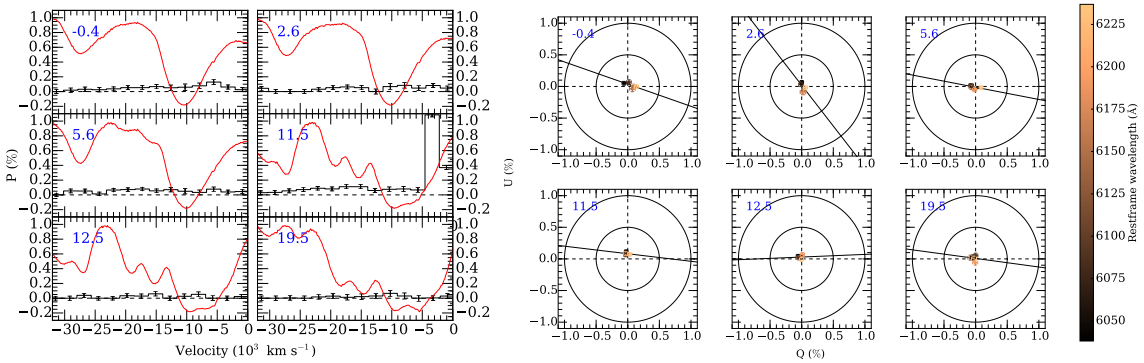

Figure C.33.: SN 2011iv. *Left:* Polarization of the Si II λ6355Å line at different epochs relative to peak brightness (black bins). The flux spectrum is shown in red. *Right:* Polarization in the Q–U plane. The color indicates the wavelength.

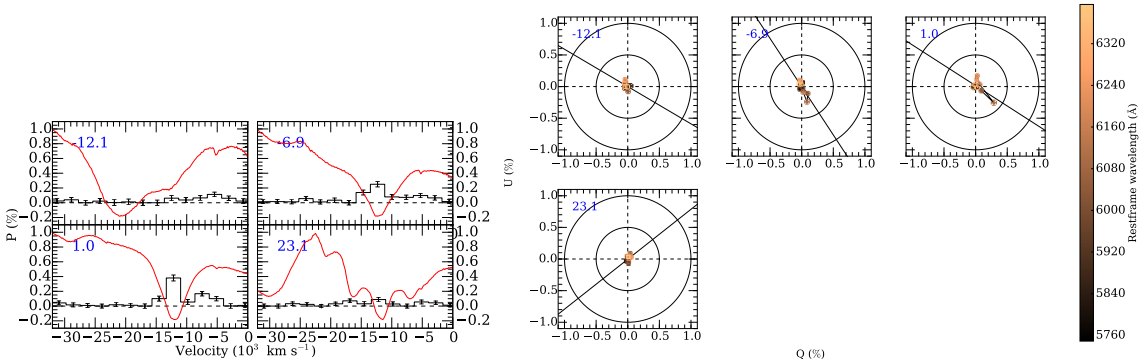

Figure C.34.: SN 2012fr. *Left:* Polarization of the Si II λ6355Å line at different epochs relative to peak brightness (black bins). The flux spectrum is shown in red. *Right:* Polarization in the Q–U plane. The color indicates the wavelength.

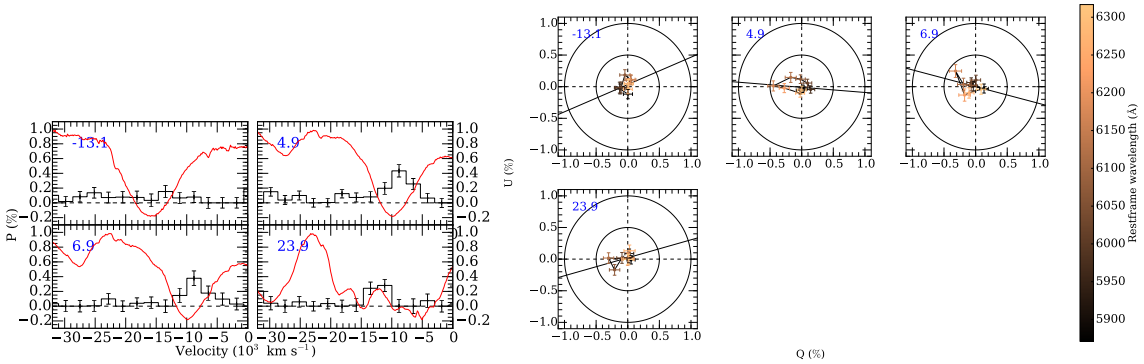

Figure C.35.: SN 2015ak. *Left:* Polarization of the Si II λ6355Å line at different epochs relative to peak brightness (black bins). The flux spectrum is shown in red. *Right:* Polarization in the Q–U plane. The color indicates the wavelength.

Acknowledgments

This thesis is dedicated to the memory of my father, who always believed in me and supported me through life and education.

Many thanks to my brother, my mother and grandparents for their support.

Special thanks to Nando Patat, for his mentorship at ESO, for introducing me to the world of spectropolarimetry, and investing many hours into discussions, reading and contributing to many papers and observing proposals that I wrote, and finally, writing many letters of recommendation. Thanks also to my fellow mentor, Annalisa De Cia, for your collaboration and support. It has been a true pleasure to work with you both!

Also, thank you Jason Spyromilio for your wise advice always when I needed it, the discussions about science ideas, and for writing many letters of recommendation. Many thanks also to Susana Deustua for your support through my education in the past decade, your hospitality at STScI, support through my job applications, and countless letters of recommendation for PhD and post-doc jobs.

Many thanks to Eric Emsellem, and the ESO's Office for Science for supporting my research and a dozen+ unforgettable international trips to conferences, collaboration visits, and observing trips. Thanks to the ESO Guesthouse in Santiago, and the La Silla and Paranal Observatory for their hospitality and taking care of me during my stay there. Special thanks to the La Silla staff for a remarkable experience, where I spend two Chilean summers, and to Tim de Zeeuw and Ivo Saviane for helping to organize a visit to the Las Campanas Observatory during Xmas 2016.

Thank you Dietrich Baade, Peter Höflich, and Mattia Bulla for many discussions and suggestions regarding my research on SNe Ia spectropolarimetry, and improving my proposals until they turn to successful ones.

Furthermore, thank you Lifan Wang, Stefano Bagnulo, Jeff Cooke, Igor Andreoni, Giorgos Leloudas, Ivo Seitenzahl, Ashley Ruiter, Joe Anderson, Mark Phillips, Simon Torres, Miguel Urbaneja, Francine Marleau, Milan Bogosavljević, and Hans Martin Schmid, for your hospitality during my visits. It is always a pleasure to exchange ideas with you.

I very appreciate to have my closest collaborators, co-authors on my papers, and colleagues not yet mentioned above. Thank you for your collaboration and your patience with me: Thiem Hoang, Stefan Taubenberger, Paola Mazzei, Nick Cox, Gioia Rau, Bruno Leibundgut, Carlo Manara, Tamar Faran, Jose Luis Ortiz, Wolfgang Kerzendorf, Na'ama Hallakun, Cosimo Inserra, Avishay Gal-Yam, Siyi Xu, Gesa Bertrang, Ting-Wan Chen and Stephen Smartt.

Thank you Eric Takasugi and Lisa Löbling for editing the language of the thesis.